



**HAL**  
open science

# Improving the sensitivity of mm-wave rotational spectroscopy in uniform supersonic flows for laboratory astrophysics applications

Omar Abdelkader Khedaoui

► **To cite this version:**

Omar Abdelkader Khedaoui. Improving the sensitivity of mm-wave rotational spectroscopy in uniform supersonic flows for laboratory astrophysics applications. Astrophysics [astro-ph]. Université de Rennes, 2022. English. NNT: 2022REN1S115 . tel-04131265

**HAL Id: tel-04131265**

**<https://theses.hal.science/tel-04131265>**

Submitted on 16 Jun 2023

**HAL** is a multi-disciplinary open access archive for the deposit and dissemination of scientific research documents, whether they are published or not. The documents may come from teaching and research institutions in France or abroad, or from public or private research centers.

L'archive ouverte pluridisciplinaire **HAL**, est destinée au dépôt et à la diffusion de documents scientifiques de niveau recherche, publiés ou non, émanant des établissements d'enseignement et de recherche français ou étrangers, des laboratoires publics ou privés.

# THESE DE DOCTORAT DE

L'UNIVERSITE DE RENNES 1

ECOLE DOCTORALE N° 596

*Matière, Molécules, Matériaux*

Spécialité : *Physique*

Par

**Omar ABDELKADER KHEDAOU**

**Improving the sensitivity of mm-wave rotational spectroscopy in uniform supersonic flows for laboratory astrophysics applications**

Thèse présentée et soutenue à Rennes, le 01/06/2022

Unité de recherche : Institut de Physique de Rennes UMR 6251

## Rapporteurs avant soutenance :

Olivier Chazot      Professeur      von Karman Institute for Fluid Dynamics, Belgique  
Kirill Prozument      Chemist      Argonne National Laboratory, Etats-Unis

## Composition du Jury :

|                 |                  |                             |   |
|-----------------|------------------|-----------------------------|---|
| Président :     | Robert Georges   | Professeur                  | Université de Rennes 1                  |
| Examineurs :    | Lam Nguyen       | Maître de Conférences (HDR) | Université Paris-Est Creteil            |
|                 | Olivier Chazot   | Professeur                  | von Karman Institute for Fluid Dynamics |
|                 | Kirill Prozument | Chemist                     | Argonne National Laboratory             |
| Dir. de thèse : | Ian Sims         | Professeur                  | Université de Rennes 1                  |

**Titre :** Amélioration de la sensibilité de détection de la spectroscopie rotationnelle millimétrique dans les écoulements supersoniques uniformes pour des applications d'astrophysique de laboratoire

**Mots clés :** CRESU, jet supersonique, spectroscopie rotationnelle, astrophysique de laboratoire

**Résumé :** Dans cette thèse, nous présentons la conception et le développement de deux nouveaux instruments afin d'optimiser les conditions expérimentales pour des applications d'astrophysique de laboratoire. L'objectif est d'étudier les processus collisionnels en phase gazeuse d'intérêt astrochimique à basse température en utilisant la technique CPUF (chirped pulse in uniform flow). Ce travail s'inscrit dans le cadre du projet CRESUCHIRP, un programme pluriannuel visant à construire un nouvel appareil CRESU (Cinétique de Réaction en Ecoulement Supersonique Uniforme) couplé à deux spectromètres CP-FTmmW (Chirped-Pulse Fourier Transform mm-Wave) dans le but de déterminer les rapports de branchement des réactions d'intérêt astrochimique. Bien que la spectroscopie CP-FTmmW soit très bien adaptée aux applications à basse température, son efficacité est affectée par de nombreuses difficultés techniques, la plus notable étant l'élargissement collisionnel, un phénomène induit par les collisions qui atténuent le signal moléculaire des espèces étudiées. Une série de mesures spectroscopiques avec un spectromètre en bande Ka a été réalisée à température ambiante pour évaluer son impact en utilisant deux molécules d'intérêt astrochimique, l'acrylonitrile et le benzonitrile sont mis en collisions avec l'hélium. Les résultats illustrent la nécessité d'optimiser l'environnement du CRESU pour permettre une détection quantitative des produits de réaction.

Dans ce travail, nous présentons le développement de l'appareil SKISURF (SKImmed uniform SUpeRsonic Flow), où le flux CRESU est échantillonné via un skimmer dans un processus d'expansion secondaire, ayant lieu dans un environnement à température et pression beaucoup plus basses en créant des conditions favorables pour la détection du signal moléculaire. Un spectromètre en bande E est utilisé pour la caractérisation et la réalisation des premières mesures du rapport de branchement de la réaction CN+ éthylène à 35 K, le sondage a été effectué à une température de ~ 5 K.

Un système d'une tuyère de Laval pulsée a été conçu, construit et caractérisé comme deuxième technique pour augmenter la sensibilité du CPUF. Il repose sur la pulsation des jets du CRESU à une fréquence synchronisée à l'aide d'un hacheur aérodynamique placé en amont de la tuyère de Laval ce qui permet d'augmenter l'efficacité du pompage et de réduire l'effet de pression. Il permet également de générer des flux à des températures beaucoup plus basses que celles de l'appareil CRESU classique, jusqu'à ~ 6 K. Le système présente aussi un avantage économique car il réduit la quantité de gaz et d'espèces consommés. Les aspects de la conception et la caractérisation à l'aide de méthodes numériques et expérimentales des instruments nouvellement développés sont évoqués.

**Title :** Improving the sensitivity of mm-wave rotational spectroscopy in uniform supersonic flows for laboratory astrophysics applications

**Keywords :** CRESU, supersonic flow, rotational spectroscopy, laboratory astrophysics

**Abstract :** In this thesis we present the design and the development of two novel instruments to optimize the experimental conditions for laboratory astrophysics applications to study gas phase collisional processes of astrochemical interest at low temperatures using the CPUF (chirped pulse in uniform flow) technique. CRESU (Cinétique de Réaction en Ecoulement Supersonique Uniforme) apparatus coupled with two Chirped-Pulse Fourier Transform mm-Wave (CP-FTmmW) spectrometers with the aim of the determination of branching ratios of multi-channel reactions relevant to astrochemistry. Although CP-FTmmW spectroscopy is very well suited for low temperature applications, its sensitivity is challenged by many technical difficulties, the most notorious is pressure broadening, a phenomenon induced by collisions that attenuates the molecular signal of the species studied. A series of spectroscopic measurements with a Ka band spectrometer were carried out at room temperature to assess its impact using two molecules of astrochemical interest, vinyl cyanide and benzonitrile colliding with a helium buffer. The results illustrate the need to optimize the CRESU environment to allow sensitive detection of reaction products. In this work we present the development of the SKISURF (SKImmed uniform SUpeRsonic Flow)

apparatus, where the CRESU flow is sampled via a skimmer in a secondary expansion process, into a much lower temperature and pressure environment creating favorable conditions for the detection of the molecular signal. An E band spectrometer is used for the characterization and conducting the first measurements of the branching ratio of the CN+ ethylene reaction at 35 K, the probing has been carried out at a temperature of ~ 5 K.

A pulsed Laval nozzle system has been designed, built and characterized as a second technique to increase the sensitivity of CPUF. It relies on pulsing the CRESU flows at a synchronized frequency with the use of an aerodynamic chopper upstream of the Laval nozzle which helps to increase the pumping efficiency and reduce the pressure effect. It also allows to generate a much lower temperature flows than the classic CRESU apparatus down to ~ 6 K. In addition, the system presents an economical advantage as it reduces the amount of gas and species consumed. The design aspects and the characterization using both numerical and experimental methods of the newly developed instruments are discussed.

*"I dare do all that may become a free man, who dares no more is none"*

## **Acknowledgments**

*I would like at the first place to express my special thanks and gratitude to my supervisor Pr. Ian Sims for giving me the opportunity to work on the CRESUCHIRP project, it has been such an inspiring and instructive adventure with all his instructions and directions during my thesis.*

*Many thanks to the team of the CRESUCHIRP project Thomas, Brian, Ilsa, Theo, Divita, Myriam and Alberto for all the great times we had together.*

*My acknowledgments go to Jonathan.C and my colleagues in the machining workshop Ewen, Alexandre, Jean-Charles, Guy, Julien and Didier with whom I worked closely for more than two years in designing and building the SKISURF apparatus and the pulsed laval nozzle system, which would not have been possible without their contribution and support especially during the difficult times of the Covid-19 pandemic.*

*I would also like to thank all my colleagues in the IPR, Ludovic, Sophie, Lucile, Jonathan.T, Olivier, Shubadip, Ahmad, Erwan and Jean-benoit, for the very nice time we had in the lab, special thanks to Abessamad, André and Robert for the interesting and fruitful discussions we had about compressible flow, Laval nozzles and CFD calculations.*

*Mach, Adel, Asma and Eszter, thank you for all the good times we spent in the lab and out and the nice restaurants we discovered in Rennes.*

*“To my dear Mother and father, no words can express how grateful I am, you have been my best support in life and to my beautiful brothers and sisters I am so lucky to have you always by my side.”*

# Table of contents

|  |             |
|--|-------------|
| <b>List of Tables</b> .....  | <b>VII</b>  |
| <b>List of Figures</b> .....   | <b>VIII</b> |
| <b>I. Introduction to gas phase chemistry and laboratory astrophysics</b> .....  | <b>1</b>    |
| I.1. Gas phase chemistry in the ISM.....   | 1           |
| I.2. Molecules in the ISM .....  | 3           |
| I.3. Laboratory astrophysics .....   | 5           |
| I.4. Introduction to reaction kinetics and gas phase collisional processes ..... | 7           |
| I.4.1. Reaction rate constant .....  | 7           |
| I.4.2. Reaction branching ratios .....   | 9           |
| I.4.3. Hard sphere collision model.....  | 10          |
| I.4.4. Reaction at low temperature .....   | 10          |
| I.5. Outlines of thesis and motivations .....                                    | 11          |
| References.....  | 13          |
| <b>II. Introduction to chirped pulse in uniform flow (CPUF)</b> .....            | <b>15</b>   |
| Introduction .....   | 15          |
| Part I: Introduction to the CRESU technique (cold supersonic flows) .....        | 16          |
| II.1. Introduction to compressible flows.....                                    | 16          |
| II.1.1. Compressible flows.....  | 17          |
| II.2. Isentropic expansions.....   | 18          |
| II.2.1. Isentropic Equations .....   | 18          |
| II.2.2. Euler equations .....  | 19          |
| II.3. Laval Nozzle.....  | 19          |
| II.4. Introduction to the CRESU technique.....                                   | 29          |
| II.4.1 Principle and theory .....  | 29          |
| II.5. Shockwaves .....   | 34          |
| II.5.1 Normal shock .....  | 35          |
| II.5.2. Oblique shock .....  | 35          |
| II.6. Comparison with other cooling technique.....                               | 36          |
| II.6.1. Cooling techniques .....   | 36          |
| II.6.2. Power of the CRESU technique.....  | 37          |
| Part II: Chirped pulse Fourier transform mm-microwave spectroscopy.....          | 38          |
| II.7. Introduction to microwave rotational spectroscopy .....                    | 38          |

|  |           |
|--|-----------|
| II.8. Chirped Pulse Fourier Transform mm-MicroWave Spectroscopy (CP-FTmm-MW) ..... | 40        |
| II.9. Microwave line intensities and shapes .....                                  | 42        |
| II.9.1. Natural linewidth .....  | 42        |
| II.9.2. Doppler broadening .....   | 42        |
| II.9.3. Pressure broadening.....   | 43        |
| II.9.4. FID modelling.....   | 44        |
| II.10. Chirped pulse in uniform flow (Spectroscopy in cold media) .....            | 45        |
| II.10.1. Boundary layer contribution to the molecular signal .....                 | 46        |
| References.....  | 48        |
| <b>III. Experimental setup and flow characterization methods.....</b>              | <b>52</b> |
| Part I: Description of the experimental setup .....                                | 53        |
| III.1. CRESU apparatus.....  | 53        |
| III.1.1. CRESU chamber .....   | 53        |
| III.1.2. Pumping group .....   | 54        |
| III.1.3. Mass flow controller system.....  | 55        |
| III.1.4. Controlled evaporation mixer (CEM) .....                                  | 55        |
| III.2. Generation of the CRESU flows.....  | 55        |
| III.2.1. Nozzle generation program .....   | 56        |
| III.2.2. Nozzle building using additive manufacturing procedure.....               | 56        |
| III.2.3. Pitot tube .....  | 60        |
| III.3. Generation of radicals using pulsed laser photolysis .....                  | 64        |
| III.3.1. Precursor flow.....   | 64        |
| III.3.2. Heat stabilizer.....  | 65        |
| III.3.3. UV-Visible spectrometer.....  | 65        |
| III.3.4. Excimer laser.....  | 65        |
| III.4. Molecular detection using CP-FTmmW spectroscopy.....                        | 66        |
| III.4.1. Spectrometer Design.....  | 66        |
| III.4.2. Sequence and data acquisition procedure .....                             | 70        |
| III.4.3. Flow cell .....   | 72        |
| Part II: Flow characterization.....  | 73        |
| III.5. Computational fluid dynamics .....  | 73        |
| III.5.1. Geometry.....   | 74        |
| III.5.2. Meshing.....  | 75        |

|  |            |
|--|------------|
| III.5.3. Setup .....   | 76         |
| III.5.4. Physical Properties .....   | 76         |
| III.5.5. Boundary conditions .....   | 77         |
| III.5.6. Initializing the solution .....   | 78         |
| III.5.7. Convergence and stability .....   | 79         |
| III.5.8. Post processing .....   | 80         |
| III.6. Pitot characterization.....   | 81         |
| III.6.1. Background .....  | 82         |
| III.6.2. Supersonic flow .....   | 82         |
| III.6.3. Accuracy and limitations.....   | 84         |
| III.7. Direct simulation Monte Carlo calculations .....  | 90         |
| III.7.1. Knudsen number .....  | 91         |
| III.7.2. DS2V program.....   | 93         |
| III.7.3. Power of DSMC over Navier-Stokes FEM.....   | 95         |
| III.8. Experimental characterization of rarefied media .....   | 96         |
| References.....  | 97         |
| <b>IV. Pressure broadening measurements using the Ka band CP-FTmmW spectrometer.....</b>   | <b>98</b>  |
| Introduction .....   | 99         |
| IV.1. Ka band Spectrometer .....   | 99         |
| IV.1.1. Instrument response .....  | 101        |
| IV.1.2. Averaging .....  | 106        |
| IV.1.3. Filtering.....   | 107        |
| IV.2. Pressure broadening measurements .....   | 108        |
| IV.2.1. Vinyl cyanide in the cell .....  | 109        |
| IV.2.2. CRESU measurements .....   | 113        |
| IV.2.3. Benzonitrile in the cell.....  | 114        |
| IV.3. Discussions and other limitations .....  | 117        |
| References.....  | 120        |
| <b>V. Secondary expansion chamber: development, characterization and application to the quantitative determination of reaction product branching ratios.....</b> | <b>124</b> |
| Introduction .....   | 124        |
| Part I: Design and characterization phase .....  | 127        |
| V.1. Secondary expansion chamber description .....   | 127        |

|  |            |
|--|------------|
| V.2. Upstream sampling CFD simulations.....                                      | 129        |
| V.2.1. Argon flow at 35 K (Ar-35K-0.28 nozzle).....                              | 131        |
| V.3. Post skimmer expansion.....   | 133        |
| V.3.1. Post-skimmer expansion simulations.....                                   | 135        |
| V.4. Power of the skimmer setup (comparison to classic CRESU) .....              | 142        |
| Part II: Experimental results .....  | 144        |
| V.5. Photolysis and bimolecular reaction results .....                           | 144        |
| V.5.1. Photolysis Results.....   | 144        |
| V.5.2. Bimolecular reactions results .....                                       | 149        |
| References.....  | 161        |
| <b>VI. Pulsed system: A new optimizing apparatus for CPUF applications .....</b> | <b>164</b> |
| VI.1. State of art.....  | 166        |
| VI.2. Design and construction.....   | 168        |
| VI.2.1. The disk geometry .....  | 168        |
| VI.2.2. The motor .....  | 170        |
| VI.2.3. The alignment.....   | 172        |
| Part II: Characterization of the CRESU flow in the pulsed mode .....             | 176        |
| VI.3. Fast Pitot measurements.....   | 176        |
| VI.4. Future work .....  | 180        |
| VI.4.1. High frequency mode.....   | 181        |
| VI.4.2. Running on microwave .....   | 181        |
| References.....  | 182        |
| <b>VII. Conclusions and perspectives.....</b>                                    | <b>184</b> |
| VII.1. Conclusions and discussions .....   | 184        |
| VII.2. Future directions .....   | 187        |
| <b>Appendix .....</b>  | <b>a</b>   |
| A.III. Flow conditions in CRESU environment.....                                 | b          |
| A. IV. Ka band and pressure broadening measurements.....                         | i          |
| A.V. Secondary expansion apparatus: tools and method of characterization .....   | l          |
| A.VI. Pulsed system: motor characteristics .....                                 | p          |
| <b>Résumé détaillé .....</b>   | <b>q</b>   |

## List of Tables

|   |     |
|---|-----|
| Table I-1: List of molecules discovered in the ISM between 2018 and 2020 <sup>10</sup> .....  | 4   |
| Table I-2: List of molecules discovered in the ISM in 2021 <sup>10</sup> .....  | 5   |
| Table II-1: Variation of the flow properties with the cross-section.....  | 23  |
| Table III-1: Different operating conditions of the nitrogen CRESU flow designed for 83 K .....  | 85  |
| Table IV-1. The electrical field strength within the flow cell.....   | 104 |
| Table IV-2. Pressure broadening coefficients for collisions with helium of different transitions of vinyl cyanide as determined to pressure broadening data. ....   | 112 |
| Table IV-3. Pressure broadening coefficients for various transitions of benzonitrile with two different collisional systems. ....   | 115 |
| Table IV-4. Pressure broadening rates for related molecules for a range of different transitions with He as the collider. ....  | 115 |
| Table IV-5. Pressure broadening coefficients for collisions with He of different transitions of vinyl cyanide as determined through different methods Uncertainties are taken as the 95% confidence interval for the linear fit to pressure broadening data. .... | 117 |
| Table IV-6. Pressure broadening coefficients for various transitions of benzonitrile. Uncertainties are taken as the 95% confidence interval for the linear fit to pressure broadening data.....  | 118 |
| Table V-1: Calibration of vinyl cyanide yielded from CN+C <sub>2</sub> H <sub>4</sub> reaction .....  | 156 |
| Table V-2: Calibration of vinyl cyanide yielded from CN+C <sub>2</sub> H <sub>4</sub> reaction .....  | 158 |
| Table VI-1. Comparison of the flow parameters of the N <sub>2</sub> -30K-0.183 in the continuous and the pulsed mode .....  | 179 |

## List of Figures

|  |    |
|--|----|
| Figure I-1. NGC 7380 star cluster illustrating the complex interplay of gas, dust and radiation present in the astronomical environment. Image by Bouhaddou Astrophotography .....   | 2  |
| Figure I-2. Cumulative number of known interstellar molecules over time. An average of 3.7 new detections of interstellar molecules per year can be seen after the commissioning of several major contributing facilities, noted with arrows. Figure from McGuire 2018 <sup>11</sup> .....   | 3  |
| Figure I-3. Violin plot of the mass of molecules detected in each wavelength range. Figure from McGuire 2018 <sup>11</sup> .....   | 4  |
| Figure I-4. Three pillars of astrochemistry, an example of benzonitrile laboratory measurements: a benzonitrile spectrum measured in this work at room temperature using the Ka band chirped pulse Fourier transform mm-wave spectrometer operating in a frequency range of 26.5 to 40 GHz (presented in chapter IV); Astronomical observation: a spectrum of benzonitrile measured by McGuire and co-workers <sup>12</sup> ; Astrochemical modelling: Results of an astrochemical model by McGuire and co-workers, <sup>12</sup> of gas-phase column densities of CN, HC <sub>3</sub> N, HC <sub>5</sub> N, HC <sub>7</sub> N, HC <sub>9</sub> N with focus on benzonitrile (in black) in TMC-1 as a function of time in solid colored lines. The dots represent the abundances of observed species. .... | 6  |
| Figure I-5. Example of the determination of the rate constant of the OH+CO reaction at 23.5 K as part of a thesis project led by Messinger and co-workers <sup>16</sup> .....  | 9  |
| Figure II-1. Flow regimes according to the Mach number.....  | 18 |
| Figure II-2. Operation principle of a convergent divergent nozzle.....   | 20 |
| Figure II-3. Gas expansion carried in a Laval nozzle.....  | 21 |
| Figure II-4. Variation of the flow properties in an isentropic expansion in a Laval nozzle along the axis of symmetry, the expansion is calculated with the computational fluid dynamics software Ansys Fluent using nitrogen as a buffer expanding from 770 mbar at room temperature to 0.11 mbar in the chamber, the expansion produces a flow at 23.5 K with Mach 7. ....   | 24 |
| Figure II-5. Determination of the isentropic core profile with the characteristic lines. Figure from by Canosa and Jiménez, Laval nozzles: Design, characterization and applications [unpublished manuscript].....   | 27 |
| Figure II-6. Nozzle profiles, in dashed black lines, the isentropic profile given by the method of characteristics and resulting the cold isentropic core (free flow) in continuous black line due to the manifestation of the boundary layer with a thickness $\delta$ , the nozzle wall contour (real nozzle profile) is given in blue line as the sum of the inviscid contour and the displacement thickness. Figure from Fournier and co-workers <sup>12</sup> .....   | 28 |
| Figure II-7. 2D temperature profile of the lowest temperature reached under continuous CRESU conditions without precooling the gas in the reservoir using helium buffer, the color shows a temperature variation between 9 and 12 K in the isentropic core, the average temperature is approximately 10 K and the flow lasts for approximately 200   |    |

|   |    |
|---|----|
| $\mu$ s, the results were acquired with impact pressure measurements using a Pitot tube as will be shown in the next chapter .....  | 30 |
| Figure II-8. Plot of the flow patterns with respect to the back pressure and the stagnation pressure ratio. Figure from Fluid Mechanics (Fifth Edition, 2012) by Kundu, P. K., Cohen, I. M., Dowling, D. R., Eds <sup>20</sup> .....  | 31 |
| Figure II-9. 2D Mach number profile of a nitrogen nozzle operating in an under expanded regime, the simulations are carried out with the computational fluid dynamics software Ansys Fluent using nitrogen as a buffer expanding from 770 mbar at room temperature to 0.05 mbar in the chamber.....   | 32 |
| Figure II-10. 2D Mach number profile of a nitrogen nozzle operating in an over expanded regime, the simulation is carried out with the computational fluid dynamics software Ansys Fluent using nitrogen as a buffer expanding from 770 mbar at room temperature to 0.30 mbar in the chamber.....   | 33 |
| Figure II-11. Shock diamonds formed in the after body of an F-15 Fighter jet (Reuters) .....  | 33 |
| Figure II-12. 2D Mach number profile of a nitrogen nozzle operating in an ideal regime, the simulation is carried out with the computational fluid dynamics software Ansys Fluent using nitrogen as a buffer expanding from 770 mbar at room temperature to 0.11 mbar in the chamber.....   | 34 |
| Figure II-13. Energy levels in asymmetric top molecules, the limits $K_a$ and $K_c$ represent the prolate and oblate symmetric top molecules. Figure adapted from Lombardi 2007. <sup>31</sup> .....  | 39 |
| Figure II-14. Chirped pulse procedure, (a) broadband excitation of molecules, (b) relaxation to initial state by FID emission, (c) rotational spectrum of vinyl cyanide acquired by Fourier transforming the FID, vinyl cyanide isotopologues have been detected, the spectrum (in red) is acquired from vinyl cyanide in an argon flow at 35 K sampled via a skimmer into a secondary expansion chamber (see chapter V), the transition in colors are synthetic spectra at 9.375 K from CDMS.....  | 41 |
| Figure II-15. Benzonitrile rotational spectra at 300K and 9.375 K given by the CDMS catalogue .....   | 45 |
| Figure II-16. Signal variation of the $J_{k_a,k_c} = 7_{0,7}-6_{0,6}$ vinyl cyanide transition between 20 K and 300 K assuming a linear radial probing of a CRESU flow generated from the nitrogen 23.5 K nozzle. The density decreases with the increasing temperature as we move away from the axis of symmetry, the intensities have been normalized with the strongest signal calculated at 20 K and corrected with the radial density profile, the results show that temperatures below 30 K make the main contribution to the molecular signal, a drop of an order of magnitude in the signal strength at temperatures above 40 K is observed. This effect is enhanced by the density gradient as we move away from the flow and two orders of magnitude at 100 K. .... | 46 |
| Figure III-1. Experimental setup CRESUCHIRP and CRESU B chamber with the E band broadcast spectrometer .....  | 54 |
| Figure III-2. (a) Mass flow controller system, (b) is the controlled evaporation mixing system .....  | 55 |

|  |    |
|--|----|
| Figure III-3. Nozzle profile generated using the program written by J,-B Marquette <sup>2</sup>  | 56 |
| Figure III-4. Laval nozzle 3D printing procedure (a) shows the preparation of the printing file of the helium 10 K nozzle using Preform software to communicate with the 3D printer, (b) displays the nozzle under UV curing after printing.....   | 58 |
| Figure III-5. Gain in the rigidity (tensile modulus) of the 3D printed pieces after UV curing. Figure from Formlabs support <sup>3</sup> .....   | 59 |
| Figure III-6. Series of Laval nozzles used in Rennes, all the 3D printed nozzles have been designed and machined in this work (All 3D printed nozzles used for this work and of colleagues are given in the Table of nozzles. See appendix A.III).....   | 59 |
| Figure III-7. Nitrogen 38 K nozzle, (a) and (b) are the two printed parts in Preform and (c) shows a picture of the assembled nozzle .....   | 60 |
| Figure III-8.(a) photo of the Pitot tube inside CRESU B chamber, (b) and (c) show the 1D and 2D profiles of temperature and density of a helium nozzle operating at $(18.72 \pm 0.45)$ K. ....   | 61 |
| Figure III-9. Characterization of the He-10K-0.128 nozzle using the Pitot tube, figure (a) shows 1D temperature, Mach number and the density profile along the axis of the chamber and (b) gives the 2D density profile, the nozzle has operating condition of 540 mbar in the reservoir and 0.128 mbar in the chamber and is able to sustain a uniform flow of more than 30 cm. ....  | 62 |
| Figure III-10. Characterization of the N <sub>2</sub> -23.5K-0.12 nozzle using the Pitot tube, figure (a) shows 1D temperature, Mach number and the density profile along the axis of the chamber and (b) gives the 2D density profile, the nozzle has operating conditions of 773.7 mbar in the reservoir and 0.12 mbar in the chamber and is able to sustain a uniform flow of more than 40 cm. ....   | 63 |
| Figure III-11. (a) glass vessel containing ICN, (b) glass vessel covered with heating pad .....  | 64 |
| Figure III-12. Configuration of the E band spectrometer .....  | 67 |
| Figure III-13. Schematic of the CRESUCHIRP chamber, the reservoir and the nozzle are in compartment B, the spectrometer is mounted on section C, the excimer laser beam passes through the axis of the chamber via the two Brewster windows fixed on the KF 40 flanges at the two ends of the chamber. An additional compartment is added between C and D for the secondary expansion chamber which will presented in Chapter V. Figure credit to Theo Guillaume ..... | 69 |
| Figure III-14. Spectroscopic probing in the CRESU chamber, (a) shows a schematic of the probing, (b) gives the different microwave pieces assembled to connect the spectrometer to the CRESU chamber .....   | 70 |
| Figure III-15. Frame of 10 $\mu$ s for signal acquisitions under the skimmer conditions, under the CRESU conditions, the frame is reduced to 2.5 $\mu$ s because of rapid quenching of the FID. ....   | 71 |
| Figure III-16. The top panel shows the signal acquisition procedure of 800 $\mu$ s of flow time, with 80 frames of 10 $\mu$ s where the blue line represents the time of the laser shot to initiate the reaction and is implemented on the 10 <sup>th</sup> frame, the bottom figure gives the corresponding time dependent signal obtained by Fourier transforming the FIDs   |    |

|  |    |
|--|----|
| contained in the 80 frames, two frames are horizontally averaged to increase the signal to noise ratio (SNR). .....  | 71 |
| Figure III-17. Schematic of the flow cell .....  | 72 |
| Figure III-18. Simulation steps diagram with the duration of each procedure .....  | 74 |
| Figure III-19. Geometry of the CRESU expansion as set in Fluent.....   | 75 |
| Figure III-20. Different types of 2D meshing, (a) shows quadrilateral meshing, (b) is the unstructured triangular meshing and (c) shows hybrid meshing between quadrilateral and triangular.....   | 76 |
| Figure III-21. Viscosity variation with temperature for nitrogen in CRESU temperature interval given by the Sutherland model in Ansys Fluent .....   | 77 |
| Figure III-22. Display of the 2D axisymmetric geometry in fluent, the figure shows the Laval nozzle with part from the reservoir and the expansion chamber, the blue arrows indicate the flow entry regions while the red ones are for the flow output, the refined mesh is in green. ....   | 78 |
| Figure III-23. Convergence criterion decrease with iterations of flow variables, results are taken from calculations of the N2-30 K-0.183 Laval expansion, the method solves the continuity, momentum and the energy equations as shown by the caption .....   | 79 |
| Figure III-24. Results given and displayed by fluent Post processing interface, (a) shows 2D mapping of the temperature profile, (b) and (c) display the temperature and the velocity profiles respectively along the axis of the geometry .....   | 80 |
| Figure III-25. Simulation procedure flow chart .....   | 81 |
| Figure III-26. Schematic of Pitot characterization of CRESU flow using a Pitot tube, the results show a 2D temperature profile from an argon flow at 35 K, a shockwave has been formed 1 mm before the tube entry.....   | 83 |
| Figure III-27. Comparison between simulation and Pitot characterization, results from nitrogen flow under CRESU conditions .....   | 84 |
| Figure III-28. 1D temperature profiles of the different operating conditions of the N2-83 K nozzle .....   | 86 |
| Figure III-29. Impact pressure measurements of nitrogen CRESU flow at 30 K carrying increasing concentrations of C <sub>2</sub> H <sub>4</sub> .....   | 87 |
| Figure III-30. Plots of impact pressure measurements from nitrogen CRESU flow at 30 K from the N <sub>2</sub> -30K-0.183 nozzle carrying different concentrations of C <sub>2</sub> H <sub>4</sub> with the corresponding errors from the original flow.....   | 88 |
| Figure III-31. 2D plot of the impact pressure of the original profile of the N <sub>2</sub> -30K-0.183 nozzle, the result indicates that impact pressures below 8.5 mbar do not characterize the isentropic core of the original conditions.....   | 89 |
| Figure III-32. Temperature profiles along the axis from impact pressure measurements of nitrogen CRESU flow at 30 K carrying increasing concentrations of CO, the inset gives a zoom on the temperature. The measurements were taken with the N <sub>2</sub> -30K-0.183 nozzle the lowest temperature nitrogen nozzle at that time. .... | 90 |
| Figure III-33. Example of a geometry of a supersonic expansion via a skimmer .....   | 91 |
| Figure III-34. Flow regimes according to the corresponding Knudsen number values .....   | 92 |

|  |     |
|--|-----|
| Figure III-35. DS2V graphical user interface.....  | 93  |
| Figure III-36. Temperature profile along the axis of a supersonic flow in a slip regime<br>.....   | 95  |
| Figure IV-1. Configuration of the Ka band spectrometer (Design credit to Thomas Hearne).....   | 100 |
| Figure IV-2. Upper panel shows a spectrogram of a 15 GHz chirp recorded across the Ka band, the strongest intensity corresponds to 0 dB, lower panel shows the recorded chirp.....   | 102 |
| Figure IV-3. The intensity of the $J_{ka,kc} = 4_{0,4} - 3_{0,3}$ transition of vinyl cyanide plot as a function of excitation duration. Excitation pulses are a single-frequency resonant with the transition energy. The fitting parameters $\tau$ and $\omega_f$ are determined by a least-squares fit of the Rabi cycle formula to the experimental data. The uncertainties given are the 95% confidence intervals for the fit. ....                       | 103 |
| Figure IV-4. Spectrograms of a 15 GHz bandwidth chirp mixed with an LO of 26 GHz (a) and with an LO of 40.2 GHz (b) across the Ka band, the strongest intensity corresponds to 0 dB. ....  | 105 |
| Figure IV-5. Power loss in a 15 GHz chirp mixed with an LO of 26 GHz (red) and with an LO of 40.2 GHz (blue).....  | 105 |
| Figure IV-6. Improvement of the SNR with averaging a molecular signal from 25000 to 5 millions, figure (a) shows the recorded FIDs and figure (b) shows their corresponding Fourier transforms .....   | 106 |
| Figure IV-7. Plot of the SNR given by the Ka band chirped pulse Fourier transform spectrometer against the square root of the number averages taken for a given signal. The black line shows ideal theoretical performance. ....   | 107 |
| Figure IV-8. Comparison between filtered (in red) and raw spectrum (in black) recorded with the Ka band targeting the $J_{ka,kc} = 3_{12} - 2_{11}$ rotational transition of vinyl cyanide at room temperature and 11 $\mu$ bar .....  | 108 |
| Figure IV-9. Recorded FIDs of the the $J = 6-5$ transition of OCS in the flow cell at room temperature, the partial pressure is maintained at $5 \times 10^{-5}$ mbar with the helium pressure is increased in the cell for every measurement. Figure adapted from Hays et al <sup>17</sup> . ....   | 109 |
| Figure IV-10. Recorded FIDs and corresponding FFTs showing (a) the $J_{ka,kc} = 3_{1,2} - 2_{1,1}$ and (b) the $J_{ka,kc} = 4_{1,3} - 3_{1,2}$ transitions of vinyl cyanide with increasing helium pressure in the flow cell at room temperature.....  | 110 |
| Figure IV-11. Time domain Voigt profile fit of (a) the $J_{ka,kc} = 3_{1,2} - 2_{1,1}$ and (b) the $J_{ka,kc} = 4_{1,3} - 3_{1,2}$ transitions of vinyl cyanide at 11 $\mu$ bar, in the left are the fits of the recorded FIDs and the residual, and on the right their give their corresponding FFTs. ....  | 111 |
| Figure IV-12. Plots of the HWHM of the Lorentzian component of the Voigt profile fit to FIDs of two different transitions of vinyl cyanide at different pressures, using the time domain Voigt fitting. Part (a) shows the pressure broadening of the $3_{1,2} \rightarrow 2_{1,1}$ transition, part (b) shows the broadening of the $4_{1,3} \rightarrow 3_{1,2}$ transition. Uncertainties are taken as the 95% confidence interval for the linear fit ..... | 112 |

Figure IV-13. Time domain Voigt profile fit of the  $J_{ka,kc} = 3_{1,2} - 2_{1,1}$  transition of vinyl cyanide at 51  $\mu$ bar (a) shows the fit of the recorded FID and the residual, figure (b) gives the corresponding FFTs. .... 113

Figure IV-14. Rotational spectrum of vinyl cyanide in a cold CRESU flow of 18.7 K recorded using a Ka band CP-FTmmW spectrometer. Each section of the spectrum was probed individually. The spectrum displayed is the magnitude of the Fourier transform of the recorded signals, normalized to the most intense peak. The experimental spectrum is compared to theoretical transition frequencies and intensities at 18.75 K taken from the CDMS.<sup>24,25</sup> ..... 113

Figure IV-15. Plot of the HWHM of the Lorentzian component of the Voigt profile fit to the Fourier transform of the FID of the  $J_{ka,kc} = 15_{2,14} - 14_{2,13}$  (a) and  $J_{ka,kc} = 14_{0,14} - 13_{0,13}$  (b) transitions of benzonitrile. The equations of the linear fit to the data are given with 95% confidence interval..... 115

Figure IV-16. Time domain signal pulse, reflections and early FID, in orange a signal recorded from flowing vinyl cyanide in the cell and in red the noise recorded from a blank scan with no gas in the cell ..... 118

Figure V-1. Spectrum of vinyl cyanide given by CDMS at 300 K (top) and 9.375 K (bottom), the E and Ka band ranges are displayed in grey and green respectively, at 9.375 K the vinyl cyanide strongest transition are shifted to the E band..... 125

Figure V-2. Schematic of the principle of beam sampling from CRESU flows ..... 126

Figure V-3. Schematic of the modified CRESU chamber containing the secondary expansion chamber, left to right: reservoir with Brewster window allowing passage of the laser beam through the Laval nozzle, followed by the skimmer chamber and its support then the turbomolecular pump. The spectrometer can be mounted via one of the three ports in the secondary expansion chamber. .... 127

Figure V-4. left figure shows an Airfoil system to sample CRESU flow from Das et al,<sup>11</sup> right figure represents a velocity profile from a CFD simulation of a reproduced airfoil geometry, simulating a uniform supersonic argon flow at 35 K, 0.28 mbar and Mach 4.7 expanding through the 5 mm aperture, the system poses a risk of forming a detached shockwave that destroys the supersonic flow and increases its temperature before it re-expands through the aperture. .... 128

Figure V-5. CFD simulations of the temperature as a flow property of the CRESU flow from the Ar-50K-0.3 nozzle being sampled with the 4 mm skimmer mounted on the non-optimized support, inset: zoom on the entry of the skimmer shows a detached shockwave formed before sampling ..... 129

Figure V-6. CFD simulations of the temperature as a flow property of the CRESU flow from the Ar-50K-0.7 nozzle being sampled with the skimmer mounted on the non-optimized support, inset: zoom on the entry of the skimmer no detached shockwave has been observed before sampling..... 130

Figure V-7. CFD simulations of the temperature as a flow property of the argon 50 K 0.3 CRESU flow being sampled with the skimmer using an optimized skimmer support's profile, inset: zoom on the entry of the skimmer no detached shockwave has been observed before sampling ..... 130

Figure V-8. Ar-35K-0.28 nozzle conditions, top panel gives the 2D density profile: the flow properties from impact pressure measurements of the CRESU flow using Pitot tube; bottom panel shows the 1D profile of temperature along the axis given by CFD simulation and Pitot tube measurements using the impact pressure. Average temperature given by CFD simulations is  $(35.1 \pm 0.2)$  K..... 131

Figure V-9. CFD simulations of the temperature as a flow property of the Ar-35K-0.28 CRESU flow being sampled with the skimmer, no normal shockwave or major disturbances have been observed ..... 132

Figure V-10. Comparison of the signal delivered from the expansion of a CRESU flow from the Ar-50K-0.3 nozzle (in orange) and the Ar-35K-0.28 (in red) expanding via the 4 mm skimmer targeting the  $J_{K_a, K_c} = 7_{0,7} - 6_{0,6}$  rotational transition of vinyl cyanide, vinyl cyanide is at 0.0066% of the total flow. the spectra are recorded under the same condition with 10,000 averaged scans. .... 133

Figure V-11. (a) Turbomolecular pump characteristic curves, (b) pressure in the secondary expansion chamber with the 4 skimmers ..... 134

Figure V-12. Vinyl cyanide signal in an argon flow at 35 K expanding in the skimmer chamber using 1,2,3 and 4 mm skimmer diameters at 20 cm from the skimmer, all spectra are recorded with the same procedure ..... 134

Figure V-13. Temperature map from simulations of the secondary expansion of the Ar-35K-0.28 nozzle in the 4 mm skimmer, top panel shows the DSMC results and the bottom panel gives CFD simulation results..... 136

Figure V-14. Temperature, density and Mach number profiles of the Ar-35K-0.28 nozzle flow expanding via the 4 mm skimmer along the axis of the secondary expansion chamber as given by DS2V program, in black is the density profile, in red is the temperature profile and in orange is the Mach number ..... 137

Figure V-15. Temperature profile along the axis of the secondary expansion chamber in blue is using the Fluent solver and in red is with the DSMC calculations..... 138

Figure V-16. Temperature profile of the argon 35 K with 4 mm skimmer, clogging has been observed at the entry of the skimmer..... 139

Figure V-17. Probing in the first port; left: spectrum of  $4.1 \times 10^{12}$  molecules  $\text{cm}^{-3}$  vinyl cyanide recorded from two chirps taken in argon flow at 35 K expanding via the 4 mm skimmer with 250,000 averages the black lines represent a synthetic spectrum from the CDMS at 9.375 K. On the right is the rotation diagram taken of the rotational transitions in the bands covered by the spectrum, the fitted rotational temperature is  $(4.8+1.7)$  K, with uncertainty given at the 95% confidence level..... 140

Figure V-18. Probing in the second port; ; left: spectrum of  $4.1 \times 10^{12}$  molecules  $\text{cm}^{-3}$  vinyl cyanide recorded from two chirps taken in argon flow at 35 K expanding via the 4 mm skimmer with 250,000 averages the black lines represent a synthetic spectrum from the CDMS at 9.375 K. On the right is the rotation diagram taken of the rotational transitions in the bands covered by the spectrum, the fitted rotational temperature is  $(8.7+0.5)$  K, with uncertainty given at the 95% confidence level..... 140

Figure V-19. Probing in the third port; left: spectrum of  $4.1 \times 10^{12}$  molecules  $\text{cm}^{-3}$  vinyl cyanide recorded from two chirps taken in argon flow at 35 K expanding via the 4

mm skimmer with 250,000 averages the black lines represent a synthetic spectrum from the CDMS at 37.5 K. On the right is the rotation diagram taken of the rotational transitions in the bands covered by the spectrum, the fitted rotational temperature is (24.9+4.8) K, with uncertainty given at the 95% confidence level..... 141

Figure V-20. Temperature plot at the three different probing locations in the skimmer chamber, the rotational temperature determined from the experiment is given in red dots, the temperature from DSMC calculations are given in orange and in purple the temperature from the Fluent solver..... 141

Figure V-21. Comparison of vinyl cyanide signal in an argon 30 K flow under CRESU conditions in orange and in red under the skimmer conditions using the 4 mm skimmer (a) shows the spectrum and (b) the corresponding FIDs, the stars on the spectrum under the CRESU conditions corresponds to spurs from the spectrometer electronics ..... 142

Figure V-22. Signal variation of vinyl cyanide at different concentration in the Ar-35K-0.28 nozzle expanding via the 4 mm skimmer, left figure shows the direct signal from the flow, right figure gives the signal variation when vinyl cyanide is photolysed by a 193 nm excimer laser. The exit of the nozzle is situated at 20 cm from the skimmer entry corresponding to 380  $\mu$ s of uniform flow conditions, for clarity the plots are offset to the same initial intensity..... 145

Figure V-23. Photolysis of vinyl cyanide with 193 nm excimer laser in the Ar-35K-0.28 flow expanding via the 4 mm skimmer at different laser beam sizes, top panel shows the laser firing through the skimmer, bottom panel when the laser is firing through the reservoir. For clarity, all the curves are offset to the same initial signal intensity, same concentration of vinyl cyanide and procedure of recording is used during the measurements while changing the diameter of the photolysing laser beam via the iris, the smallest iris size corresponds to 4 mm the diameter of the skimmer while the larger size corresponds to the diameter of the nozzle throat  $\sim$ 7.3 mm..... 147

Figure V-24. Photolysis of vinyl cyanide with 193 nm excimer laser in the argon 35 K flow expanding via the 4 mm skimmer, on top figure a 2D temperature profile of the argon 35 K flow generated from the Ar-35K-0.28 nozzle, the middle figure shows the CFD density profile on a logarithmic scale along the axis inside the Ar-35K-0.28 nozzle and in the CRESU chamber, the bottom figure shows the vinyl cyanide depletion in black, the HC<sub>3</sub>N and the HCN formation in orange and red probed on the  $J_{K_a, K_c} = 7_{07} - 6_{06}$ ,  $J = 7-6$  and  $J = 1-0$  respectively. Vinyl cyanide plot is offset by -5 on the signal intensity scale. .... 148

Figure V-25. HC<sub>3</sub>N from CN+C<sub>2</sub>H<sub>2</sub> reaction in the Ar-35K-0.28 flow expanding via the 4 mm skimmer; (a) is the spectrum of  $J=7-6$  rotational transition of HC<sub>3</sub>N taken at different times of the reaction in the uniform flow, (b) is the corresponding time dependent signal, the signal is recorded by averaging 4 scans of 100,000 averages ..... 150

Figure V-26. Vinyl cyanide from CN+C<sub>2</sub>H<sub>4</sub> reaction in the Ar-35K-0.28 flow expanding via the 4 mm skimmer; (a) is the spectrum of  $J_{K_a, K_c} = 7_{07} - 6_{06}$  rotational transition of vinyl cyanide taken at different times of the reaction in the uniform flow, (b) is the

|  |     |
|--|-----|
| corresponding time dependent signal, , the signal is recorded by averaging a scan of 100,000 averages.....   | 151 |
| Figure V-27. ICN stability curve during a scan.....  | 152 |
| Figure V-28. Photolysis of ozone with 248 nm excimer laser in the Ar-35K-0.28 flow expanding via the 4 mm skimmer, inset represents the O <sub>3</sub> time dependent spectra .....  | 153 |
| Figure V-29. Vinyl cyanide from the CN+C <sub>2</sub> H <sub>4</sub> reaction; (a) is the spectrum of J <sub>K<sub>a</sub>,K<sub>c</sub></sub> = 7 <sub>0,7</sub> - 6 <sub>0,6</sub> rotational transition of vinyl cyanide taken at different times of the reaction in the uniform flow, (b) is the corresponding time dependent signal.....  | 154 |
| Figure V-30. Calibration of vinyl cyanide from reaction; in orange J <sub>K<sub>a</sub>,K<sub>c</sub></sub> = 7 <sub>0,7</sub> - 6 <sub>0,6</sub> rotational transition of vinyl cyanide from reaction 3, in red same transitions of a well-known concentration of vinyl cyanide from a flow source .....  | 155 |
| Figure V-31. Comparison of the vinyl cyanide transitions in red J <sub>K<sub>a</sub>,K<sub>c</sub></sub> = 7 <sub>0,7</sub> - 6 <sub>0,6</sub> and in orange J <sub>K<sub>a</sub>,K<sub>c</sub></sub> = 9 <sub>0,9</sub> - 8 <sub>0,8</sub> .....  | 157 |
| Figure V-32. π/2 pulse HCN and vinyl cyanide: a) the J= 1-0 HCN transition, b) vinyl cyanide J <sub>K<sub>a</sub>,K<sub>c</sub></sub> = 9 <sub>0,9</sub> -8 <sub>0,8</sub> transition.....   | 157 |
| Figure V-33. The J=1-0 and J <sub>K<sub>a</sub>,K<sub>c</sub></sub> = 9 <sub>0,9</sub> -8 <sub>0,8</sub> transitions of HCN and vinyl cyanide respectively recorded from a two-color pulse in the Ar-35K-0.28 flow expanding through the 4 mm skimmer, Black and orange lines represent the signal before and after the laser shot respectively. ....  | 158 |
| Figure V-34. Photolysis of vinyl cyanide in the Ar-35K-0.28, Ar-50K-0.3 and Ar-50K-0.7 expanding through the 4 mm skimmer. For clarity, the plots are offset to the same initial signal intensity.....   | 160 |
| Figure VI-1. Schematic showing the principle of pulsed Laval flows.....  | 165 |
| Figure VI-2. Pulsed nozzle system developed by Rowe and co-workers <sup>7</sup> left figure gives a schematics of the Laval nozzle with; 1 Convergent part, 2 upstream contour of the divergent part, 3 downstream contour of the divergent part, 4 ball-springs, 5 stainless steel ring, 6 aerodynamic chopper, 7 aperture, and 8 45° rollers. The right figure shows the impact pressure of a gas pulse, details about the design and more results can be found in the reference ..... | 167 |
| Figure VI-3. Nozzle expansion status at different times in the helium nozzle that operates at 6 K as given by CFD simulations, the reservoir pressure is 635 mbar and chamber pressure is 0.04 mbar .....  | 169 |
| Figure VI-4. The 8 mm disk with a theoretical gain of 14.45 used for primary tests of the pulsed system.....   | 170 |
| Figure VI-5. Hydraulic plant and electrical cabinet for the hydraulic motor (a, b and c) represent different views of the hydraulic plant and (d) and (e) shows the electrical cabinet and the command screen.....   | 171 |
| Figure VI-6. Adjustment system for the parallelism of the disk, inset is a zoom on the adjusting screws, the system has a mechanical ball installed between the two pieces of the rotation stage allowing to adjust the system on the z and x axes. ....   | 172 |
| Figure VI-7. Schematic of the pulsed system, 1. Rotating disk; 2. Disk orifice; 3. Nozzle; 4. Adjustable stages; 5. Port for stepper motor actuator; 6. Brewster window; 7. Port   |     |

|   |     |
|---|-----|
| for gas inputs and pressure gauge connection; 8. Hydraulic connection feedthrough port; 9. Hydraulic motor; 10. Mechanical coupling; 11. Bearing; 12. Aligning bearing housing; 13. Fibre optic placement; 14. Parallel frontal flange. ....  | 174 |
| Figure VI-8. left figure shows the pulsed system mounted in the CRESU B chamber, right figure shows the N <sub>2</sub> -30K-0.183 nozzle and the rapid pressure sensor.....   | 175 |
| Figure VI-9. Left figure gives a frontal view in the direction of the flow of the rapid pressure sensor, right figure shows amplifier-filter and the Kulite conditioner (left to right), the filter has been used to filter the high frequency with a 3 KHz low pass filter .....   | 175 |
| Figure VI-10. Signal recorded by the fast pressure sensor from the N <sub>2</sub> -30K-0.183 operating in the pulsed mode, the signal is amplified and displayed on the oscilloscope, in red, the recorded signal averaged from 200 acquisitions.....   | 176 |
| Figure VI-11. Plot of the chamber pressure with respect to recorded signal by the rapid pressure sensor.....  | 177 |
| Figure VI-12. Plot of the impact pressures measured with the rapid pressure sensor at different position of the CRESU flow generated by the N <sub>2</sub> -30K-0.183 nozzle.....   | 177 |
| Figure VI-13. Impact pressure and temperature profiles along the axis of the chamber of the N <sub>2</sub> -30K-0.183 nozzle are given by (a) and (b) respectively, the temperatures are determined from impact pressure measurements by the rapid pressure sensor. The values for the pulsed mode are given in red and the values for the continuous mode are given in black, only three points were taken under this mode. .... | 178 |
| Figure VI-14. Flow pulses in 1 second duty cycle from the N <sub>2</sub> -30K-0.183 nozzle, the frequency of pulses is 6.2 Hz corresponding to 370 rpm while the input frequency to the motor is 800 rpm.....   | 180 |
| Figure VII-1. Rotation diagrams determined from recorded spectra of vinyl cyanide in the E band from expanding the flow generated by the AR35K0.28 nozzle via the the 2 mm skimmer (left) and the 4 mm skimmer (right), the fitted rotational temperatures are (4.8±1.7) K for the 4 mm skimmer and (12.9±7.2) K for the 2mm skimmer, with uncertainty given at the 95% confidence level.....                                     | 185 |
| Figure VII-2. 2D radial temperature profile of the N <sub>2</sub> -23.5K-0.21 nozzle given by CFD simulation, the figure shows the region sampled by the 4 mm skimmer in white circle and in black dashed line the region covered by the horn in the CRESU environment. ....  | 186 |
| Figure VII-3. Left figure shows the multiple channel from the CN + propene reaction. Right figure gives the vinyl cyanide Time dependent signal intensity from the reactions of CN with ethylene and propene as a function of time. (Figure credit to Divita Gupta) .....   | 188 |

# I. Introduction to gas phase chemistry and laboratory astrophysics

## Introduction

The last half century has seen a plethora of ground to space based observatories and space missions starting with the Orbiting Astronomical Observatory OAO-2, the first successful space observatory launched in 1968 and from Hubble to James Webb Space Telescope, Cassini-Huygens, Rosetta and many more, all with the aim of studying and understanding the structure of the Universe focusing in many cases on its chemical composition. Astrochemistry is the discipline situated at the intersection of chemistry and astrophysics that is concerned with the study of different processes of formation and destruction of chemical species and their abundances in different space environments and astronomical objects such as the interstellar medium and planetary atmospheres, environments with various extreme conditions of temperatures and densities.

### I.1. Gas phase chemistry in the ISM

The interstellar medium (ISM) in particular, representing the matter existing between stars, harbors a rich chemistry, being the host of many stars and exposed to all sorts of radiation, cosmic rays and solar wind. It is constituted of three principal regions, the first one is the cold dense phase consisting of molecular clouds and cold neutral medium where temperatures vary from 10 to 150 K and densities can reach  $10^6$  particles  $\text{cm}^{-3}$ . This is the densest region in the ISM and is responsible for the many process that lead to the formation of stars. The warm neutral and ionized media are constituted of neutral and ionized gas with temperatures that can reach 6000 to 10000 K, these regions are mostly rarefied with densities much lower than the cold neutral

medium, around  $0.2-0.6 \text{ cm}^{-3}$ , and finally we have the very hot ionized media with temperatures on the order of  $10^6 \text{ K}$  and densities between  $10^{-2}$  and  $10^{-4} \text{ cm}^{-3}$ .<sup>1,2</sup> More than 200 species including molecules, atoms and ions have been discovered in the last 80 years with hydrogen being the most abundant species followed by helium and then carbon, oxygen and nitrogen, the ISM also contains about 1% of its mass as dust which forms icy grains constituted mostly of water, methanol, ammonia, carbon monoxide and dioxide that are responsible for the formation of many complex organic molecules through thermal desorption in the warm regions.<sup>3-5</sup> This work is of relevance to the gas phase in the cold neutral medium of the ISM.



**Figure I-1. NGC 7380 star cluster illustrating the complex interplay of gas, dust and radiation present in the astronomical environment. Image by Bouhaddou Astrophotography**

## I.2. Molecules in the ISM

The advancement of radio telescopes and the commissioning of large observatories such as The Robert C. Byrd Green Bank Telescope (GBT),<sup>6</sup> the Atacama Large Millimeter/submillimeter Array (ALMA)<sup>7,8</sup> and recently Yebes observatory<sup>9</sup> has pushed the astronomical observation of chemical species to their highest rates (see Figure I-2 and Figure I-3 ) making unprecedented numbers of discoveries of molecules, radicals and ions. Thanks to the possibility of implementing multiple broad band receivers at the same time, more than 20 molecules have been discovered in the ISM between 2018 and 2020 as shown in Table I.1, a number almost doubled in 2021, (see Table I.2).<sup>10</sup>

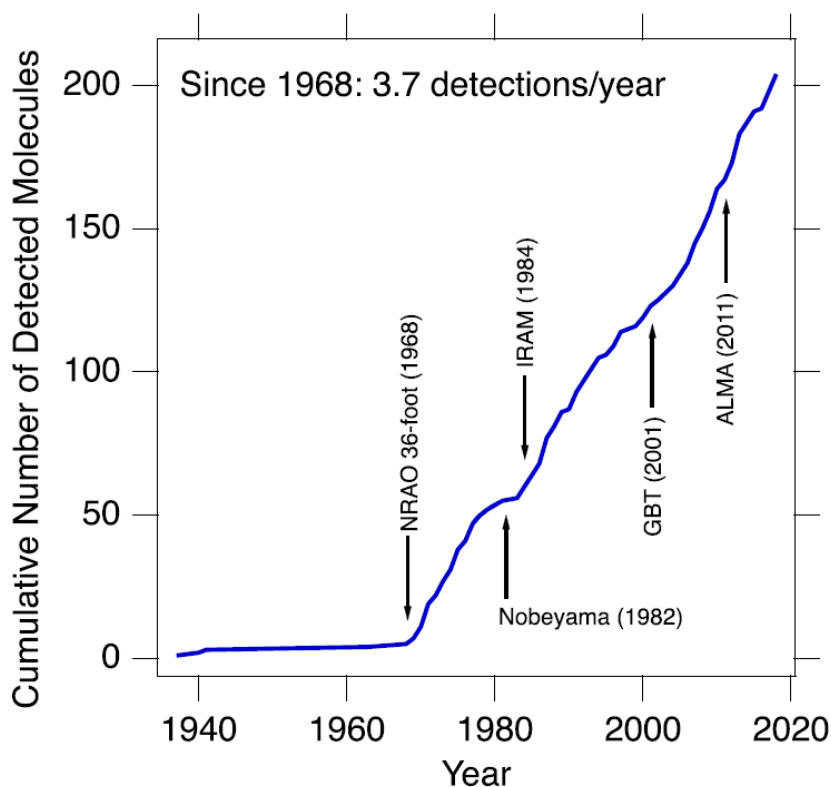


**Figure I-2. Cumulative number of known interstellar molecules over time. An average of 3.7 new detections of interstellar molecules per year can be seen after the commissioning of several major contributing facilities, noted with arrows. Figure from McGuire 2018<sup>11</sup>**

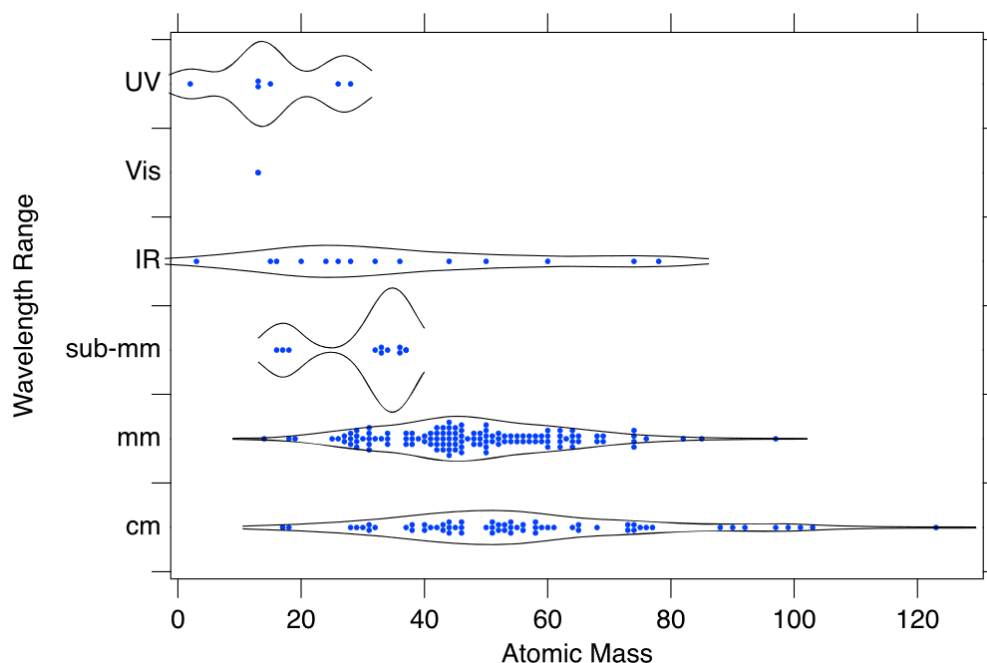


Figure I-3. Violin plot of the mass of molecules detected in each wavelength range. Figure from McGuire 2018<sup>11</sup>

Table I-1: List of molecules discovered in the ISM between 2018 and 2020<sup>10</sup>

| Year | Species                              | Astronomical object |
|------|--------------------------------------|---------------------|
| 2018 | c-C <sub>6</sub> H <sub>5</sub> CN   | TMC-1               |
|      | NS <sup>+</sup>                      | TMC-1, B1b, L483,   |
|      | HCS                                  | L483                |
|      | HSC                                  | L483                |
|      | NCO                                  | L483                |
|      | CNCN                                 | L483 (TMC-1)        |
| 2019 | Z-HNCHCN                             | G+0.693             |
|      | HOCH <sub>2</sub> CN                 | IRAS 16293-2422 B   |
|      | trans-HONO                           | IRAS 16293-2422 B   |
|      | VO                                   | VY CMa              |
|      | HeH <sup>+</sup>                     | NGC 7027            |
|      | CaNC                                 | IRC +10216          |
|      | (NH <sub>2</sub> ) <sub>2</sub> CO   | Sgr B2(N)           |
|      | MgC <sub>3</sub> N                   | IRC +10216          |
|      | MgC <sub>4</sub> H                   | IRC +10216          |
| 2020 | NH <sub>2</sub> OH                   | G+0.693-0.027       |
|      | CH <sub>3</sub> COCH <sub>2</sub> OH | IRAS 16293-2422 B   |
|      | Z-HNCHCCH                            | G+0.693-0.027       |
|      | HC <sub>4</sub> NC                   | TMC-1               |
|      | HCCCH <sub>2</sub> CN                | TMC-1               |
|      | HC <sub>3</sub> O <sup>+</sup>       | TMC-1               |
|      | HC <sub>5</sub> NH <sup>+</sup>      | TMC-1               |

One of the most interesting recent astrochemical discoveries was conducted by McGuire and co-workers in 2018,<sup>12</sup> when the group observed transitions of benzonitrile in the K band between 18 and 23 GHz from the TMC-1 molecular cloud using the GBT. Benzonitrile is the first simple aromatic molecule ever detected using radio spectroscopy and believed to be a precursor for the formation of many polycyclic aromatic hydrocarbons (PAHs).

**Table I-2: List of molecules discovered in the ISM in 2021<sup>10</sup>**

| Species                             | Astronomical object          | Species  | Astronomical object          |
|-------------------------------------|------------------------------|--|------------------------------|
| c-C <sub>5</sub> H <sub>5</sub> CN  | TMC-1                        | NH <sub>2</sub> CH <sub>2</sub> CH <sub>2</sub> OH | G+0.693-0.027                |
| HC <sub>11</sub> N                  |                              | H <sub>2</sub> C <sub>5</sub>                      | TMC-1                        |
| HC≡CCH=CHC≡N                        |                              | HCSCN  | TMC-1                        |
| H <sub>2</sub> C=CHC <sub>3</sub> N |                              | HCSCCH   | TMC-1                        |
| HC <sub>3</sub> S <sup>+</sup>      |                              | HNCN   | G+0.693-0.027                |
| CH <sub>3</sub> CO <sup>+</sup>     | TMC-1, L483,<br>L1527, L1544 | c-C <sub>6</sub> H <sub>4</sub>                    | TMC-1                        |
| c-C <sub>5</sub> H <sub>5</sub> CN  | TMC-1                        | H <sub>2</sub> CCCHC <sub>3</sub> N                | TMC-1                        |
| C <sub>10</sub> H <sub>7</sub> CN   |                              | MgC <sub>5</sub> N                                 | IRC +10216                   |
| C <sub>10</sub> H <sub>7</sub> CN   |                              | MgC <sub>6</sub> H                                 | IRC +10216                   |
| CH <sub>2</sub> CHCCH               |                              | C <sub>2</sub> H <sub>5</sub> CONH <sub>2</sub>    | Sgr B2(N1)                   |
| H <sub>2</sub> CCCHCCH              |                              | C <sub>2</sub> H <sub>3</sub> NH <sub>2</sub>      | G+0.693-0.027                |
| CH <sub>2</sub> CCH                 |                              | C <sub>2</sub> H <sub>5</sub> NH <sub>2</sub>      | G+0.693-0.027                |
| NCS                                 |                              | C <sub>2</sub> H <sub>5</sub> NCO                  | G+0.693-0.027                |
| HCCS                                |                              | CH <sub>2</sub> CCCN                               | TMC-1                        |
| H <sub>2</sub> CCS                  |                              | H <sub>2</sub> NC                                  | L483, PKS 1820-<br>211, B1-b |
| H <sub>2</sub> CCCS                 |                              | c-C <sub>5</sub> H <sub>5</sub> CCH                | TMC-1                        |
| C <sub>4</sub> S                    |                              | c-C <sub>5</sub> H <sub>5</sub> CCH                | TMC-1                        |
| HC(O)SH                             |                              | C <sub>6</sub> H <sub>5</sub> CCH                  | TMC-1                        |
| c-C <sub>3</sub> HCCH               |                              | HCCCO  | TMC-1                        |
| c-C <sub>5</sub> H <sub>6</sub>     |                              | C <sub>5</sub> O                                   | TMC-1                        |

### I.3. Laboratory astrophysics

Following the advancements being made in developing sophisticated broadband instruments and technologies that allow to conduct astronomical observations of the multiple and complex species in the ISM in particular, the interpretation of those observations and converting data into tangible results is required.

Laboratory astrophysics contributes to expanding our understanding of the physical processes involved in the formation of the observed species by reproducing the conditions of the medium of interest in the laboratory then performing experiments to determine fundamental constants and physical properties. It helps in creating a database for species of astronomical interest with information about their origins, molecular structure, lifetime as well as the processes and reactions that lead to their formation and dissociation. These databases will give theoreticians the required inputs to perform calculations for astrochemical modelling to study the formation and destruction routes of species.

Laboratory astrophysics and numerical modelling, complement astronomical observations and together form the fundamental pillars of astrochemistry.

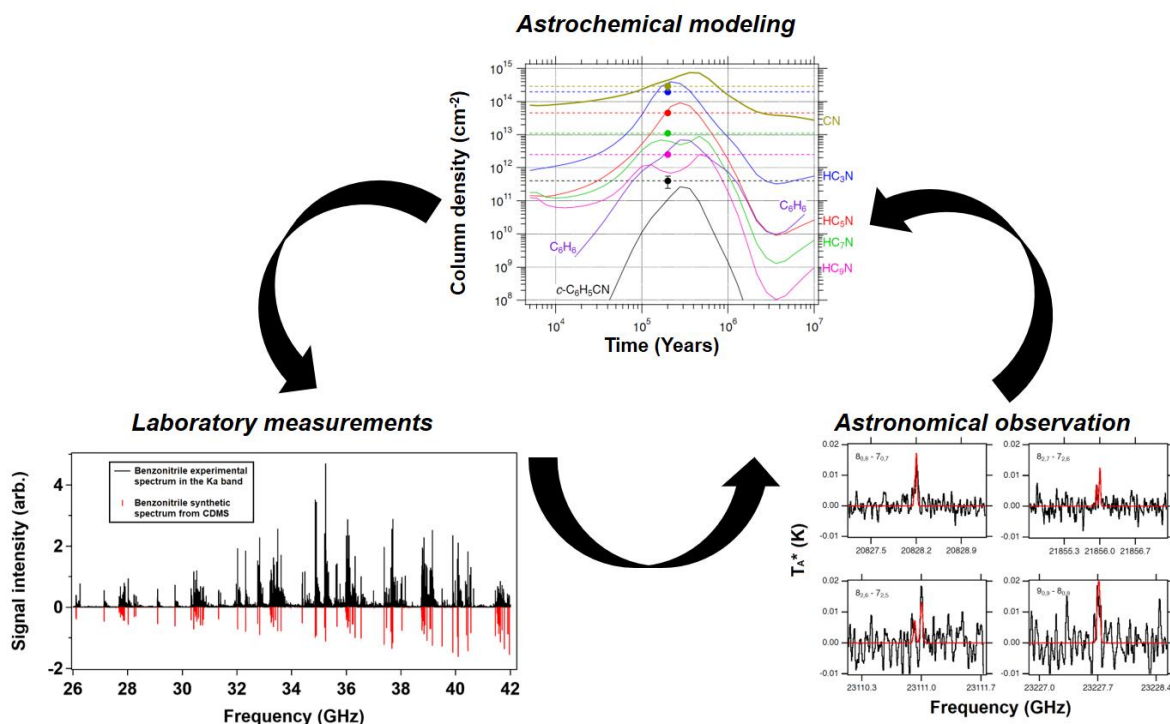


**Figure I-4. Three pillars of astrochemistry, an example of benzonitrile laboratory measurements: a benzonitrile spectrum measured in this work at room temperature using the Ka band chirped pulse Fourier transform mm-wave spectrometer operating in a frequency range of 26.5 to 40 GHz (presented in chapter IV); Astronomical observation: a spectrum of benzonitrile measured by McGuire and co-workers<sup>12</sup>; Astrochemical modelling: Results of an astrochemical model by McGuire and co-workers,<sup>12</sup> of gas-phase column densities of CN, HC<sub>3</sub>N, HC<sub>5</sub>N, HC<sub>7</sub>N, HC<sub>9</sub>N with focus on benzonitrile (in black) in TMC-1 as a function of time in solid colored lines. The dots represent the abundances of observed species.**

### **I.3.1. Laboratory astrophysics in Rennes**

In the Rennes laboratory astrophysics group, the field of interest is studying the kinetics of gas-phase reactions<sup>13</sup> and energy transfer processes at different temperatures<sup>14</sup> as well as the study of the spectroscopy of media under extreme conditions. Space conditions are created with the CRESU (Cinétique de Réaction en Ecoulement Supersonique Uniforme) technique (See chapter II) capable of generating gas flows over a large temperature interval ranging from room temperature down to 5.5 K covering the ISM and most of the atmospheric temperatures in our solar system. Four operating CRESU reactors are used for the measurements of reaction kinetics including two reactors presented in this work (see chapter III). Another CRESU reactor fitted with a high enthalpy source is used to generate spectra at high temperatures in the infrared with the interest of studying hot atmospheres of exoplanets such as hot Jupiters.<sup>15</sup>

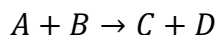
It is important to highlight that the chemistry in the ISM takes years to evolve due to low density of molecules resulting in infrequent collisions. In the cold neutral medium, the densest region of the ISM has a density that is orders of magnitude lower than of the Earth's atmosphere and it corresponds to the best vacuum we can create in the laboratory. The CRESU technique being able to generate local thermodynamic equilibrium conditions as will be explained later helps accelerating the studied processes under laboratory condition with the assumption that the reactions of interest are not pressure dependent. Collisions of hydrogen in the densest region of the ISM at 10 K take 12 hours to occur. Other species at lower density regions, can take years to collide.

## **I.4. Introduction to reaction kinetics and gas phase collisional processes**

Reactions are characterized by two major parameters, the rate constants that measure the reaction speed and branching ratios measuring the efficiency of the multiple product channels attributed to the reaction.

### **I.4.1. Reaction rate constant**

The rate constant for a bimolecular reaction as shown below is related to the time-dependent concentrations of reactants and products by Equation I-1.



$$-\frac{d[A]}{dt} = -\frac{d[B]}{dt} = \frac{d[C]}{dt} = \frac{d[D]}{dt} = k[A][B] \quad \text{Equation I-1}$$

For a first order reaction where  $A \rightarrow C + D$ , we can give the following,

$$-\frac{d[A]}{dt} = k[A] \quad \text{Equation I-2}$$

First order kinetics can be extended to study bimolecular reactions by setting the initial concentration of either one of the reactants, usually the most stable, for example species B, in excess so that no matter how much it reacts with A, the variation of its concentration can be neglected, this is known as the pseudo first order kinetics and Equation I-1 becomes:

$$-\frac{d[A]}{dt} = k[A][B]_0 \quad \text{Equation I-3}$$

Then we can define

$$k_{1st} = k[B]_0 \quad \text{Equation I-4}$$

For our reactions we consider the precursor/radical as the limiting reagent while the other stable reactant,  $C_2H_4$  for example, is injected in excess with a ratio of at least 10 to a 100.

To have accurate measurement of  $k$ , the reaction must be carried out with multiple concentrations of the species B and the extracted  $[k_{1st}]_i$  are then plotted against their associated  $[B]_i$ . The slope of that plot gives the overall reaction rate constant  $k$ . The final relation for the rate constant of a pseudo first order reaction is then given by,

$$[A]_t = [A]_0 e^{-k[B]_0.t} \quad \text{Equation I-5}$$

The example below shows the determination of the rate constant for a bimolecular reaction between OH and CO at 23.5 K in a nitrogen bath, the OH (from  $H_2O_2$  precursor) concentration was kept constant while varying the CO concentration in the flow, at each concentration of CO, the  $k_{1st}$  was determined, the reaction rate constant  $k$  at 23.5 K is given by Figure I-5.

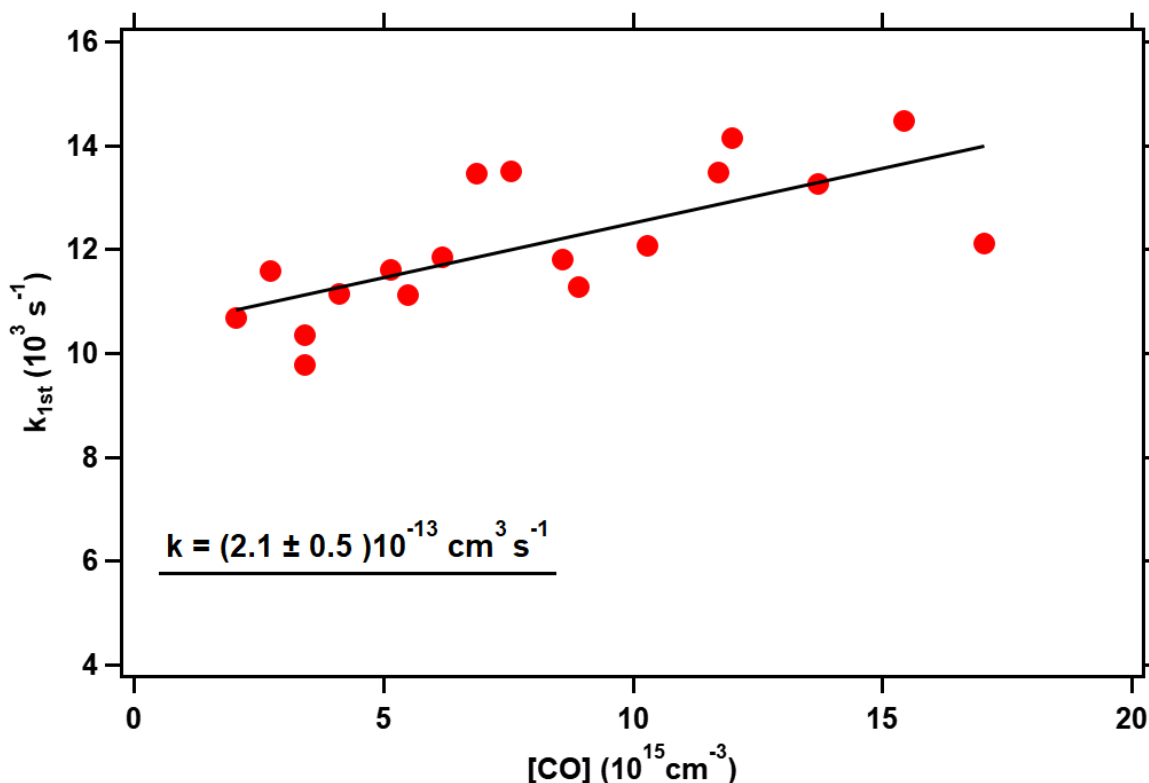
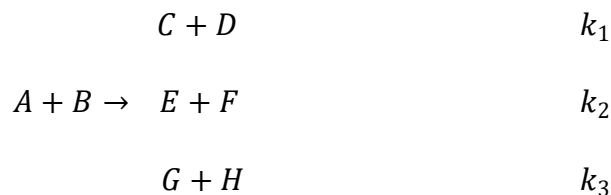


Figure I-5. Example of the determination of the rate constant of the OH+CO reaction at 23.5 K as part of a thesis project led by Messinger and co-workers<sup>16</sup>

#### I.4.2. Reaction branching ratios

As reactions are susceptible to have multiple pathways they could proceed through, relying on the rate constant solely to characterize a reaction cannot be sufficient.<sup>17</sup> The reaction shown in I.3.1 with three possible channels can be characterized by the following;



Where each channel has its own rate constant and the overall rate constant is given by  $k = k_1 + k_2 + k_3$  and the branching ratios are given by the following coefficients;

$$\alpha_1 = \frac{k_1}{k}; \quad \alpha_2 = \frac{k_2}{k}; \quad \alpha_3 = \frac{k_3}{k} \quad \text{Equation I-6}$$

### I.4.3. Hard sphere collision model

In the simple collision model, molecules are considered as hard rigid spheres with linear trajectories, a reaction occurs when two molecules collide with each other on the condition that they carry enough energy to overcome the reaction barrier which leads to the concept known as the activation energy (see Equation I-10).

The collision takes place when the distance between the two molecules A and B is less than  $d_{AB} = r_A + r_B$  where  $r$  is the van der Waals radius of the associated molecule, we can then consider collision cross section  $\sigma = \pi d_{AB}^2$ . The collision frequency is then given by,

$$Z_{A,B} = N_A N_B \pi d_{AB}^2 \sqrt{\frac{8k_B T}{\pi \mu_{AB}}} \quad \text{Equation I-7}$$

$N_A$  is the number density of A molecules in the system,  $N_B$  is the number density of B molecules in the system,  $k_B$  is the Boltzmann constant;  $k_B = 1.38 \times 10^{-23} \text{ J.K}^{-1}$ ,  $T$  is the temperature in Kelvin  $\mu_{AB}$  is the reduced mass in kg;  $\mu_{AB} = \frac{m_A m_B}{m_A + m_B}$

If we consider that every collision induces a reaction, this will lead to an overestimation of the reaction rate, one must therefore take into account the reaction barrier known as the threshold energy  $\epsilon^*$ , this introduces the following equation;

$$k(T) = \pi d_{AB}^2 \sqrt{\frac{8k_B T}{\mu_{AB}}} \exp\left(-\frac{\epsilon^*}{KT}\right) \quad \text{Equation I-8}$$

The simple collision model is further enhanced by adding the steric factor  $p$ , a characteristic parameter that can favor the occurrence of the reaction based on the orientation of the colliding molecules, for instance for some reactions the barrier can be lower if the collision between the two reactants is collinear than at an angle.

$$k(T) = p \pi d_{AB}^2 \sqrt{\frac{8k_B T}{\mu_{AB}}} \exp\left(-\frac{\epsilon^*}{KT}\right) \quad \text{Equation I-9}$$

### I.4.4. Reaction at low temperature

We can define the Arrhenius law given by Equation I-10 which describes the behavior of most reactions.

$$k(t) = A \exp\left(-\frac{E_A}{k_B T}\right) \quad \text{Equation I-10}$$

With  $A$  is a pre-exponential factor and  $E_A$  is the activation energy. Most chemical reactions between stable molecules slow down at very low temperatures because the reactants lack the energy needed to surmount energy barrier as can be shown by the inverse proportional relation between the temperature and the logarithm of the reaction rate constant in the Arrhenius equation. However, many reactions involving radicals are barrierless reactions implying that they remain efficient at lower temperatures, and some even become faster at lower temperatures.<sup>18,19</sup> These reactions include many neutral-neutral reactions which can play a major role in the chemistry of cold medium of the ISM and other planetary atmospheres such as Saturn's giant moon Titan.<sup>2,20</sup>

## I.5. Outlines of thesis and motivations

Motivated by the many recent discoveries of molecules with radio astronomy and the lack of low temperature-relevant to astrochemistry-reaction branching ratios in databases due to instrumental difficulties.<sup>17</sup> This work is a part of the CRESUCHIRP project to design and build a new CRESU reactor fitted with two chirped pulse Fourier transform mm wave spectrometers operating in broad bands covering the Ka band from 26.5 to 40 GHz and the E band from 60 to 90 GHz with the aim of the determination of the branching ratios of low temperature reactions of astrophysical interest, in particular those taking place in the interstellar medium.

This thesis focuses on the instrumental limitations of coupling the CRESU technique with chirped pulse Fourier transform microwave spectroscopy and presents the development of two instruments to optimize the detection of the species of interest and the determination of reaction branching ratios.

**Chapter II** introduces the CPUF technique which stands for chirped pulse in uniform flow. The CRESU technique and its different aspects will be discussed at length in the first part of the chapter. Chirped pulse Fourier transform mm wave spectroscopy is presented in the second part.

In **chapter III**, we present the development and the construction of the experimental setup in the first part, while the second part is dedicated to the methods of characterization of cold supersonic flows in the CRESU and rarefied environments using numerical and experimental tools.

**Chapter IV** discusses and assesses the limitations of the CPUF technique, particularly the impact of pressure on the microwave signal, by conducting pressure broadening measurements of vinyl cyanide and benzonitrile in the Ka band.

**Chapter V and VI** presents the development of two optimizing instruments to further lower the temperature and pressure of the CRESU flows to improve the microwave signal.

**Chapter V** presents the SKImmed uniform SUPersonic Flow (SKISURF) apparatus, a new instrument developed to optimize the flow conditions in the CRESU technique by generating secondary expansions via the use of skimmers. The reaction of CN with ethylene is studied and its corresponding branching ratio is measured.

**Chapter VI** presents the development of a pulsed CRESU system, a second instrument to optimize the CPUF technique, where the CRESU technique will operate in a pulsed mode by implementing an aerodynamic chopper.

**In Conclusions and Perspectives**, we will present the different directions of the project and the new perspectives that can be explored after the implementation of the two optimizing instruments.

## References

- (1) Agúndez, M.; Wakelam, V. Chemistry of Dark Clouds: Databases, Networks, and Models. *Chem. Rev.* **2013**, *113* (12), 8710–8737. <https://doi.org/10.1021/cr4001176>.
- (2) Herbst, E. Chemistry of Star-Forming Regions. *J. Phys. Chem. A* **2005**, *109* (18), 4017–4029. <https://doi.org/10.1021/jp050461c>.
- (3) Caselli, P.; Hasegawa, T. I.; Herbst, E. Chemical Differentiation between Star-Forming Regions: The Orion Hot Core and Compact Ridge. *The Astrophysical Journal* **1993**, *408*, 548. <https://doi.org/10.1086/172612>.
- (4) Garrod, R. T.; Weaver, S. L. W.; Herbst, E. Complex Chemistry in Star-Forming Regions: An Expanded Gas-Grain Warm-up Chemical Model. *ApJ* **2008**, *682* (1), 283. <https://doi.org/10.1086/588035>.
- (5) Burke, D. J.; Puletti, F.; Woods, P. M.; Viti, S.; Slater, B.; Brown, W. A. Trapping and Desorption of Complex Organic Molecules in Water at 20 K. *The Journal of Chemical Physics* **2015**, *143* (16), 164704. <https://doi.org/10.1063/1.4934264>.
- (6) Green Bank Observatory <https://greenbankobservatory.org/> (accessed 2022 -04 -23).
- (7) Atacama Large Millimeter/submillimeter Array | ALMA <https://www.almaobservatory.org/en/home/> (accessed 2022 -04 -23).
- (8) Palmer, M. Y.; Cordiner, M. A.; Nixon, C. A.; Charnley, S. B.; Teanby, N. A.; Kisiel, Z.; Irwin, P. G. J.; Mumma, M. J. ALMA Detection and Astrobiological Potential of Vinyl Cyanide on Titan. *Science Advances* **3** (7), e1700022. <https://doi.org/10.1126/sciadv.1700022>.
- (9) Astronomía : Acerca de <https://astronomia.ign.es/web/guest/icts-yebes/acercade> (accessed 2022 -04 -23).
- (10) molecules [CDMS classic documentation] <https://cdms.astro.uni-koeln.de/classic/molecules> (accessed 2022 -04 -23).
- (11) McGuire, B. A. 2018 Census of Interstellar, Circumstellar, Extragalactic, Protoplanetary Disk, and Exoplanetary Molecules. *ApJS* **2018**, *239* (2), 17. <https://doi.org/10.3847/1538-4365/aae5d2>.
- (12) McGuire, B.; Burkhardt, A.; Kalenskii, S.; Shingledecker, C.; Remijan, A.; Herbst, E.; McCarthy, M. Detection of the Aromatic Molecule Benzonitrile (c-C<sub>6</sub>H<sub>5</sub>CN) in

- the Interstellar Medium. *Science (New York, N.Y.)* **2018**, 359, 202–205. <https://doi.org/10.1126/science.aao4890>.
- (13) Cooke, I. R.; Sims, I. R. Experimental Studies of Gas-Phase Reactivity in Relation to Complex Organic Molecules in Star-Forming Regions. *ACS Earth Space Chem.* **2019**, 3 (7), 1109–1134. <https://doi.org/10.1021/acsearthspacechem.9b00064>.
- (14) Mertens, L. A.; Labiad, H.; Denis-Alpizar, O.; Fournier, M.; Carty, D.; Le Picard, S. D.; Stoecklin, T.; Sims, I. R. Rotational Energy Transfer in Collisions between CO and Ar at Temperatures from 293 to 30K. *Chemical Physics Letters* **2017**, 683, 521–528. <https://doi.org/10.1016/j.cplett.2017.05.052>.
- (15) Dudas, E.; David, N.; Brahmachary, S.; Kulkarni, V.; Benidar, A.; Kassi, s; Charles, C.; Georges, R. High-Temperature Hypersonic Laval Nozzle for Non-LTE Cavity Ringdown Spectroscopy. *The Journal of Chemical Physics* **2020**, 152. <https://doi.org/10.1063/5.0003886>.
- (16) Messinger, J. P. H. Spectroscopy and Kinetics of Atmospheric and Astrochemical Reactions. 114.
- (17) Seakins, P. W. Product Branching Ratios in Simple Gas Phase Reactions. *Annu. Rep. Prog. Chem., Sect. C: Phys. Chem.* **2007**, 103 (0), 173–222. <https://doi.org/10.1039/B605650B>.
- (18) Dulieu, O.; Osterwalder, A. *Cold Chemistry: Molecular Scattering and Reactivity Near Absolute Zero*; Royal Society of Chemistry, 2017.
- (19) Smith, I. W. M. Laboratory Studies of Atmospheric Reactions at Low Temperatures. *Chem. Rev.* **2003**, 103 (12), 4549–4564. <https://doi.org/10.1021/cr020512r>.
- (20) Flasar, F. M.; Achterberg, R. K.; Conrath, B. J.; Pearl, J. C.; Bjoraker, G. L.; Jennings, D. E.; Romani, P. N.; Simon-Miller, A. A.; Kunde, V. G.; Nixon, C. A.; Bézard, B.; Orton, G. S.; Spilker, L. J.; Spencer, J. R.; Irwin, P. G. J.; Teanby, N. A.; Owen, T. C.; Brasunas, J.; Segura, M. E.; Carlson, R. C.; Mamoutkine, A.; Gierasch, P. J.; Schinder, P. J.; Showalter, M. R.; Ferrari, C.; Barucci, A.; Courtin, R.; Coustenis, A.; Fouchet, T.; Gautier, D.; Lellouch, E.; Marten, A.; Prangé, R.; Strobel, D. F.; Calcutt, S. B.; Read, P. L.; Taylor, F. W.; Bowles, N.; Samuelson, R. E.; Abbas, M. M.; Raulin, F.; Ade, P.; Edgington, S.; Piorz, S.; Wallis, B.; Wishnow, E. H. Temperatures, Winds, and Composition in the Saturnian System. *Science* **2005**, 307 (5713), 1247–1251. <https://doi.org/10.1126/science.1105806>.

## II. Introduction to chirped pulse in uniform flow (CPUF)

### Introduction

Studying the kinetics of cold chemical reaction requires the combination of a cooling technique to create the low temperature conditions with an instrument of detection capable of tracking the evolution of species during the reaction. Coupling the CRESU technique with microwave spectroscopy for the detection of species of astrochemical interest was first established in a collaboration between the groups of Arthur Suits, Bob Field and Ian Sims and appeared in a series of publications under the term CUPF (chirped pulse in uniform flow) in 2014<sup>1,2</sup>, the most relevant to our study was the determination of branching ratios of CN and propyne reaction in 2015<sup>3</sup> which has proven the ability of the technique in studying cold bimolecular reactions through the quantitative determination of the associated branching ratios. The CRESU technique uses Laval nozzles to generate supersonic and isentropic expansions of compressible flows offering a suitable environment to study reactions at low temperatures, while chirped pulse spectroscopy as a broadband distinctive detection technique, especially at lower temperatures allows the detection of multiple species at the same time. This constitutes a promising approach to determine reaction branching ratios, and the theory of these two techniques will be presented in this chapter.

## Part I: Introduction to the CRESU technique (cold supersonic flows)

The first part will be dedicated to introduce the CRESU technique and the theory of Laval nozzles by first explaining the concept of compressible flows and the different flow regimes in addition to isentropic expansions and their application in the CRESU technique, finally we will discuss the associated CRESU flow regimes and the phenomena they could appear following the implementation of certain conditions such as uniformity and shockwaves.

### II.1. Introduction to compressible flows

The motion of a viscous compressible Newtonian fluid, including its energy variation, is described by the governing equations of Navier-Stokes in the unsteady form listed below. Equation II-1 results from conservation of mass of the fluid, Equation II-2 results from Newton's second law that is that the rate of change of momentum equals the sum of the forces on a fluid particle, and finally Equation II-3 results from the conservation of energy equation and the first law of thermodynamics, that is that the rate of change of energy is equal to the sum of the rate of heat addition to and the rate of work done on a fluid particle.

Continuity equation

$$\frac{\partial \rho}{\partial t} + \text{div}(\rho \vec{v}) = 0 \quad \text{Equation II-1}$$

Momentum equation

$$\frac{\partial \rho \vec{v}}{\partial t} = -\text{div}(\rho \vec{v} \vec{v}) + \text{div} \bar{\bar{\sigma}} + \rho \vec{f} \quad \text{Equation II-2}$$

The energy equation

$$\frac{\partial \rho E}{\partial t} = -\text{div}(\rho E \vec{v}) + \text{div}(\vec{v} \bar{\bar{\sigma}} \cdot \vec{v}) - \text{div}(\vec{q}) + \rho \vec{f} \quad \text{Equation II-3}$$

Where  $p$  is the pressure,  $\rho$  is the density,  $v$  is the velocity,  $E$  is the total energy,  $\bar{\bar{\sigma}}$  is the viscosity tensor,  $q$  is the heat flux and  $\vec{f}$  is the external force, usually gravity.

These differential equations are too difficult to solve analytically but numerical techniques such as finite element methods can give very accurate predictions of the pressure, temperature, and density of the fluid. Results from so-called Computational Fluid Dynamics also known as CFD, of high speed flows will be presented in this

chapter and further details about procedures and CFD models are given in the second part of chapter III.

Alongside the Navier-Stokes equations that are widely used in characterizing the motion of hydrodynamic systems, there are other parameters that describe the different flow regimes and behaviors, including the Reynolds number and the Mach number.

### Reynolds number

Denoted by  $Re$ , the Reynolds number is the ratio between the kinetic and the viscous forces, it is given by

$$Re = \frac{\rho v d}{\mu} \quad \text{Equation II-4}$$

Where  $d$  is a characteristic length and  $\mu$  is the dynamic viscosity

### Mach number

Denoted by  $M$ , the Mach number is the ratio between the velocity of the fluid and the speed of sound in the medium, it represents the ratio between the kinetic energy and the thermal agitation of the molecules in the fluid, higher Mach numbers indicate that a considerable amount of the internal energy of the fluid is converted to kinetic energy. The Mach number is given by the following equation.

$$M = \frac{v}{a} \quad ; \text{where} \quad a = \sqrt{\gamma \cdot r \cdot T} \quad \text{Equation II-5}$$

Where  $a$  is the speed of sound in the medium,  $\gamma$  is the specific heat ratio and  $T$  is the temperature. The Mach number introduces the notion of the compressibility effect in a fluid, it is considered as a characteristic parameter for compressible flows particularly at supersonic speeds.

#### II.1.1. Compressible flows

In incompressible flows which cover most of the applications of the Navier-Stokes equations, the density and the volume of the flow remain constant or its variation is negligible. In this case  $\frac{\partial \rho}{\partial t} = 0$  and the conservation of mass equation becomes  $div(\vec{v}) = 0$ . The flows involved in our measurements however are compressible meaning that their volumes and therefore their densities change. Figure II-1 shows the state of compressibility of the fluid according to its associated Mach number.

## II.1.2 Supersonic flows

Beyond the compressibility effect lies another concept of characterizing the flow based on its Mach number. Compressible flow can be considered as subsonic when  $M < 0.8$ ; transonic for  $0.8 < M < 1.2$ ; supersonic with  $1 < M < 5$  and hypersonic when  $M > 5$  as shown in Figure II-1. Incompressible flow has a Mach number less than 0.3.

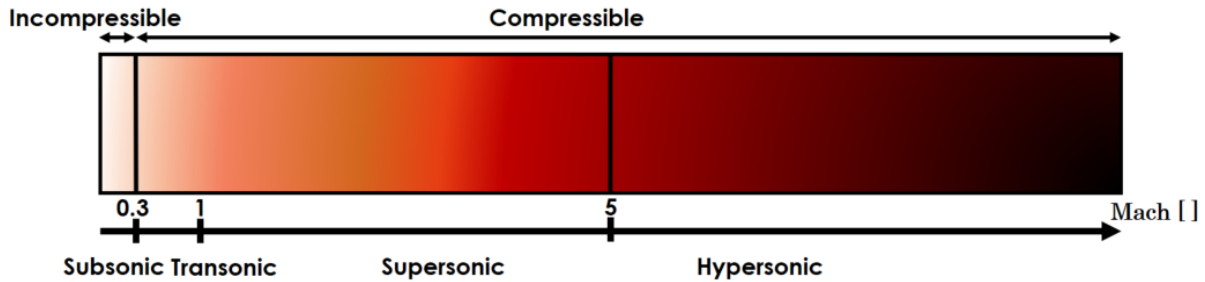


Figure II-1. Flow regimes according to the Mach number

## II.2. Isentropic expansions

Supersonic flows are usually generated from rapid isentropic expansion of a given gas, the process is adiabatic and reversible meaning that there is no heat exchange between the flow and the surrounding medium i.e.  $\delta q = 0$  and there is no friction with the walls therefore the shear stress and viscosity effects can be neglected.

An adiabatic process does not mean that the temperature remains constant as there is no heat exchange, in fact during the expansion the temperature of the flow is lowered as a result of the difference in pressure created in an increasing volume.

### II.2.1. Isentropic Equations

Using the first principle of thermodynamics of the variation of the internal energy

$$\delta q = dU + pdV = 0$$

And 
$$\gamma = \frac{c_p}{c_v}$$

We obtain 
$$\frac{p_2}{p_1} = \left(\frac{V_2}{V_1}\right)^{-\gamma} \quad \text{therefore} \quad pV^\gamma = cst \quad \text{Equation II-6}$$

Using the ideal gas equation 
$$\frac{p}{\rho} = rT$$

We deduce 
$$\frac{p_2}{p_1} = \left(\frac{\rho_2}{\rho_1}\right)^\gamma \quad \text{and} \quad \frac{p_2}{p_1} = \left(\frac{T_2}{T_1}\right)^{\gamma/(\gamma-1)} \quad \text{Equation II-7}$$

These equations relate the three fundamental parameters of the flow, the temperature, pressure and density, they can also be expressed as a function of the Mach number as will be shown later. Since the expansion does not exhibit any heat exchange or friction, the motion of the flow can be modelled by the Euler equations a simplified version of the Navier-Stokes equations.

## II.2.2. Euler equations

For compressible unidirectional flow in the stationary regime where the viscosity is neglected, the governing equations of fluid motion are given by the Euler equations

$$\frac{\partial(\rho v_x)}{\partial x} = 0 \quad \text{Equation II-8}$$

$$\rho v_x \frac{dv_x}{dx} = -\frac{dp}{dx} \quad \text{Equation II-9}$$

$$\rho(\vec{v} \cdot \overrightarrow{grad})e = -p \frac{dv_x}{\partial x} \quad \text{Equation II-10}$$

These compressible supersonic flows are generated by Laval nozzles (presented in the next section) and the Euler equations along with the isentropic equations and the Mach number are used to model the cold supersonic region of the Laval nozzle flows, known as the isentropic core, see Figure II-3. Now we have defined the theory of compressible and supersonic flows, we introduce the key device that generate these flows, that is the Laval nozzle.

## II.3. Laval Nozzle

It is known from the Venturi effect that when a fluid is put in motion, the pressure drops in a converging section while velocity increases, the flow reaches the maximum speed at the throat, the reverse process occur in the diverging section, Laval nozzles have approximately the same geometry as Venturi tubes and both use the Venturi effect to accelerate the gas by narrowing the duct cross-section, however the flow behaves differently in a Laval nozzle under certain conditions, specifically in the diverging section.

### II.3.1. Definition and functioning principle

The Laval nozzle as described by Gustaf de Laval in 1888, is an axisymmetric convergent-divergent shaped device that generates uniform supersonic flows by submitting a gas to an isentropic expansion created by a difference in pressure

between upstream and downstream of the nozzle. The higher pressure is imposed at a space in contact with the convergent part known as the stagnation region usually a reservoir containing the static gas while the lower pressure is generated in the other part of the nozzle known as the expansion medium.

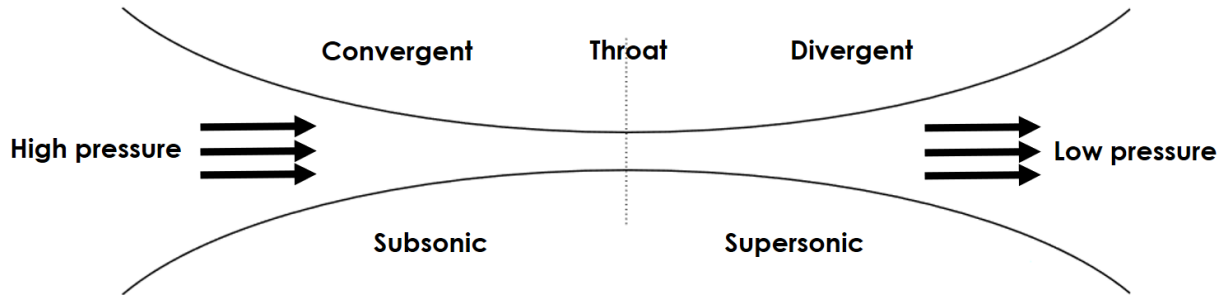


**Figure II-2. Operation principle of a convergent divergent nozzle**

The difference in pressure creates a gradual progressive process beginning at the convergent part where the velocity of flow starts increasing as the cross-section gets smaller until it reaches Mach 1 at the throat, the process continues in the divergent section where velocity exceeds Mach 1 creating a low temperature flow with supersonic conditions that potentially pushes beyond Mach 5 under certain conditions.

Following the velocity increase the other flow properties also change isentropically, the density of the flow, its temperature and pressure, will decrease accordingly. Laval nozzles are widely used in rocketry, space and aircraft engineering and have been adapted to study kinetics at low temperatures at the beginning of the 1980's (see section II.4) which makes them valuable tools for our project.<sup>4</sup>

### II.3.2. Concept and theory of Laval nozzles

The key equation that explains the functioning principle of a Laval nozzle is expressed by Bernoulli's equation relating the stagnation conditions in the reservoir and any point of the expansion. The initial velocity is taken to be zero and gravity effects are neglected and it is derived using the definition of the enthalpy of a system

$$H = U + pV$$

The conservation of energy equation is as follows;

$$c_p T_0 = c_p T_{flow} + \frac{v_{flow}^2}{2} \quad \text{Equation II-11}$$

Where  $T_0$  is the stagnation temperature (at the reservoir) and  $T_{flow}$  is the temperature at the flow and  $V_{flow}$  is the speed at the associated point. The terms  $c_p T$  and  $\frac{V^2}{2}$  represent respectively the specific enthalpy and the kinetic energy in  $J/Kg$ .

Equation II-11 describes the process of transformation of energy within the nozzle and in the expansion medium where the initial internal energy is converted to kinetic energy during the isentropic expansion. At  $T_{flow} \approx T_0$ , kinetic energy is insignificant as the energy is stored in form of heat in the high pressure environment, when the gas accelerates, the  $T_{flow}$  starts decreasing to reach cryogenic temperatures while the speed reaches supersonic values. Theoretically, if we manage to convert all the internal energy to kinetic energy then  $T_{flow} \rightarrow 0$  and:

$$V_{\infty} = \sqrt{2C_p T_0} \quad \text{Equation II-12}$$

Reaching absolute zero with Laval nozzles is not a straightforward task especially with the CRESU technique that uses relatively high flow rates as will be explained in section II.4, such extreme conditions requires implementing a huge pumping capacity group to generate a significant pressure difference between the high pressure environment and the vacuum environment, however there are some other cooling techniques that allow to go ultra cold flows on the scale of hundreds of millikelvins as will be described in section II.6.

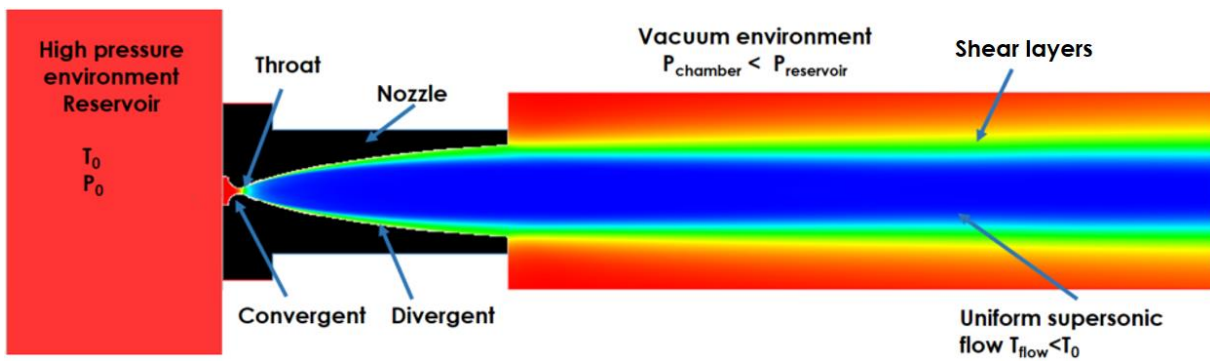


**Figure II-3. Gas expansion carried in a Laval nozzle**

From Equation II-11 we can deduce the temperature equation as a function of the Mach number

$$\frac{T_0}{T_{flow}} = 1 + \frac{\gamma-1}{2} M^2 \quad \text{Equation II-13}$$

### II.3.2.1. Principle and hypothesis of compressible flows in Laval nozzles

Now we have established how the different parameters of supersonic flows are acquired via the isentropic equations, we can describe how the compressible flow responds to changes in the area it is flowing through and how the associated properties vary. Based on the Euler equations we can write the following;

#### Conservation of mass for a steady quasi 1-dimensional flow

$$\frac{d\rho}{\rho} + \frac{dv}{v} + \frac{dA}{A} = 0 \quad \text{Equation II-14}$$

Where  $\rho$  is the density,  $v$  the speed and  $A$  is the area cross-section, the equation shows that the variations of these three quantities must sum to zero in order for the mass to be conserved, thus any change in the cross-section must be followed by changes in the flow velocity and also its density, unlike for incompressible flow where  $d\rho = 0$  meaning that the imbalance created by the cross-section narrowing or dilation must be compensated by velocity.

We can also derive the equations for the pressure and density variation with velocity:

#### Pressure variation with velocity

The momentum equation with the assumptions made above gives the following:

$$\frac{dp}{\rho} + vdv = 0 \quad \text{Equation II-15}$$

Equation II-15 shows that velocity and pressure always change in an opposite way, the flow accelerates from the high pressure to the lower pressure environment.

#### Density variation with velocity

Using the momentum equation combined with Mach number we find

$$\frac{d\rho}{\rho} = -M^2 \frac{dv}{v} \quad \text{Equation II-16}$$

Equation II-16 explains the compressibility effect in the two different regimes, for subsonic flows where ( $M^2 < 1$ ) the density variation is much smaller than the velocity variation between the two regions and vice versa, for supersonic flows the density change is more important, this demonstrates that the higher the Mach number the more compressible the flow is, see Figure II-1, another aspect is highlighted by Equation

II-16, that density and velocity always have to change in opposite directions so when the gas accelerates, its density follows by decreasing.

And finally we derive the equations for the velocity and pressure variation with the nozzle cross-section.

### Velocity variation with the cross-section

By replacing Equation II-16 in Equation II-14 we obtain Equation II-17 relating the velocity and the cross-section variation as a function of the Mach number.

$$\frac{dv}{v} = \frac{1}{M^2-1} \frac{dA}{A} \quad \text{Equation II-17}$$

The change in velocity depends on whether the term  $(M^2-1)$  is positive or negative, hence in the case of a supersonic flow, the velocity increases with the increase of the area cross-section in contrast to the subsonic flow where they change in opposite directions.

### Pressure variation with the cross-section

The same deduction is made for pressure variation with the cross-section by combining Equation II-15 and Equation II-17 which gives the following equation:

$$\frac{dp}{\rho v^2} = \frac{1}{1-M^2} \frac{dA}{A} \quad \text{Equation II-18}$$

Equation II-18 shows that unlike velocity, pressure decreases with the increasing area in supersonic flows and changes in the same direction in subsonic flow.

Table II-1 summarizes the variation of properties in compressible flow with the variation of the cross-section.

**Table II-1: Variation of the flow properties with the cross-section**

|          | $M < 1$                             | $M > 1$                             |
|----------|-------------------------------------|-------------------------------------|
| $dA < 0$ | $dv > 0$<br>$dp < 0$<br>$d\rho < 0$ | $dv < 0$<br>$dp > 0$<br>$d\rho > 0$ |
| $dA > 0$ | $dv < 0$<br>$dp > 0$<br>$d\rho > 0$ | $dv > 0$<br>$dp < 0$<br>$d\rho < 0$ |

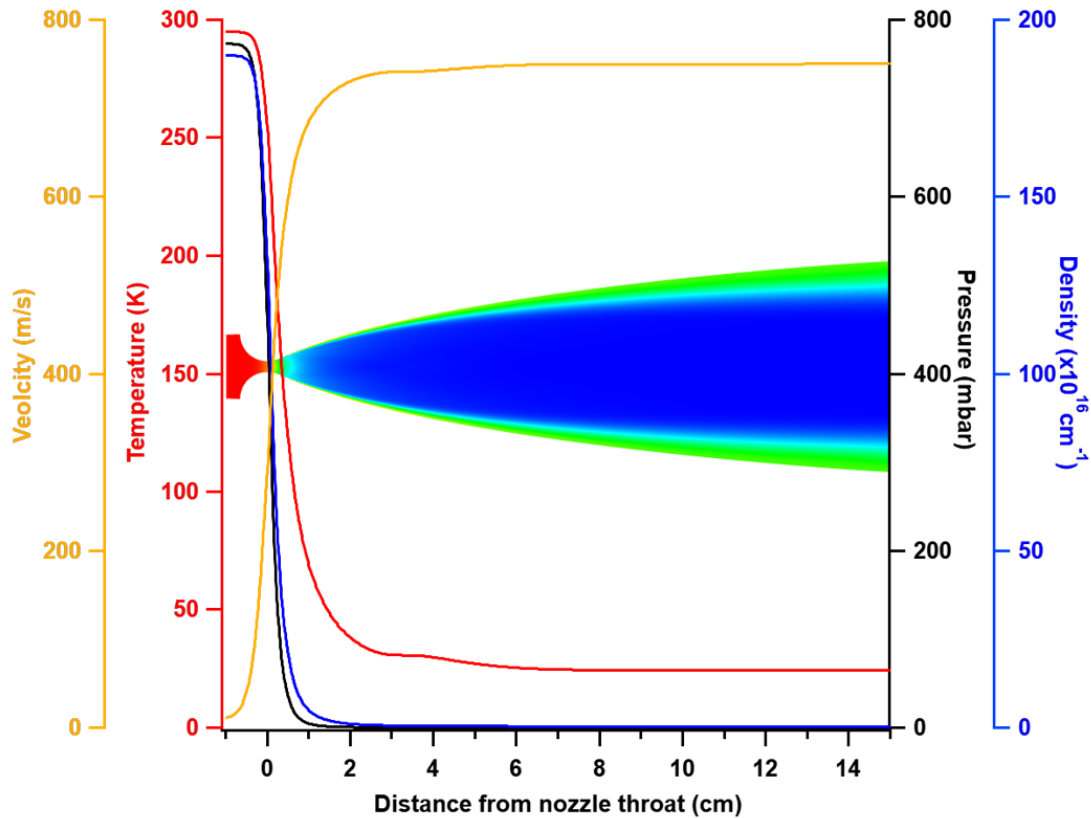


**Figure II-4.** Variation of the flow properties in an isentropic expansion in a Laval nozzle along the axis of symmetry, the expansion is calculated with the computational fluid dynamics software Ansys Fluent using nitrogen as a buffer expanding from 770 mbar at room temperature to 0.11 mbar in the chamber, the expansion produces a flow at 23.5 K with Mach 7.

### II.3.2.2. Sonic regime (Nozzle throat)

The passage from subsonic to supersonic regime in a Laval nozzle occurs in the narrowest region between the convergent and the divergent section known as the throat where the Mach number is equal to 1.

From Equation II-18 and by setting  $\frac{dA}{A} = 0$  we find that  $M = 1$

the sonic speed corresponding to Mach 1 can only occur when the area is not changing meaning that the regime changes either at a maximum or a minimum cross section, Equation II-17 states that a converging nozzle accelerates a subsonic flow and decelerates a supersonic one and a divergent nozzle does the opposite, meaning that the only possible scenario is that the sonic regime is reached at a minimum area, the conditions at the throat are given by the following equations:

$$\frac{T_0}{T^*} = \frac{\gamma+1}{2} \quad \text{Equation II-19}$$

$$\frac{p_0}{p^*} = \left(\frac{\gamma+1}{2}\right)^{\gamma/\gamma-1} \quad \text{Equation II-20}$$

$$\frac{\rho_0}{\rho^*} = \left(\frac{\gamma+1}{2}\right)^{1/\gamma-1} \quad \text{Equation II-21}$$

$$v^* = 2\gamma r T_0 \left(\frac{1}{\gamma+1}\right)^{\frac{1}{2}} \quad \text{Equation II-22}$$

We then deduce the mass flow rate through the nozzle

$$m^* = A^* P_0 \left[ \frac{\gamma}{r T_0} \left(\frac{2}{\gamma+1}\right)^{\frac{(\gamma+1)}{(\gamma-1)}} \right]^{\frac{1}{2}} \quad \text{Equation II-23}$$

From the continuity equation  $\dot{m} = \rho \cdot V \cdot A = \rho^* \cdot V^* \cdot A^*$ , we develop Equation II-24 that relates the cross section at the throat to any given point in the flow via the Mach number at that point, usually the exit point of the nozzle where the final Mach is reached.

$$\frac{A}{A^*} = \frac{1}{M} \left(\frac{2}{\gamma+1}\right)^{\frac{1}{2} \frac{\gamma+1}{\gamma-1}} \left(1 + \frac{\gamma-1}{2} M^2\right)^{\frac{1}{2} \frac{\gamma+1}{\gamma-1}} \quad \text{Equation II-24}$$

Where  $A^*$  is the cross-section at the throat and  $A$  is the cross-section at a region of the expansion defined by the Mach number.

**Choked flow:** when the flow reaches  $M=1$  at the throat, it becomes choked, the pressure changes then can no longer be communicated upstream as the speed at which these pressure changes are propagated is limited by the speed of sound, the upstream side (convergent) then is isolated from the downstream side at the throat (divergent) and so further reductions in downstream pressure will only accelerate the fluid from the throat unlike non-choked flow where reducing the outlet pressure results an increase of both the flow rate and velocity. This holds true until the flow rate is increased to the point that the fluid reaches the local sonic velocity at the throat and becomes choked. Changes in the upstream pressure affect the local speed of sound at the throat and can change the conditions downstream

### II.3.3. Nozzle design theory

Real flows generated by Laval nozzles cannot be characterized by the Euler equations alone, one must also consider viscosity effects and friction with the walls, which create a region of a strong gradient of the flow properties that envelops the cold isentropic

flow and is known as the boundary layer. The cold supersonic flow described earlier via the isentropic equations is called the isentropic core. To design the profile of the nozzle, the problem must be solved with a numerical procedure consisting of a process with two stages describing the two flow regimes separately.

The first stage concerns only the isentropic core region where the assumptions made above for isentropic compressible flow are valid and the Euler Equations, along with the isentropic equations can be used to extract the flows parameters based on the operating conditions of the nozzle and the nature of the carrier gas in use.

This procedure relies on calculating the isentropic profile coordinates along and across the axis  $(z,r)^{5-8}$  considering a perfect fluid by mean of the method of the characteristics, to solve the equation of an isentropic irrotational perfect gas in the stationary regime is given by,

$$(a^2 - v_z^2) \frac{\partial v_z}{\partial z} + (a^2 - v_r^2) \frac{\partial v_r}{\partial r} - 2v_z v_r \frac{\partial v_z}{\partial r} + \frac{a^2 v_r}{r} = 0 \quad \text{Equation II-25}$$

Where  $v_z$  and  $v_r$  are the axial and radial components of the velocity.

The calculations start by determining the mass flow rate at the throat region that according to the continuity equation is constant along the nozzle, then the exit radius of the nozzle

$$r_e = \left( \frac{2m_e}{v_e(1-v_e^2)^{\frac{1}{\gamma-1}}} \right)^{\frac{1}{2}} \quad ; \text{with} \quad v_e = \frac{M_e}{\left( \frac{2}{\gamma-1} + M_e^2 \right)^{\frac{1}{2}}} \quad \text{Equation II-26}$$

Where  $r_e$   $m_e$   $M_e$  are the parameters at the nozzle exit, radius, masse flow rate and velocity respectively. The nozzle length is given by

$$z_e = b + h \quad \text{Equation II-27}$$

Where  $b$  is an arbitrary length parameter and  $h = \frac{M_e}{\tan \alpha}$ ;  $\alpha$  is the Mach angle between the Mach line and the axis of the nozzle and given by  $\alpha = \sin^{-1} \left( \frac{1}{M_e} \right)$ .

The determination of the contour of the isentropic wall of the nozzle requires the use of characteristic lines which make an angle  $\alpha$  with a given streamline of property (usually velocity vectors making an angle  $\theta$  with the axis of the flow), along these lines the motion along the  $r$  axis and displacement is given by

$$\frac{dr}{dz} = \tan(\theta \mp \alpha) \quad \text{Equation II-28}$$

The calculation of the characteristic lines is reproduced by successive iterations, from the first streamline and the Mach cone and going backwards to the nozzle throat <sup>6,9,10</sup> and at every point  $(z_i, r_i)$ , the flow parameters are determined. The solution is considered to be converged when the flow rate is equal or larger than the mass flow rate at throat. The isentropic wall is then deduced by interpolation of the calculated points. The process can also start from the throat and towards the Mach cone as shown by Figure II-5.

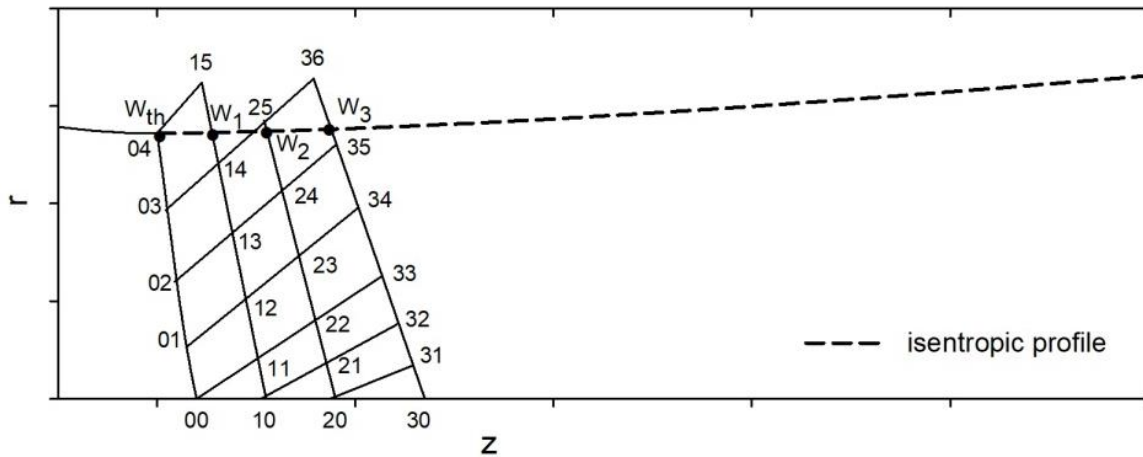


**Figure II-5. Determination of the isentropic core profile with the characteristic lines. Figure from by Canosa and Jiménez, Laval nozzles: Design, characterization and applications [unpublished manuscript]**

The second stage aims to characterize the boundary layers surrounding the isentropic core induced by friction and viscosity effects which makes the process irreversible in the boundary layers. The temperature increases across the boundary layers to attain the temperature of the walls  $T_{wall}$ , similarly, the velocity drops from supersonic speeds in the isentropic core to zero at the walls and so do the other parameters such as the density. The displacement parameter measures length that had to be added to the radius of the isentropic core to compensate the mass flow loss caused by the gradient of parameters and the velocity effect being zero at the wall in order to maintain the profile of the isentropic core. The real nozzle profile will include the isentropic core profile plus the displacement thickness  $\delta_1$ . This parameter is determined by integrating the Von Karman equation using the Michel's integral method.<sup>11</sup> The nozzle wall will be the original isentropic profile determined by the method of characteristics plus the displacement thickness.

$$r_{wall} = r_{isentropic\ core} + \delta_1 \quad \text{Equation II-29}$$

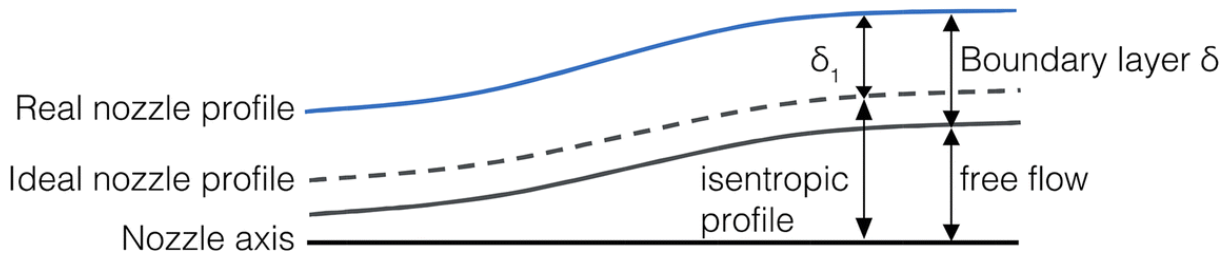


**Figure II-6. Nozzle profiles, in dashed black lines, the isentropic profile given by the method of characteristics and resulting the cold isentropic core (free flow) in continuous black line due to the manifestation of the boundary layer with a thickness  $\delta$ , the nozzle wall contour (real nozzle profile) is given in blue line as the sum of the inviscid contour and the displacement thickness. Figure from Fournier and co-workers<sup>12</sup>**

The convergent section of the nozzle with the subsonic flow is the least critical region in the nozzle, Owen and Sherman used a quarter circle set by the tangent of the throat to ensure the continuity of the divergent profile the radius of the convergent section is determined by the following equation:

$$r_{conv} = 5(r^* + \delta_1^*) - \delta_1^* \quad \text{Equation II-30}$$

The factor 5 in the equation above is an empirical choice set by Owen and represents the radius of curvature at the throat.

A program developed and written in Turbo Basic by J.B Marquette<sup>6,10,13</sup> has been used in the laboratory astrophysics group in Rennes to generate the nozzle profiles, the generated profiles are tested numerically then characterized experimentally before use to ensure they produce the design conditions (temperature, Mach number, density ...etc.). The procedure and the characterization of the generated Laval nozzle flows using fluid dynamic simulations and impact pressure characterization will be presented in the next chapter. We now introduce the CRESU technique which makes use of Laval nozzles and all the aspects of compressible and supersonic flows presented above to generate environments with extreme conditions of astronomical interest.

## II.4. Introduction to the CRESU technique

### II.4.1 Principle and theory

CRESU is a French acronym standing for Cinétique de Réaction en Ecoulement Supersonique Uniforme or reaction kinetics in uniform supersonic flow. It is the primary cooling technique used at the IPR (Institut de Physique de Rennes) for laboratory astrophysics applications, and was developed in the 1980s by Bertrand Rowe and Jean-Baptiste Marquette at the laboratoire d'Aérothermique de Meudon.<sup>6,13,14</sup> It is nowadays widely used to generate low temperature gas phase conditions relevant to multiple space environments including the interstellar medium (in particular dense clouds) and planetary atmospheres.<sup>15</sup> The CRESU technique uses the Laval nozzles explained earlier to generate uniform supersonic flows by expanding the gas from high pressure environment usually a reservoir into vacuum created in the expansion environment known as the CRESU chamber, the difference in pressure is created by a large pumping group able to create sufficiently low pressures with high mass flow rates. The CRESU technique introduces the concept of uniformity meaning that isentropic core does not exhibit any axial and radial variations of the flow properties, which makes the technique ideal for studying reaction kinetics and dynamics in a stable environment with uniform temperature and pressure. The use of relatively high flow rates compared to other cooling techniques is necessary in order to support uniformity for longer times. The uniform flows can endure up to a few decimeters which corresponds to times of hundreds of microseconds depending on the nature of the gas. The relationship below shows that uniformity is boosted by the mass flow rate and decreased by gas viscosity.<sup>16,17</sup>

$$\frac{\delta}{L} \sim \frac{1}{20} Re ; \quad L \sim 0.06 \frac{Q_m}{\mu} \quad \text{Equation II-31}$$

Regardless of viscosity which is an intrinsic property of the gas and its temperature, the uniformity can be extended by increasing the flow rate.

So far the lowest temperature attained by the CRESU technique with the reservoir at room temperature was measured in Rennes at 10 K in the continuous regime using helium as a buffer as part of this work (see Figure II-7). Another option involves precooling the gas in the reservoir using liquid nitrogen. This enabled to generate helium flows down to 7 K<sup>18</sup> and hydrogen flows as low as 5.5 K.<sup>19</sup>

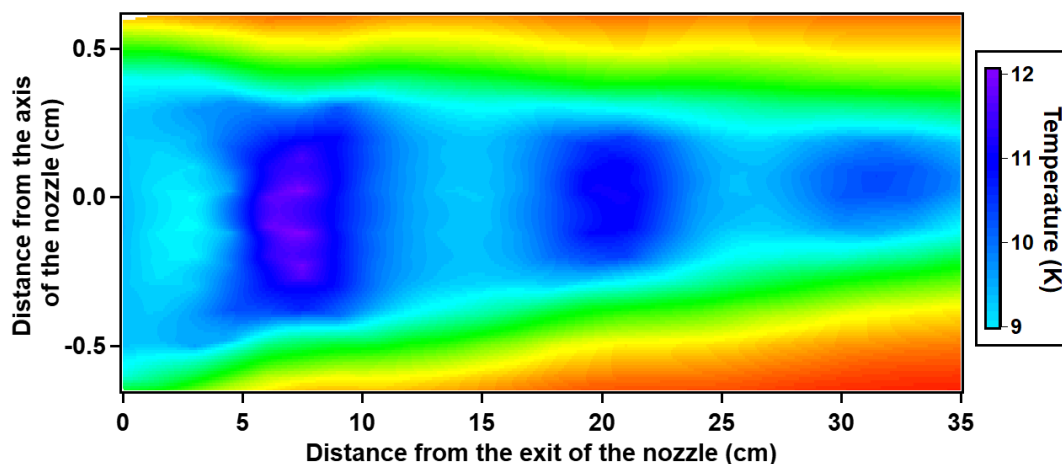


**Figure II-7. 2D temperature profile of the lowest temperature reached under continuous CRESU conditions without precooling the gas in the reservoir using helium buffer, the color shows a temperature variation between 9 and 12 K in the isentropic core, the average temperature is approximately 10 K and the flow lasts for approximately 200  $\mu$ s, the results were acquired with impact pressure measurements using a Pitot tube as will be shown in the next chapter.**

Beside the flow uniformity which is a critical parameter to study the kinetics of reactions, the relatively high gas density, values varying between  $10^{16}$  and  $10^{17}$   $\text{cm}^{-3}$  in the uniform supersonic flow, induces frequent collisions during the expansion and subsequent flow which ensures thermal equilibrium in the flow. Despite the high density flows, the CRESU apparatus represents a wall less cooling reactor which makes it not susceptible to condensation, a privilege that allows us to go to low temperatures without threatening the uniform properties of the CRESU flow. This applies to carrier flows, when injecting larger molecules of interest in the flow, the operator must take heed to the concentrations used in order not to form van der Waals complexes, either molecule-molecule or molecule-buffer, more details are given in the second part of chapter III.

#### II.4.2. Flow pattern and operating conditions

In order for the CRESU apparatus to generate uniform supersonic flows, the operating conditions must be optimized and in particular the stagnation pressure in the reservoir and chamber pressure. Having Mach 1 at the throat of the nozzle does not necessarily mean that the uniform supersonic flow will be established, the ratio between stagnation pressure and the chamber pressure is critical to carry out the expansion and maintain a uniform flow, the conditions of  $\frac{P_{ch}}{P_s} \leq \left[ \frac{P_{ch}}{P_s} \right]_{supersonic}$  must be verified; Where

$\left[\frac{P_{ch}}{P_s}\right]_{supersonic}$  represents the maximum value of the chamber pressure  $P_{ch}$  and the stagnation pressure  $P_s$  ratio able to create the supersonic flow. Beyond this value, the flow is subsonic. The other condition is that the chamber pressure needs to be maintained equal to the nozzle exit pressure. Figure II-8 illustrates the multiple flow patterns that may be generated according to the operating conditions (ratio between the chamber pressure in the expansion chamber and the stagnation pressure in the reservoir).

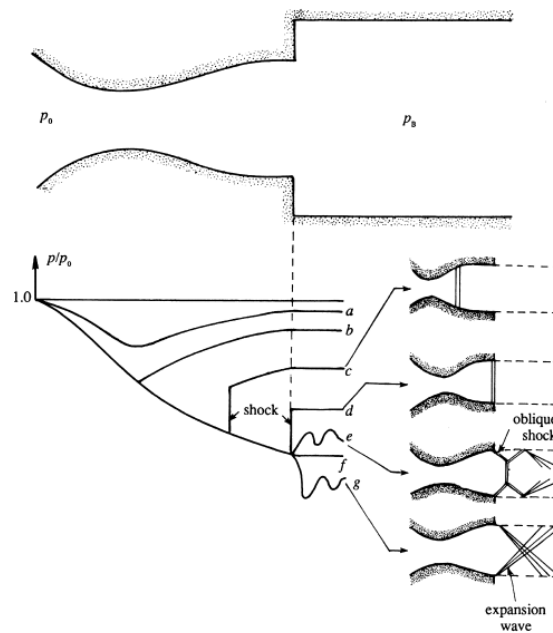


**Figure II-8. Plot of the flow patterns with respect to the back pressure and the stagnation pressure ratio. Figure from Fluid Mechanics (Fifth Edition, 2012) by Kundu, P. K., Cohen, I. M., Dowling, D. R., Eds<sup>20</sup>**

In case (a) the nozzle behaves like a Venturi tube, the flow accelerates toward the throat of the nozzle but does not reach Mach 1 as the pressure ratio is not low enough, it then begins to decelerate as the cross section increases as explained in Table II-1. The Bernoulli and conservation of mass equations are used for speed calculation.

By reducing the exit  $P_s$  pressure further in case (b), the flow accelerates faster but as the imposed chamber pressure is not low enough to satisfy the supersonic pressure ratio condition, the flow in the divergent section cannot cross the supersonic barrier and the pressure starts increasing with the increasing cross-section

In cases (c) and (d) where the chamber pressure is reduced further the flow reaches supersonic conditions in the divergent section and the pressure gradually decreases,

however when the exit pressure is not perfectly low to carry out the full expansion, somewhere in the divergent section of the nozzle, shockwaves, a non isentropic dissipative phenomenon that manifests with an abrupt and severe variation of the conditions, tend to block the expansion, destroying the subsequent uniformity of the flow (see section II.5).

The scenario (c) demonstrates that reducing the chamber pressure of a choked flow creates a supersonic flow within the diverging section of the nozzle, so if pressure is reduced to the optimum value, the expansion resumes and the flow accelerates to its maximum Mach number. The shock wave is suppressed (case f) or pushed further to the nozzle exit in case the pressure is slightly different than the optimum as shown in cases (e) and (g).

The last three scenarios are the most commonly encountered in the CRESU environment, the mismatch between the chamber pressure and the optimum operating pressure of the flow induces perturbations outside the nozzle creating different expanding flow patterns, these operating conditions have been applied to simulation of nitrogen nozzle that generate a flow at 23.5 K with its design conditions, the results are shown below,

**Underexpanded flow:** When chamber pressure is lower than the exit pressure, the flow exiting the nozzle will resume the expansion started in the nozzle. Known as underexpanded, this regime is mostly seen in rocket engines where a maximum force of thrust is needed. Figure II-9 shows the Mach profile of the 23.5 K nitrogen flow operating in an under expanded regime.

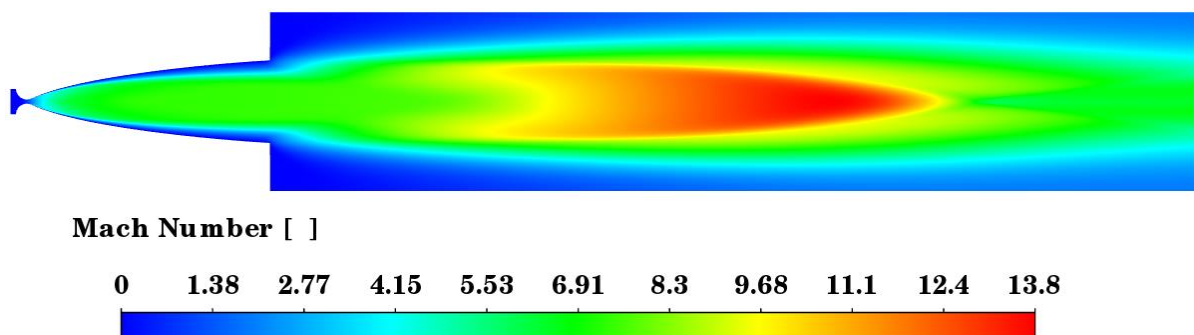


**Figure II-9. 2D Mach number profile of a nitrogen nozzle operating in an under expanded regime, the simulations are carried out with the computational fluid dynamics software Ansys Fluent using nitrogen as a buffer expanding from 770 mbar at room temperature to 0.05 mbar in the chamber.**

**Overexpanded flow:** when the chamber pressure is higher than exit pressure, the flow compresses inward at the exit of the nozzle, it occurs as the flow has over expanded in the nozzle. Since the chamber pressure is not much higher than the exit pressure, the flow will not be destroyed completely as in cases (c) and (d) in Figure II-8 but rather forms an oblique shockwave (see section II.5) where the flow properties do not necessarily drop to the subsonic regime. The flow pressure then increases after the shock but under the effect of the lower chamber pressure it re-expands, this process repeated several times until the shock gets weaker and the flow fades away.

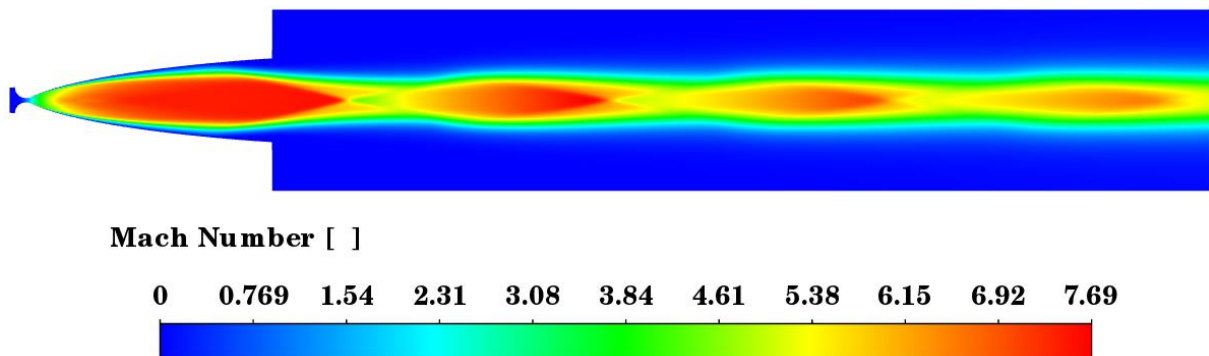


**Figure II-10.** 2D Mach number profile of a nitrogen nozzle operating in an over expanded regime, the simulation is carried out with the computational fluid dynamics software Ansys Fluent using nitrogen as a buffer expanding from 770 mbar at room temperature to 0.30 mbar in the chamber.

This phenomenon is known as shock diamonds and is widely observed in jet rocket exhausts (see Figure II-11).



**Figure II-11.** Shock diamonds formed in the after body of an F-15 Fighter jet (Reuters)

**Ideal flow:** occurs when the operating conditions are similar to the design conditions, with the chamber pressure being equal to the exit pressure. The flow maintains uniform properties as shown in Figure II-12 for a nitrogen flow that lasts for more than 700 microseconds.

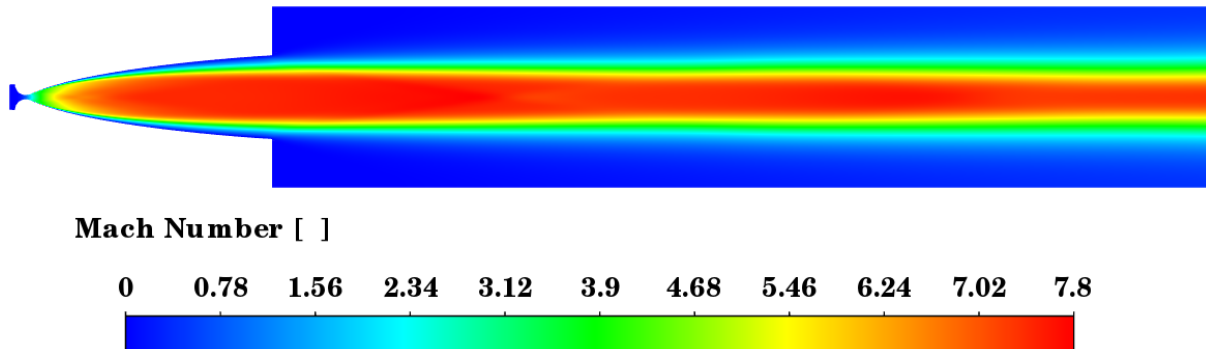


**Figure II-12.** 2D Mach number profile of a nitrogen nozzle operating in an ideal regime, the simulation is carried out with the computational fluid dynamics software Ansys Fluent using nitrogen as a buffer expanding from 770 mbar at room temperature to 0.11 mbar in the chamber.

Even with the appropriate operating conditions the uniform flow will not endure indefinitely, boundary layers eventually take over and the isentropic core disappears as results of transport phenomena such as diffusion to boundaries and friction with the viscous layers in a progressive gradual process that can take hundreds of microseconds, unlike shockwaves that lead to a drastic sudden variation in flow properties.

## II.5. Shockwaves

CRESU flows and supersonic flows in general, are often associated with phenomena of disturbance known as shockwaves, that can disrupt the flow uniformity and potentially destroy the supersonic flow entirely. Shockwaves are non-isentropic processes in supersonic flows, they occur as a result of gas moving at supersonic speeds therefore unable to sense the presence of an obstacle or a divergence in optimum conditions in downstream regions, as a result of the information that travels below speed of sound as explained earlier. A shockwave manifests itself by a compression front on the order of few molecular mean free paths separating two regions in the flow,<sup>21</sup> upstream of the shock the supersonic regime is maintained and downstream the subsonic regime may be established depending on the strength and

the type of the shock. In an oblique shockwave, it is possible that the supersonic regime is preserved, in contrast to a normal shockwave where the flow is compelled to drop to the subsonic regime. In both shockwaves the flow properties upstream change abruptly and suddenly, the static temperature, pressure and density increase while the velocity and the Mach number decrease. Although being irreversible as the entropy increases after the shock there is no heat transfer from outside the flow, therefore the process is still adiabatic. Both shockwave types are encountered in the CRESU technique, and will be discussed further in chapter III where the concept of normal shockwave is used as a working principle for characterizing the CRESU flows with a Pitot tube apparatus, and in chapter V where we use a beam sampling technique to re-expand the CRESU flow with the use of a skimmer; oblique and normal shockwaves can manifest and hinder the measurements. Here we define the basic governing equations of shockwaves that enables us to characterize the supersonic flow upstream and downstream of the shock layer for both normal and oblique shockwaves.

### II.5.1 Normal shock

Using the conservation of mass, momentum and energy equation, we can write the ratio between the flow properties upstream and downstream the shock layer with index 1 and 2 respectively, static pressure ratio is given by the following

$$\frac{p_2}{p_1} = \frac{2\gamma M_1^2 - (\gamma - 1)}{\gamma + 1} \quad \text{Equation II-32}$$

The static temperature ratio is given by

$$\frac{T_2}{T_1} = \frac{[2\gamma M_1^2 - (\gamma - 1)][(\gamma - 1)M_1^2 + 2]}{(\gamma + 1)^2 M_1^2} \quad \text{Equation II-33}$$

The density ratio is given by

$$\frac{\rho_2}{\rho_1} = \frac{(\gamma + 1)M_1^2}{(\gamma - 1)^2 M_1^2 + 2} \quad \text{Equation II-34}$$

### II.5.2. Oblique shock

On the contrary to normal shocks, oblique shockwaves do not necessarily change the supersonic regime to subsonic only strong shocks do. The ratio between the static pressure upstream and downstream, that besides the Mach number and the specific heat ratio, depends also on  $\beta$  the shock angle, is given by

$$\frac{p_2}{p_1} = \frac{2\gamma M_1^2 \sin^2(\beta) - (\gamma - 1)}{\gamma + 1} \quad \text{Equation II-35}$$

The static temperature ratio is given by

$$\frac{T_1}{T_0} = \frac{[2\gamma M_1^2 \sin^2(\beta) - (\gamma - 1)][(\gamma - 1)M_1^2 \sin^2(\beta) + 2]}{(\gamma + 1)^2 M_1^2 \sin^2(\beta)} \quad \text{Equation II-36}$$

The density ratio is given by

$$\frac{\rho_1}{\rho_0} = \frac{(\gamma + 1)M_1^2 \sin^2(\beta)}{(\gamma - 1)^2 M_1^2 \sin^2(\beta) + 2} \quad \text{Equation II-37}$$

## II.6. Comparison with other cooling technique

### II.6.1. Cooling techniques

As explained earlier, generating cold flows is highly important for studying collisional processes in the cold regions of the interstellar medium by recreating those conditions in the laboratory. This requires the implementation of a cooling technique, besides CRESU we can enumerate some of the most currently used techniques to cool down gases for laboratory astrophysics applications.

#### II.6.1.1. Free jet expansions

The technique relies on the same principle as the CRESU technique, generating an expansion from high pressure in the reservoir into a low pressure in the chamber through a convergent nozzle or a pinhole<sup>22,23</sup> creating a region with extremely low temperature followed by a shock wave known as the Mach disk the distance at which this shock disk appears is determined by the following equation:

$$\frac{L}{d} = 0.67 \sqrt{\frac{p_{res}}{p_{ch}}} \quad \text{Equation II-38}$$

where  $d$  is the diameter of the hole and  $L$  is the distance of cold region also known as the zone of silence. The technique uses relatively low flow rates allowing it to generate more differential pressure and therefore go to extremely low temperatures with lower collision rate which makes it ideal for spectroscopic measurements. The technique does present some limitations however related to the large velocity distribution due to the radial deviation and the strong gradient along the axis and the low collision rate

resulting in the flow being in a non-thermal equilibrium condition. The technique is therefore not very well-suited for reaction studies.

### **II.6.1.2. Molecular beam sampling**

The limitation of the aforementioned technique can be improved by coupling it with molecular beam sampling technique that uses a skimmer to sample a portion of the expanded jet and potentially followed by a collimator to narrow the velocity distribution of the skimmed molecules, this requires a series of differential pumping between the three compartments.<sup>24</sup>

### **II.6.1.3. Cryogenic cooling and collisional cooling**

One of the classic techniques of cooling that relies on flowing a cooling fluids such as liquid nitrogen at 77 K or liquid helium at 4 K in a double walled chamber, the buffer in the chamber is cooled down via collisions with the chamber walls. The technique presents a good environment to study kinetics and energy transfer processes, but the major limitation is condensation that may occur while colliding with the cryogenic walls, the buffer and the reactants must be kept below their vapor pressures at the wall temperature. A more recent version of this technique involves injecting the species of interest in a cell containing a cold buffer, usually helium or neon, the species are cooled and thermalized via collisions with the buffer.<sup>25-28</sup>

## **II.6.2. Power of the CRESU technique**

The CRESU technique presents numerous advantages at multiple aspects over other cooling techniques. It generates a wall less flow in a vacuum environment which limits the possibility of forming condensates of the gas whether by colliding with the nozzle walls during the expansion or with the chamber walls. This flow is able to self-sustain its uniformity and properties without further collision with the chamber walls, furthermore, CRESU flows are thermally equilibrated due to the frequent collisions which makes them ideal environments to study reaction kinetics and collisional energy transfer processes. On the other hand it consumes large quantities of gas in order to support longer hydrodynamic times, and the high collision rate can significantly weaken the sensitivity of some detection techniques such as microwave spectroscopy in particular, as will be shown in the next part of the chapter.

## Part II: Chirped pulse Fourier transform mm-microwave spectroscopy

In this second part of the chapter we introduce the chirped pulse Fourier transform microwave spectroscopic technique (CP-FTMW) based on microwave rotational spectroscopic theory,<sup>29,30</sup> in this thesis extended to the mm-wave band (CP-FTmmW), we will discuss the rotational line shapes and intensities in addition to coupling the CP-FTmmW with the CRESU technique introduced in part I of the chapter, the instrumental developments and limitations of the CPUF technique will be discussed in chapters III and IV respectively.

### II.7. Introduction to microwave rotational spectroscopy

Microwave rotational spectroscopy relies on the interaction of the dipole of molecule with an exciting electromagnetic radiation pulse to measure transitions between rotational energy state of a given molecules in the gas phase. The technique is used for the detection of polar molecules and their molecular structures via the associated moments of inertia. The relation between moment of inertia, bond length, angles and masses of atoms constituting the molecule gives access to nature of atoms and their geometrical disposition in space (see Equation II-39).

$$I = \sum_i m_i r_i^2 \quad \text{Equation II-39}$$

Where  $I$  is the moment of inertia,  $m_i$  and  $r_i$  represent the mass of the  $i^{\text{th}}$  atom and its distance from the rotation axis respectively.

Using the definition given by Equation II-39, we define the three orthogonal axes of inertia passing through the center of mass of the molecule defining three moments of inertia,  $I_a, I_b$  and  $I_c$  where by convention,  $a$  corresponds to the axis with least moment of inertia, and  $c$  with the greatest one i.e  $I_c \geq I_b \geq I_a$ , we can classify molecules based on their rotational symmetry. First, we have spherical top molecules defined by equal moments of inertia they are highly symmetrical and have no dipole. Molecules with permanent dipole can be linear molecules such as HCN or HC<sub>3</sub>N, when  $I_c = I_b$  and  $I_a = 0$ . Linear polyatomic molecules behave like diatomic molecules in simple rotation modeled by a rigid rotor which assumes that molecular bonds between atoms are rigid, a more realistic model involves including a parameter which takes into account the centrifugal distortion parameter of the molecule. In this model we consider the

molecular bonds as springs, therefore the rotations will be associated with stretching of the bonds. The energy levels for linear polyatomic molecules are characterized by the  $J$  total rotational angular momentum quantum number, the rotational transitions occur as such,  $J'' \leftarrow J'$  with  $J''$  is the quantum number of the initial rotational energy state and  $J'$  is the quantum number of the final rotational energy state.

Symmetric top molecules have two equal moments of inertia and can either have a prolate shape, this is when  $I_c > I_b = I_a$  or oblate shape when  $I_c = I_b > I_a$ . Thus it is necessary to introduce the quantum number  $K$  corresponding to the projection of the rotational angular momentum along the rotational axis and the rotational state is denoted by  $J_K$  where  $K$  is always equal to or less than  $J$ .

Asymmetric top molecules such as vinyl cyanide and benzonitrile (used in this work) have three moments of inertia different from each other associated with the principal axes a, b and c, the rotational constants are related to the moments of inertia of a given molecule by the following equations:

$$A = \frac{h}{8\pi^2 c I_a}; \quad B = \frac{h}{8\pi^2 c I_b}; \quad C = \frac{h}{8\pi^2 c I_c} \quad \text{Equation II-40}$$

Rotational transitions occur between energy levels expressed by  $J_{K_a, K_c}$  where  $K_a$  and  $K_c$  represent the K values that the molecule would have in the limiting oblate and prolate cases, respectively. The energy levels of asymmetric top molecules are therefore determined by approximations based on symmetric top molecules as shown by Figure II-13.

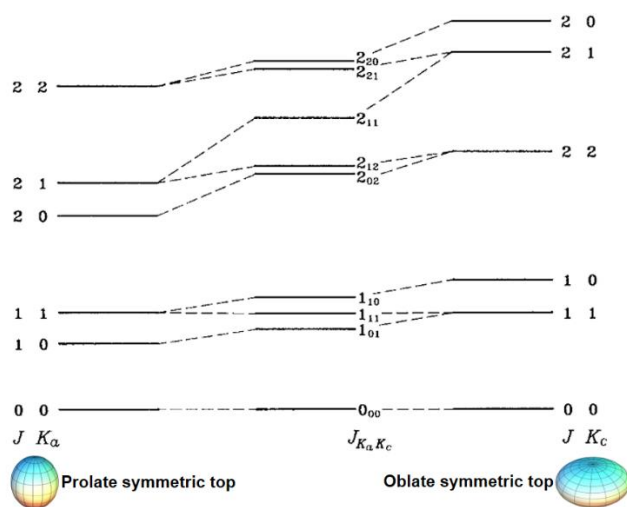


**Figure II-13. Energy levels in asymmetric top molecules, the limits  $K_a$  and  $K_c$  represent the prolate and oblate symmetric top molecules. Figure adapted from Lombardi 2007.<sup>31</sup>**

In this work we are not interested in obtaining information about the structures of molecules as the targeted species are known but the aim is to determine the branching fractions of reaction yielding those species by measuring the relative intensities of their rotational transitions without the need to know the concentrations i.e absolute intensities. Spectroscopic databases such as the Cologne Database for Molecular Spectroscopy CDMS<sup>32,33</sup> or the Molecular Spectroscopy database of the Jet Propulsion Laboratory JPL, provide catalogs containing the rotational transitions with their assigned frequencies and intensities at room temperatures and down to 9 K (see Figure II-15. These databases use the SPFIT/SPCAT routines developed by Pickett et al<sup>34</sup> to either generate catalog files for molecules using rotation constants as input parameters or as output results in order to determine the molecular structure by fitting experimentally measured transitions.

## **II.8. Chirped Pulse Fourier Transform mm-MicroWave Spectroscopy (CP-FTmm-MW)**

Chirped Pulse Fourier Transform mm-MicroWave Spectroscopy (CPFTmm-MW) is a new development in microwave spectroscopic instruments that enables broadband measurements of molecular transitions in a single acquisition thanks to the recent technological developments providing sophisticated electronic components such as broadband amplifiers, arbitrary waveform generators and fast acquisition cards. Invented by Pate and coworkers in the late 2000's,<sup>35,36</sup> CP-FTMW spectroscopy represents an upgraded version of the Fabry-Perot cavity microwave spectrometer<sup>37</sup> developed in the early 1980's which uses single frequency pulses per acquisition. The first CP-FTMW spectrometer generated chirps with 11 GHz bandwidth from 7 to 18 GHz a first step that paved the way for further exploring of the higher frequency bands up to terahertz domain.<sup>38,39</sup>

The technique consists in polarizing molecules with dipole transitions in the targeted range of the chirped pulse by exposing them to an electromagnetic field for a short period of time that excite them to higher rotational energy levels creating a phase of coherent rotation, when the electromagnetic radiation pulse is over, excited molecules start losing the state of coherence and relaxing back to their initial state, in the process they emit an electromagnetic signal known as the Free Induction Decay (FID). This

time dependent signal contains the fingerprints of molecules present in the irradiated sample, the Fourier transform of the FID gives molecular spectrum. The technique is considered to be very distinctive as being able to differentiate between the molecules, uniquely defined by the rotational transitions, including isotopologues, isomers and conformers. The signal  $S$  emitted by the polarized molecules is derived from the optical Bloch equations<sup>40</sup> and shown by the following relationship

$$S \propto \omega \mu^2 E_{pulse} \Delta N_0 \left(\frac{\pi}{\alpha}\right)^{\frac{1}{2}} \quad \text{Equation II-41}$$

Where  $\omega$  is the frequency,  $\mu$  is the transition dipole moment,  $E_{pulse}$  is the electric field magnitude,  $\Delta N_0$  is the population difference at equilibrium and  $\alpha$  is the sweep rate.

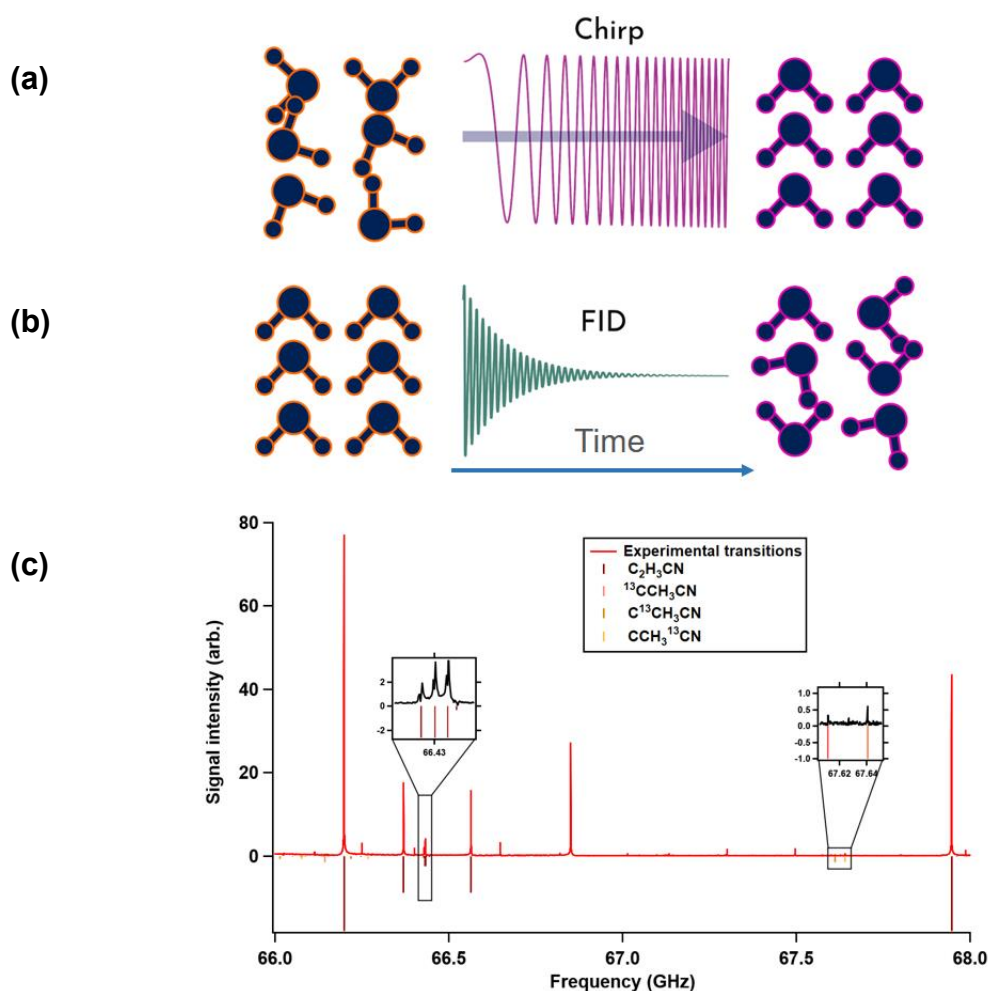


**Figure II-14.** Chirped pulse procedure, (a) broadband excitation of molecules, (b) relaxation to initial state by FID emission, (c) rotational spectrum of vinyl cyanide acquired by Fourier transforming the FID, vinyl cyanide isotopologues have been detected, the spectrum (in red) is acquired from vinyl cyanide in an argon flow at 35 K sampled via a skimmer into a secondary expansion chamber (see chapter V), the transition in colors are synthetic spectra at 9.375 K from CDMS.

## II.9. Microwave line intensities and shapes

Besides spectral line intensity which depends on the transition frequency, the electric dipole moment<sup>34</sup> and the experimental conditions as shown by Equation II-41, line shapes and in particular linewidth are important characteristics of the spectrum and reflect information about the molecule as well as the environment where the probing is carried out.

### II.9.1. Natural linewidth

Transitions occurring between two energy levels  $E_1, E_2$  arising from spontaneous emissions are always associated with a certain width called the natural linewidth, resulting from Heisenberg's uncertainty principle when a given energy state is populated for a certain time  $\Delta t$

$$\Delta E \times \Delta t \geq \frac{h}{2\pi} \quad \text{Equation II-42}$$

The full width of the line is determined at the half of its height and given by

$$\Delta\gamma_{nat.FWHM} = \frac{1}{2\pi} \left[ \frac{1}{\tau_1} + \frac{1}{\tau_2} \right] \quad \text{Equation II-43}$$

Where  $\tau_1$  and  $\tau_2$  are the lifetimes of population in the lower and the excited states respectively. Rotational relaxations are on the order of  $10^{-12}$  s, therefore often in experiments, the natural band width of a transition line is over shadowed by more significant widths that stem from other contributions related to the experimental environment, the most important ones are Doppler and pressure broadening.

### II.9.2. Doppler broadening

The Doppler broadening corresponds to the line broadening due to the motion of the gas, it involves thermal Doppler resulting from the Maxwell-Boltzmann distribution of velocities induced by the thermal agitation of molecules, plus the macroscopic velocity of the gas with the respect to the probing direction causing a frequency shift, this is known as the Doppler effect and is given by the following equation:

$$f = f_0 \left( 1 \pm \frac{v}{c} \right) \quad \text{Equation II-44}$$

where  $f_0$  is the transition frequency emitted by the molecule and  $f$  is frequency received by spectrometer and  $v$  is the transversal velocity of molecules and  $c$  is the

speed of light. The line broadening occurs as a result of the velocity distribution at a given temperature. The Doppler component of the linewidth is given by

$$\Delta\gamma_{Dopp.FWHM} = f_0 \left( \frac{8kT \ln 2}{mc^2} \right)^{1/2} \quad \text{Equation II-45}$$

Characterized by a Gaussian profile, Doppler broadening is considered to be inhomogeneous as atoms or molecules in the sample could have different velocities and temperatures. It is mostly predominant in collision-free environments with thermally agitated atoms/molecule where low pressure limit values are achieved and combined with high temperatures. In this work the probing is perpendicular to the direction of the flow (see Figure III.13 in Chapter III), and the Doppler effect can be neglected, thermal Doppler however remains as contributing factor in the line shape.

### II.9.3. Pressure broadening

Pressure broadening also known as collisional broadening, induced by collisions between molecules, it manifests from pressures of  $10^{-3}$  mbar and above.<sup>41</sup> The line broadening occurs as result of energy transfer due to inelastic collisions leading to perturbations of the energy levels.

Assuming that each collision results in a transition between two states then the line width due to the pressure component is given by

$$\Delta\gamma_{pres.FWHM} = \frac{1}{2\pi\tau_{collision}} \quad \text{Equation II-46}$$

Where  $\tau_{collision}$  is the mean time between collisions. The pressure broadening rate varies linearly with pressure as follows:

$$\Delta\gamma_{pres} = \gamma_{pres} \cdot p \quad \text{Equation II-47}$$

where  $\gamma_{pres}$  is the pressure broadening coefficient and depends on the temperature by the following relation:

$$\gamma_{pres}(T) = \gamma_0 \left( \frac{T_0}{T} \right)^n \quad \text{Equation II-48}$$

where  $\gamma_0$  is the coefficient at a reference temperature  $T_0$  and  $n$  is a constant. The pressure coefficient can be measured by fitting the line shape to a Lorentzian profile to extract the pressure broadening rate at the varying pressures, the determination of the

pressure broadening coefficient at different temperatures will give the degree of the temperature dependence coefficient  $n$ .

In the CRESU environment, pressure broadening is induced by collisions between radiating molecules and the perturbing buffer gas, in fact it is considered as a major limiting factor for the detection of the molecular signal. During the relaxation process of the radiator, buffer atoms or molecules collide with the radiating molecules causing them to lose phase coherence and undergo the relaxation without emitting photons which results to a quick quenching of the FIDs leading to molecular spectra with weak signal to noise ratio.

Microwave spectroscopy is frequently performed in the limit where Doppler broadening is the dominant dephasing mechanism. The CRESU environment however generates thermally equilibrated flows favored by frequent collisions, the pressure component is then the dominant component in the FID as will be shown in chapter IV. However, the Gaussian type function accounting for the Doppler component is still included for accurate results.

$$\Delta\gamma_{Pres} > \Delta\gamma_{Dopp} \gg \Delta\gamma_{nat} \quad \text{Equation II-49}$$

#### II.9.4. FID modelling

The FIDs can be modeled with a time domain Voigt function that accounts for the Doppler broadening induced by the translational temperature and the radial velocity component of the flow beam as well as the pressure broadening component induced by collisions. The Voigt profile is given by the following equation:

$$f(t) = A \exp\left(-2\pi\Delta\gamma_{pres}t - \frac{\pi^2\Delta\gamma_{Dopp}^2 t^2}{\ln 2}\right) \cos(2\pi ft + \varphi) \quad \text{Equation II-50}$$

where  $f(t)$  is the signal intensity as a function of time,  $A$  is the initial amplitude of the FID,  $\Delta\gamma_{pres}$  is the pressure broadening rate,  $\Delta\gamma_{Dopp}$  is the Doppler broadening rate,  $f$  is the frequency of the transition, and  $\varphi$  is the phase of the signal, the Voigt profile is used in this work to fit vinyl cyanide and benzonitrile transitions to determine their associated pressure broadening rates and coefficients at room temperature in order to assess the impact of the pressure on the molecular signal in the CRESU environment, the results are given in chapter IV.

## II.10. Chirped pulse in uniform flow (Spectroscopy in cold media)

The CRESU technique presents favorable environment for CP-FTmmW spectroscopic detection particularly in terms of temperature. Reducing the temperature of the probed flow increases sensitivity by concentrating the population at lower energy levels thus strengthening the signal of particular transitions of interest.

For many molecules of astrochemical interest such as benzonitrile, at 300 K the population is distributed among many energy levels giving a highly congested spectra with lower intensities. Lowering the temperature to 9 K increases the signal by approximately two orders of magnitude and decreases the congestion of transitions by depopulating most of the higher energy levels and shifting the population to bands from 18 to 75 GHz. Most of these transition frequencies are covered by our spectrometers as will be shown in chapter III and IV, and the same considerations apply to the other molecules studied in this work; vinyl cyanide and cyanoacetylene.

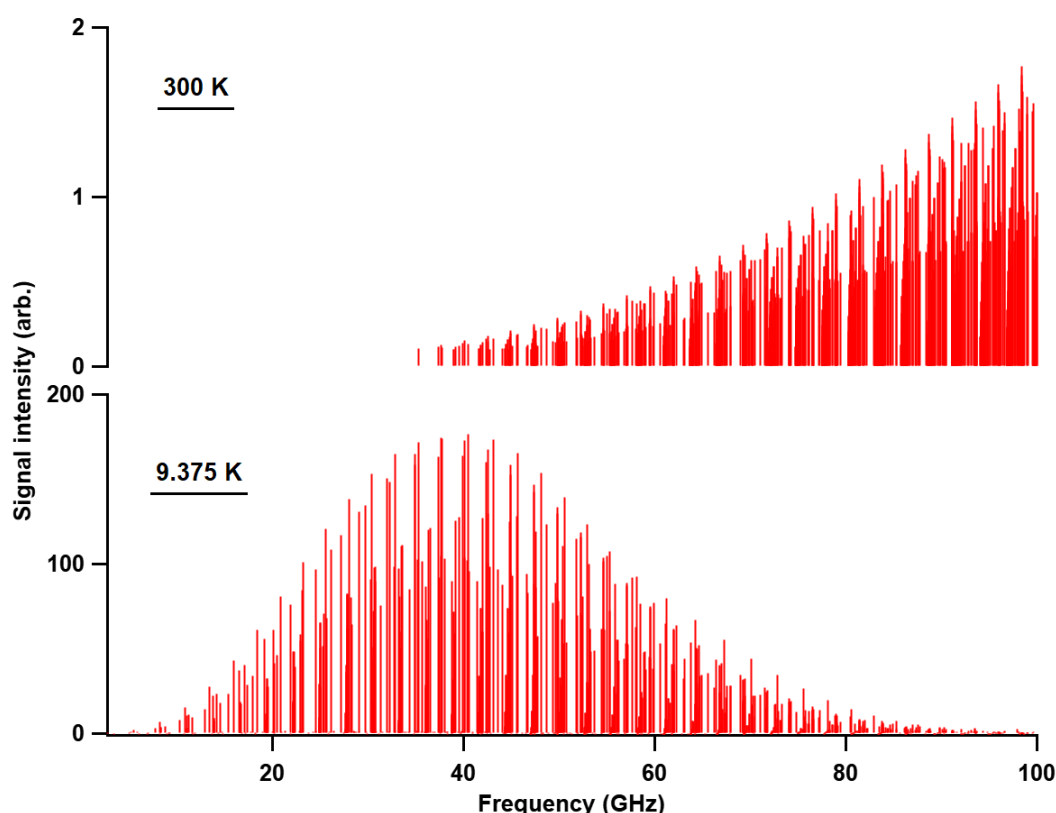


**Figure II-15. Benzonitrile rotational spectra at 300K and 9.375 K given by the CDMS catalogue**

In addition to line broadening, CPUF does present other challenges and limitations related primarily to the CRESU environment.

### II.10.1. Boundary layer contribution to the molecular signal

In a CRESU flow, radiating molecules are not only present in the isentropic core but can also be in boundary layers which initiate a contribution of a warm component, a parameter that must be considered in the overall molecular signal. This problem is more important for stable molecules injected directly in the CRESU flow as for transient molecules such as reactants or yielded products, we can exclude the warm contribution from the layers by photolysing only the isentropic core region by narrowing the laser beam with the use of an iris as will be shown in the next chapters.

Calculations were made using the SPCAT/SPFIT program to predict the evolution of molecular spectra at different temperatures and measure the attributed contribution in the overall signal. This uses rotational constants and dipole moments of vinyl cyanide to generate spectra at the required temperature. Assuming a linear probing across CRESU flow, the signal intensity variation with radial temperature and density is given in Figure II-16.

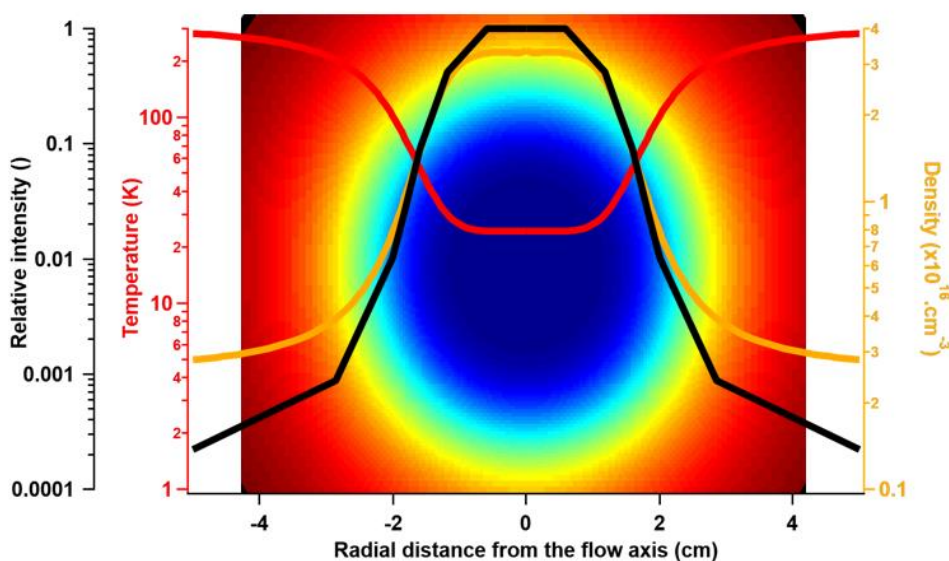


**Figure II-16. Signal variation of the  $J_{ka,kc} = 7_{0,7}-6_{0,6}$  vinyl cyanide transition between 20 K and 300 K assuming a linear radial probing of a CRESU flow generated from the nitrogen 23.5 K nozzle. The density decreases with the increasing temperature as we move away from the axis of symmetry, the intensities have been normalized with the strongest signal calculated at 20 K and corrected with the radial density profile, the results show that temperatures below 30 K make the main contribution to the molecular signal, a drop of an order of magnitude in the signal strength at temperatures above 40 K is observed. This effect is enhanced by the density gradient as we move away from the flow and two orders of magnitude at 100 K.**

Figure II-16 demonstrates that the contribution of boundary layers is minor but only for cold flows for example the contribution of the warm layer in a nitrogen 23.5 K flow would be higher than for a helium flow at 10 K, however the radial distribution of density must be considered in the boundary layer region where there is a gradient of temperature and density, therefore the signal must take into account for the radial density profile.

All the limitations aforementioned in addition to others that could jeopardize the molecular signal detection such as reflections of the exciting pulses on CRESU chamber walls which is purely experimental phenomenon related to the probing environment will be further discussed, experimentally measured and presented in chapter IV, while chapters V and VI propose solutions to overcome those problems.

## References

- (1) Oldham, J. M.; Abeysekera, C.; Joalland, B.; Zack, L. N.; Prozument, K.; Sims, I. R.; Park, G. B.; Field, R. W.; Suits, A. G. A Chirped-Pulse Fourier-Transform Microwave/Pulsed Uniform Flow Spectrometer. I. The Low-Temperature Flow System. *J. Chem. Phys.* **2014**, *141* (15), 154202. <https://doi.org/10.1063/1.4897979>.
- (2) Abeysekera, C.; Zack, L. N.; Park, G. B.; Joalland, B.; Oldham, J. M.; Prozument, K.; Ariyasingha, N. M.; Sims, I. R.; Field, R. W.; Suits, A. G. A Chirped-Pulse Fourier-Transform Microwave/Pulsed Uniform Flow Spectrometer. II. Performance and Applications for Reaction Dynamics. *J. Chem. Phys.* **2014**, *141* (21), 214203. <https://doi.org/10.1063/1.4903253>.
- (3) Abeysekera, C.; Joalland, B.; Ariyasingha, N.; Zack, L. N.; Sims, I. R.; Field, R. W.; Suits, A. G. Product Branching in the Low Temperature Reaction of CN with Propyne by Chirped-Pulse Microwave Spectroscopy in a Uniform Supersonic Flow. *The Journal of Physical Chemistry Letters* **2015**, *6* (9), 1599–1604. <https://doi.org/10.1021/acs.jpcllett.5b00519>.
- (4) Clarke, C. J.; Carswell, B. *Principles of Astrophysical Fluid Dynamics*; Cambridge ; New York : Cambridge University Press, 2007.
- (5) J. M. Owen. "An Improved Method of Supersonic Nozzle Design for Rarefied Gas Flows," Ph.D. Thesis (University of California, 1950).
- (6) Dupeyrat, G.; Marquette, J. B.; Rowe, B. R. Design and Testing of Axisymmetric Nozzles for Ion-Molecule Reaction Studies between 20 °K and 160 °K. *Phys. Fluids* **1985**, *28* (5), 1273. <https://doi.org/10.1063/1.865010>.
- (7) Anderson, J. D. *Fundamentals of Aerodynamics*, 3rd ed.; McGraw-Hill series in aeronautical and aerospace engineering; McGraw-Hill: Boston, 2001.
- (8) J. M. Owen and F. S. Sherman, Design and Testing of a Mach 4 Axially Symmetric Nozzle for Rarefied Gas Flows, Engineering Project Report: He 150-104, University of California Berkeley (1952).
- (9) CRONVICH, L. L. A Numerical-Graphical Method of Characteristics for Axially Symmetric Isentropic Flow. *Journal of the Aeronautical Sciences* **2012**. <https://doi.org/10.2514/8.11533>.

- (10) Durif, O. Design of de Laval Nozzles for Gas-Phase Molecular Studies in Uniform Supersonic Flow. *Physics of Fluids* **2022**, *34* (1), 013605. <https://doi.org/10.1063/5.0060362>.
- (11) R. Michel, *Aérodynamique : Couches Limites, Frottement et Transfert de Chaleur* (ENSAE, 1963).
- (12) Fournier, M.; Picard, S. D. L.; Sims, I. R. CHAPTER 1 Low-Temperature Chemistry in Uniform Supersonic Flows. **2017**, 1–45. <https://doi.org/10.1039/9781782626800-00001>.
- (13) Marquette, J.-B. Une Approche Expérimentale de l'astrochimie : La Méthode CRESU, Principe et Applications. These de doctorat, Paris 7, 1988.
- (14) Rowe, B. R.; Dupeyrat, G.; Marquette, J. B.; Gaucherel, P. Study of the Reactions  $N^+ + 2N_2 \rightarrow N^+ + 4N_2$  and  $O^+ + 2O_2 \rightarrow O^+ + 4O_2$  from 20 to 160 K by the CRESU Technique. *The Journal of Chemical Physics* **1984**, *80* (10), 4915–4921. <https://doi.org/10.1063/1.446513>.
- (15) Potapov, A.; Canosa, A.; Jiménez, E.; Rowe, B. Uniform Supersonic Chemical Reactors: 30 Years of Astrochemical History and Future Challenges. *Angewandte Chemie International Edition* **2017**, *56* (30), 8618–8640. <https://doi.org/10.1002/anie.201611240>.
- (16) *Low Temperatures and Cold Molecules*; Smith, I. W. M., Ed.; Imperial College Press: London, 2008.
- (17) Jiménez, E.; Ballesteros, B.; Canosa, A.; Townsend, T. M.; Maigler, F. J.; Napal, V.; Rowe, B. R.; Albaladejo, J. Development of a Pulsed Uniform Supersonic Gas Expansion System Based on an Aerodynamic Chopper for Gas Phase Reaction Kinetic Studies at Ultra-Low Temperatures. *Review of Scientific Instruments* **2015**, *86* (4), 045108. <https://doi.org/10.1063/1.4918529>.
- (18) James, P. L.; Sims, I. R.; Smith, I. W. M. Rate Coefficients for the Vibrational Self-Relaxation of  $NO(X^2\Pi, v = 3)$  at Temperatures down to 7 K. *Chemical Physics Letters* **1997**, *276* (5), 423–429. [https://doi.org/10.1016/S0009-2614\(97\)00849-X](https://doi.org/10.1016/S0009-2614(97)00849-X).
- (19) Labiad, H.; Fournier, M.; Mertens, L. A.; Faure, A.; Carty, D.; Stoecklin, T.; Jankowski, P.; Szalewicz, K.; Le Picard, S. D.; Sims, I. R. Absolute Measurements of State-to-State Rotational Energy Transfer between CO and H<sub>2</sub> at Interstellar Temperatures. *Phys. Rev. A* **2022**, *105* (2), L020802. <https://doi.org/10.1103/PhysRevA.105.L020802>.

- (20) Chapter 15 - Compressible Flow. In *Fluid Mechanics (Fifth Edition)*; Kundu, P. K., Cohen, I. M., Dowling, D. R., Eds.; Academic Press: Boston, 2012; pp 729–778. <https://doi.org/10.1016/B978-0-12-382100-3.10015-0>.
- (21) Rathakrishnan, E. *Applied Gas Dynamics*; John Wiley & Sons, 2019.
- (22) Campargue, R. High Intensity Supersonic Molecular Beam Apparatus. *Review of Scientific Instruments* **1964**, 35 (1), 111–112. <https://doi.org/10.1063/1.1718676>.
- (23) Campargue, R. Progress in Overexpanded Supersonic Jets and Skimmed Molecular Beams in Free-Jet Zones of Silence. *J. Phys. Chem.* **1984**, 88 (20), 4466–4474. <https://doi.org/10.1021/j150664a004>.
- (24) McLean, W. J.; Sawyer, R. F. Molecular Beam Sampling from High-Pressure Sources. *Acta Astronautica* **1974**, 1 (3–4), 523–540. [https://doi.org/10.1016/0094-5765\(74\)90113-1](https://doi.org/10.1016/0094-5765(74)90113-1).
- (25) Patterson, D.; Doyle, J. M. A Slow, Continuous Beam of Cold Benzonitrile. *Phys. Chem. Chem. Phys.* **2015**, 17 (7), 5372–5375. <https://doi.org/10.1039/C4CP03818E>.
- (26) Patterson, D.; Rasmussen, J.; Doyle, J. M. Intense Atomic and Molecular Beams via Neon Buffer-Gas Cooling. *New J. Phys.* **2009**, 11 (5), 055018. <https://doi.org/10.1088/1367-2630/11/5/055018>.
- (27) Goyette, T. M.; De Lucia, F. C.; Willey, D. R. Collisional Cooling as an Environment for Planetary Research. *Journal of Geophysical Research: Planets* **1991**, 96 (E2), 17455–17461. <https://doi.org/10.1029/91JE01775>.
- (28) Willey, D. R.; Crownover, R. L.; Bittner, D. N.; De Lucia, F. C. Very Low Temperature Spectroscopy: The Pressure Broadening Coefficients for CO–He between 4.3 and 1.7 K. *J. Chem. Phys.* **1988**, 89 (4), 1923–1928. <https://doi.org/10.1063/1.455089>.
- (29) Kakkar, R. *Atomic and Molecular Spectroscopy*; Cambridge University Press, 2015.
- (30) Bernath, P. F. *Spectra of Atoms and Molecules*; Oxford University Press, USA, 2005.
- (31) Lombardi, J. R. Radiation Interaction with Molecules. In *The Optics Encyclopedia*; John Wiley & Sons, Ltd, 2007. <https://doi.org/10.1002/9783527600441.oe082>.
- (32) Müller, H. S. P.; Schlöder, F.; Stutzki, J.; Winnewisser, G. The Cologne Database for Molecular Spectroscopy, CDMS: A Useful Tool for Astronomers and Spectroscopists. *Journal of Molecular Structure* **2005**, 742 (1), 215–227. <https://doi.org/10.1016/j.molstruc.2005.01.027>.

- (33) Endres, C. P.; Schlemmer, S.; Schilke, P.; Stutzki, J.; Müller, H. S. P. The Cologne Database for Molecular Spectroscopy, CDMS, in the Virtual Atomic and Molecular Data Centre, VAMDC. *Journal of Molecular Spectroscopy* **2016**, *327*, 95–104. <https://doi.org/10.1016/j.jms.2016.03.005>.
- (34) Pickett, H. M.; Poynter, R. L.; Cohen, E. A.; Delitsky, M. L.; Pearson, J. C.; Müller, H. S. P. SUBMILLIMETER, MILLIMETER, AND MICROWAVE SPECTRAL LINE CATALOG. *Journal of Quantitative Spectroscopy and Radiative Transfer* **1998**, *60* (5), 883–890. [https://doi.org/10.1016/S0022-4073\(98\)00091-0](https://doi.org/10.1016/S0022-4073(98)00091-0).
- (35) Brown, G. G.; Dian, B. C.; Douglass, K. O.; Geyer, S. M.; Pate, B. H. The Rotational Spectrum of Epifluorohydrin Measured by Chirped-Pulse Fourier Transform Microwave Spectroscopy. *Journal of Molecular Spectroscopy* **2006**, *238* (2), 200–212. <https://doi.org/10.1016/j.jms.2006.05.003>.
- (36) Brown, G. G.; Dian, B. C.; Douglass, K. O.; Geyer, S. M.; Shipman, S. T.; Pate, B. H. A Broadband Fourier Transform Microwave Spectrometer Based on Chirped Pulse Excitation. *Review of Scientific Instruments* **2008**, *79* (5), 053103. <https://doi.org/10.1063/1.2919120>.
- (37) Balle, T. J.; Flygare, W. H. Fabry–Perot Cavity Pulsed Fourier Transform Microwave Spectrometer with a Pulsed Nozzle Particle Source. *Review of Scientific Instruments* **1998**, *52* (1), 33. <https://doi.org/10.1063/1.1136443>.
- (38) Lampin, J.-F.; Pirali, O.; Buchanan, Z. S.; Eliet, S.; Martin-Drumel, M.-A.; Turut, J.; Roy, P.; Hindle, F.; Mouret, G. Broadband Terahertz Heterodyne Spectrometer Exploiting Synchrotron Radiation at Megahertz Resolution. *Opt. Lett., OL* **2019**, *44* (20), 4985–4988. <https://doi.org/10.1364/OL.44.004985>.
- (39) Hearne, T. S.; Mammez, M.-H.; Mammez, D.; Martin-Drumel, M.-A.; Roy, P.; Pirali, O.; Pirali, O.; Eliet, S.; Barbieri, S.; Hindle, F.; Mouret, G.; Lampin, J.-F. Unlocking Synchrotron Sources for THz Spectroscopy at Sub-MHz Resolution. *Opt. Express, OE* **2022**, *30* (5), 7372–7382. <https://doi.org/10.1364/OE.448147>.
- (40) McGurk, J. C.; Schmalz, T. G.; Flygare, W. H. Fast Passage in Rotational Spectroscopy: Theory and Experiment. *The Journal of Chemical Physics* **1974**, *60* (11), 4181–4188. <https://doi.org/10.1063/1.1680886>.
- (41) Gordy, W.; Cook, R. L. *Microwave Molecular Spectra*, 3rd ed.; Techniques of chemistry; Wiley: New York, 1984.

### III. Experimental setup and flow characterization methods

#### Introduction

In the previous chapter we have established that CPUF can be a capable technique to study the kinetics of cold chemical reactions of astronomical interest. In this chapter we will continue with the description of the CPUF technique by presenting the CRESUCHIRP apparatus where the CRESU reactor is coupled with a CP-FTmmW spectrometer and the pulsed laser photolysis technique to study reaction kinetics by conducting time dependent measurements of product formations and determination of associated branching ratios. Coupling pulsed laser photolysis techniques to generate radicals with chirped pulse in uniform flow to study the reaction dynamics is referred to as PLP-CPUF. The design and the construction of the multiple devices and instruments that constitute the experimental setup will be discussed in the first part of this chapter while the second part is dedicated to the characterization of the cold supersonic flows via computational fluid dynamic calculations, the direct simulations Monte Carlo method and experimental characterization using a Pitot tube in addition to spectroscopic measurements.

## Part I: Description of the experimental setup

The first set of elements of the experimental setup is the CRESU apparatus which involves the CRESU chamber, the reservoir and the pumping group, along with the associated instruments such as flow controllers and vacuum gauge systems that ensure a constant stable flow rate of the buffer and the species of interest to the CRESU chamber.

### III.1. CRESU apparatus

#### III.1.1. CRESU chamber

The CRESU chamber is the important section in the PLP-CPUF experiment, the setup is composed of two CRESU chambers, the first chamber referred to as CRESU B has been built in Birmingham,<sup>1</sup> it is a 4 m long stainless steel cylinder with 500 mm diameter standing on adjustable metallic chassis, inside the chamber there is a 12 l cylindrical double walled reservoir to be filled with the carrier gas to create the high pressure environment, Laval nozzles can be mounted on the reservoir to generate the expansion, the reservoir itself is mounted on cylindrical rails that allows it to move via a stepper motor along the chamber to maintain, via a sensitive displacement detector, a well-defined distance from the detection zone. The chamber is also equipped with 6 pairs of holes facing one another other from the lateral sides that are used for probing and connect the different electronic and hydraulic tubes via feed through flanges, on the axis of the two ends of the chamber, 2 Brewster windows are mounted to allow the laser beam to pass through the reservoir and the chamber. The CRESU B chamber is mostly used for laser induced fluorescence measurements and conducting Pitot characterization, it has also been used for the first tests of the characterization of the pulsed system that is going to be presented in chapter VI.

A new CRESU chamber has been built for the CRESUCHIRP project to be used for microwave detection. This chamber is an upgraded version and complements the CRESU B one, with relatively the same length and dimensions, the diameters used in the lateral flanges have been increased to 250 and 360 mm to facilitate the access and the management inside the chamber. An additional compartment has been added to the chamber for implementing the secondary expansion chamber for lower pressure measurements using a skimmer setup as will be described in chapter V. Both

chambers are connected to the pumping group in order to generate the vacuum via a long 500 mm diameter tube and can be sealed with a motorized butterfly valve (Pro-axiss) that is used to adjust the pressure in the chamber to reach the operating nozzle flow conditions.

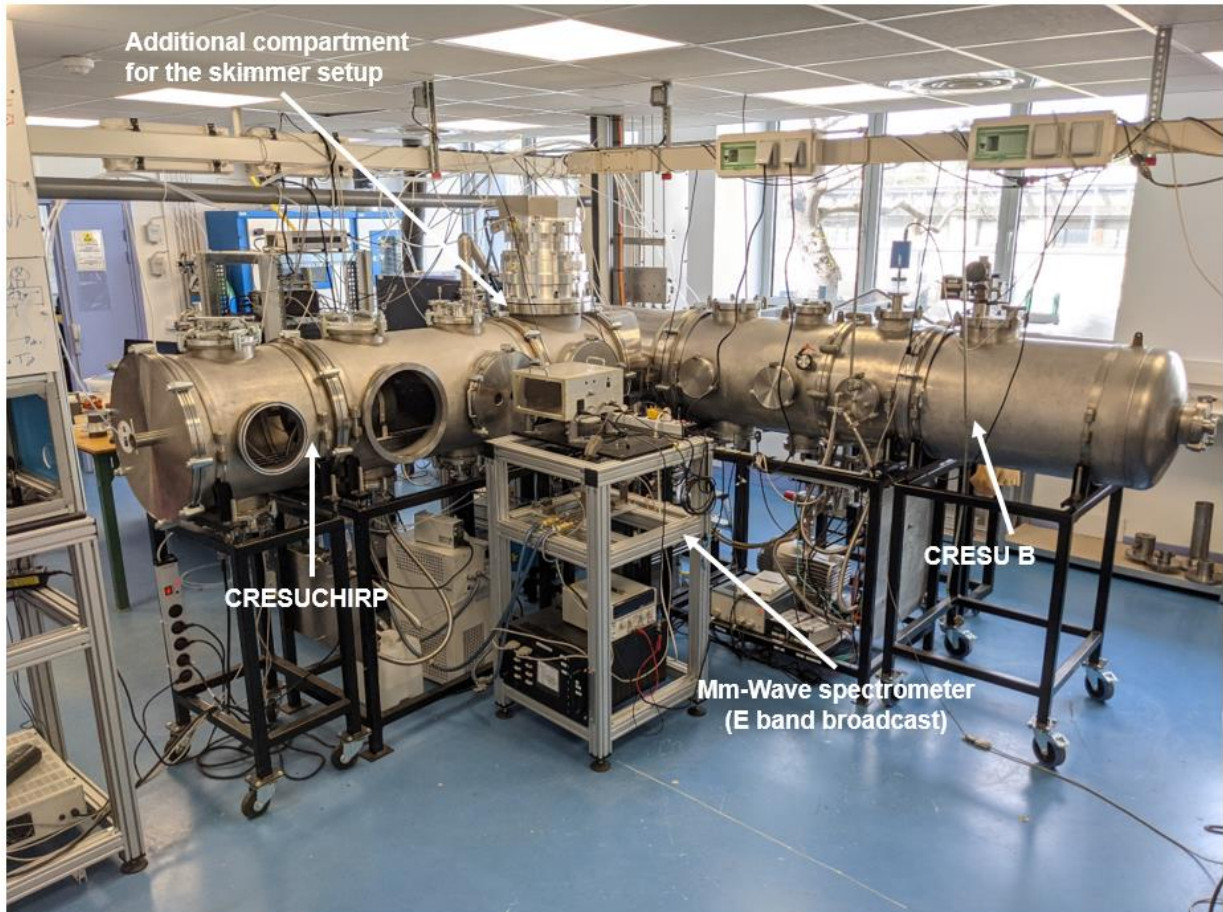


**Figure III-1. Experimental setup CRESUCHIRP and CRESU B chamber with the E band broadcast spectrometer**

### III.1.2. Pumping group

The CRESU technique uses large flow rates of gas, this requires large pumping capacity system to create the vacuum, the two chambers are connected to an ensemble of  $500 \text{ m}^3 \cdot \text{h}^{-1}$ ,  $2,000 \text{ m}^3 \cdot \text{h}^{-1}$  and  $8,000 \text{ m}^3 \cdot \text{h}^{-1}$  (Pfeiffer Vacuum) pumps mounted in series with two  $18,000 \text{ m}^3 \cdot \text{h}^{-1}$  mounted in parallel to provide a nominal pumping flow rate of  $36,000 \text{ m}^3 \cdot \text{h}^{-1}$ . Under typical pumping conditions (0.1-1 mbar), the observed real pumping capacity is around  $32000 \text{ m}^3 \cdot \text{h}^{-1}$ . (See pumping curves in appendix (A.III)).

### III.1.3. Mass flow controller system

A system combining multiple thermal mass flow controllers (MFCs) ensures high accuracy flow rates to the reservoir in the CRESU chamber, the main buffer (Air Liquide He  $\geq 99.995\%$ , N<sub>2</sub>  $\geq 99.995\%$ , Ar  $\geq 99.998\%$ ) arrives via a Brooks SLA 5800 series 100 slm flow controller. Another range of flow controllers from 20 sccm to 5 slm of the BROOKS GF series are used to transport the reactants and the precursor vapour. All of these flow controllers are connected to a serv'instrumentation power supply controller which is linked by a USB cable to the computer that controls the experiment.

### III.1.4. Controlled evaporation mixer (CEM)

A Bronkhorst Controlled evaporation mixer (CEM) is used to vaporize liquid chemicals required for reaction and/or for direct signal detection measurements, the CEM is connected to two flow controllers, a 0.1-100 g/h Coriolis MFC (Bronkhorst mini CORIFLOW ML120V00) that brings the liquid species, while the other is a 5 slm thermal MFC (Bronkhorst EL-FLOW Prestige) to transport the gas (usually the buffer), the liquid is heated up to vaporization and mixed with the buffer in the CEM (Bronkhorst W-202A-222-K) and then injected in the reservoir.

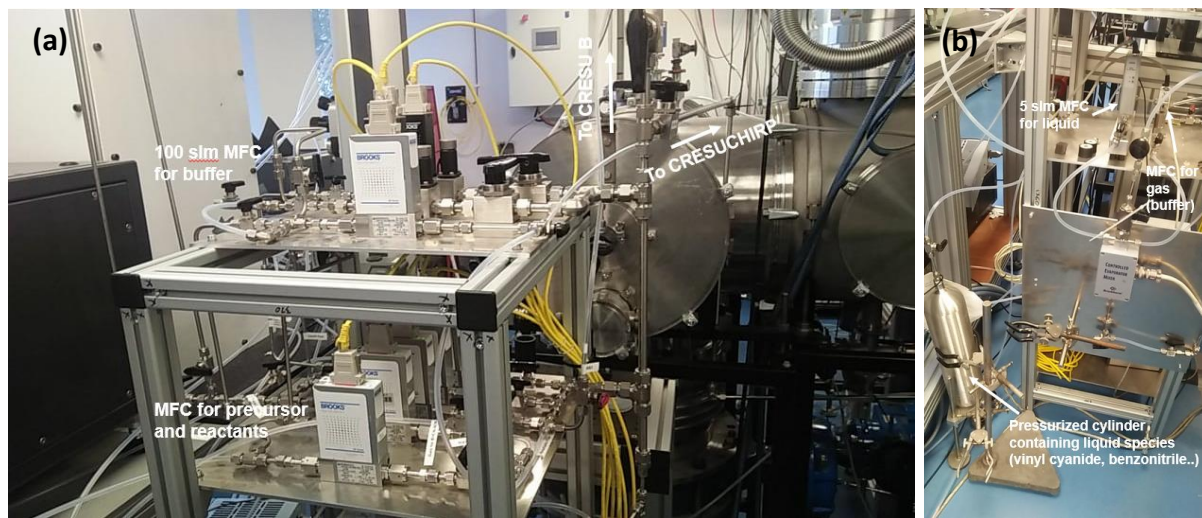


Figure III-2. (a) Mass flow controller system, (b) is the controlled evaporation mixing system

## III.2. Generation of the CRESU flows

As explained in Chapter II, the Laval nozzle is a key device in the CRESU apparatus, these nozzles are generated by a program developed by Marquette et Rowe, they are

then machined and tested numerically and finally characterized experimentally with impact pressure measurements using a Pitot tube.

### III.2.1. Nozzle generation program

In this program written in Turbo Basic, the user defines the design operating conditions of the Laval nozzle, that is the nature of the buffer gas carried by the nozzle thus defining the  $\gamma$ , the mass flow rate ( $m$ ), the temperature in the reservoir  $T_0$  and the temperature of the CRESU jet  $T_{flow}$ , the program then will calculate the Reynolds number which must be kept in the vicinity of the laminar regime. The reservoir pressure, the nozzle throat and the exit diameter along with the Mach number at the exit are determined, the user then must set the length parameter discussed in the previous chapter which helps determine the length of the nozzle, the step parameter must be input and is set by default  $10^{-4}$  for all the nozzles used in this work, the final wall is then determined and the radius of the isentropic core beside the boundary layer thickness are given as outputs.

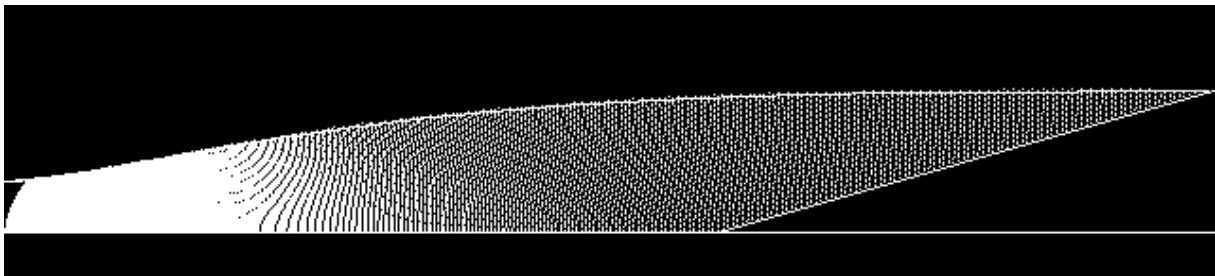


**Figure III-3. Nozzle profile generated using the program written by J,-B Marquette<sup>2</sup>**

### III.2.2. Nozzle building using additive manufacturing procedure

Laval nozzles are machined in the laboratory workshop using different materials like Teflon and aluminum, such machining usually takes between 1-2 weeks for each nozzle depending on the complication of the profile and the diameter of the throat in particular. In order to reduce this delay both in the context of this thesis and those of colleagues, a new procedure for production of Laval nozzles has been developed using additive manufacturing technology with a Form 2, 3D printer ensuring high quality and precision nozzle profiles.

### III.2.2.1. Presentation of Form2

Form 2 (Formlabs) is a 3D printer that uses stereolithography technology, equipped with a class 1, 405 nm laser with a spot size of 140 microns. The printing material is a light activated resin that photo polymerizes under the effect of the printer's laser to make 3D solid objects. The Form2 printer can build models with dimensions of 145 × 145 × 175 mm. To ensure a printing of quality, the resin must be kept in good shape (liquid form) and that is why an auto heating system and a peel mechanism are installed with the resin tank.

Stereolithography (SLA) is a form of additive manufacturing technology used in 3D printers to build objects and models layer by layer using a photo-polymerization process on a photosensitive liquid resin, where a spot of light causes chains of monomers that constitute the resin to link, forming polymers which ultimately makes a three-dimensional solid body. The UV laser beam is focused and draws a 2D section of the design on a thin layer of liquid photopolymer resin. The photosensitive resin then reacts photochemically and solidifies forming a single 2D layer of the design. The build platform then is raised one-layer height while still in contact with the resin and new layer of resin is applied to the object. The process is repeated for each layer of the design until the 3D object is complete. The resolution that refers to the quality of printing in terms of the roughness represents the layer thickness and depends on the resin type. Using a technical professional resin for engineering application, the printer can ensure a resolution of 50 or 100 microns.

The object files are uploaded to the printer via a communication software known as Preform that hosts the object designed by computer-aided design software to prepare it before sending it to printing. Preform allows to define the rotation of the object to be printed, its position on the building platform, and it allows also to change the dimension and generate the supports that holds the objet (see Figure III-4 (a)).

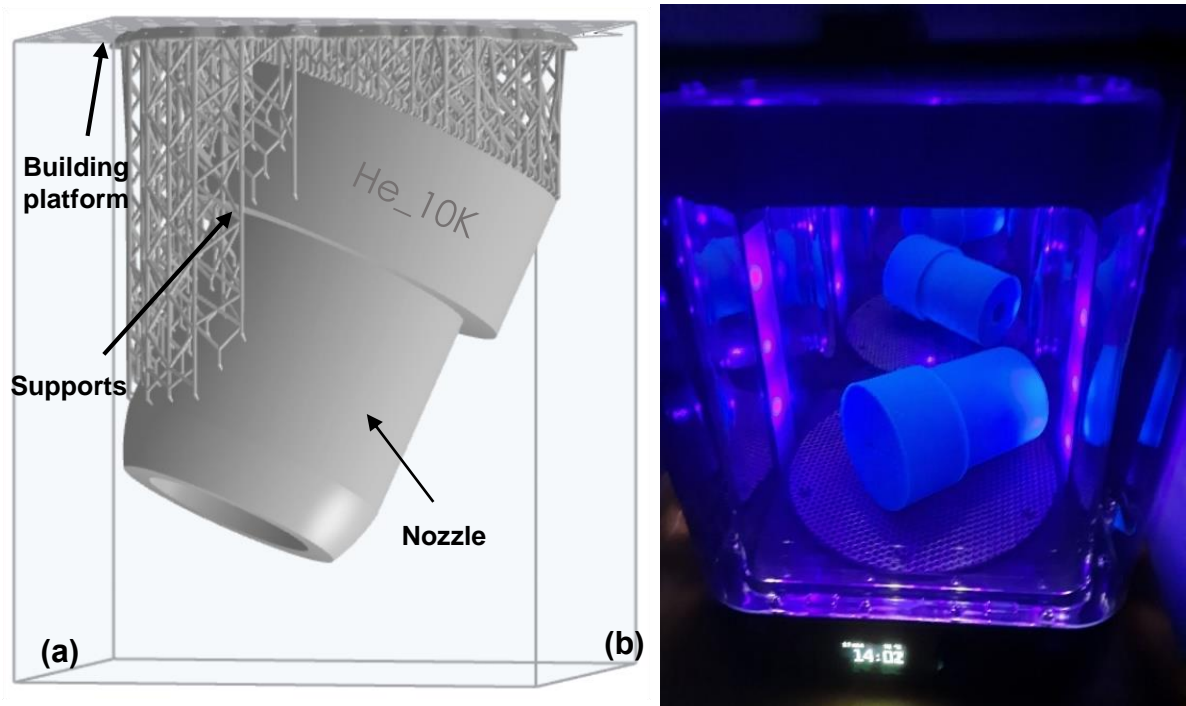


**Figure III-4.** Laval nozzle 3D printing procedure (a) shows the preparation of the printing file of the helium 10 K nozzle using Preform software to communicate with the 3D printer, (b) displays the nozzle under UV curing after printing.

Since the model is built upside down, generating supports is necessary to protect the model from collapsing, however it is extremely important for the support not to be in anyway near crucial parts of the nozzle like the inner profile of the nozzle for example.

#### III.2.2.2. Post treatments

As a results of the technology used in these types of printer post-printing treatment is required, models must be washed with IPA (isopropyl alcohol) to remove non polymerized resin from the surface. This process takes 20 minutes, after that the model is put to dry for few minutes.

Further post curing using a UV generator is also needed for Laser-curing during the printing helps bring the model to what is known to be the green state (see Figure III-5). However, some polymer connections are not yet fully reacted. Post-curing exposes parts to light and heat and strengthens crosslinks in the polymer structure. Due to the increased number of bonds the material becomes more tightly packed, as result minor shrinkage in the geometry of printed models may occur.

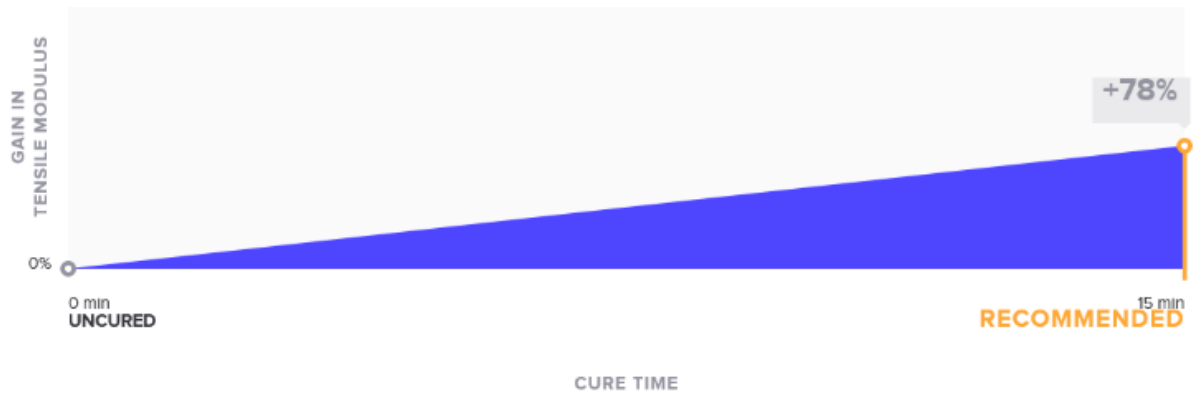


Figure III-5. Gain in the rigidity (tensile modulus) of the 3D printed pieces after UV curing. Figure from Formlabs support<sup>3</sup>

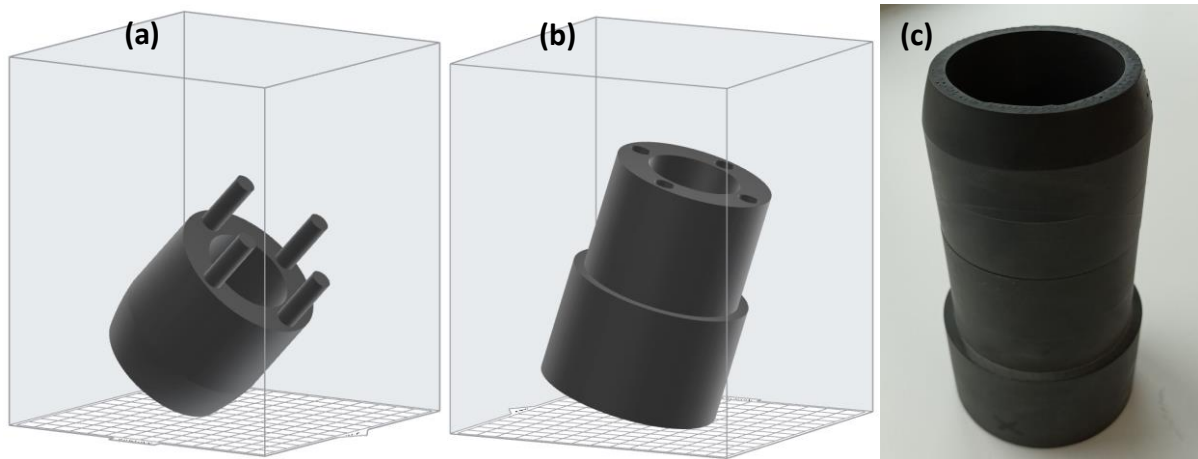


Figure III-6. Series of Laval nozzles used in Rennes, all the 3D printed nozzles have been designed and machined in this work<sup>1</sup> (All 3D printed nozzles used for this work and of colleagues are given in the Table of nozzles. See appendix A.III)

Some nozzles can be much larger than the building capacity of Form 2, it is the case for the N<sub>2</sub>-38K-0.148 nozzle with a length of 179.1 mm, such nozzles has to be printed

<sup>1</sup> All the nozzles including the 3D printed are referred to as Buffer-Temperature (in K)-chamber pressure (in mbar)

with two separate parts and then assembled as shown in Figure III-7, the high precision and the quality delivered by the 3D printer ensures smooth nozzle profiles.



**Figure III-7. Nitrogen 38 K nozzle, (a) and (b) are the two printed parts in Preform and (c) shows a picture of the assembled nozzle**

A new version of Formlabs 3D printers is the Form 3L with a building capacity of 335 x 200 x 300 mm and the same high performances as the Form 2, it is now available and could replace the Form 2 for future work and constructions in the project. Once the nozzle is printed it is characterized experimentally using impact pressure measurements to determine the flow conditions; pressure, temperature, density and the Mach number, these measurements are carried out using a Pitot tube.

### III.2.3. Pitot tube

The pitot tube is a 10 cm long, 1 mm diameter tube connected to a Brooks capacitance manometer (10-100 mbar), it measures the impact pressure from the shock created by the supersonic buffer flow hitting the tube at the stagnation point, then converted to the different flow properties characterizing the CRESU flow using Equation III-7 to Equation III-10.

The tube is mounted on two translational stages that can move 60 cm along the CRESU chamber and 9 cm across. The two stages are commanded with two stepper motors with 1 mm steps, this allows to characterize the CRESU flows in the two dimensions and conduct 2D mapping of the thermodynamic properties. The tube elevation can also be adjusted with a 15 mm course micrometer for better alignment on the axis of the flow.

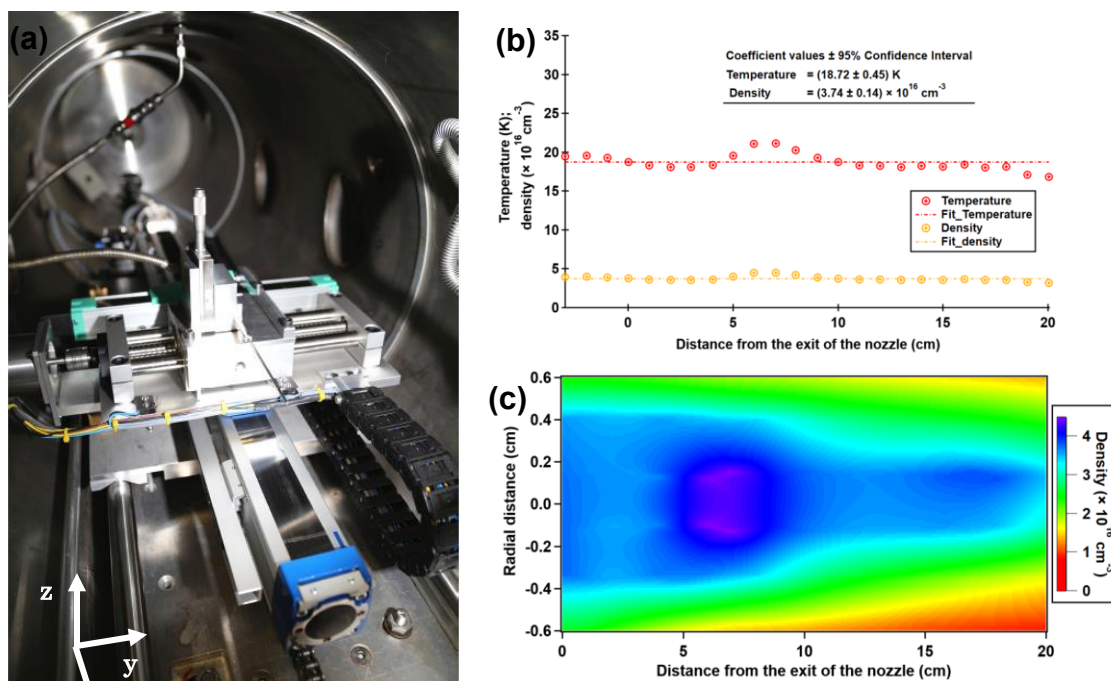


**Figure III-8.** (a) photo of the Pitot tube inside CRESU B chamber, (b) and (c) show the 1D and 2D profiles of temperature and density of a helium nozzle operating at  $(18.72 \pm 0.45)$  K.

The 2D characterization or Pitot mapping is mainly carried out to determine the size of the isentropic core, the coldest region of the CRESU flow with the highest gas density which contributes the most in the molecular signal strength of stable molecules being probed as explained in the previous chapter. The lowest temperature nozzles designed and characterized so far were the He-10K-0.128 and the N<sub>2</sub>-23.5K-0.12. Both nozzles expand the gas from the reservoir at 295 K and do not require precooling the gas to reach these temperatures in continuous mode. The He-10K-0.128 nozzle was used primarily for studying the CN+C<sub>2</sub>H<sub>6</sub> reaction yielding HCN as a product, the HCN microwave signal takes advantage of the low temperature and increases significantly which is why this reaction is one of the first reactions we studied to characterize the setup. The CN+C<sub>2</sub>H<sub>2</sub> reaction yielding HC<sub>3</sub>N was also studied and HC<sub>3</sub>N was detected. Details can be found in the thesis of Theo Guillaume. The N<sub>2</sub>-23.5K-0.12 nozzle has been designed and characterized along with a series of nitrogen nozzles at different temperatures and pressures as collaboration with the group of Mitchio Okumura to measure the rate constant of OH +CO reaction which produces HOCO a relevant species to atmospheric studies that can potentially dissociate and form CO<sub>2</sub> which makes the reaction of astrochemical interest as well. This work has been discussed at length in the thesis of Joseph Messinger from the Mitchio Okumura's group.<sup>4</sup>

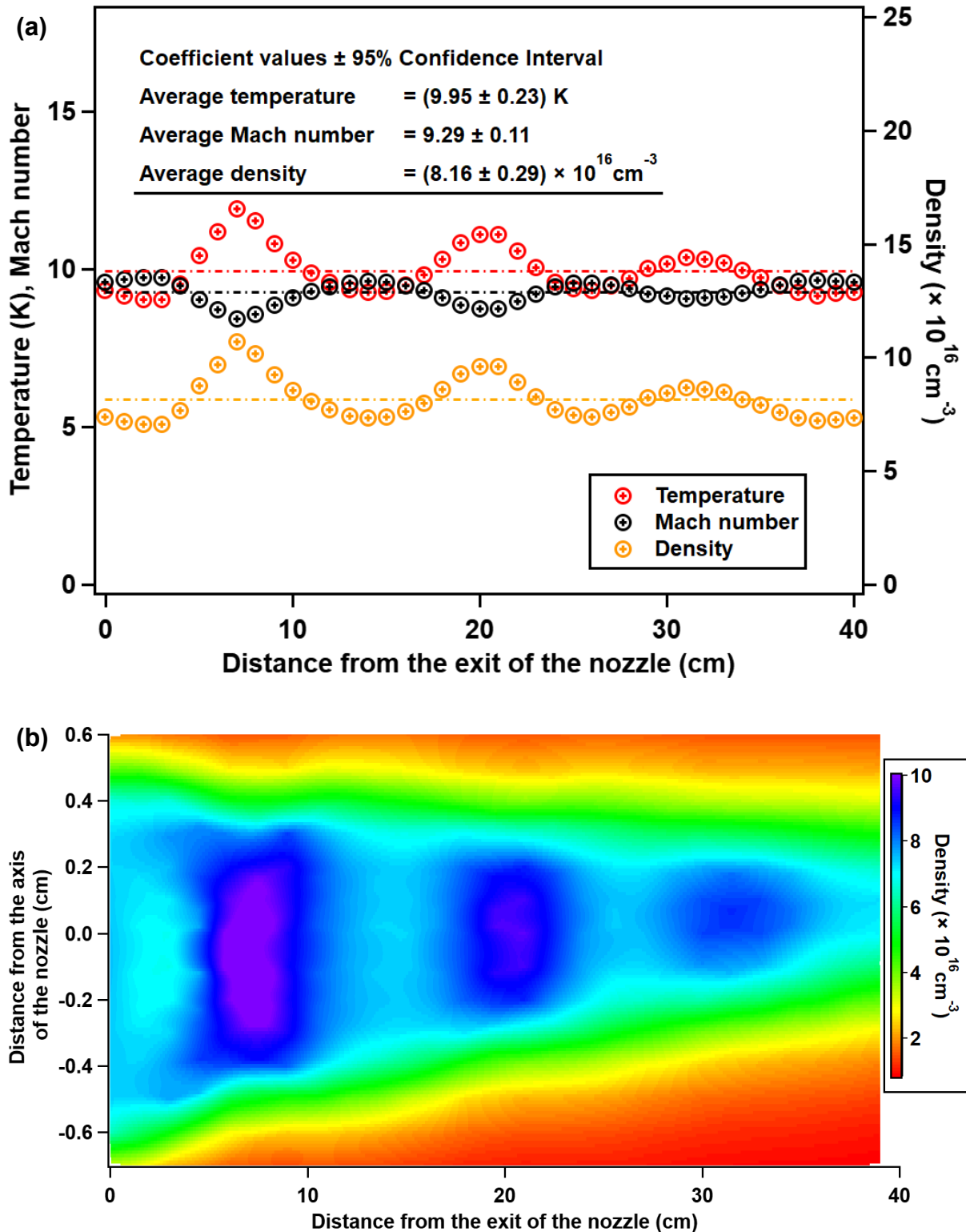


Figure III-9. Characterization of the He-10K-0.128 nozzle using the Pitot tube, figure (a) shows 1D temperature, Mach number and the density profile along the axis of the chamber and (b) gives the 2D density profile, the nozzle has operating condition of 540 mbar in the reservoir and 0.128 mbar in the chamber and is able to sustain a uniform flow of more than 30 cm.

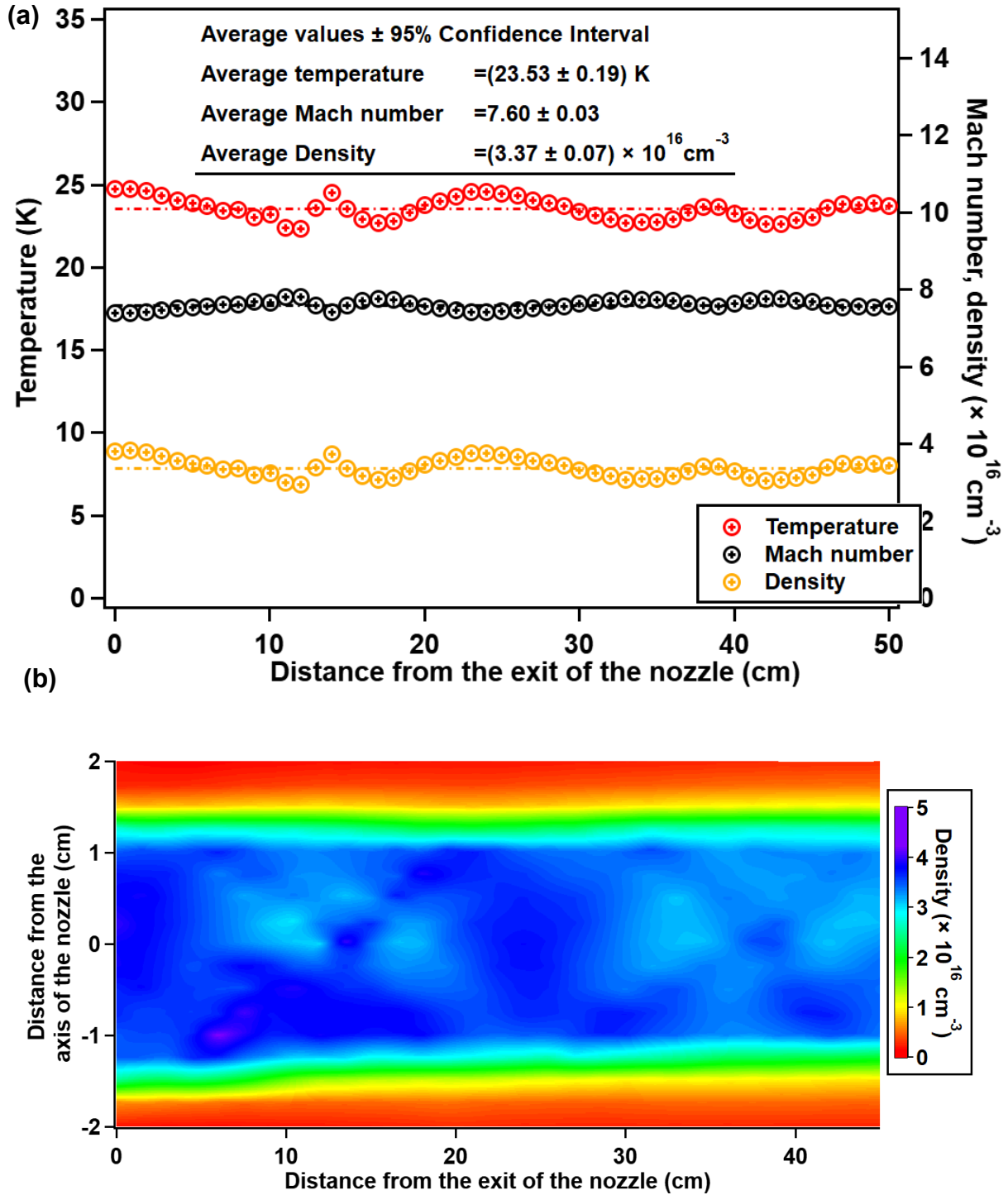


Figure III-10. Characterization of the N<sub>2</sub>-23.5K-0.12 nozzle using the Pitot tube, figure (a) shows 1D temperature, Mach number and the density profile along the axis of the chamber and (b) gives the 2D density profile, the nozzle has operating conditions of 773.7 mbar in the reservoir and 0.12 mbar in the chamber and is able to sustain a uniform flow of more than 40 cm.

Details about the flow characterization using the Pitot tube and other numerical and spectroscopic techniques are discussed in the 2<sup>nd</sup> part of this chapter.

### III.3. Generation of radicals using pulsed laser photolysis

For reaction kinetics studies, radicals are generated by photolysing precursors, and then react with species injected in the reservoir. Precursors are stable molecules and do not react before photolysis, therefore the photolysis time is considered as the triggering time zero of the reaction.

#### III.3.1. Precursor flow

Cyanide-containing molecules are used in almost all the systems studied in this work, and have been particularly chosen to characterize the two microwave spectrometers for their high dipole moment enhanced by the CN radical. ICN and BrCN are the main precursors used to generate the CN radicals. The ICN powder (BrCN crystal) is put in a 30 cm long glass vessel where the buffer flows through via a 2 slm Brooks flow controller to sublimate the ICN (BrCN), the pressure in the vessel is adjusted with a needle valve for precise regulation, the vapour then passes through a UV-vis cell to determine the concentration of ICN before being delivered to the reservoir.

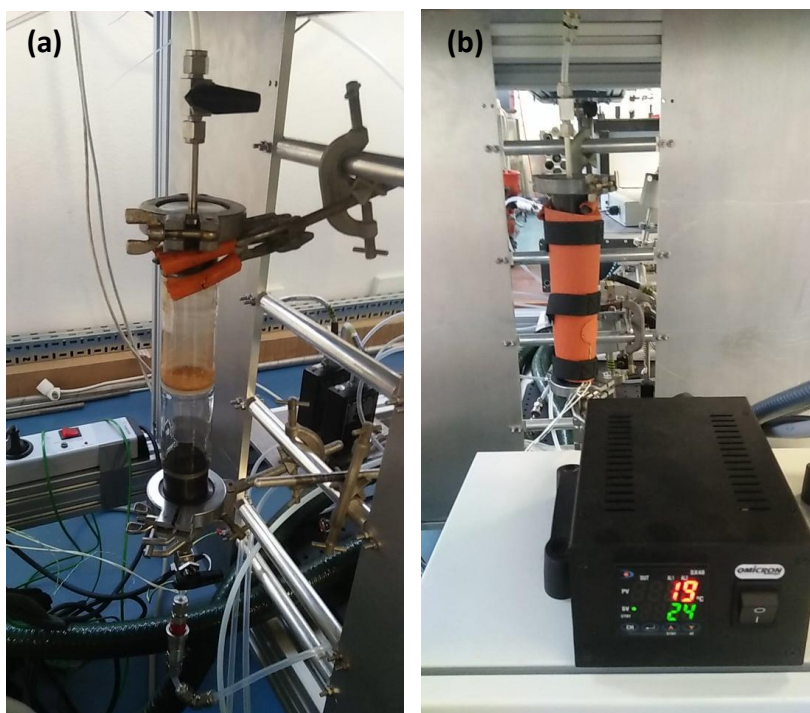


Figure III-11. (a) glass vessel containing ICN, (b) glass vessel covered with heating pad

### III.3.2. Heat stabilizer

A heat generator is also used to stabilize the temperature of the precursor in the vessel which tends to decrease during the sublimation process causing a decrease of the concentration of the precursor in the flow, the results are presented in Chapter V (see Figure V.27).

### III.3.3. UV-Visible spectrometer

A UV-Visible spectrometer (UV-Vis) with a light source (ocean Insight DH2000-DUV) having two options, a deuterium lamp and a halogen lamp to cover a range of 190-2500 nm transmitted via an optic fiber (QP600-2-XSR) is used to determine the absolute concentration of radicals in the CRESU using the Beer Lambert law  $\ln(I - I_{off}) / (I_o - I_{off}) = -\sigma Nd$ ; where  $I_o$  is the intensity of the deuterium lamp source over the wavelength range 190–250 nm,  $I_{off}$  is the background/stray intensity with the lamp off,  $I$  is the measured intensity when precursor is flowing,  $\sigma$  is the corresponding absorption cross-section. In this BrCN and ICN were used as precursors as will be shown in chapter V the absorption cross section are measured by Felps and co-workers,<sup>5</sup>  $d$  is the length of the absorption path and  $N$  is the number density of the species. The latter is calculated and averaged over the measured wavelength range of 200–250 nm. The spectrometer is mounted on a 63 cm long flow cell with quartz windows at its two ends, followed by lenses. The length of the cell can be adjusted according to the absorbance of the molecules of interest. More details can be found in the thesis of Divita Gupta.

### III.3.4. Excimer laser

The precursor is photolysed with a Coherent LPX 210 excimer laser operating at a repetition rate of 100 Hz using 193 nm radiation for BrCN and 248 nm for ICN to generate the CN radicals. The laser is also used for other photolysis processes, for example, to study the photolysis of vinyl cyanide and ozone, the results will be presented in chapter V. Measuring the laser fluence with the precursor number density in the flow given by the UV-Vis, we can determine the radical number density involved in the reaction.

### III.4. Molecular detection using CP-FTmmW spectroscopy

The last part of the experimental setup is the spectrometer, two CP-FTmmMW spectrometers have been designed and built to operate in the Ka band (26.5-40 GHz) and the E-band (60-90 GHz), the design and the characterization of the E band have been presented in the thesis of Theo Guillaume and published by Hays and co-workers in 2020<sup>6</sup>, this spectrometer has been used for most of the measurements and the reactions studied in this work and that of Theo Guillaume. Here we present the E band spectrometer and the acquisition routine, the Ka band spectrometer and its characterization will be discussed in the next chapter.

#### III.4.1. Spectrometer Design

The spectrometer uses an arbitrary waveform generator (AWG, Keysight M8195A, 64 GSa/s) to produce frequencies in the range of 1-16 GHz. That gets up-converted in a mixer (Marki M11850H) using a phase-locked dielectric resonator oscillator (PDRO, Microwave Dynamics PLO-2070-29.00) operating at 29 GHz as the local oscillator (LO) source. The upper sideband is selected using a broadband high-pass filter (Reactel 9HS-X30/45G-K11R) before entering the preamplifier (Quinstar QPW-205020525-J0). This signal is then input into a Quinstar integrated system (QBM-609025E0U0R), that includes a passive frequency doubler to bring the frequency range to 60-90 GHz (Quinstar QPM-75002E), a waveguide splitter (Quinstar QJH-EUFBZIL), two millimeter wave power amplifiers (Quinstar QPW-60752530-C2W0 and Quinstar QPW-75902530-C2W0), and a waveguide switch (Quinstar QWZ-ET2800). One amplifier operates between 60-75 GHz while the other operates between 75-90 GHz. Both amplifiers output about 300 mW of RF power over each band, with significant power up to 94 GHz for the higher frequency amplifier. The amplifiers are controlled via TTL signals for fast turn-on times of around 20 ns. The waveguide switch is a low-loss (0.7 dB) but slow (50 ms) electromechanical switch which selects the amplifier to be used. The radiation is output through a 23 dBi gain horn antenna (Quinstar QWH-EPRR00).

## E Band Spectrometer

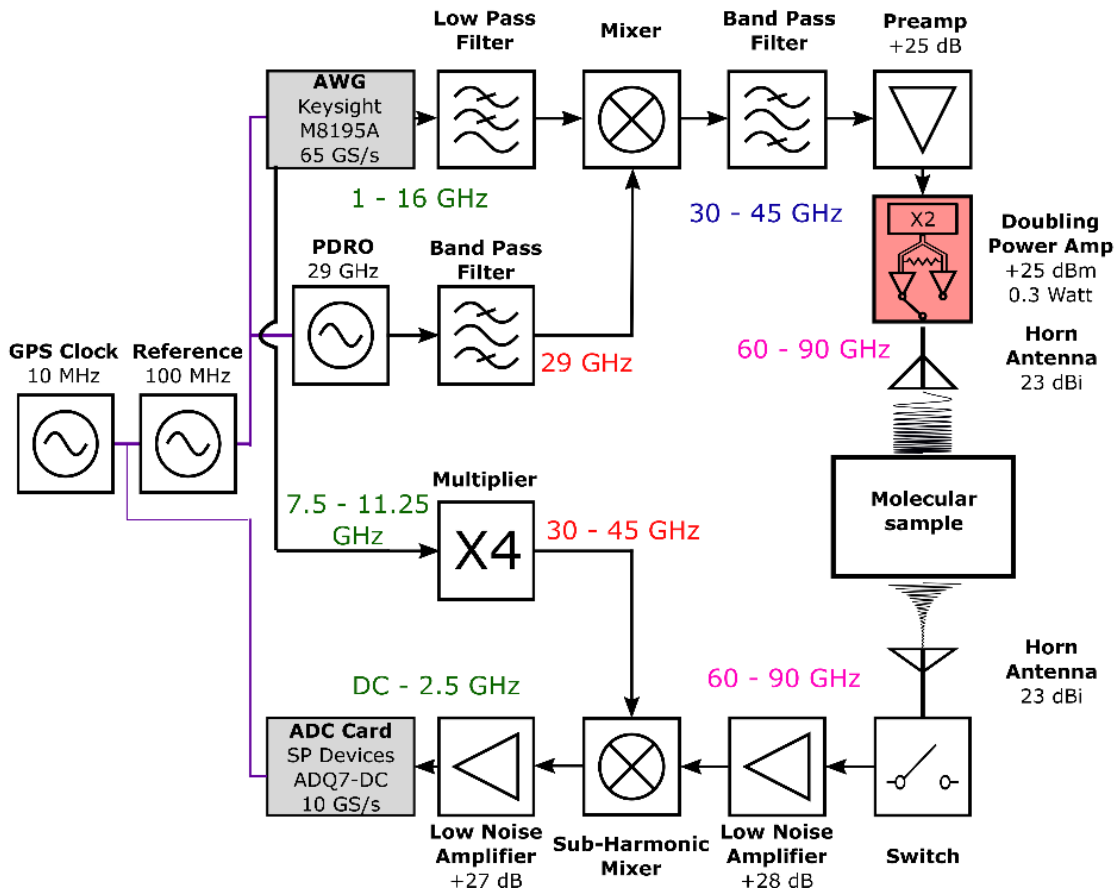
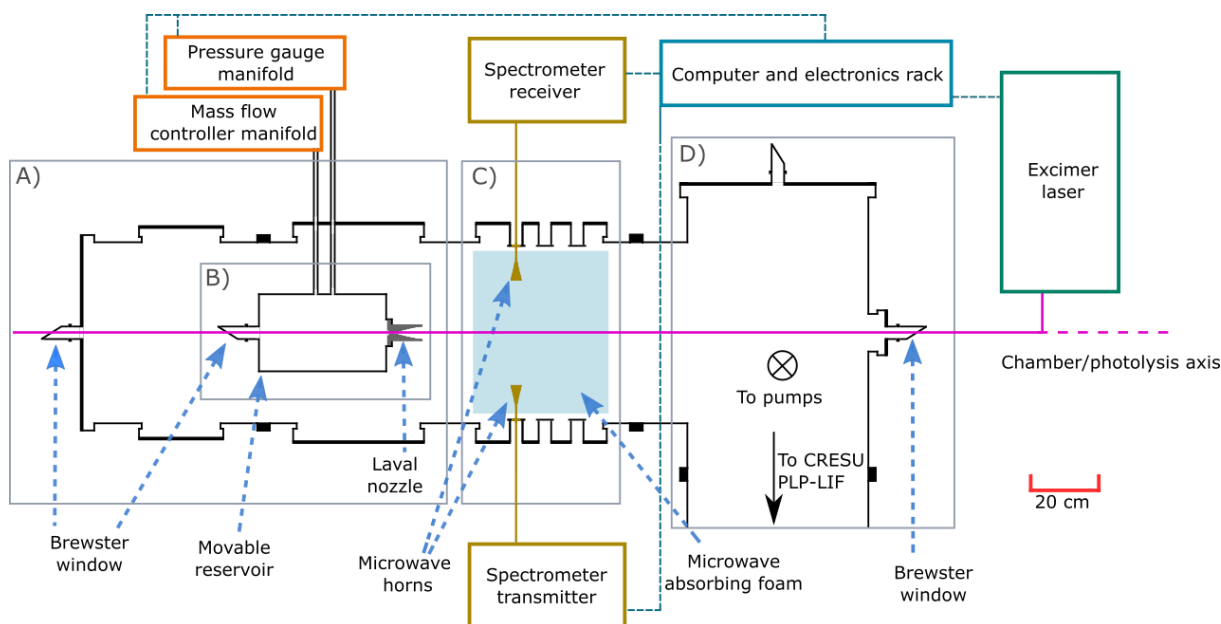


Figure III-12. Configuration of the E band spectrometer

The receiver side is composed of an identical horn antenna (Quinstar QWH-EPRR00) to collect the signal followed by a variable attenuator that attenuates signals by up to 30 dB (Quinstar QAL-E00000), for monitoring pulse power while running experiments. The signal then enters a fast single pole-single throw PIN switch operating in the 60-90 GHz range (Millimeter Wave Products 911E/387TTL) to protect the electronics behind it from the initial polarizing pulse, it has a 10 ns 10%-90% transition time to either transmission or isolation, with around 3 dB insertion loss across the band, and over 30 dB of isolation. The low noise amplifier (Millitech LNA-12-02350) has  $(28 \pm 4)$  dB of gain across the E band. It has a 3 dB noise figure, rising to 4.5 dB below 67 GHz. After the low-noise amplifier is a subharmonic mixer (Virginia Diodes WR12SHM), which has a dual sideband conversion loss of 6 dB with a 3 dB bandwidth of DC-15 GHz at the intermediate frequency (IF) port. The output from the IF is further amplified using a low noise amplifier with 25 dB of gain and a 2.5 dB noise figure (Miteq AFS4-

00101800-25-S-4). The LO can come from one of two sources: a PDRO operating at 37.5 GHz (Microwave Dynamics PLO-2070-37.50) or the second channel of the AWG sent through a quadrupler (Quinstar QMM-38150504J) providing an LO between 30-45 GHz. The digitizer is a Teledyne SP Devices ADQ7DC-PCIE digitizer running at 10 GS/s with a 2.5 GHz 3 dB bandwidth used for high speed acquisitions, it can record a frame of up to 200  $\mu$ s, with a fast repetition rate of up to 30 kHz. The onboard field-programmable gate array (FPGA) can sum up to 262,144 repetitions, at which point the data is transferred to the host computer and the card re-arms itself. This allows for a substantial improvement in recording speed over the oscilloscope, which can record typically at a rate of 30 acquisitions per second in these conditions. However, since it can only record up to 2.5 GHz of bandwidth at the 3 dB level, it is necessary to set the LO frequency in the downconversion stage to within 2.5 GHz of the transition to be probed in order for the FID to be detectable by the card. Here we note that the digitizer can record 200  $\mu$ s frame at 10 GS/s, it can also record longer frames at lower sampling rates by skipping the recording of determined samples, for example it can record 400  $\mu$ s at 5GS/s with sample skip of 2, 800  $\mu$ s at 2.5 GS/s with sample skip 4 and 1600  $\mu$ s at 1.25 GS/s with sample skip 8. This gives the opportunity to cover long regions in the probing environment as will be shown in section III.4.2. The digitizer is triggered by pulses from an AWG marker channel, the switch and pulsed amplifiers are controlled by a BNC 575 digital pulse/delay generator (DDG), which is triggered by another marker channel on the AWG to protect the low noise receiver from the intense polarizing pulse. The system, particularly the AWG, the PDRO's, the oscilloscope, is synchronized to a 100 MHz oven-controlled crystal oscillator (Precision Test Systems GPS10-eR-50) which is locked to a GPS-disciplined Rb clock (Stanford Research Systems FS740) operating at 10 MHz. The higher-frequency 100 MHz signal is used to improve phase stability compared to the lower-frequency 10 MHz standard. The digitizer and the DDG are synchronized to the 10 MHz clock. The electronic components are of them are mounted on heat-sink blocks to be maintained at a constant temperature of 25 °C by a water chiller (ACCEL series 250 PHP). Further details about the instrument benchmarking and the post processing data analysis routines can be found in Theo Guillaume's thesis.



**Figure III-13. Schematic of the CRESUCHIRP chamber, the reservoir and the nozzle are in compartment B, the spectrometer is mounted on section C, the excimer laser beam passes through the axis of the chamber via the two Brewster windows fixed on the KF 40 flanges at the two ends of the chamber. An additional compartment is added between C and D for the secondary expansion chamber which will be presented in Chapter V. Figure credit to Theo Guillaume**

The spectrometer (Broadcast and receiver) is mounted on two independent 1.15 m high tables built in 60x60 aluminum profile. On top of each, an optical breadboard to ensure proper alignment of the waveguide for coupling with the fixed element of the experiment. It is connected to the CRESUCHIRP chamber via the lateral side flanges on section C as shown in Figure III-13, with the broadcast side and receiver side facing one another. The probing takes place inside the CRESU environment, the horn antennas are connected to the spectrometer via a series of microwave components. The horn antennas are connected to a 50 mm waveguide via a gasket with a clamped 100 microns Teflon window to separate the CRESU environment from atmospheric conditions outside the chamber. The waveguide bulkheads are fixed on ISO KF 40 O-ring supports for an easy and quick mounting on the chamber flange (see Figure III-14).

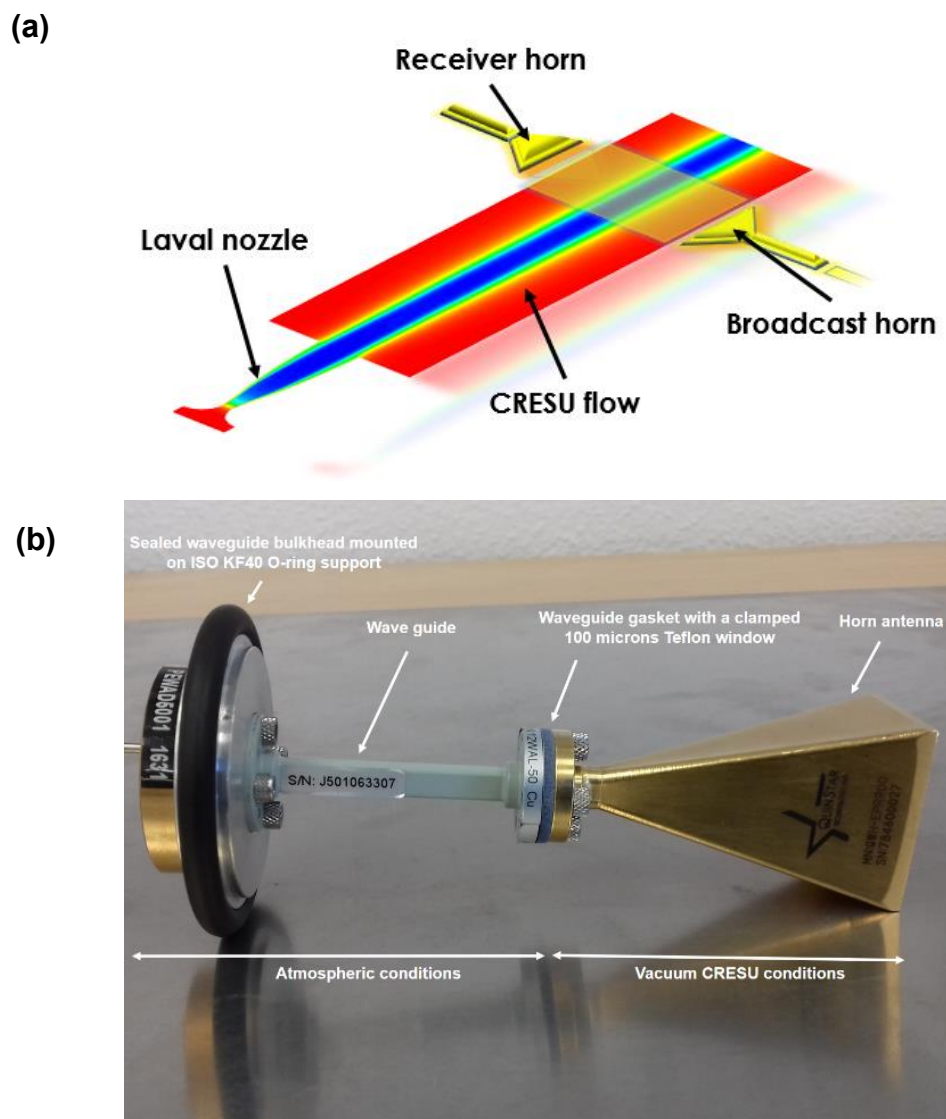


**Figure III-14. Spectroscopic probing in the CRESU chamber, (a) shows a schematic of the probing, (b) gives the different microwave pieces assembled to connect the spectrometer to the CRESU chamber.**

The probing is carried out perpendicularly to the CRESU flow to limit the Doppler effect as referred to in the previous chapter (see Figure III-14 (a))

### III.4.2. Sequence and data acquisition procedure

A 10  $\mu\text{s}$  frame containing the polarizing pulse with the triggering times and delays for the spectrometer main amplifier and the switch is set in a sequence procedure to acquire the data. The frame is repeated numerous times to cover the different regions of the CRESU flow, this procedure is mainly useful for photolysis and bimolecular reactions as we can follow the product formation status at every time step of the reaction in the different CRESU flow regions. A frame with a laser trigger is used in the

sequence to initiate the reaction, it corresponds to the time zero of the reaction, the signals recorded before that time gives the background noise as the reaction is yet to start. Horizontal averaging of multiple frames to increase the SNR of the radiating product is possible to acquire but with a cost on time resolution.

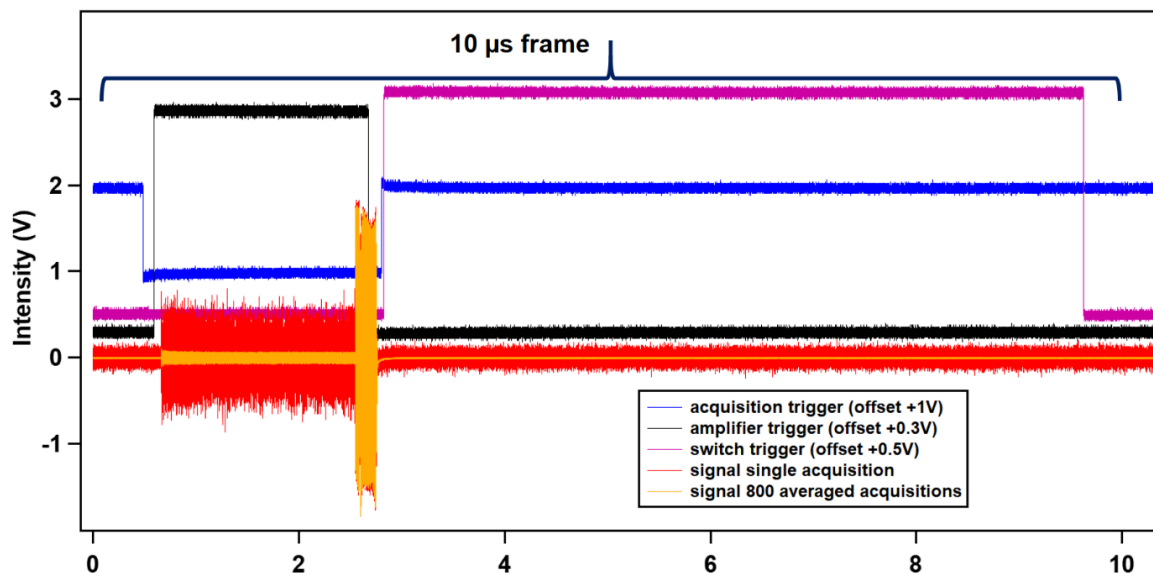


Figure III-15. Frame of 10  $\mu\text{s}$  for signal acquisitions under the skimmer conditions, under the CRESU conditions, the frame is reduced to 2.5  $\mu\text{s}$  because of rapid quenching of the FID.

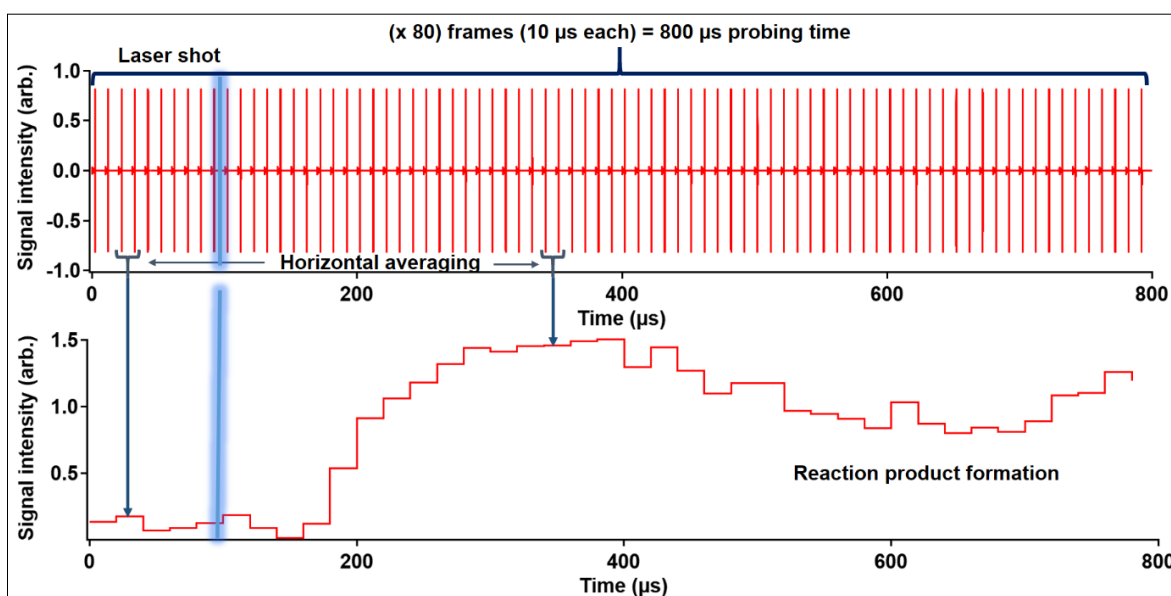


Figure III-16. The top panel shows the signal acquisition procedure of 800  $\mu\text{s}$  of flow time, with 80 frames of 10  $\mu\text{s}$  where the blue line represents the time of the laser shot to initiate the reaction and is implemented on the 10<sup>th</sup> frame, the bottom figure gives the corresponding time dependent signal obtained by Fourier transforming the FIDs contained in the 80 frames, two frames are horizontally averaged to increase the signal to noise ratio (SNR).

Implementing the mm-wave spectrometer in the CRESU environment requires the use of an absorbing foam (Eccosorb HR 25, Laird) to limit the reflections generated from the excitation pulses rebounding on the metallic chamber walls, more details are given in chapter IV and V. The extension of the experimental setup will be described in chapter V where a secondary expansion chamber will be integrated with the CRESU chamber.

### III.4.3. Flow cell

A flow cell has been built to conduct spectroscopic measurements at room temperature, the cell was used for the first tests of the characterization of the spectrometer, it is a 16 cm diameter, 1.5 m long cell composed of three parts connected with ISO 160 flanges. 8 ISO KF 40 half nipples are designed for gas inputs, pressure gauges and vacuum pumps. The ends of the cell are closed with 1 cm thick 10 cm diameter wedged Teflon windows. Similarly, to the CRESU chamber, the interior of the cell is covered with a 2 cm layer of the absorbing foam to reduce reflections. Pressure broadening measurements of vinyl cyanide and benzonitrile with helium as a collider were carried out in the cell, the results will be presented in the next chapter, where we introduce the development and the characterization of a new mm-wave spectrometer operating in the Ka band frequencies (26.5-40 GHz).

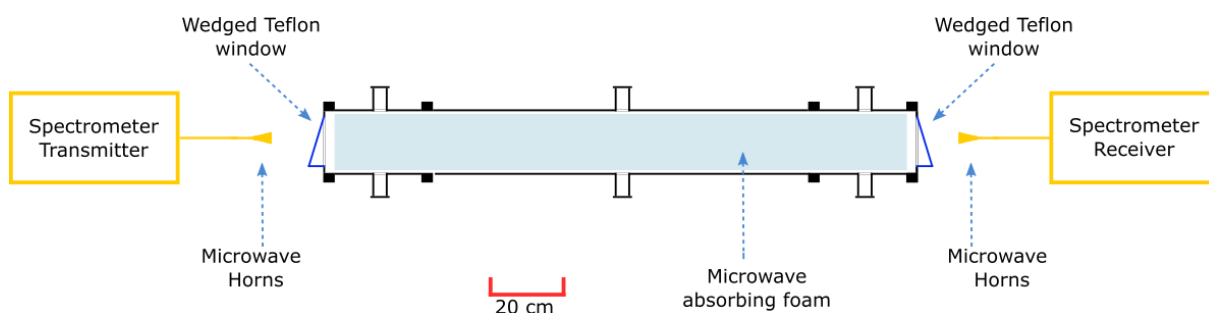


Figure III-17. Schematic of the flow cell

## Part II: Flow characterization

### III.5. Computational fluid dynamics

The Laval nozzle profiles are numerically tested before proceeding to the machining phase, the Ansys fluent package is used to simulate the supersonic flows generated by the Laval nozzle and foresee their associated properties, in particular the temperature, the density and the time of the uniformity.

Ansys workbench is a multiphysics software package developed starting in 1970 by John A. Swanson the founder of ANSYS corporation to conduct calculations using Finite Element Methods (FEM) and Finite Volume Methods (FVM) in order to model engineering problems. It contains multiple solvers allowing to carry out fluid dynamics, electronics and physics analysis, the most relevant to our field of research being the structural mechanics and the fluid solver also known as Fluent.

ANSYS Fluent allows to model a wide range of fluid dynamic problems including incompressible and compressible flows, both laminar, and at turbulent at a steady state or in the transient regime. The solver is fitted with multiple features to model the problem with a highest level of accuracy providing a total control and flexibility to the user via a graphic interface allowing one to set complex geometries with meshing grids of different degrees of refinement in addition to mathematical models and numerical assets to adapt the conditions of the simulation to the real scenario. Beside this, Ansys Fluent provides results with high reliability which is why it is mostly used for many industrial applications and in Research and development departments, and it is considered as a reference for other open source software such as OpenFoam. Despite requiring a licence, Ansys launches a free limited version of the software with twelve months' licence renewable and upgraded every year for academic purposes and is widely used among CFD communities.

We will be using Fluent to model compressible flow at supersonic speeds generated from the Laval nozzles using helium, nitrogen and argon as main carrier gases in the steady state regime for most of the nozzles that are involved in the measurements except for the helium nozzle at 6 K that was designed to work under periodic conditions with the pulsed system, we also used the software for hypersonic flows and shockwave investigations as will be shown in chapters V and VI.

All of these flows are axisymmetric, therefore and for time and computation efficiency, the 2D axisymmetric option has been used in the modelling, this reduces the number of elements in the mesh and also limits the risk of divergence during calculations. Figure III-18 shows the diagram of the different steps of a simulation with fluent considering an example of simulating a supersonic expansion from reservoir to the CRESU chamber via a Laval nozzle<sup>2</sup>.

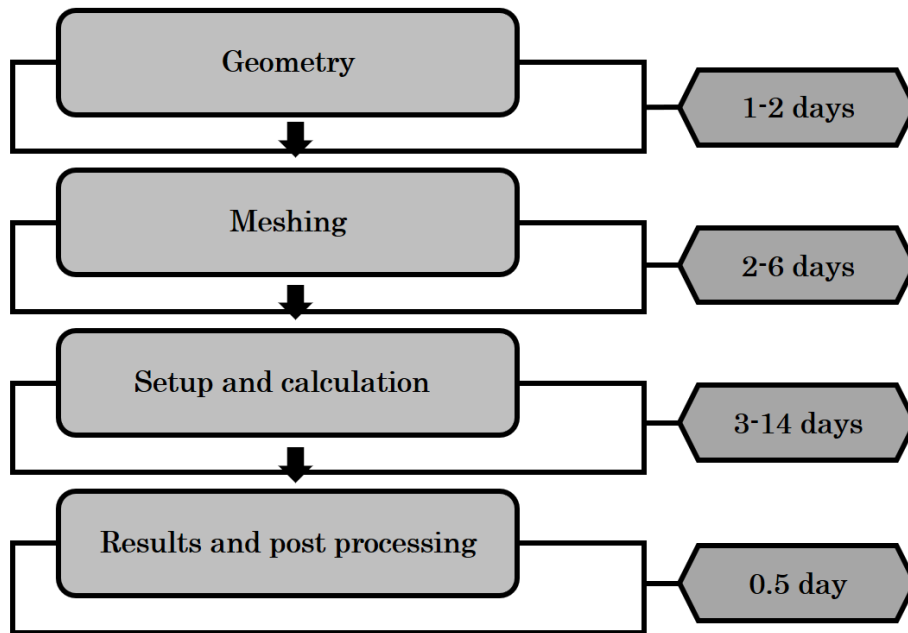


**Figure III-18. Simulation steps diagram with the duration of each procedure**

### III.5.1. Geometry

The nozzle profile can be imported to the Fluent design modeler either from computer assisted design files or as text file of coordinates in the three space dimensions, the geometry is then extended to include the reservoir and the CRESU chamber, the latter is important to measure the hydrodynamic time of the supersonic flow. The final geometry is then divided to different compartments called faces to help in setting the meshing elements, the segments forming the geometry known as edges are used to define the boundary conditions. As shown in Figure III-19 only a half part of the 2D of the Laval nozzle is simulated, the results of the other half can be deduced after the calculations by defining the lower edge of the geometry as an axis of symmetry, the

<sup>2</sup> All the calculations were run on a personal computer Intel(R) Core(TM) i5-8250U CPU@1.60GHz 16Go RAM

inlet and the outlet represent the flow entry and exit respectively, the nozzle profile is characterized by the wall condition where the gas molecules can neither leave nor injected. In order to accelerate the computation, the geometry of the reservoir and the chamber is scaled down compared to the real scenario and their associated boundaries are set as secondary inlet and outlet respectively.

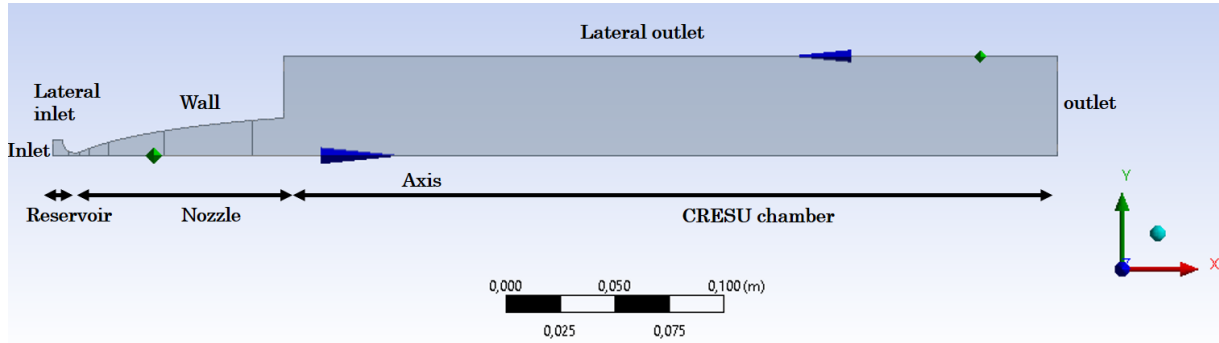


**Figure III-19. Geometry of the CRESU expansion as set in Fluent**

### III.5.2. Meshing

The second step to start the calculation is the meshing. Meshing is a very important phase of the simulation, a good meshing can lead to a solution convergence while a mediocre meshing can potentially result in slow convergence or even lead to complete divergence. The meshing needs to be generated uniformly across the geometry with smooth refining of the critical regions where the conditions vary significantly such as the throat region and the early expansion in the divergent part of the nozzle as well as near the wall where the boundary layer starts manifesting by a gradient of the flow properties. The mesh is generated by setting a progressive number of elements with uniform size in the different faces of the geometry. For 2D simulations, there are two types of meshing: quadrilateral and triangular grids. For most of our simulations we used the quadrilateral grid, which is a structured type of meshing that helps with convergence and accounts for flow parameter variations. In some of the simulations, a hybrid meshing was invoked by using triangular meshing, that is more suited for complex geometries but may impede accuracy and convergence, in limited parts of the geometry such as along the convergent part of the nozzle and near the throat region. The academic version of Fluent is limited to 512k cells that can be used for meshing. Depending on the geometry of the nozzle, for most of the conducted simulations, less than 300k cells are required for a well refined mesh. The final mesh is set considering the quality, the time of calculation and the computational expense.

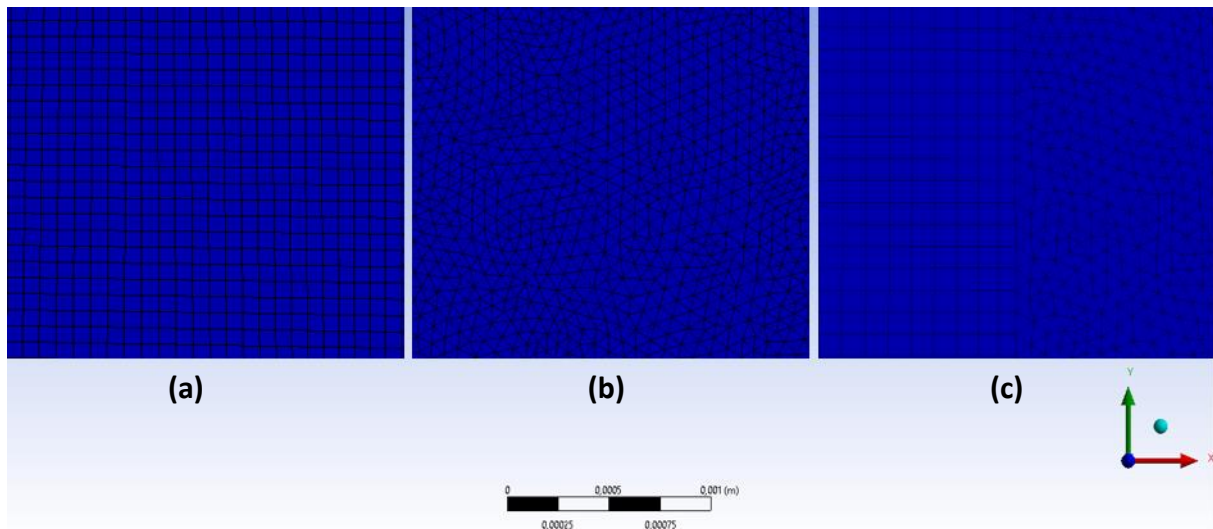


**Figure III-20.** Different types of 2D meshing, (a) shows quadrilateral meshing, (b) is the unstructured triangular meshing and (c) shows hybrid meshing between quadrilateral and triangular.

### III.5.3. Setup

After the meshing, the user proceeds to set the models and the conditions governing the simulation, starting by the type of the solver to use whether it is the pressure based or the density based, for compressible flow it is recommended for older versions of the program to use the density based one to account for the high speed velocity flow, the pressure based solver in recent versions has been extended to solve high speed flow problems. The calculations are carried out at a steady state which does not require the determination of the flow properties at every time step. The calculation time is therefore reduced and so is the computation cost, this being one major advantage of Fluent over OpenFoam.

### III.5.4. Physical Properties

The Fluent software provides the ability to model problems with high levels of complexity through the multiple options and a solid database of the numerous parameters characterizing the different materials, the software also gives the possibility to import models and values out of the external database and compile them in the setup to characterize the parameters of interest.

Fluent contains over 500 molecules in its database, once the molecule to simulate is selected the solver provides its associated properties such as the molecular weight, the specific heat, the thermal conductivity, the user can also set expressions,

polynomial, exponentials, etc., to account for the variation of the parameter in question with temperature. For CRESU flow modelling, we consider the buffer to behave as an ideal gas at a laminar regime.

Viscosity and its variation with temperature which is a very important physical property for the simulation is modeled with the Sutherland law that predicts the dynamic viscosity using three constants determined experimentally as shown by Equation III-1

$$\mu = \mu_0 \left( \frac{T}{T_0} \right)^{3/2} \frac{T_0 + S}{T + S} \quad \text{Equation III-1}$$

Where  $\mu$  is the viscosity in kg/m.s,  $\mu_0$  is a reference value in kg/m.s,  $T$  is the static temperature,  $T_0$  is a reference temperature and  $S$  is an effective temperature known as the Sutherland constant, all the temperatures are in kelvin. Figure III-21 shows the viscosity variation of nitrogen with temperature in the range of cold CRESU conditions.

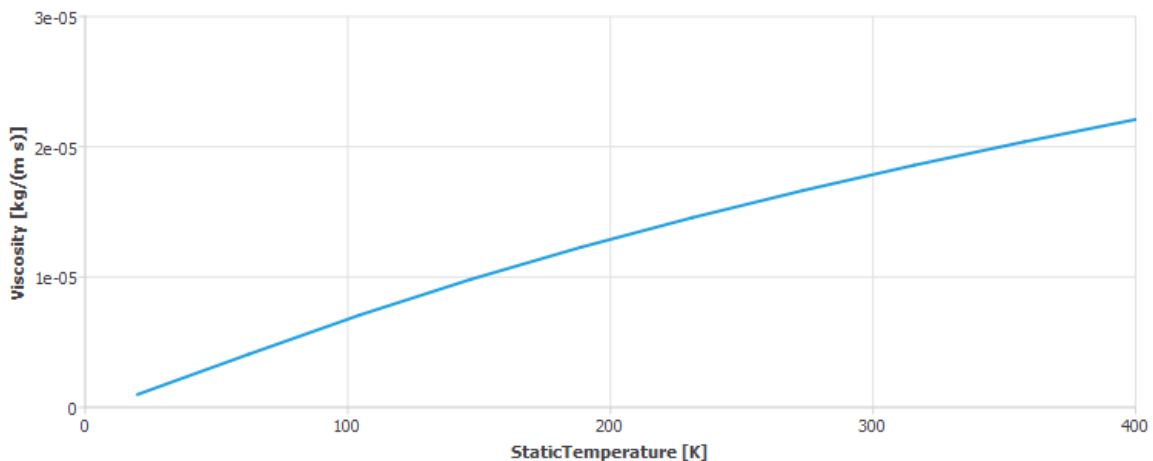


**Figure III-21. Viscosity variation with temperature for nitrogen in CRESU temperature interval given by the Sutherland model in Ansys Fluent**

### III.5.5. Boundary conditions

As shown in Figure III-19, the boundary conditions are determined at each edge of the geometry, the inlet and the lateral inlet are considered as flow entry conditions, they are defined as pressure inlet conditions where the user defines only the pressure and temperature of the flow given that the flow speed is zero at initial state before the expansion, however in other cases where the flow conveys a kinetic energy, Fluent allows to define boundary conditions including flow velocity input, velocity inlet, pressure far field and mass flow inlet beside temperature and pressure, with speed

information either as velocity magnitude, Mach number or as a mass flow rate. These types of boundary conditions have been used in shock wave investigation and secondary expansions via the skimmer where the gas has already expanded through the Laval nozzles and therefore it undergoes the secondary expansion with an initial kinetic energy, the results will be shown in chapter V. The outlet and lateral outlet are defined as pressure outlets with the same parameters to determine, the walls representing the nozzle geometry profile and parts of the chamber are defined as a stationary wall with a no-slip condition where the relative velocity of the flow is zero. Thanks to the axis of symmetry for axisymmetric flows, Fluent gives access to the other half of the 2D geometry as shown in Figure III-22, along this axis of symmetry there is no flux of any quantity, the normal velocity component is zero, also there is no diffusion flux, therefore the normal gradients of the flow variables are zero.

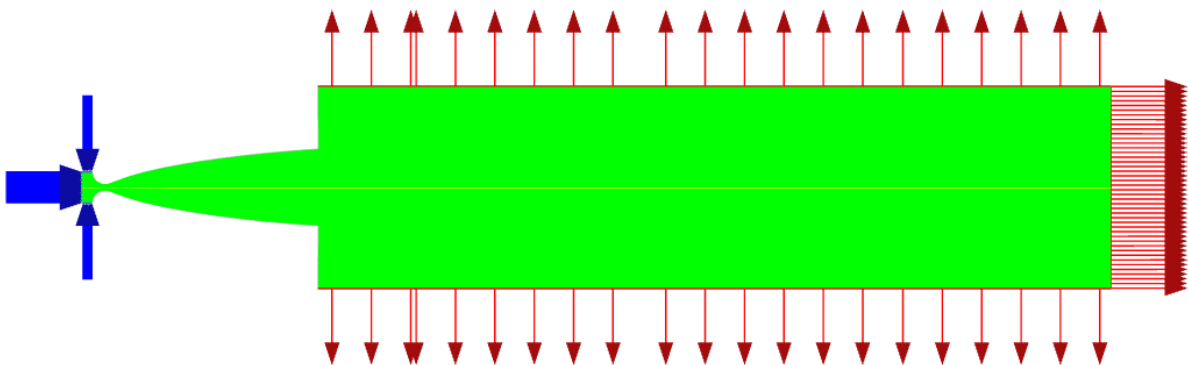


**Figure III-22. Display of the 2D axisymmetric geometry in fluent, the figure shows the Laval nozzle with part from the reservoir and the expansion chamber, the blue arrows indicate the flow entry regions while the red ones are for the flow output, the refined mesh is in green.**

### III.5.6. Initializing the solution

Before starting the calculations, user must provide an initial guess for the solution flow field known as initialization step which can be done manually by initializing the entire flow field or at specific region boundaries of the flow by giving values of temperature pressure and velocity. In the recent versions of Fluent, the solution can be initialized by selecting the hybrid option which solves the Laplace equation of the flow field parameters to give the initial guessing values. For transient simulations, the calculation is carried out for a number of iterations set by the user for every time step.

### III.5.7. Convergence and stability

The calculations start by giving a number of iterations to reach the convergence of the solution. The residuals which measures the quality of convergence starts decaying to small value, this stage of convergence is known as “round-off”, it can take tens of thousands of iterations depending on the number of computational cell and the complexity of the problem, before reaching the “level out” phase when they stop changing. To be able to follow the convergence criterion, the residuals are scaled to the maximum change after a number of iterations set by the user (5 iterations is the default). The convergence ratio, a scaled parameter of residuals, can drop by orders of magnitude before reaching the round-off (see Figure III-23).

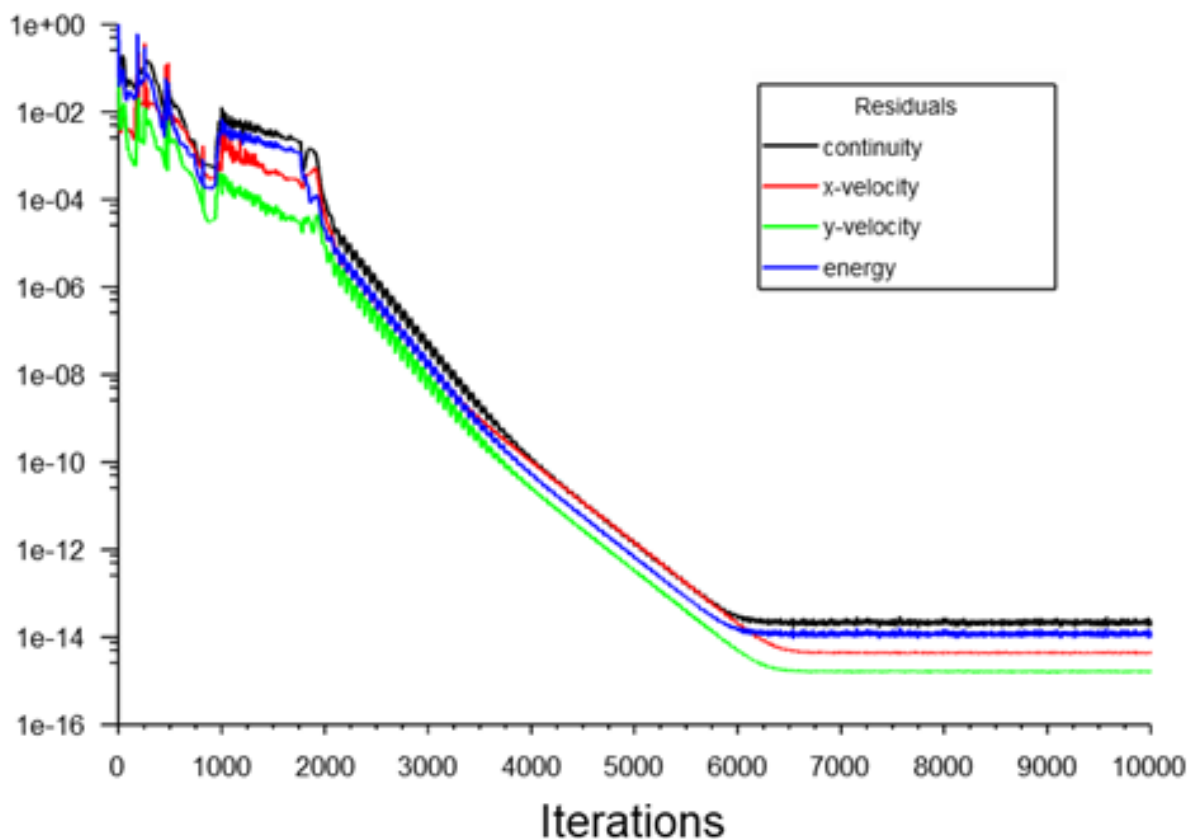


**Figure III-23. Convergence criterion decrease with iterations of flow variables, results are taken from calculations of the N2-30 K-0.183 Laval expansion, the method solves the continuity, momentum and the energy equations as shown by the caption.**

### III.5.8. Post processing

Once the solution has converged, the software gives access to all the parameters related to the simulation. Temperature, pressure, Mach number and density which are the main conditions of interest to characterize our CRESU flow are given at every point of the simulated geometry.

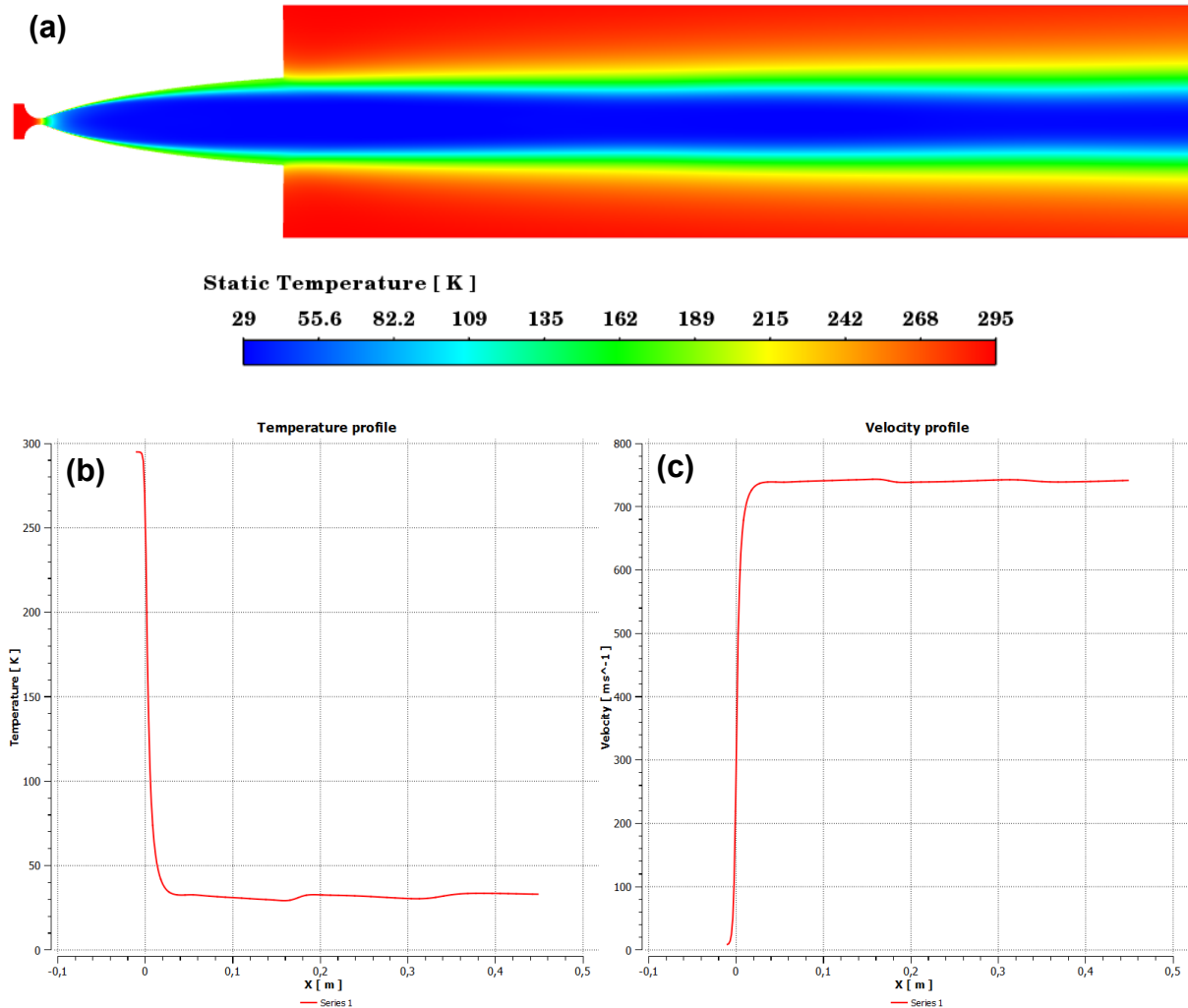
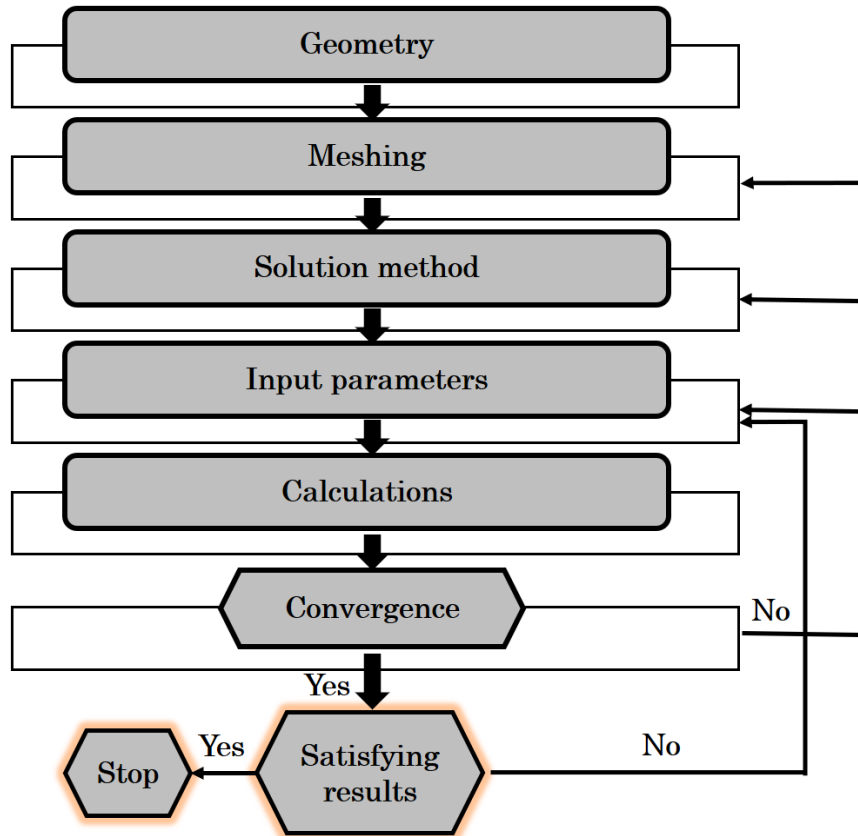


Figure III-24. Results given and displayed by fluent Post processing interface, (a) shows 2D mapping of the temperature profile, (b) and (c) display the temperature and the velocity profiles respectively along the axis of the geometry



**Figure III-25. Simulation procedure flow chart**

**Figure III-25** shows a flow chart of the procedures to follow in the simulations, as formally explained, the user must set the geometry, generate the mesh, select the models, define the boundary conditions and the other input parameters and finally launch the calculation, if the convergence is not reached, it may be caused by inappropriate definition of the parameters or the calculation models, second possibility is because of a poor meshing quality, critical regions in the simulations such as the boundary layers must have refined grids to account for the strong gradients of parameters. Should the solution converge, the user must inspect the results. For example the parameters could be tuned according to Equation III-8, Equation III-9 and Equation III-10 in the essence of uniformity or temperature of the CRESU flow. Simulation results of CRESU flows involving argon and helium as carrier gas will be presented in chapters V and VI respectively.

### III.6. Pitot characterization

After 3D printing, Laval nozzles are tested experimentally to compare the outcomes of the flow properties such as the temperature, density and the Mach number with the

simulation results. This can be achieved by doing Pitot characterization via impact pressure measurements.

### III.6.1. Background

The Pitot tube measures the total pressure in a reverse process of the expansion by transforming the kinetic energy of the flow into potential energy in the form of heat. The conversion takes place at what is called a stagnation point, where the flow speed becomes zero, located at the Pitot tube entrance.

For incompressible flows, velocity which measures the dynamic pressure is determined from the Bernoulli equation and given by:

$$v = \sqrt{\frac{2}{\rho}(P_{tot} - P_{stat})} \quad \text{Equation III-2}$$

For compressible subsonic flows, the velocity is determined from Equation II.11 as follows:

$$v = \sqrt{2 C_p \left( 1 - \left( \frac{P_{tot}}{P_{stat}} \right)^{\frac{\gamma-1}{\gamma}} \right)} \quad \text{Equation III-3}$$

For both cases the flow regime is maintained while measuring the pressures using the Pitot tube, the flow streamlines are diverted by the tube with minimum perturbation of its conditions.

### III.6.2. Supersonic flow

Unlike subsonic flows, when a supersonic flow comes to the stagnation point, the impact will be so strong that it creates a normal shockwave few millimetres before the entrance of the tube. The flow properties will therefore change drastically, pressure, temperature and density will increase instantaneously and the Mach number drops to subsonic values before stagnation. In this case, the Pitot tube measures the impact pressure at the stagnation point, the ratio of the latter combined with the known reservoir pressure allow us to determine the Mach number and the other thermodynamic parameters. Considering four regions in the CRESU flow as shown in Figure III-26, with  $P_0$ ,  $P_1$ ,  $P_2$  and  $P_i$  are the reservoir, the CRESU jet, the post shock and the stagnation pressures respectively.

$$\frac{P_i}{P_0} = \frac{P_i}{P_2} \times \frac{P_2}{P_1} \times \frac{P_1}{P_0} \quad \text{Equation III-4}$$

Given that  $P_0$  and  $P_i$  are measured with pressure sensors,  $P_2$  does not need to be determined, therefore using Equation II-32 which relates pre-shock and post-shock pressures we can find Equation III-5 that expresses the relationship between the impact pressure and reservoir pressure of the supersonic flow before the shockwave as a function of the Mach number.

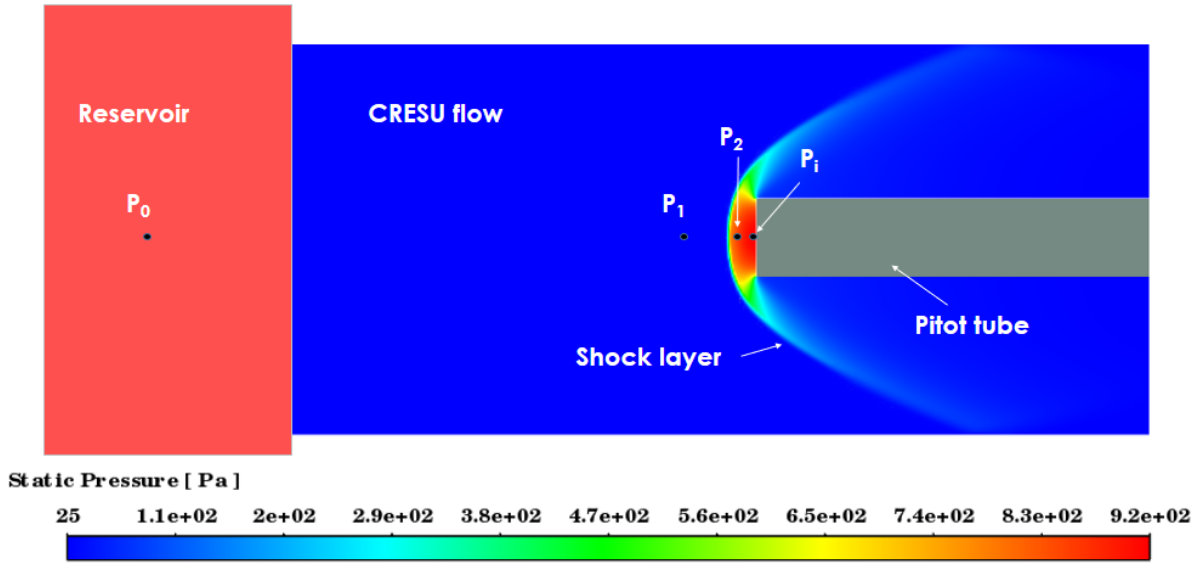


**Figure III-26. Schematic of Pitot characterization of CRESU flow using a Pitot tube, the results show a 2D temperature profile from an argon flow at 35 K, a shockwave has been formed 1 mm before the tube entry.**

$$\frac{P_i}{P_0} = \left( \frac{(\gamma+1)M_1^2}{2+(\gamma-1)M_1^2} \right)^{\frac{\gamma}{\gamma-1}} \left( \frac{1-\gamma+2\gamma M_1^2}{\gamma+1} \right)^{\left(-\frac{1}{\gamma-1}\right)} \quad \text{Equation III-5}$$

Using  $\frac{P_i}{P_2} = \left( 1 + \frac{(\gamma-1)}{2} M_2^2 \right)^{\frac{\gamma}{\gamma-1}}$  where;  $M_2^2 = \left( \frac{(\gamma-1)M_1^2+2}{2\gamma M_1^2+1-\gamma} \right)$  Equation III-6

We can extract the relationship between the impact pressure and the chamber pressure from Equation III-7 which gives the Rayleigh Pitot tube formula.

$$\frac{P_i}{P_1} = \left( \frac{(\gamma+1)^2 M_1^2}{4\gamma M_1^2 - 2(\gamma-1)} \right)^{\frac{\gamma}{\gamma-1}} \left( \frac{1-\gamma+2\gamma M_1^2}{\gamma+1} \right) \quad \text{Equation III-7}$$

The other flow properties such as temperature and density are deduced from the isentropic equations introduced in chapter II and given by the following equations:

$$\frac{P_o}{P_{flow}} = \left(1 + \frac{(\gamma-1)}{2} M_1^2\right)^{\frac{\gamma}{\gamma-1}} \quad \text{Equation III-8}$$

$$\frac{T_o}{T_{flow}} = \left(\frac{P_{i0}}{P_{flow}}\right)^{\frac{\gamma-1}{\gamma}} \quad \text{Equation III-9}$$

$$\frac{\rho_o}{\rho_{flow}} = \left(\frac{P_{i0}}{P_{flow}}\right)^{-\frac{1}{\gamma}} \quad \text{Equation III-10}$$

### III.6.3. Accuracy and limitations

The impact pressure characterization using the Pitot tube is a very accurate procedure, the only possible errors comes from the pressure measurements. The 1, 10 and 100 torr Brooks gauges that are mostly used for Pitot measurements have an accuracy of 0.15 % of the reading values a very small error compared to other vacuum measurement technologies. The Pitot gives results that are very similar to predictions from CFD simulations, it has been tested with multiple nozzles with different properties and the results tend to be within the error ranges. Figure III-27 shows the temperature profiles along the axis of a nitrogen nozzle designed to operate at 23.5 K from the N<sub>2</sub>-23.5K-0.12. The average temperature and fluctuations are within the error range.

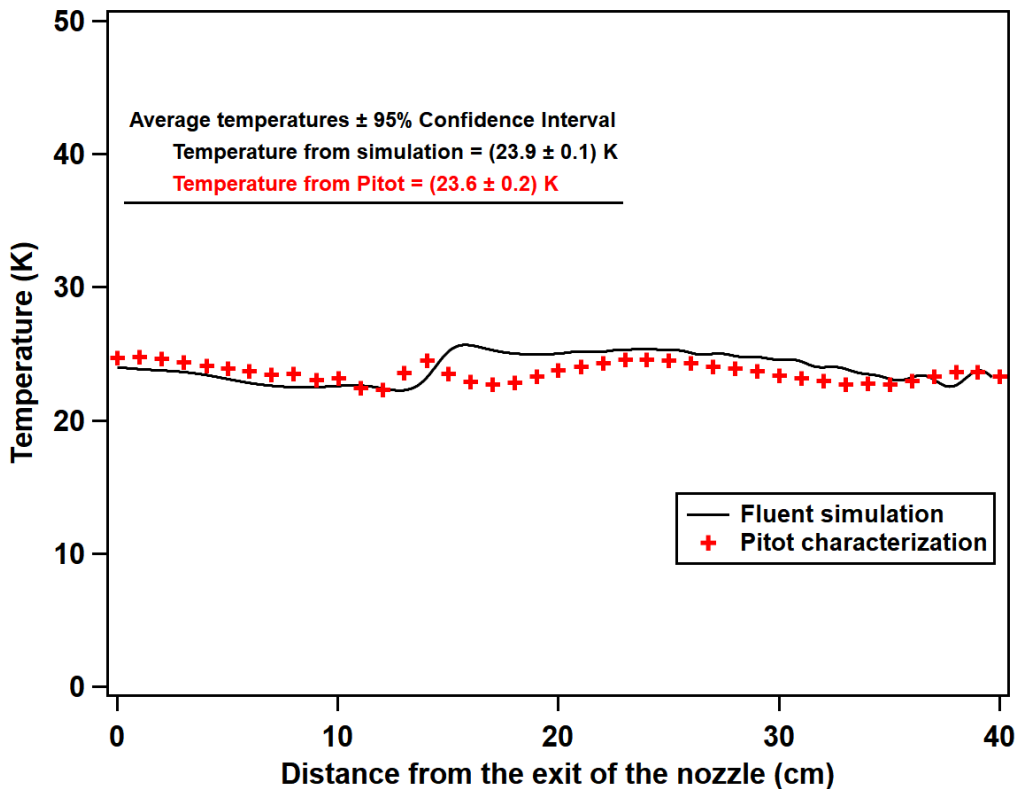
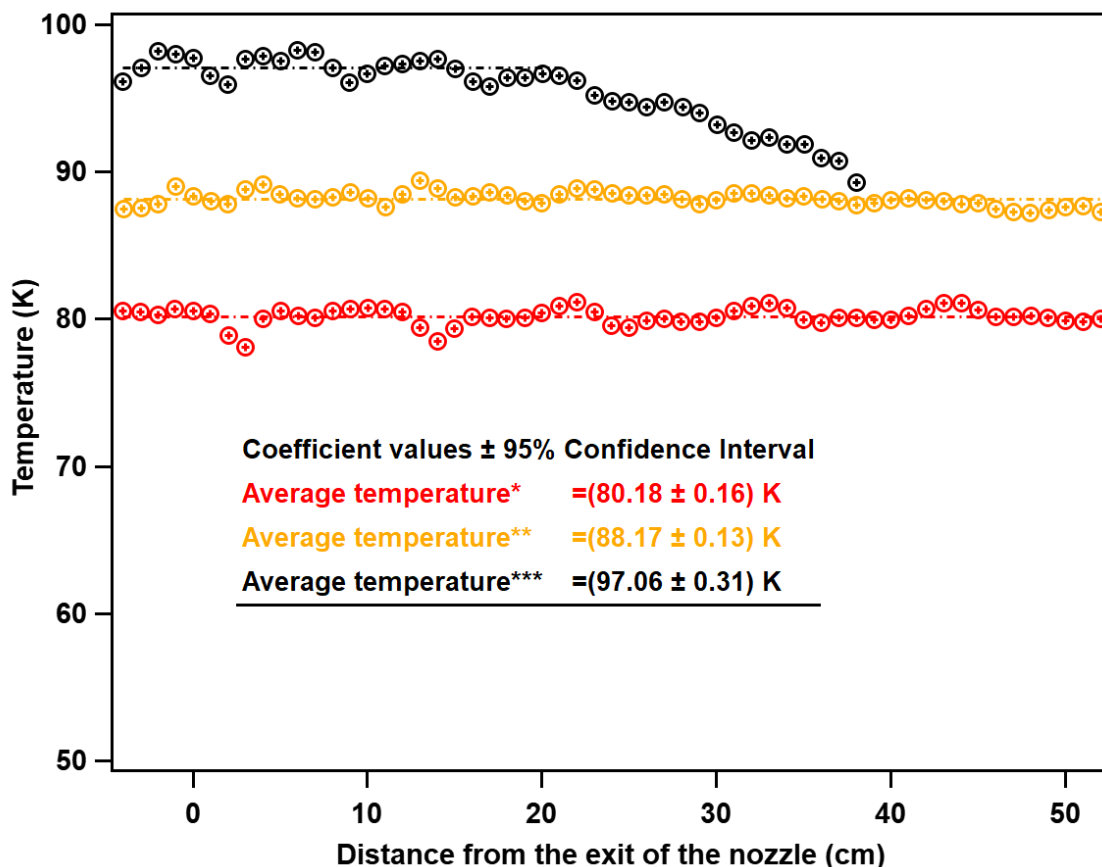


Figure III-27. Comparison between simulation and Pitot characterization, results from nitrogen flow under CRESU conditions.

Experimental operating conditions are susceptible to possible adjustments either minor ones to reduce fluctuations or increase the hydrodynamic time of the uniform flow or major ones by changing the flow rates and or the pressure ratio to set a new operating conditions, for example a helium nozzle designed to operate at 20 K (He-20K) nozzle that gives two different temperatures and densities (see A.III in the appendix). Initially the nozzle was designed to operate at 20 K but then the experimental conditions were adjusted to operate at 18.7 K, new conditions were then used by increasing the flow rate and to have more gain on the hydrodynamic time and decreasing the pressure to go to a lower temperature of 17 K, another example is the N<sub>2</sub>-83 K (design temperature) which operates at three different temperatures 80.2 K, 88.2 K and 96.8 K at a decreased flow rate and pressure ratio respectively, this helps in conducting pressure and temperature dependence measurements with the same nozzle (see Table III-1).

**Table III-1: Different operating conditions of the nitrogen CRESU flow designed for 83 K**

| Nozzle (design)        | CRESU jet temperature (K) | Reservoir pressure (mbar) | Chamber pressure (mbar) | Flow rate (slm) | Length of uniform flow (cm) |
|------------------------|---------------------------|---------------------------|-------------------------|-----------------|-----------------------------|
| N <sub>2</sub> at 83 K | 80.2                      | 47,8                      | 0.49                    | 47.77           | 53                          |
|                        | 88.2                      | 22.73                     | 0.31                    | 24.73           | 50                          |
|                        | 97                        | 11.83                     | 0.219                   | 14.84           | 26                          |



**Figure III-28. 1D temperature profiles of the different operating conditions of the N2-83 K nozzle**

This procedure can be extended to using nozzles with multiple buffers such as the Ar-50K-0.3 that works also with helium at 71.6 K (see Appendix Table A.III.).

The Pitot method does however present some limitations related to its geometry and mounting, first the interior diameter which one may consider to better have it as large as possible for a fast equilibrated pressure and thus quick acquisition, this leads to a loss of the resolution especially for supersonic flows with narrow isentropic cores. Second is that the tube must be perpendicular to the flow cross section at the axis of the nozzle which requires careful alignment of the tube in the x, y, z dimensions (see Figure III-8). This is verified by aligning the tube on the axis of the chamber, which is also the axis of the nozzle, using a helium-neon laser source.

The formation of shockwaves in the Pitot method which manifest by an abrupt and considerable heating may cause any condensates in the flow to evaporate and lead to erroneous measuring of the impact pressure which is why a quantitative characterization using the spectrometer is always required to remain in the linear non

clustering regime as will be shown in chapter V (see Figure V-21). This however does not present a significant constraint to our measurements as the concentration of molecules is always kept under 1% of the total density of the carrier gas in order not to cause any perturbation of the flow properties or completely destroy its uniformity if clusters are formed massively.

The Pitot method has been used to measure the impact of the increasing concentrations of molecules in a carrier gas in supersonic flows. Nitrogen was used as a carrier gas from the N<sub>2</sub>-30K-0.183 nozzle, C<sub>2</sub>H<sub>4</sub> one of the relevant reactants used in the reactions studied in this work (see chapter V) was used for these measurements by varying its concentration in the nitrogen flow. Figure III-29 shows the impact pressures measured by the Pitot tube at different concentrations of C<sub>2</sub>H<sub>4</sub> in the nitrogen flow at 30 K.

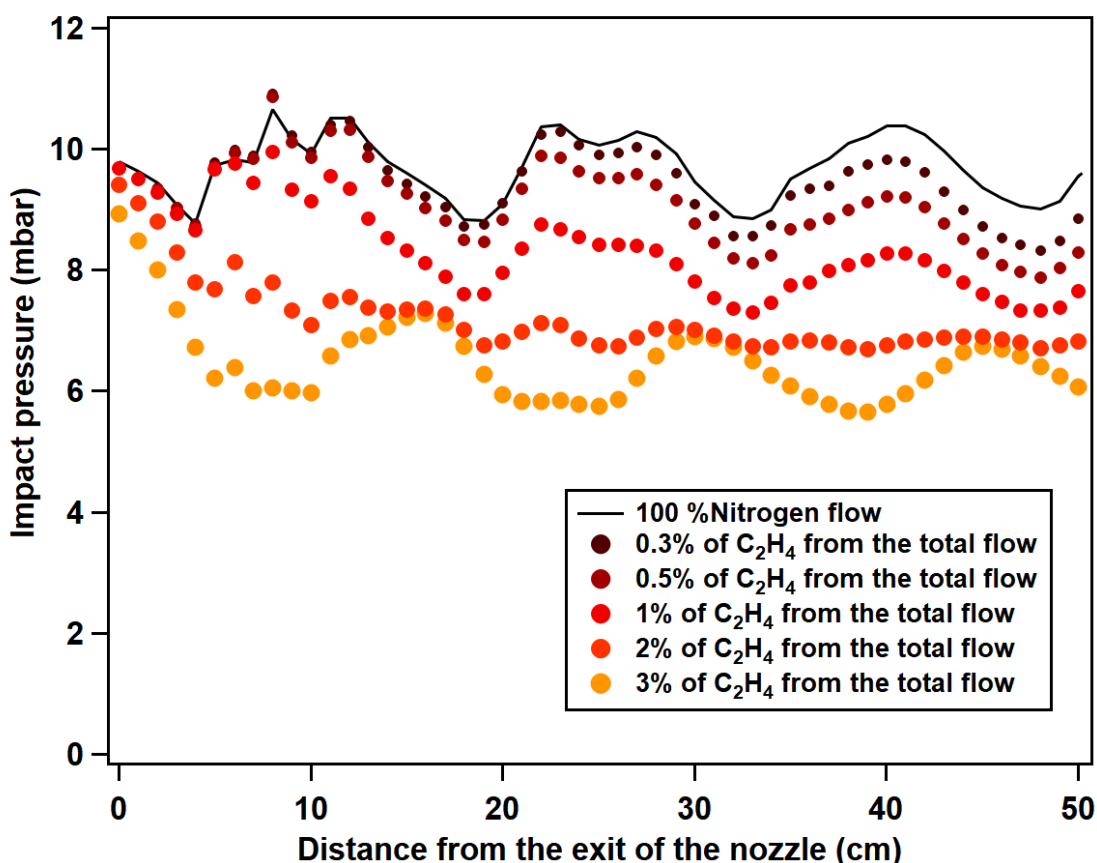


**Figure III-29. Impact pressure measurements of nitrogen CRESU flow at 30 K carrying increasing concentrations of C<sub>2</sub>H<sub>4</sub>**

At 0.5 % of the total density and below, there is a gap of less than 10 % from the original CRESU flow that keeps increasing with the increased C<sub>2</sub>H<sub>4</sub> density beyond the

1 %, above this value the impact pressure measurements given by the Pitot indicate a drastic change in the flow conditions, Figure III-31 gives a 2D profile of the impact pressure of the original nitrogen flow at 30 K showing that the isentropic core (cold supersonic region of the flow) has impact pressures above 9 mbar, below this value the boundary layers start manifesting indicating the subsonic regime and therefore no presence of a shockwave which implies that the flow conditions and mainly the temperature have changed. In Figure III-30, we see the impact pressure profiles along the axis of the chamber from two different concentrations and their associated disparities from the original flow. As explained earlier, for higher concentrations the flow properties change considerably however this is not a serious problem as in our reaction kinetics studies the reactant concentrations are always kept much below 1%. At 0.3% the two profiles are identical but as from 25 cm and beyond, the discrepancy starts increasing until reaching 5 % which is an indication of a possible clustering process that manifests more with time.

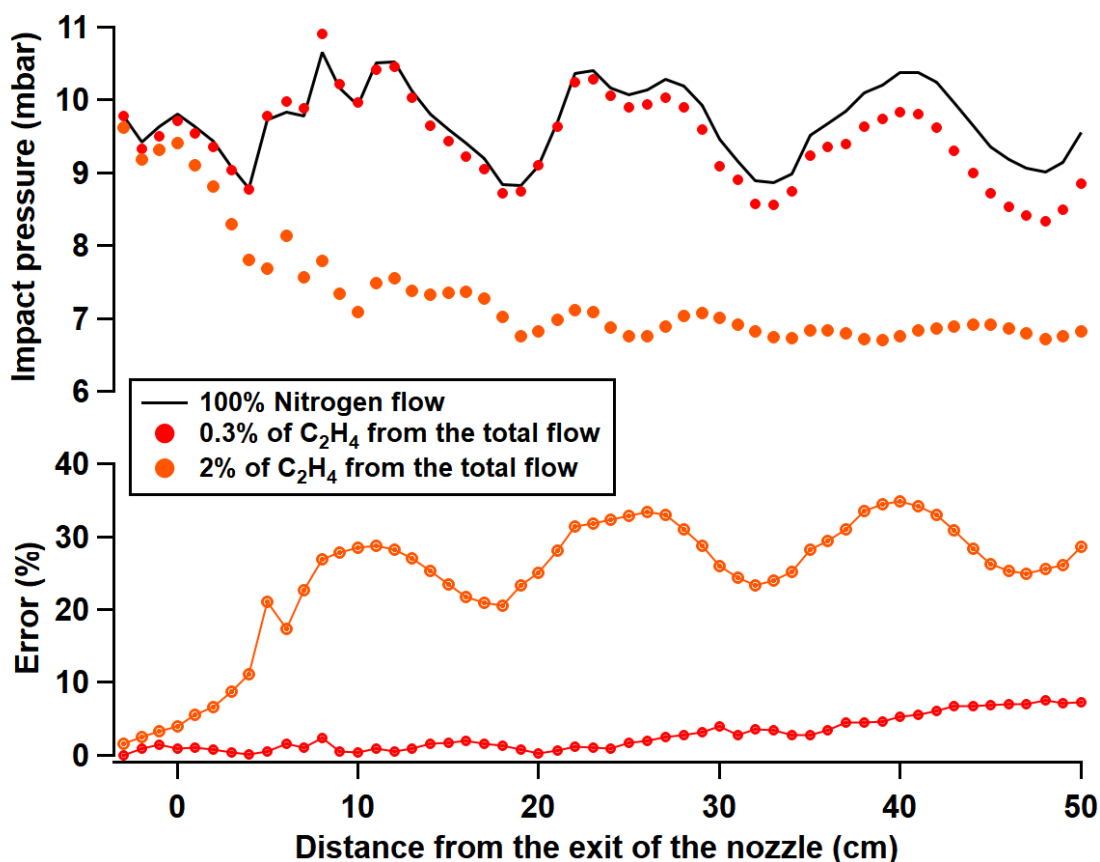
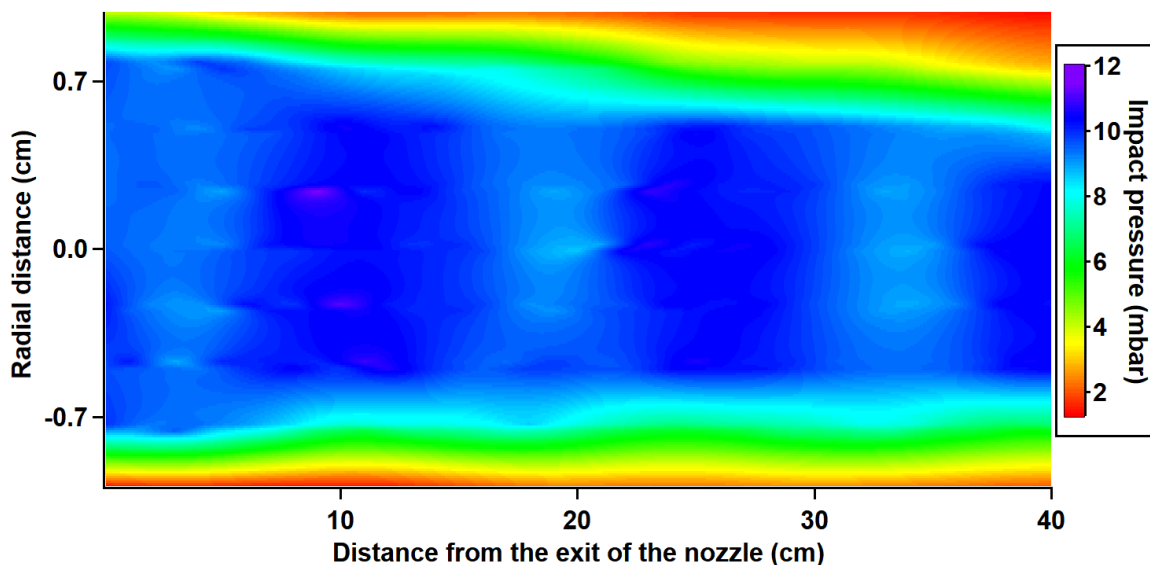
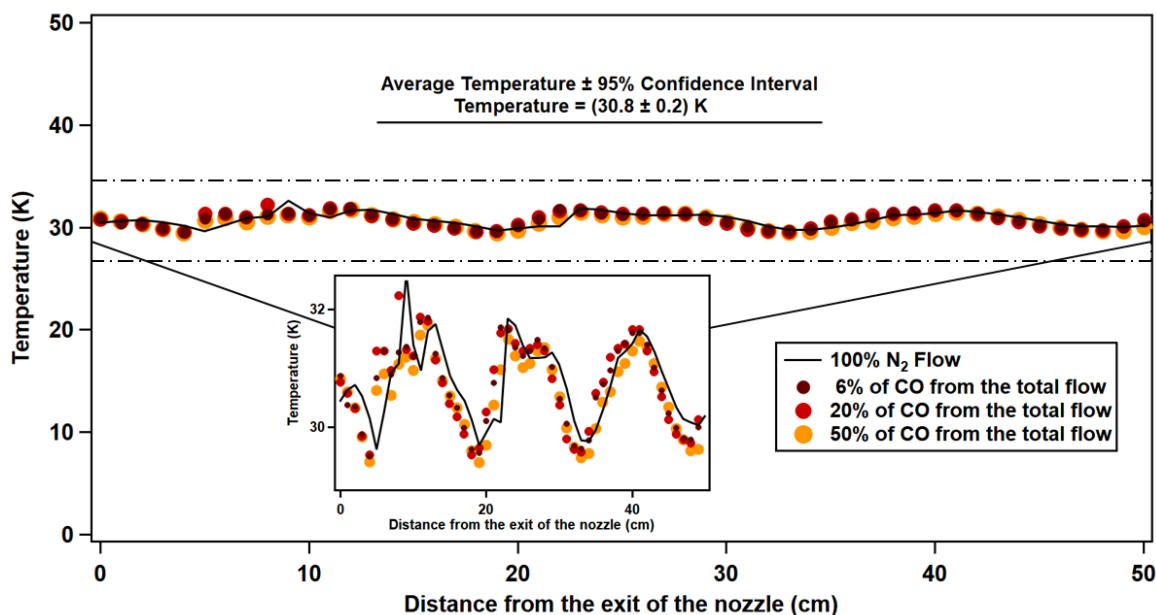


Figure III-30. Plots of impact pressure measurements from nitrogen CRESU flow at 30 K from the N<sub>2</sub>-30K-0.183 nozzle carrying different concentrations of C<sub>2</sub>H<sub>4</sub> with the corresponding errors from the original flow.



**Figure III-31. 2D plot of the impact pressure of the original profile of the N<sub>2</sub>-30K-0.183 nozzle, the result indicates that impact pressures below 8.5 mbar do not characterize the isentropic core of the original conditions.**

Another measurement was conducted with the same nozzle but with carbon monoxide CO as a reactant molecule. This was in the context of studying the OH+CO reaction at very low temperatures and the kinetics results are reported in the thesis of Jopseph Messinger.<sup>4</sup> As the OH+CO reaction is much slower than other reactions studied in this thesis, it was necessary to go to much higher CO concentrations, Figure III-32 shows the temperature profiles along the axis of the chamber calculated from the impact pressure measurements with increasing concentrations of CO up to 50% of the total flow. The output temperatures were all within the 0.2 K error compared with the one from the original profile. This stems from the similarities between CO and N<sub>2</sub> as they both share the same specific heat capacity ratio, molecular weight and have a difference of only 3-6.5% of their viscosity values at lower temperatures.



**Figure III-32.** Temperature profiles along the axis from impact pressure measurements of nitrogen CRESU flow at 30 K carrying increasing concentrations of CO, the inset gives a zoom on the temperature. The measurements were taken with the N<sub>2</sub>-30K-0.183 nozzle the lowest temperature nitrogen nozzle at that time.

Another limitation with the respect to the Pitot tube involves the incapacity to characterize flows in nearly and non-continuum regimes generated from molecular beam sampling and free jet expansions for example, this will be developed further in the next section.

### III.7. Direct simulation Monte Carlo calculations

When the pressure is lowered to medium and high vacuums (less than  $10^{-2}$  mbar), collisions between molecules become less frequent, the flow can no longer maintain thermal equilibrium and shifts to non-thermally equilibrated regime, also known as the rarefied regime. Under these conditions the flow must not be considered as a continuum any more, but should rather be regarded at a discrete molecular level meaning that the conventional CFD models that solve the Navier-Stokes equations in the continuum regime can no longer predict the flow properties under the rarefied conditions, and a particle-based approach is required. Ideally, a molecular dynamics approach would be involved simulating the trajectory of every particle computed from Newton's equations but the computational expense would be exorbitant. Instead, a statistical approach is used to simulate the flow at the molecular level which relies on

numerically solving the Boltzmann equation<sup>7,8</sup> a nonlinear integral differential equation that has no analytical solution. In 1963, Professor Graeme Bird from the University of Sydney first proposed a probabilistic numerical method applicable for solving Boltzmann equations known as the direct simulation Monte Carlo (DSMC) method.<sup>9</sup>

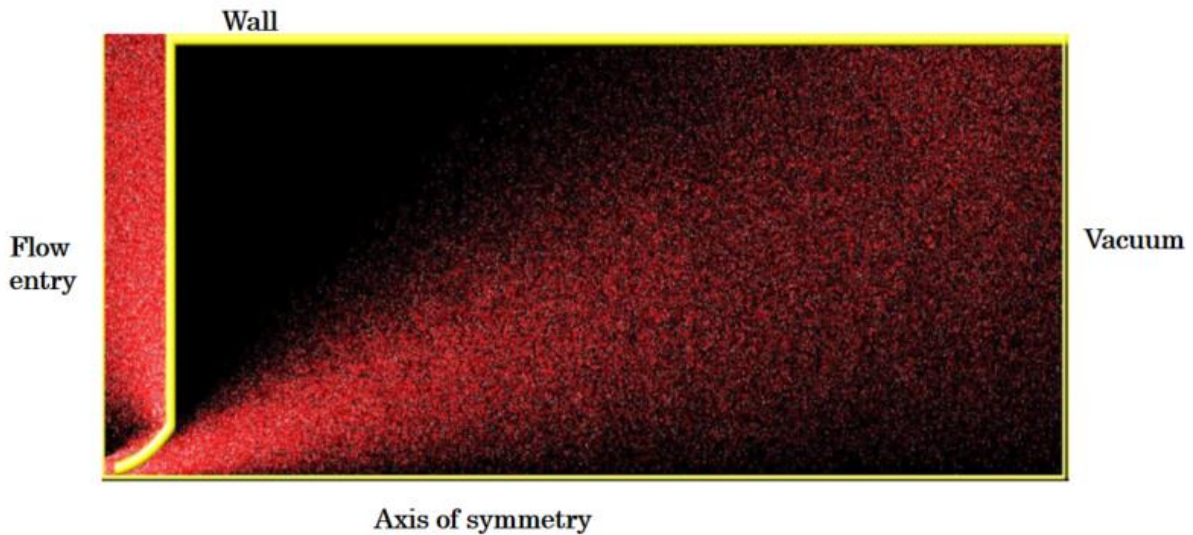


**Figure III-33. Example of a geometry of a supersonic expansion via a skimmer**

The DSMC method models flows by simulating a large number of real molecules in a stochastic simulation to solve the Boltzmann equation. Molecules are moved through intermolecular collisions and molecule-surface interactions in a simulation of physical space coupled with time such that unsteady flow characteristics can be modelled. A key parameter must be considered in order to characterize these types of flow: The Knudsen number.

### III.7.1. Knudsen number

The Knudsen number<sup>10</sup> is a parameter that measures the degree of rarefaction in the medium, denoted by  $Kn$ , it is given by

$$Kn = \frac{\lambda}{D} \quad \text{Equation III-11}$$

where  $\lambda$  is the mean free path and  $D$  is a characteristic length (in our case the diameter of the skimmer), depending on the value of this parameter the flow regime is determined;

|                   |                     |
|-------------------|---------------------|
| $Kn < 0.01$       | Continuum flow      |
| $0.01 < Kn < 0.1$ | Slip flow           |
| $0.1 < Kn < 10$   | Transitional flow   |
| $Kn > 10$         | Free molecular flow |

Figure III-34 shows the relationship between the different degrees of rarefaction of compressible flows and the model to use to predict the flow properties based on the value of the Knudsen number.

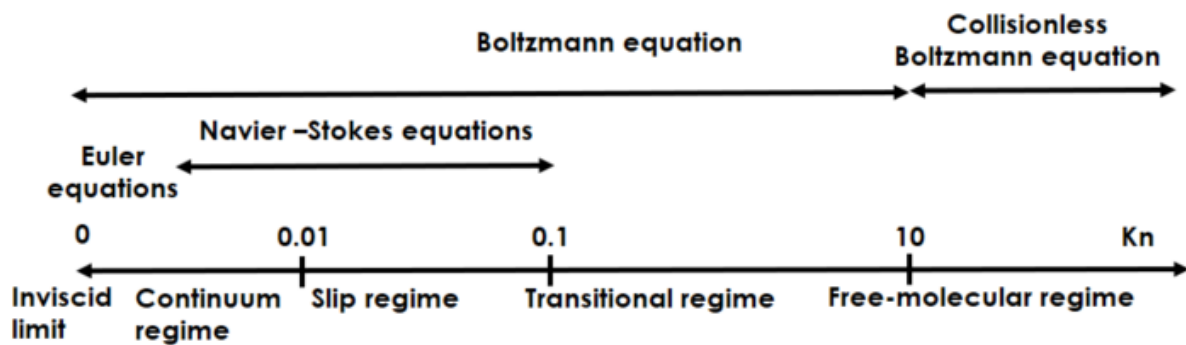


**Figure III-34. Flow regimes according to the corresponding Knudsen number values**

As the Knudsen number tends to zero the flow can be characterized as inviscid, it is modelled by the Euler equations which ignores the viscosity as demonstrated in chapter II. When the Knudsen number tends to infinity, the mean free path becomes much larger than the characteristic length, therefore collisions become very infrequent even after the particles hitting the surface, they reflect away, the flow is considered in a free molecular regime where intermolecular collisions are neglected (collision-free flow).

The zone between free molecular regime and the limit of validity of the Navier-Stokes equations is generally referred to as the transitional regime where both the collisions between particles and with the surface assume importance. At the lower limit of this region there is what is called the slip regime, this term is used to refer to the velocity slip near the boundaries. This regime is also called near continuum regime, the mean free path is 10 to 100 times less than the characteristic length. The slip regime is the dominating environment of most of the measurements in the secondary expansion chamber, more details about this regime are given in modelling skimmer expansions in intermediate vacuums in chapter V.

### III.7.2. DS2V program

DS2 is a program coded in standard FORTRAN 95 written by G.A Bird to conduct 2D Monte Carlo simulation, the program is supplied with a graphical user interface to facilitate DATA setting and output post processing, it allows to model rarefied flows of different Knudsen number down to 0.001 for multiple applications and problems. The user can create and modify geometries of different complexity, set the boundary conditions and all the flow properties. The output files containing the results can be post processed via DS2V, a console that allows a direct and simple interactive visualization.

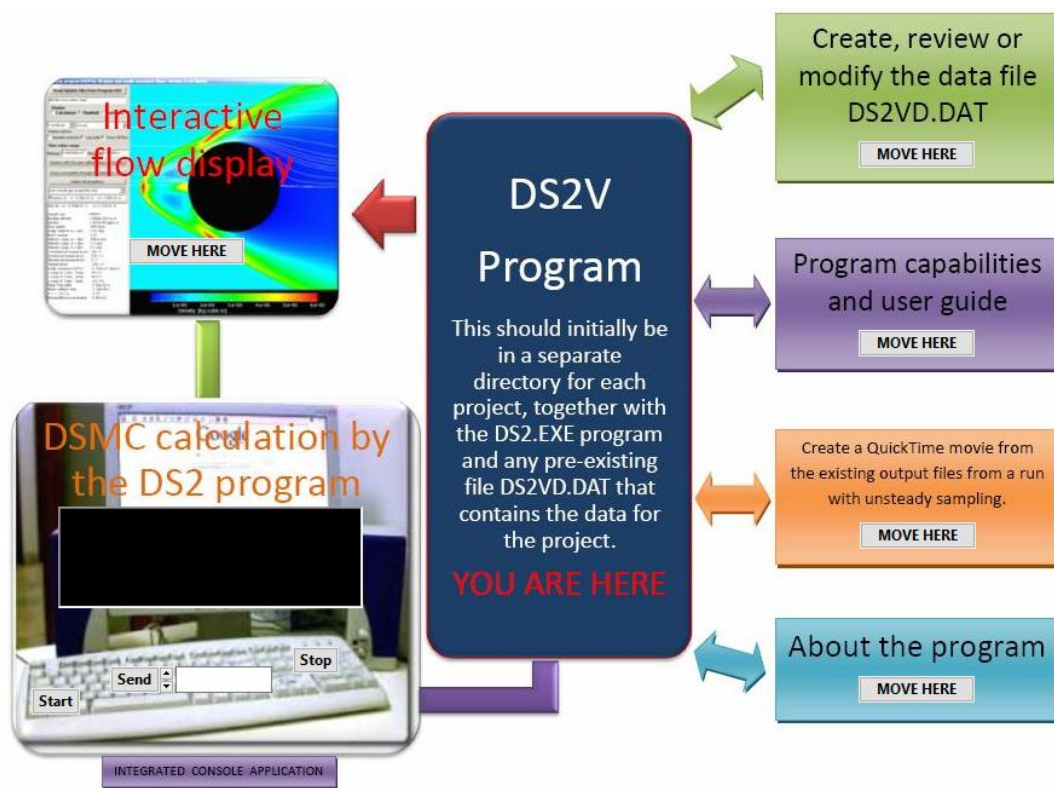


Figure III-35. DS2V graphical user interface

The DS2V has the same features and steps to conduct the calculation as Fluent

#### III.7.2.1. Geometry

At first, a simulation box is created by setting the minimum and maximum dimensions in the x and y directions forming a rectangular flow field, the geometry is then set manually through an ensemble of straight lines and/or arc segments with the associating coordinates to create a surface in which the simulation is carried out, the surface must either be closed or its edges connected to the simulation box.

### III.7.2.2. Grid

The DS2V generates a background rectangular grid that covers the simulation box which is uniformly spaced in each direction. Every division of this grid is then divided into a finer grid of elements, the standard value is 100 elements in each division.

### III.7.2.3. Setting the conditions

The program is equipped with a database containing multiple gas molecules with their associated parameters such the molar mass, reference diameter...etc, as well as the molecular collision model which defines molecule-molecule collisions and the surface interaction model representing collisions of molecules with the wall surface. The variable hard sphere collision has been implemented to characterize the molecular collisions. For gas-surface Interaction, we used the Diffuse reflection with full accommodation to the surface temperature model meaning that molecules will be scattered at the temperature of the surface after hitting the walls of the medium.

In a similar way to the continuum regime simulations in the CRESU environment using Fluent, free jet expansion and secondary expansions via skimmers can also generate axisymmetric flows, and with DS2V, one can set the minimum y boundary as axis of such a flow. The flow input is set through the minimum x boundary as a constant pressure boundary with velocity set by mass flux (the user gives the velocity value with the number density of the gas). The output condition is set to a vacuum Interface which prevents molecules from entering the flow and the ones hitting this boundary are removed from the flow. it is also possible to set periodic Boundaries.

### III.7.2.4. Output files

The program outputs all the flow properties within the simulation box, the DS2V gives a 2D profile of the conditions at each point of the flow. The calculation time depends on the geometry, the degree of rarefaction and the time step, for our calculation that will be presented in chapter V it took between 1-3 weeks<sup>2</sup> for the permanent regime to establish.

### III.7.2.5. MCS/MFP Ratio

The calculations can be stopped when the ratio of the mean collision separation (MCS) and the mean free path (MFP) is very small compared to unity, the results then are

considered to be satisfactory. The results can always be optimized by increasing the number of simulating molecules to approach the real number of molecules but this tends to be too computationally expensive for slip and transitional regimes.

### III.7.3. Power of DSMC over Navier-Stokes FEM

There is no iterative procedure or convergence to the final solution in DSMC in contrast to the FEM Navier-stokes solvers like fluent or OpenFoam, neither does it require an initial approximation to the flow field before starting the calculations. Frequent sampling however does help to decrease the variance which reduces the scattering in the profiles of the flow properties. Figure III-36 shows scattered temperature profile along the axis of an expansion given by DS2V.

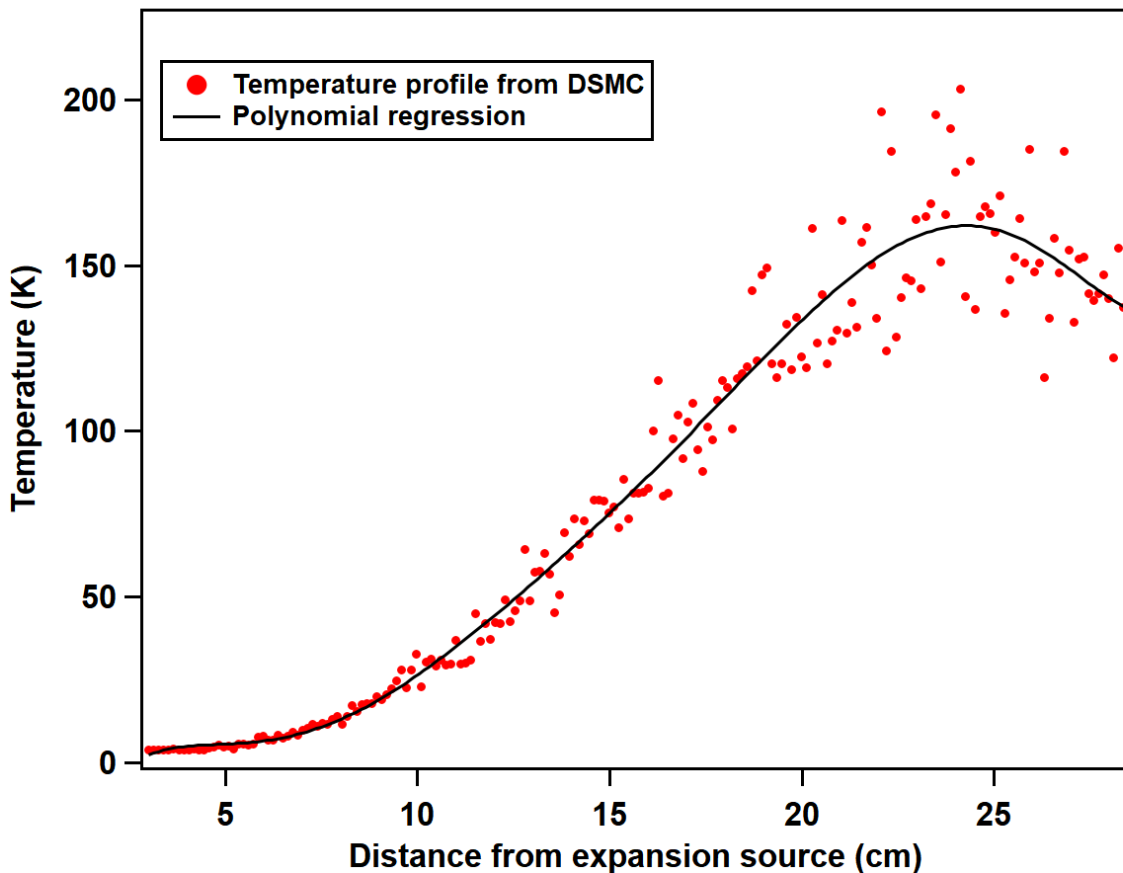


**Figure III-36. Temperature profile along the axis of a supersonic flow in a slip regime**

The DSMC can model flows in the slip and even the continuum regime, for two-dimensional and axially symmetric flows it is possible to carry out calculations with overall Knudsen numbers in the range of 0.01 to 0.001. The main limitation however

is that it is computationally expensive particularly for lower Knudsen numbers and larger geometries and 3D problems. Results from DSMC calculations will be presented in Chapter V when characterizing the post skimmer expansion of a sampled CRESU flow into the secondary expansion chamber.

### III.8. Experimental characterization of rarefied media

The experimental characterization of non-thermalized flows cannot be conducted via the impact pressure characterization using a Pitot tube as we do for CRESU flows, as the flow properties vary at a very high rate as we move away from the flow axis. However, conducting spectroscopic measurements with a CP-FTmmW spectrometer allows us to have access to the temperature of the probed region. By probing different transitions of a given molecule in the flow we can extract its rotational temperature from the Boltzmann plot of populations with respect to their corresponding energy levels. Depending on the density of the medium, the rotational temperature will likely be the same as the translational temperature of the buffer gas, or a few degrees higher as shown by the following;

$$\tau_{collision} < \tau_{tran} < \tau_{rot} \ll \tau_{vib}$$

where  $\tau_{collision}$  is the mean collision time and  $\tau_{tran}$ ,  $\tau_{rot}$  and  $\tau_{vib}$  are respectively the relaxation times for translational, rotational and vibrational energy modes.

Rotation diagrams of sampled CRESU flows in the secondary expansion chamber will be presented in Chapter V to determine the temperature at different regions of the secondary expansion via the skimmer.

## References

- (1) James, P. L.; Sims, I. R.; Smith, I. W. M.; Alexander, M. H.; Yang, M. A Combined Experimental and Theoretical Study of Rotational Energy Transfer in Collisions between  $\text{NO}(X\ 2\Pi_{1/2}, V=3, J)$  and He, Ar and  $\text{N}_2$  at Temperatures down to 7 K. *J. Chem. Phys.* **1998**, *109* (10), 3882–3897. <https://doi.org/10.1063/1.476517>.
- (2) Marquette, J.-B. Une Approche Expérimentale de l'astrochimie : La Méthode CRESU, Principe et Applications. These de doctorat, Paris 7, 1988.
- (3) Form Cure time and temperature settings [https://support.formlabs.com/s/article/Form-Cure-Time-and-Temperature-Settings?language=en\\_US](https://support.formlabs.com/s/article/Form-Cure-Time-and-Temperature-Settings?language=en_US) (accessed 2022 -04 -27).
- (4) Messinger, J. P. H. Spectroscopy and Kinetics of Atmospheric and Astrochemical Reactions. 114.
- (5) Felps, W. S.; Rupnik, K.; McGlynn, S. P. Electronic Spectroscopy of the Cyanogen Halides. *J. Phys. Chem.* **1991**, *95* (2), 639–656. <https://doi.org/10.1021/j100155a028>.
- (6) Hays, B. M.; Guillaume, T.; Hearne, T. S.; Cooke, I. R.; Gupta, D.; Abdelkader Khedaoui, O.; Le Picard, S. D.; Sims, I. R. Design and Performance of an E-Band Chirped Pulse Spectrometer for Kinetics Applications: OCS – He Pressure Broadening. *Journal of Quantitative Spectroscopy and Radiative Transfer* **2020**, *250*, 107001. <https://doi.org/10.1016/j.jqsrt.2020.107001>.
- (7) Bird, G. A. *Molecular Gas Dynamics and the Direct Simulation of Gas Flows*; Clarendon Press ; Oxford University Press: Oxford; New York, 1994.
- (8) Kogan, M. N. *Rarefied Gas Dynamics*; Springer, 2013.
- (9) Bird, G. A. Direct Simulation and the Boltzmann Equation. *Phys. Fluids* **1970**, *13* (11), 2676. <https://doi.org/10.1063/1.1692849>.
- (10) Lockerby, D.; Reese, J.; Struchtrup, H. Switching Criteria for Hybrid Rarefied Gas Flow Solvers. *Proceedings of The Royal Society A: Mathematical, Physical and Engineering Sciences* **2009**, *465*, 1581–1598. <https://doi.org/10.1098/rspa.2008.0497>.

## IV. Pressure broadening measurements using the Ka band CP-FTmmW spectrometer

In this chapter we will present the construction and the characterization of a new CP-FTmmW spectrometer operating in the Ka band (26.5-40 GHz) through a series of pressure broadening measurements of multiple species of astrochemical interest. The design phase and the characterization of this instrument was mostly undertaken by Thomas Hearne. The Ka band spectrometer is designed based on the work of Zaleski and coworkers<sup>1</sup> and built in a similar way to the E band spectrometer presented in the previous chapter. The work reported in this chapter has resulted in a publication in 2020, Hearne et al,<sup>2</sup> here we will give more details about the measurements and results with more focus on the themes related to the work in this thesis, specifically the problem of pressure broadening and the assessment of its impact on molecular signal detection. This will show the need to optimize the experimental conditions in order to be able to achieve the ultimate goal of the project, that is to determine the branching ratios of bimolecular reactions at low temperatures.

## Introduction

A novel CP-FTmmW spectrometer operating in the Ka band (26.5 – 40.0 GHz) has been designed, built and characterized. The Ka band spectrometer complements the existing E band spectrometer that has been presented in the last chapter. The Ka band spectrometer has been characterized and benchmarked by conducting room temperature pressure broadening measurements<sup>3,4</sup> in the flow cell on cyanide-containing molecules that, besides their relevance to astrochemistry, have been selected for their strong dipole moment which makes them ideal for rotational spectroscopic measurements.

Vinyl cyanide<sup>5</sup> and benzonitrile<sup>6</sup> are both molecules that have been detected in interstellar space, but relatively little is known about their pressure broadening. Considering that these molecules are potential candidates for reaction products studied by the CPUF technique, the important transitions within the Ka band for the species of vinyl cyanide and benzonitrile have been identified and their FIDs characterized in order to determine their pressure broadening coefficients in helium flows at room temperature. Vinyl cyanide was also studied in a cold, high-pressure CRESU flow. Previous studies of collisional broadening with helium as a perturbing collider with methyl cyanide (CH<sub>3</sub>CN)<sup>7,8</sup>, cyanoacetylene (HC<sub>3</sub>N)<sup>9-12</sup>, and hydrogen cyanide (HCN)<sup>13-15</sup> are used as a comparison with the pressure broadening results presented in this chapter.

### IV.1. Ka band Spectrometer

In designing the spectrometer, priority was given to phase-stability and the signal-to-noise ratio (SNR), utilizing the latest technology available. The design was based upon the Ka band spectrometer detailed in Zaleski *et al.*<sup>1</sup> Figure IV-1 shows the configuration of the Ka band spectrometer used for the measurements in this work.

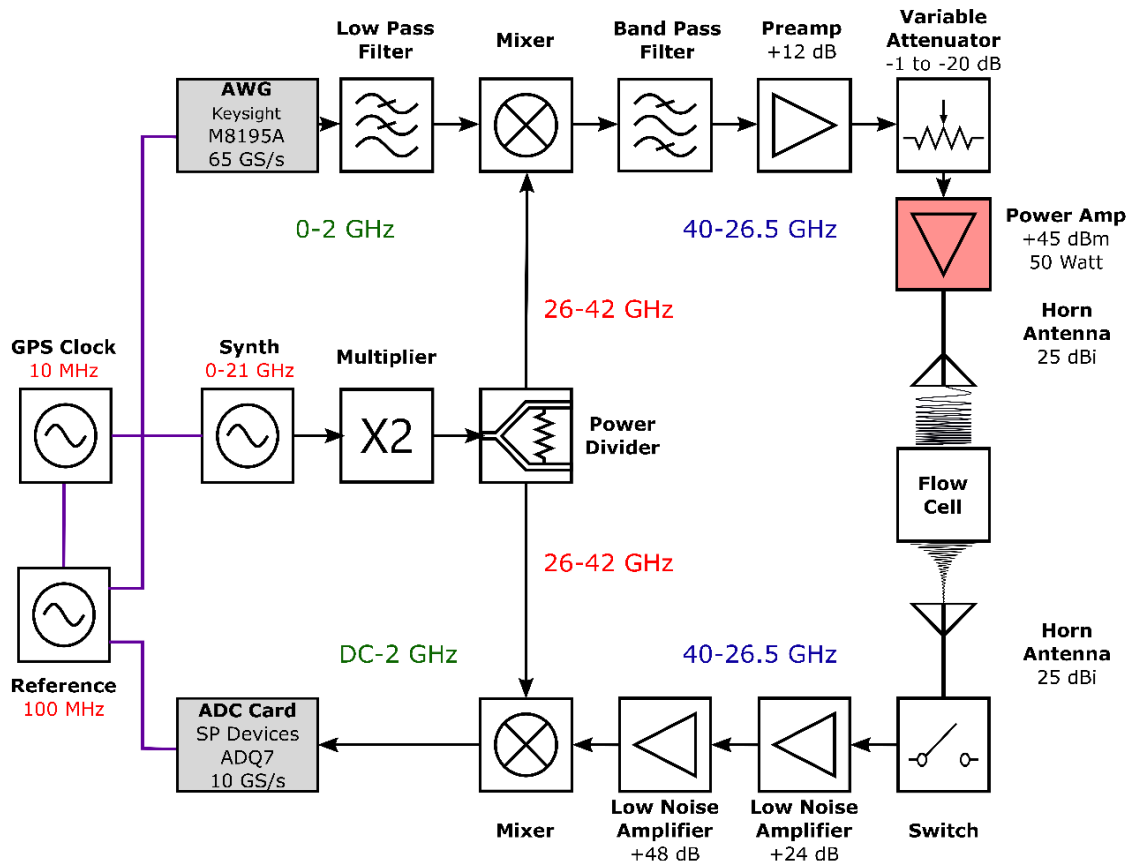


**Figure IV-1. Configuration of the Ka band spectrometer (Design credit to Thomas Hearne)**

Similar to the E band, the signal buildup begins with chirped pulses generated by the Keysight arbitrary waveform generator (AWG – M8195A) from 1-16 GHz.<sup>16</sup> The chirped pulses are up-converted to the Ka band through a Marki double-balanced mixer (MM1-1850H), using a 0.5-21 GHz Signal Core synthesizer (SC1150A), after doubling in a Marki frequency doubler (ADA-1020), to provide an LO tunable within the range of 26-42 GHz. The upconverted pulse passes through an RF-Lambda preamplifier (R24G40GSC) and a variable attenuator (RLC AV-26540) for careful level matching to the power amplifier. The power amplifier is a 50 W solid state broadband amplifier manufactured by Meuro (MPH260400G4547R), its output of is coupled to a 25 dBi gain horn antenna (Sage SAR-2507-28-S2), which directs radiation through a Teflon window into the cell, containing the species of interest.<sup>17</sup> The interior of the vacuum chamber is lined with microwave-absorbent material (Laird Eccosorb HR-10) in order to dampen reflections of the excitation pulse within the cell.

At the opposite end of the flow chamber, radiation exits through another Teflon window, before it is received by a second 25 dBi rectangular horn. The signal then passes through a waveguide variable attenuator (Sage STA-30-28-M2) which is used to protect the receiver circuit when testing the switch timings. The switch itself (Millitech PSP-28-SIAHF) is immediately behind the attenuator, it has a rise time of 70 ns and isolates from 40-50 dB across the Ka band. The switch is precisely timed to absorb signal when the high-power excitation pulse is active, and to pass signal immediately after the end of the pulse, to allow the FID to proceed to the LNA stage. After the switch, the signal is amplified by two cascaded, coaxial Ka band LNAs (RF-Lambda R24G40GSB, Miteq LNA-40-26004000-35-15P) with a combined gain of 64 dB and a combined noise figure of 2.01 dB. The amplified signal is downconverted through an identical Marki mixer to the upconversion stage, using the same LO source for the frequency upconversion generated from synthesizer passing through the power divider. The intermediate frequency (IF) from the mixer is then collected by a fast digitizer card for data acquisition, the same SP-Devices (ADQ7) card at 10 GS/s as used for the E band spectrometer. Same 10 MHz and 100 MHz timing signals as the E band spectrometer are used to ensure phase stability, the AWG and the oscilloscope are all locked to this 100 MHz signal. The 2 marker channels from the AWG are used to trigger the recording ADC card to trigger the acquisition, and the digital delay generator (DDG – BNC 575), locked to the 10 MHz clock signal, which triggers the receiver-side switch and the amplifier. The spectrometer was designed so that the same LO source is used for both the upconversion and downconversion stages which eliminates any phase-noise introduced by the LO source.

#### **IV.1.1. Instrument response**

##### **IV.1.1.1. Broadcast side**

The oscilloscope (Tektronix DPO 71604C, 16 GHz of analog bandwidth ) was used to measure the instrument response across the band instead of the digitizer for its ability to provide larger bandwidths, this comes at cost of the recording speed (30 Hz instead of the 30 KHz with the digitizer) which makes it less well suited for measurements requiring lot of averaging. A chirped pulse between 25.4 to 40.6 GHz over a time of 1  $\mu$ s is recorded after having been upconverted from a 0-15 GHz chirp mixed with a doubled LO of 40.2 GHz generated from the synthesizer, amplified and emitted then

downconverted and displayed on the oscilloscope. The two LNAs have been removed while recording the chirp. Figure IV-2 shows a spectrogram of the recorded chirp and the time domain signal

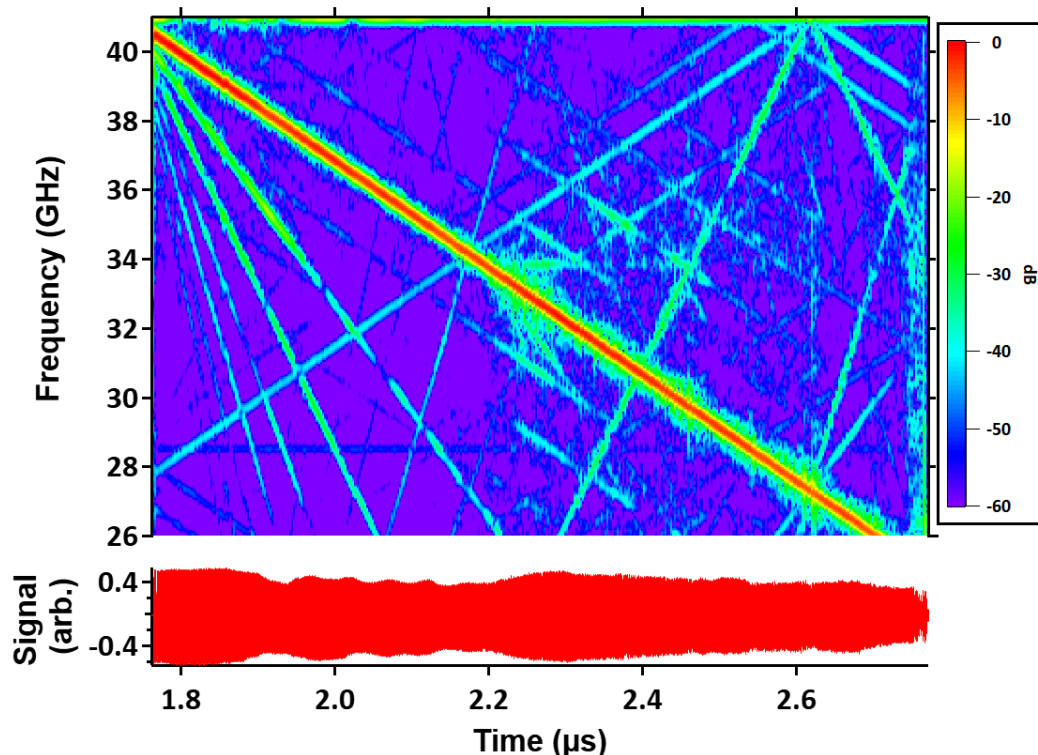


**Figure IV-2. Upper panel shows a spectrogram of a 15 GHz chirp recorded across the Ka band, the strongest intensity corresponds to 0 dB, lower panel shows the recorded chirp.**

The spectrogram shows a relatively flat response across the range of the instrument, the power loss measured between the most intense frequency (34.85 GHz) and the weakest frequency (26.5 GHz) is 5.5 dB. The spectrogram shows also the appearance of harmonics from the main frequencies of the chirps, most of these harmonics however are below -25 dB which makes their effect on the signal very low. The instrument response across the broadcast side was further investigated by measuring the electric field generated by the spectrometer.

The strength of the electrical field is determined via measuring the change of the molecular signal intensity of the FFT of the FID of a transition against the duration of the excitation pulse.<sup>18</sup> This produces an oscillating plot known as the Rabi cycle, defined by the following formula:

$$S \propto e^{-\frac{t_p}{T_2}} |\sin(\omega_r t_p)| \quad \text{Equation IV-1}$$

Where  $\omega_r$  is the Rabi frequency,  $t_p$  is the length of the pulse, and  $T_2$  represents the decay time of the FID. The frequency of the cycle depends only on the transition dipole moment and the electric field strength in the relation:

$$\omega_r = \frac{\mu_{ij}\mathcal{E}(\omega)}{\hbar} \quad \text{Equation IV-2}$$

Where  $\mu_{ij}$  is the transition dipole moment,  $\hbar$  is the reduced Planck's constant, and  $\mathcal{E}(\omega)$  is the electric field strength at the transition frequency. The transition dipole moments were extracted from the CDMS by dividing the square-root of the line strength factor ( $S_{ij}$ ) by the square-root of the lower state degeneracy ( $g''$ ) and multiplying this value by the dipole moment along the molecular axis ( $\mu_x$ ).

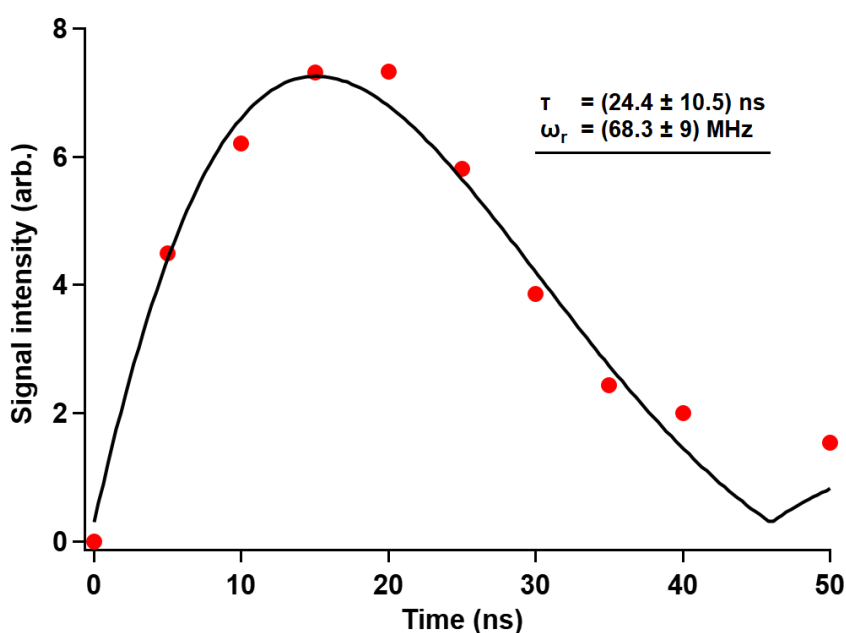


**Figure IV-3.** The intensity of the  $J_{ka,kc} = 4_{0,4}-3_{0,3}$  transition of vinyl cyanide plot as a function of excitation duration. Excitation pulses are a single-frequency resonant with the transition energy. The fitting parameters  $\tau$  and  $\omega_r$  are determined by a least-squares fit of the Rabi cycle formula to the experimental data. The uncertainties given are the 95% confidence intervals for the fit.

Table IV-1 shows the electric field strength determined experimentally by targeting the  $J_{ka,kc} = 4_{0,4}-3_{0,3}$  vinyl cyanide transition and with the expected value taking into account the amplifier power, horn gain and free-space loss but neglecting loss from the window and any other extra attenuating factors. The free space loss is determined via the following equation:

$$FSPL = 20 \log_{10}(d) + 20 \log_{10}(f) + 20 \log_{10}\left(\frac{4\pi}{c}\right) - G_t - G_r \quad \text{Equation IV-3}$$

Where  $d$  is the distance between the antennas,  $f$  is the transition frequency  $G_t$  and  $G_r$  are the gain of the transmitting antenna and the receiving antenna respectively and  $c$  is the speed of light in vacuum.

The theoretical electric field is calculated using the following equation:

$$Ave = \frac{1}{x_2 - x_1} \int_{x_1}^{x_2} \frac{\sqrt{30 P 10^{G_t/10}}}{x} dx \quad \text{Equation IV-4}$$

Where  $x_1$  is the distance of the start of the flow cell from the antenna,  $x_2$  is the distance of the end of the flow cell from the antenna,  $P$  is the power of the broadcast amplifier in Watts, and  $G_t$  is the gain of the broadcast antenna. There is a distance of 0.25 m from the output of the amplifier to the start of the molecular sample; the calculation neglects any loss from the cell window.

**Table IV-1. The electrical field strength within the flow cell**

| Method of determination  | Electric Field Strength (V/m) |
|--------------------------|-------------------------------|
| Vinyl cyanide Rabi cycle | $778 \pm 86$                  |
| Theoretical              | 893                           |

#### IV.1.1.2. Receiver side

Similarly, to the broadcaster side, the oscilloscope was used to record a chirp covering the Ka band in order to investigate the instrument response of the receiver side, this time with the LNAs mounted. A 15 GHz chirp from 0.5 to 15.5 GHz was mixed with two doubled LO frequencies at 26 GHz and 40.2 GHz. The resulting chirps are illustrated by Figure IV-4, the two spectrograms of the recording chirps also show the harmonic and the spurious content as a function of spectrometer frequency.

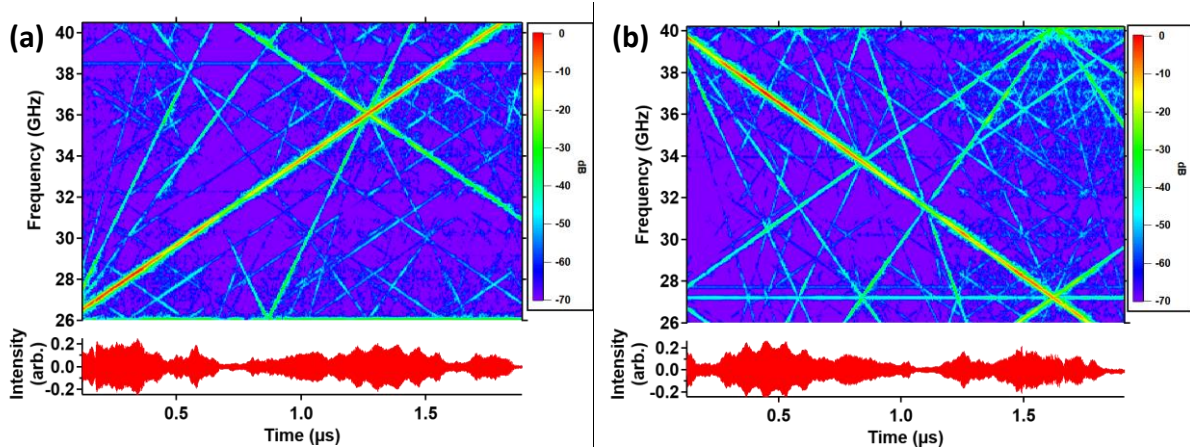


**Figure IV-4. Spectrograms of a 15 GHz bandwidth chirp mixed with an LO of 26 GHz (a) and with an LO of 40.2 GHz (b) across the Ka band, the strongest intensity corresponds to 0 dB.**

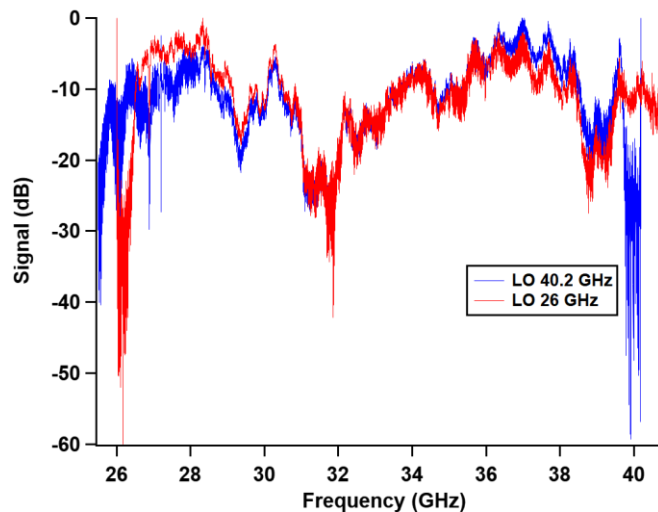


**Figure IV-5. Power loss in a 15 GHz chirp mixed with an LO of 26 GHz (red) and with an LO of 40.2 GHz (blue).**

Both LOs selected have the same response across the Ka range with strong decays at the edges of the band which makes the 40.2 GHz LO suited for targeting high frequency transitions in the Ka band while the 26 GHz LO is more efficient for lower frequencies. The results also demonstrate that the effective range of the spectrometer can be extended down to 26 GHz up 40.5 in the GHz which provides a 1 GHz in addition to the design (26.5-40 GHz).

The response at different frequencies varies across the spectral range and the recorded signal shows strong attenuations of more than 10 dB around 29 GHz frequency and across 31-32 GHz and 38.5-39.5 GHz regions. This is probably caused by the addition of the LNAs that each has a varying response and may cause

attenuations across the band (see Appendix A.IV). The power in the regions expressing poor response can be boosted by adjusting the output power of the preamplifier, this of course come at cost of further attenuations in other regions but in most of the measurements, we use  $\pi/2$  single or multi frequency pulses and short ranged chirps, thus careful tuning of the spectrometer can be used to obtain optimal response at each frequency.

### IV.1.2. Averaging

The importance of the clock in frequency phase stability is most important during averaging processes. A single frequency pulse targeting the  $J_{ka,kc} = 4_{0,4} - 3_{0,3}$  transition of vinyl cyanide at 37.9048 GHz was used to investigate phase stability, Figure IV-6 shows the attenuation of the random noise and the improvement of the SNR by averaging from 25000 to 5 million scans.

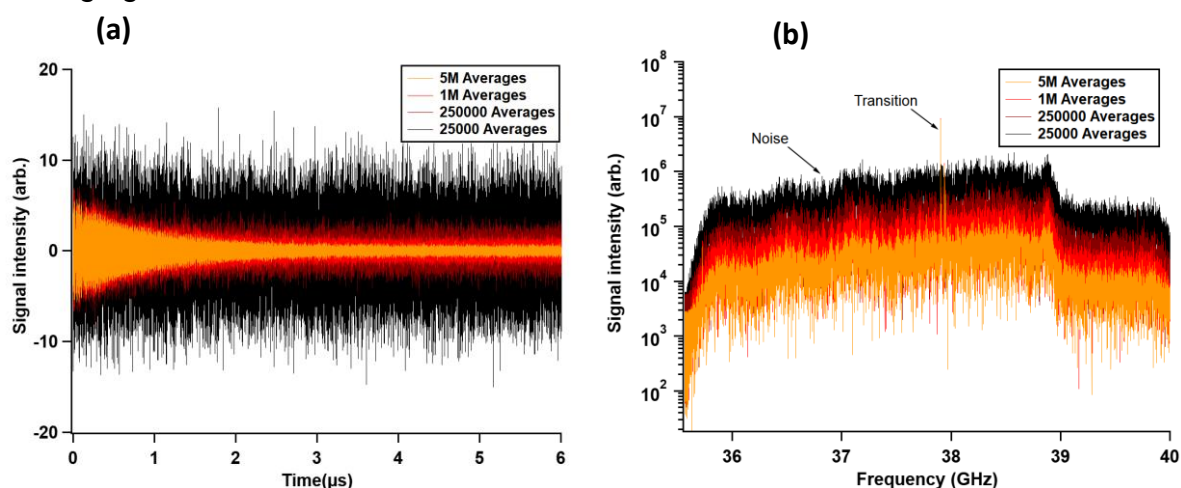


**Figure IV-6. Improvement of the SNR with averaging a molecular signal from 25000 to 5 millions, figure (a) shows the recorded FIDs and figure (b) shows their corresponding Fourier transforms.**

Extensive averaging tests were also performed to ensure the expected SNR gain with increasing number of averages, Figure IV-7 shows the improvement rate of the SNR by averaging up to 6 million scans.

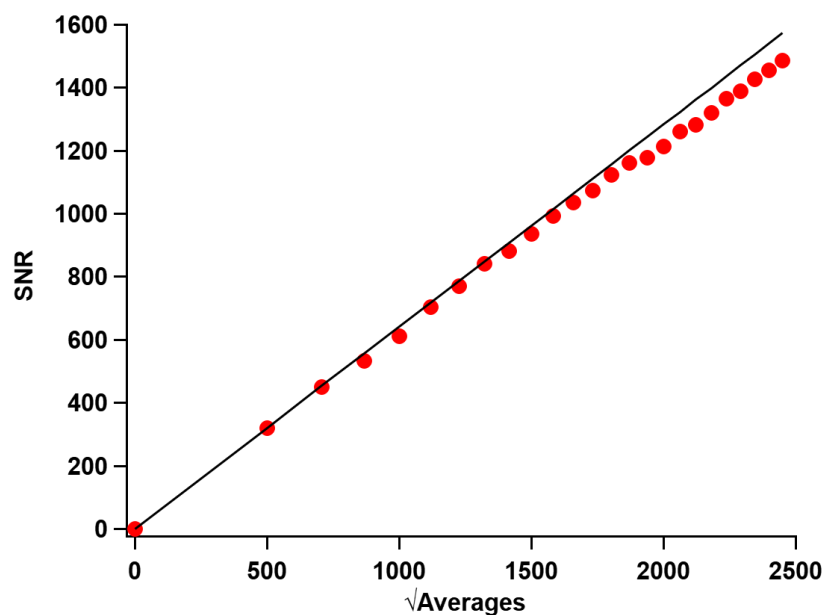


**Figure IV-7. Plot of the SNR given by the Ka band chirped pulse Fourier transform spectrometer against the square root of the number averages taken for a given signal. The black line shows ideal theoretical performance.**

At 6 million averages, there is a loss of about 6% of the expected signal given perfect phase-coherence most of the experiments presented in this work are performed between 10,000 to 100,000 averages, the maximum equivalent of 16 minutes in acquisition time with 100 Hz repetition rate which is the maximum excimer laser frequency. With these averaging values there are no significant losses and for measurements requiring more averaging, it is better to conduct multiple 100,000 averaged scans to avoid additional losses coming from the flow variations and laser output power instability along long scans, photolysis and bimolecular reactions results will be shown in the next chapter.

### IV.1.3. Filtering

Filtering is very important in the post processing data analysis procedure, raw FIDs sampled with digitizer card are encumbered with noise, spurs and harmonics (see Figure IV-2 and Figure IV-4) the most significant is the one introduced by the digitizer at 2.5 GHz in addition to 100 MHz and 10 MHz, these three spurs come from clock inputs whereas another 5 GHz spur appears as a results of a slight DC offset produced from the interleaving of the two analog to digital converters (ADCs). These undesirable signal components are efficiently removed from the resulting spectrum by using a correlation filter, built from the final part of the acquisition after the FID has decayed

away. This is then subtracted from the FID (see Figure IV-8). More details can be found in Theo Guillaume's thesis on the experimental procedure in the description of the E band spectrometer.

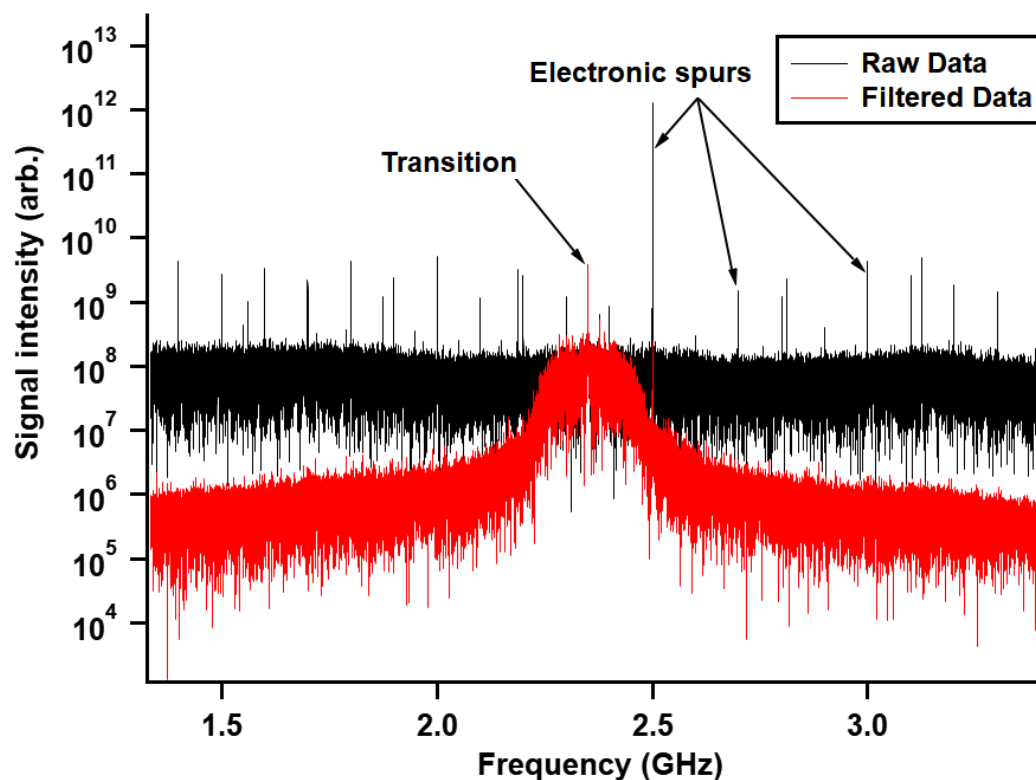


**Figure IV-8. Comparison between filtered (in red) and raw spectrum (in black) recorded with the Ka band targeting the  $J_{ka,kc} = 3_{12} - 2_{11}$  rotational transition of vinyl cyanide at room temperature and 11  $\mu$ bar.**

## IV.2. Pressure broadening measurements

As explained previously, pressure broadening is a serious limitation that can jeopardize the detection of microwave signals in high density media like CRESU, for collisions, specifically the ones between the radiator and the perturbing buffer, can reduce the relaxation time of population, and can even lead to emission-free relaxations. A study work was led by Brian Hays to measure the pressure broadening of OCS in a helium bath using the E band spectrometer, the broadening rate of OCS was determined at room temperature at a range of pressures from 0.005 mbar to 0.32 mbar. In this work the recorded OCS FIDs show an increasing attenuation of the molecular signal under the effect of collision induced by the increasing pressures of the buffer in the flow (see

Figure IV-9). More details can be found in the published paper of Hays et al<sup>17</sup> and the thesis of Theo Guillaume.

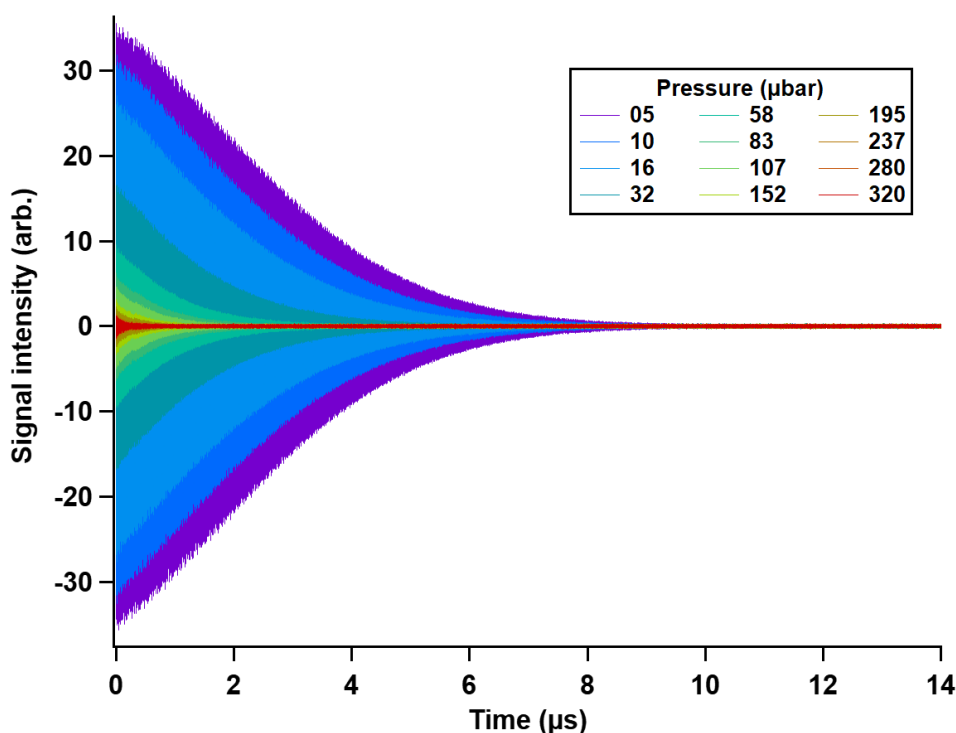


**Figure IV-9.** Recorded FIDs of the the  $J = 6-5$  transition of OCS in the flow cell at room temperature, the partial pressure is maintained at  $5 \times 10^{-5}$  mbar with the helium pressure is increased in the cell for every measurement. Figure adapted from Hays et al<sup>17</sup>

#### IV.2.1. Vinyl cyanide in the cell

In a similar way to the E band study of OCS-He pressure broadening, a series of measurements were carried out in the flow cell in order to determine the pressure broadening rates<sup>19,20</sup> in a mixture of vinyl cyanide and helium. 14 mbar of vinyl cyanide is mixed with 1.48 bar of He (0.95 % by pressure) in a gas cylinder and used for these experiments. The vinyl cyanide was subjected to multiple freeze-pump-thaw cycles before each use. The 0.95% vinyl cyanide/helium mixture was flowed into the cell along with additional helium to vary the pressure within the cell while the vinyl cyanide partial pressure remains constant. All flow cell experiments were performed at room temperature.

Two different transitions of vinyl cyanide were targeted for pressure broadening measurements  $J_{ka,kc} = 4_{1,3} - 3_{1,2}$  and  $J_{ka,kc} = 3_{1,2} - 2_{1,1}$ . A fixed flow of the vinyl

cyanide/helium mixture was introduced into the flow cell, the FIDs over a range of increasing pressures corresponding to increasing flow rates of pure helium were recorded from the excitation of these transitions with 200 MHz chirps then Fourier transformed giving the frequency domain signals.

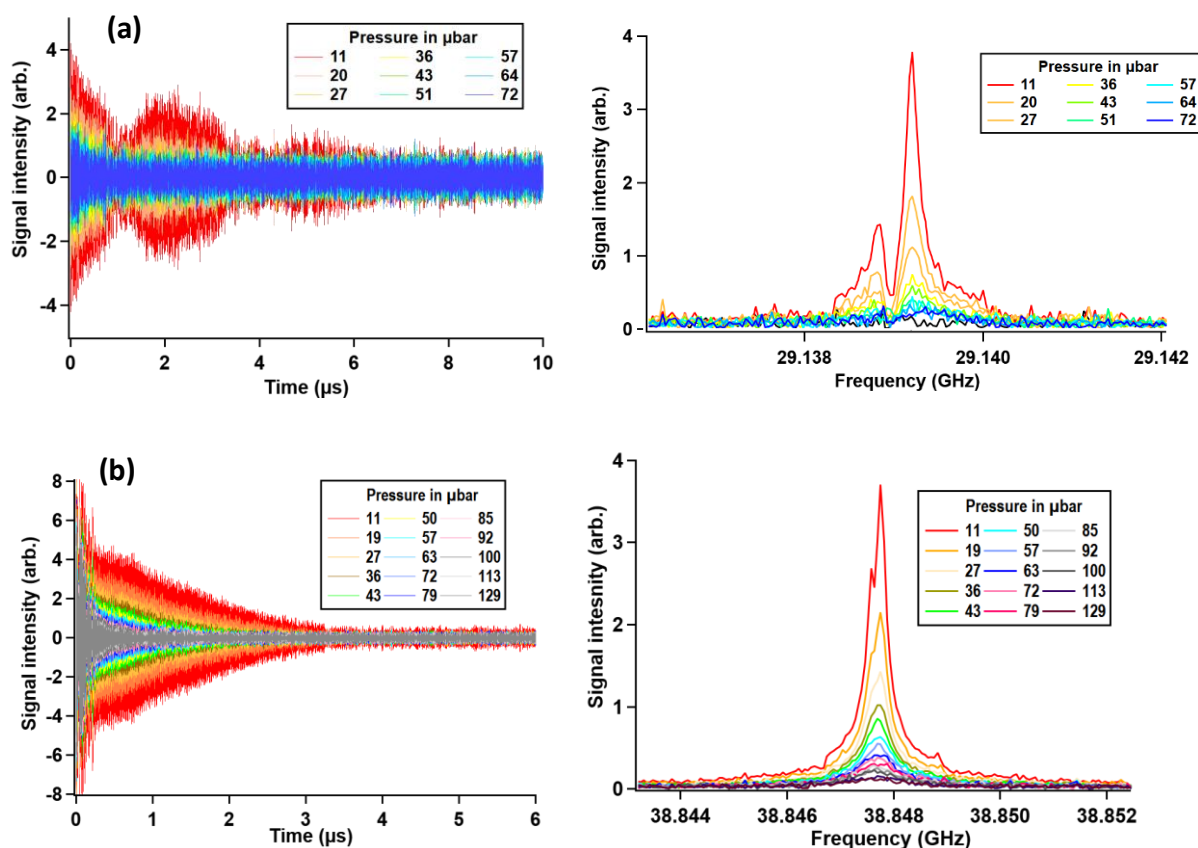


**Figure IV-10. Recorded FIDs and corresponding FFTs showing (a) the  $J_{ka,kc} = 3_{1,2} - 2_{1,1}$  and (b) the  $J_{ka,kc} = 4_{1,3} - 3_{1,2}$  transitions of vinyl cyanide with increasing helium pressure in the flow cell at room temperature.**

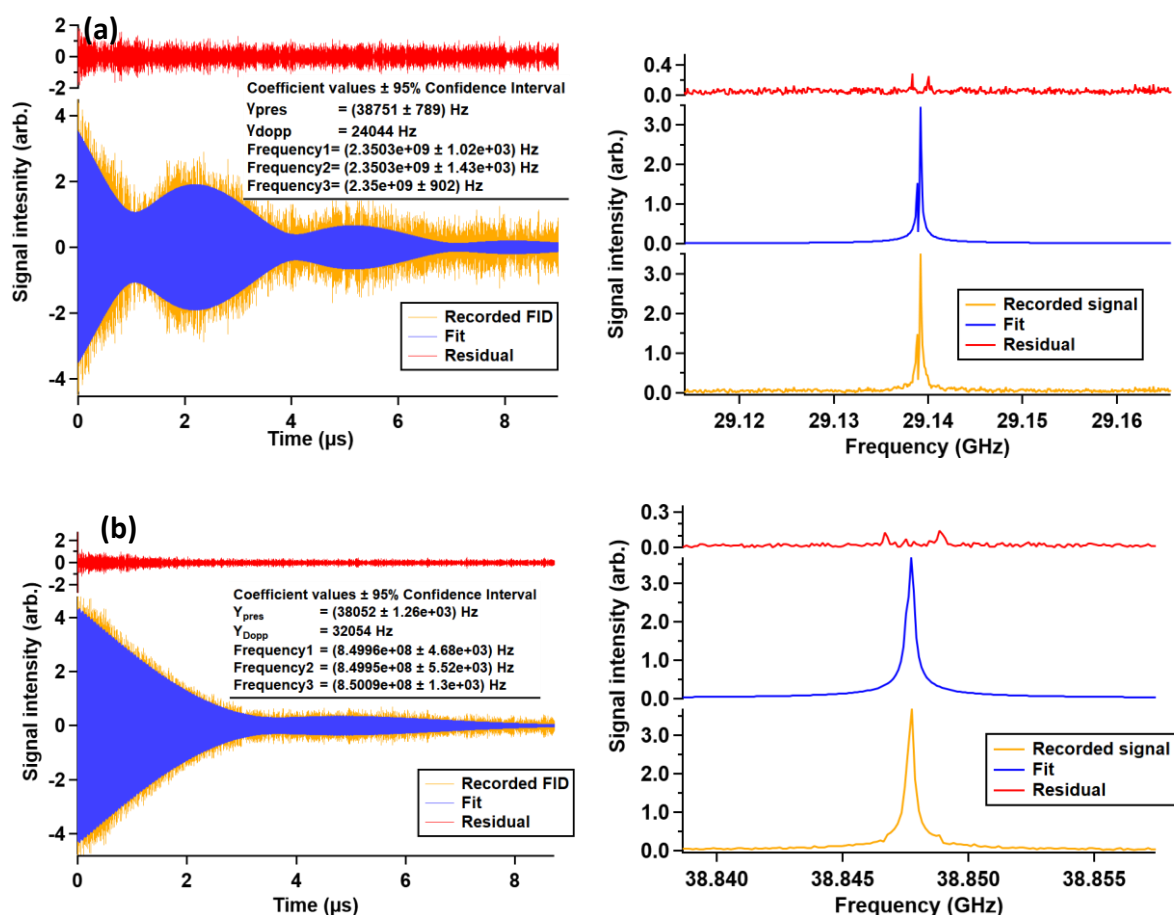
Figure IV-10 shows that pressure has a significant impact on the molecular signal, the magnitude and the duration of the FID are quenched and the spectra of transitions get weaker and broader with increasing pressure leading to a poor resolution, hyper fine splitting and weak congested lines do not appear any more, further increase of pressure (more than 72  $\mu\text{bar}$ ) makes the detection of the transition not possible.

The recorded FIDs were then fitted to a multiple frequency Voigt profile in the time domain<sup>17</sup> given by Equation II.53, while Doppler broadening was maintained constant along the pressure range, its value is given at the half width half max deduced from Equation II.48;

$$\Delta\gamma_{Dopp_{HWHM}} = f_0 \sqrt{\frac{2kT \ln 2}{mc^2}} \quad \text{Equation IV-5}$$

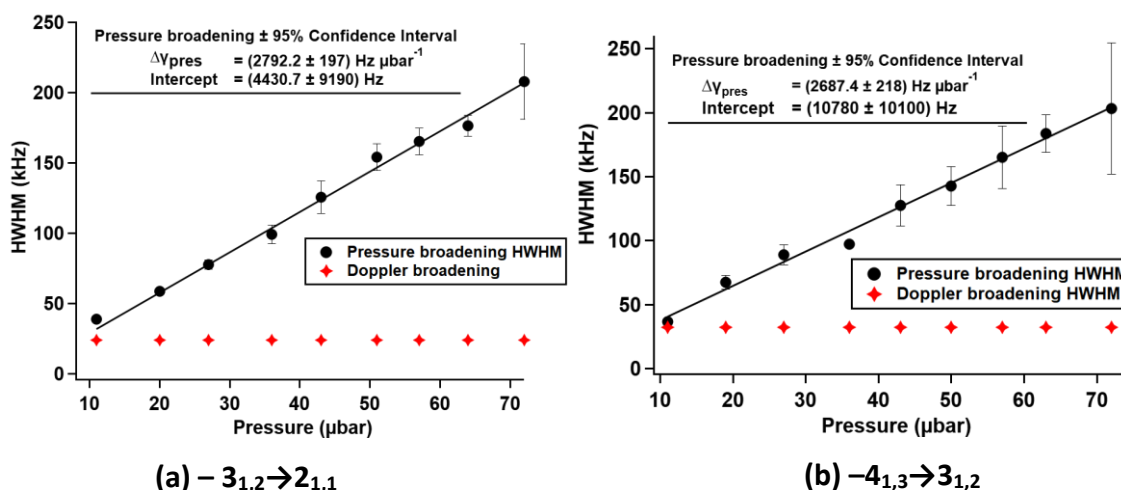
where  $\Delta\gamma_{Dopp_{HWHM}}$  is the Doppler broadening rate half width at half max and  $f_0$  is the frequency of transition.

Conducting a multiple frequency fit in the time domain is privileged over the frequency domain considering the hyperfine splitting of rotational lines which makes the frequency domain fitting not straightforward, the results are shown in Figure IV-11.



**Figure IV-11. Time domain Voigt profile fit of (a) the  $J_{ka,kc} = 3_{1,2} - 2_{1,1}$  and (b) the  $J_{ka,kc} = 4_{1,3} - 3_{1,2}$  transitions of vinyl cyanide at 11  $\mu$ bar, in the left are the fits of the recorded FIDs and the residual, and on the right their give their corresponding FFTs.**

The pressure broadening coefficient is given by the slope of the linear regression from the plot of the fitted Voigt HWHM against their respective pressures as shown in Figure IV-12.



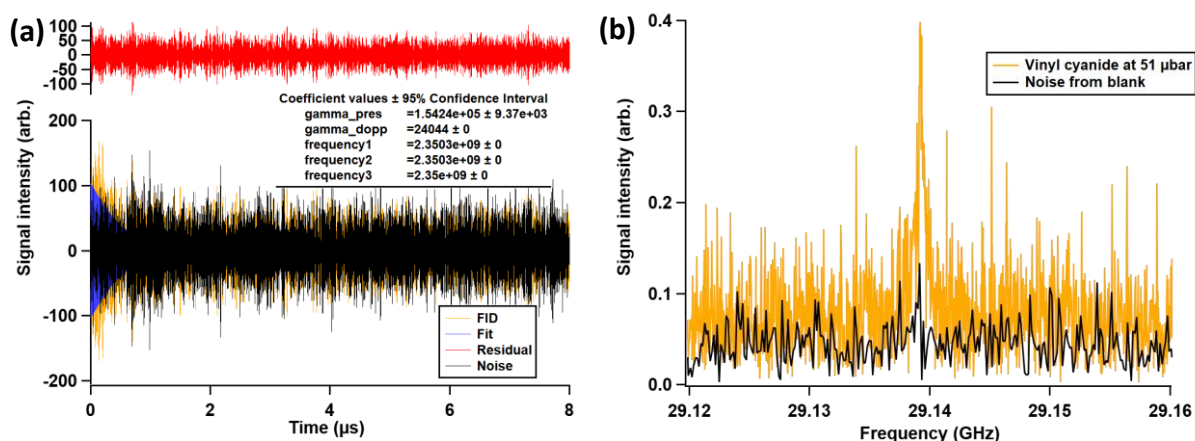
**Figure IV-12.** Plots of the HWHM of the Lorentzian component of the Voigt profile fit to FIDs of two different transitions of vinyl cyanide at different pressures, using the time domain Voigt fitting. Part (a) shows the pressure broadening of the  $3_{1,2} \rightarrow 2_{1,1}$  transition, part (b) shows the broadening of the  $4_{1,3} \rightarrow 3_{1,2}$  transition. Uncertainties are taken as the 95% confidence interval for the linear fit.

Table IV-2 displays the pressure broadening rates that were determined for the two transitions of vinyl cyanide.

**Table IV-2.** Pressure broadening coefficients for collisions with helium of different transitions of vinyl cyanide as determined to pressure broadening data.

| Rotational transition ( $J, k_a k_c$ ) | Frequency (MHz) | $\Delta\nu_{\text{pres}}$ (MHz mbar $^{-1}$ ) |
|--|-----------------|---|
| $3_{1,2} - 2_{1,1}$                    | 29139.1         | $2.79 \pm 0.20$                               |
| $4_{1,3} - 3_{1,2}$                    | 38847.7         | $2.69 \pm 0.22$                               |

At higher pressures, the FIDs are attenuated very quickly, in less than 1  $\mu\text{s}$ , the frequency domain signal is also heavily affected, at 51  $\mu\text{bar}$  which is about half of the pressure in the CRESU environment the SNR of vinyl cyanide is 2. Although temperatures under CRESU conditions are lower and the geometrical loss should be less, the pressure impact on the signal remains. Figure IV-13 shows the vinyl cyanide signal of  $J_{k_a, k_c} = 3_{1,2} - 2_{1,1}$  transition at 51  $\mu\text{bar}$  in the time and the frequency domain exhibiting a massive attenuation under the effect of pressure compared to same transition under 11  $\mu\text{bar}$  (see Figure IV-11 (b)).



**Figure IV-13.** Time domain Voigt profile fit of the  $J_{ka,kc} = 3_{1,2}-2_{1,1}$  transition of vinyl cyanide at 51  $\mu\text{bar}$  (a) shows the fit of the recorded FID and the residual, figure (b) gives the corresponding FFTs.

## IV.2.2. CRESU measurements

The Ka band spectrometer was then mounted on the CRESU chamber to conduct low temperature measurements,<sup>21,22,23</sup> the mounting system is similar to the one presented for the E band spectrometer in chapter III. Multiple vinyl cyanide transitions have been detected under the CRESU conditions using 10 ns single frequency pulses in the helium flow at 18.7 K.

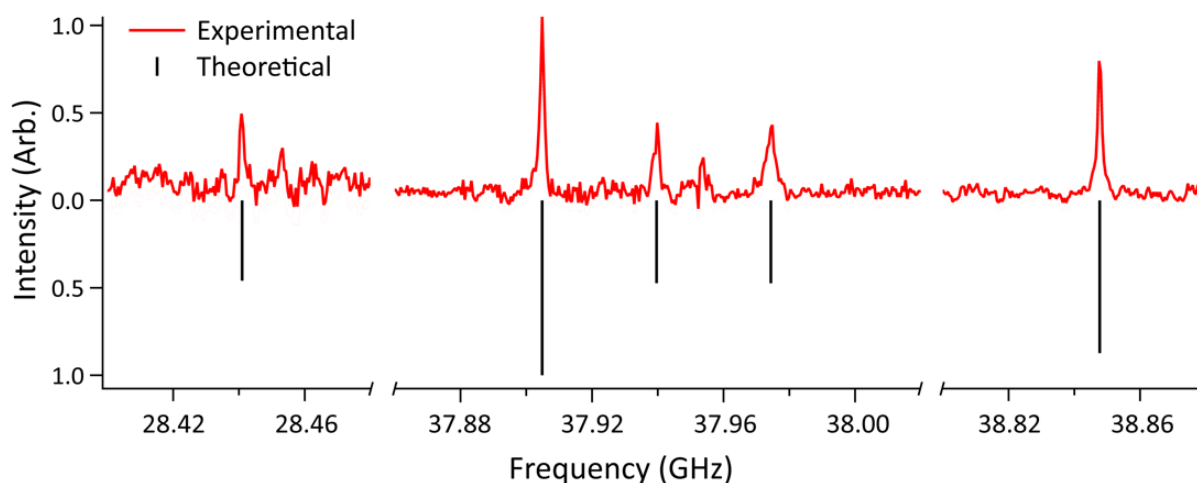


**Figure IV-14.** Rotational spectrum of vinyl cyanide in a cold CRESU flow of 18.7 K recorded using a Ka band CP-FTmmW spectrometer. Each section of the spectrum was probed individually. The spectrum displayed is the magnitude of the Fourier transform of the recorded signals, normalized to the most intense peak. The experimental spectrum is compared to theoretical transition frequencies and intensities at 18.75 K taken from the CDMS.<sup>24,25</sup>

As explained in chapter II and confirmed by OCS and vinyl cyanide pressure broadening measurements, the decay constant  $T_2$  representing the loss of coherence in a polarized system and related to the pressure broadening rate by  $T_2 = 1/2\pi \gamma_{pres} p$  highlights the role of pressure and demonstrates that high pressure flows are ill-suited for microwave signal detection.<sup>3,26,27</sup> On the other hand, there are other parameters affecting the collisions rather than pressure, the frequency collision equation suggests that the effect of pressure should be considerable for bigger molecules with larger collisional cross sections. Although heavier molecules induce less collisions, the collision cross section weighs more than the molecular mass and therefore the loss on the signal should be much higher in this case. To put this theory into test, benzonitrile was a perfect candidate for those measurements, a large molecule that have been detected in interstellar space, but little is known about its pressure broadening behavior.

### **IV.2.3. Benzonitrile in the cell**

A mixture of 1.3 mbar of benzonitrile with 0.15 bar of helium (0.87 % by pressure) were used for these experiments, benzonitrile has many transitions within the range of the Ka band spectrometer, which complicates the determination of pressure-broadening parameters. The lack of intensity and the presence of many lines within a single record, even for single-frequency pulses, meant that time-domain fitting was infeasible. However, since most transitions are well separated in frequency, adequate fitting was able to be achieved in the frequency domain. The hyperfine contributions were neglected in this fit as the widths of the peaks were much larger than the splittings for each transition. The pressure broadening rates measured at each pressure are given for the different J-levels in Figure IV-15. Table IV-3 shows the resulting pressure broadening coefficients from the linear fits of two transitions of benzonitrile in collisions with helium.

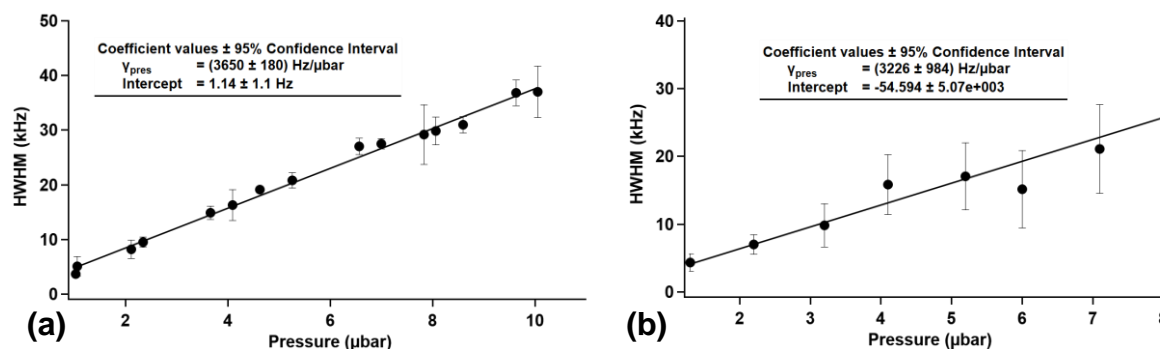


Figure IV-15. Plot of the HWHM of the Lorentzian component of the Voigt profile fit to the Fourier transform of the FID of the  $J_{ka,kc} = 15_{2,14} - 14_{2,13}$  (a) and  $J_{ka,kc} = 14_{0,14} - 13_{0,13}$  (b) transitions of benzonitrile. The equations of the linear fit to the data are given with 95% confidence interval.

Table IV-3. Pressure broadening coefficients for various transitions of benzonitrile with two different collisional systems.

| Transition ( $J_{ka,kc}$ )              | Frequency (MHz) | $\Delta\gamma_{pres}$ (MHz mbar <sup>-1</sup> ) |
|---|-----------------|---|
| 14 <sub>0,14</sub> - 13 <sub>0,13</sub> | 35249.2         | 3.23 ± 0.98                                     |
| 15 <sub>2,14</sub> - 14 <sub>2,13</sub> | 39897.9         | 3.65 ± 0.18                                     |

A comparison of the pressure broadening constants of multiple size cyanide-containing molecules involving this work was carried out the results are shown in Table IV-4.

Table IV-4. Pressure broadening rates for related molecules for a range of different transitions with He as the collider.

| Species (transition)  | $\Delta\gamma_{pres}$ (MHz mbar <sup>-1</sup> ) |
|---|---|
| HCN ( $J=1-0$ )* <sup>14</sup>  | 1.51 ± 0.02                                     |
| CH <sub>3</sub> CN ( $J=0-1$ $K=0$ , $J=1-2$ $K=\pm 1$ )* <sup>7</sup>                    | 2.57 ± 0.03, 2.70 ± 0.02                        |
| HC <sub>3</sub> N ( $J=3-2$ )* <sup>10</sup>  | 3.1 ± 0.1                                       |
| CH <sub>2</sub> CHCN ( $J_{ka,kc}=3_{1,3}-2_{1,2}$ , $J=4_{1,3}-3_{1,2}$ )* <sup>**</sup> | 2.79 ± 0.20, 2.69 ± 0.22                        |
| C <sub>6</sub> H <sub>5</sub> CN ( $J_{ka,kc}=15_{2,14}-14_{2,13}$ )* <sup>**</sup>       | 3.65 ± 0.18                                     |

\*From reference

\*\*From this work

The results fit a general trend of increasing pressure broadening rates with increasing molecular size. The constants for the transitions of vinyl cyanide are similar to cyanoacetylene ( $\text{HC}_3\text{N}$ ), which would be expected given the similarity in size and composition of the two molecules. Looking towards heavier molecules, which are of interest to the CRESUCHIRP project using the Ka band spectrometer, a significant increase in pressure broadening for benzonitrile compared to the smaller molecules is observed. The concern for studying such a molecule in an environment such as a CRESU flow is the increase in pressure broadening at lower temperatures. For the related molecule fluorobenzene, Patterson and Doyle determined the collisional cross section with helium to be  $2.8 \cdot 10^{-14} \text{ cm}^2$  at 8 K for the  $J_{k_a, k_c} = 2_{1,1}-3_{1,2}$  transition, which corresponds to a pressure broadening constant of  $86 \text{ MHz mbar}^{-1}$ .<sup>28</sup> This value is at least 3 times greater than the pressure broadening rate for vinyl cyanide, implying that benzonitrile would be extremely difficult to detect in a high-pressure CRESU flow.

An observation for the pressure broadening data for all molecules is a small non-zero intercept for the linear fit. This suggests that there is some other source of broadening for the species besides collisions with helium and Doppler broadening. For example, wall-collisions may give a small contribution to the broadening of the transitions, although in this case this effect is most likely negligible. Also, self-collisions between species of interest would contribute a small, fixed amount to pressure broadening, as would any background water or air within the flow cell although the background pressure in the cell is normally around  $10^{-3} \text{ } \mu\text{bar}$ , so collisions with background species such as water and nitrogen are likely to be negligible. Since these effects are relatively small compared to helium collisions and are fixed for experiments varying helium pressure, they should not influence the pressure broadening constant. Furthermore, non-Voigt effects such as Dicke-narrowing and the speed-dependence of collisions<sup>29,30</sup> are likely to be small in the case of a collision between a heavy species and helium, and unobservable given the sensitivity of this experiment.

### IV.3. Discussions and other limitations

Pressure broadening data with a helium collider were also determined for different transitions vinyl cyanide and benzonitrile in the Ka band to investigate the variation of pressure broadening with the J-level. The data did not show much variation between the different transitions of the molecules studied over this frequency range, but higher precision experiments may show the expected inverse dependence on J-level.

**Table IV-5. Pressure broadening coefficients for collisions with He of different transitions of vinyl cyanide as determined through different methods. Uncertainties are taken as the 95% confidence interval for the linear fit to pressure broadening data.**

| Vibrational level       | Transition quantum numbers ( $J_{Ka,Kc}$ ) | Frequency (MHz) | $\gamma_{pres}$ (MHz mbar <sup>-1</sup> ) |
|-------------------------|--|-----------------|---|
| <b>v=0</b>              | 3 <sub>1,3</sub> -2 <sub>1,2</sub>         | 27767.4         | 3.03 ± 0.19                               |
| <b>v=0</b>              | 3 <sub>0,3</sub> -2 <sub>0,2</sub>         | 28441.0         | 3.30 ± 0.34                               |
| <b>v=0</b>              | 3 <sub>2,2</sub> -2 <sub>2,1</sub>         | 28456.9         | 3.37 ± 0.21                               |
| <b>v=0</b>              | 3 <sub>2,1</sub> -2 <sub>2,0</sub>         | 28470.8         | 2.87 ± 0.27                               |
| <b>v=0</b>              | 3 <sub>1,2</sub> -2 <sub>1,1</sub>         | 29139.1         | 2.81 ± 0.17                               |
| <b>v<sub>11</sub>=1</b> | 3 <sub>1,3</sub> -2 <sub>1,2</sub>         | 27833.2         | 2.76 ± 0.41                               |
| <b>v<sub>11</sub>=1</b> | 3 <sub>1,2</sub> -2 <sub>1,1</sub>         | 29239.2         | 3.13 ± 0.31                               |
| <b>v=0</b>              | 4 <sub>1,4</sub> -3 <sub>1,3</sub>         | 37018.9         | 2.99 ± 0.20                               |
| <b>v=0</b>              | 4 <sub>0,4</sub> -3 <sub>0,3</sub>         | 37904.8         | 2.94 ± 0.10                               |
| <b>v=0</b>              | 4 <sub>2,3</sub> -3 <sub>2,2</sub>         | 37939.6         | 3.10 ± 0.06                               |
| <b>v=0</b>              | 4 <sub>2,2</sub> -3 <sub>2,1</sub>         | 37974.4         | 3.22 ± 0.06                               |
| <b>v=0</b>              | 4 <sub>1,3</sub> -3 <sub>1,2</sub>         | 38847.7         | 3.05 ± 0.15                               |
| <b>v<sub>11</sub>=1</b> | 4 <sub>1,4</sub> -3 <sub>1,3</sub>         | 37106.4         | 2.59 ± 0.27                               |
| <b>v<sub>11</sub>=1</b> | 4 <sub>2,2</sub> -3 <sub>2,1</sub>         | 38087.2         | 3.11 ± 0.27                               |

Table IV-6. Pressure broadening coefficients for various transitions of benzonitrile. Uncertainties are taken as the 95% confidence interval for the linear fit to pressure broadening data.

| Transition ( $J_{Ka,Kc}$ )             | Frequency (MHz) <sup>a</sup> | $\gamma_{pres}$ (MHz mbar <sup>-1</sup> ) |
|--|------------------------------|---|
| 13 <sub>2,12</sub> -12 <sub>2,11</sub> | 34864.9                      | 3.29 ± 0.71                               |
| 12 <sub>2,10</sub> -11 <sub>2,9</sub>  | 34898.8                      | 4.02 ± 0.70                               |
| 14 <sub>0,14</sub> -13 <sub>0,13</sub> | 35249.2                      | 3.23 ± 0.98                               |
| 15 <sub>2,14</sub> -14 <sub>2,13</sub> | 39897.9                      | 3.65 ± 0.18                               |
| 16 <sub>0,16</sub> -15 <sub>0,15</sub> | 40090.9                      | 5.25 ± 0.21                               |

Although vinyl cyanide was successfully detected in a cold CRESU flow at 18.7 K from a liquid source flow, no signal of vinyl cyanide as a reaction product from ethylene and cyano radical has been detected in the uniform flow including with the E band spectrometer. This returns to the higher pressure flows under the CRESU conditions which shortens the FIDs duration to hundreds of nanoseconds instead of microseconds. The early stage of the FID is also inaccessible owing to reflections (see Figure IV-16), and so the SNR of the molecular signal is significantly attenuated.

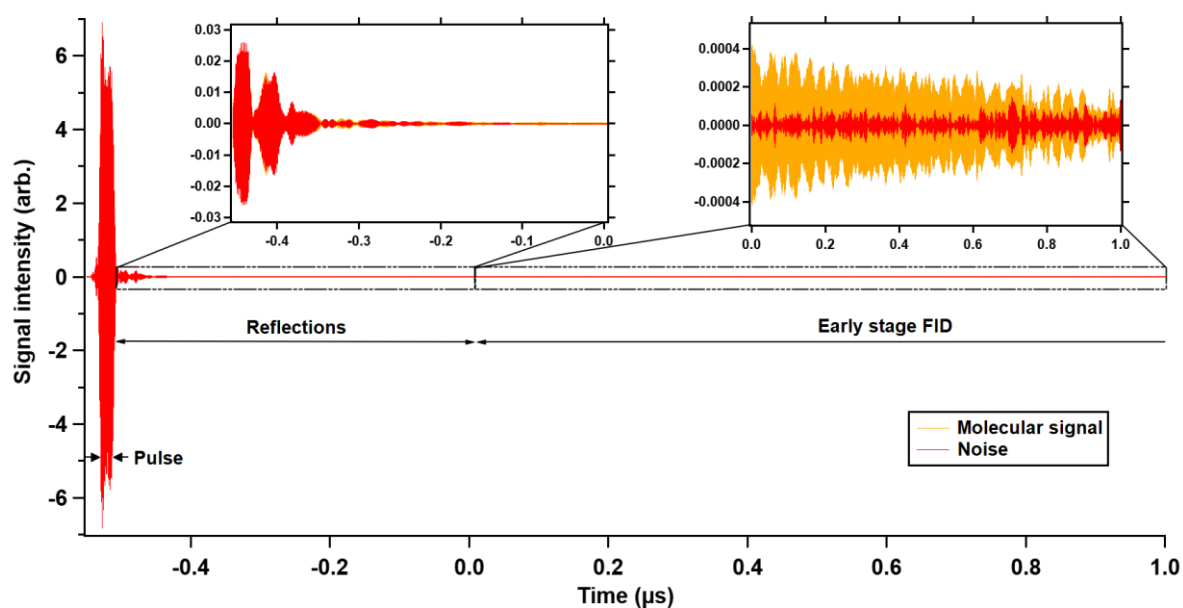


Figure IV-16. Time domain signal pulse, reflections and early FID, in orange a signal recorded from flowing vinyl cyanide in the cell and in red the noise recorded from a blank scan with no gas in the cell.

Despite the use of an absorbent material within the flow cell, reflections from the excitation pulse lasted up to 500 ns after the end of the pulse. These signals could originate from reflections between the broadcast and receiver horns, or come from the electrical path of the receiver, due to standing waves arising from slight mismatches in impedance between the different components. The electric field strength as determined by the Rabi cycle plots is slightly less than that predicted simply using the output power of the amplifier and the gain of the broadcast horn. This is likely due to losses from the Teflon window, and absorbance of the beam by the Eccosorb within the flow cell. Park and coworkers observe a similar reduction in power from basic estimations.<sup>18</sup>

In order to be able to study potential multichannel reactions and conduct sensitive reaction product measurements which can be yielded at very low concentrations, optimization procedures must be carried out two axes, first improving the sensitivity of the spectrometers, which has been discussed in Theo Guillaume's thesis for the E band spectrometer, as for the Ka band spectrometer it will be discussed in future work. The second axis which is the mostly covered in this work is by acting on the flow conditions and developing techniques to adapt the classical CRESU technique and render it suitable to be coupled with different detection instruments and in particular microwave and mm wave spectrometers where the molecular signal detection in the CRESU is limited by multiple constraints such as pressure broadening and reflections. The conception and the development of these optimizing methods will be discussed in the next two chapters.

## References

- (1) Zaleski, D. P.; Neill, J. L.; Muckle, M. T.; Seifert, N. A.; Brandon Carroll, P.; Widicus Weaver, S. L.; Pate, B. H. A Ka-Band Chirped-Pulse Fourier Transform Microwave Spectrometer. *Journal of Molecular Spectroscopy* **2012**, *280*, 68–76. <https://doi.org/10.1016/j.jms.2012.07.014>.
- (2) Hearne, T. S.; Abdelkader Khedaoui, O.; Hays, B. M.; Guillaume, T.; Sims, I. R. A Novel Ka-Band Chirped-Pulse Spectrometer Used in the Determination of Pressure Broadening Coefficients of Astrochemical Molecules. *J. Chem. Phys.* **2020**, *153* (8), 084201. <https://doi.org/10.1063/5.0017978>.
- (3) Gordy, W.; Cook, R. L. *Microwave Molecular Spectra*, 3rd ed.; Techniques of chemistry; Wiley: New York, 1984.
- (4) Cook, R. L. Microwave Molecular Spectroscopy. In *Encyclopedia of Physical Science and Technology (Third Edition)*; Meyers, R. A., Ed.; Academic Press: New York, 2003; pp 799–852. <https://doi.org/10.1016/B0-12-227410-5/00447-6>.
- (5) Gardner, F. F.; Winnewisser, G. The Detection of Interstellar Vinyl Cyanide /Acrylonitrile/. *ApJ* **1975**, *195*, L127. <https://doi.org/10.1086/181726>.
- (6) Mcguire, B.; Burkhardt, A.; Kalenskii, S.; Shingledecker, C.; Remijan, A.; Herbst, E.; McCarthy, M. Detection of the Aromatic Molecule Benzonitrile (c-C<sub>6</sub>H<sub>5</sub>CN) in the Interstellar Medium. *Science (New York, N.Y.)* **2018**, *359*, 202–205. <https://doi.org/10.1126/science.aao4890>.
- (7) Mäder, H.; Bomsdorf, H.; Andresen, U. The Measurement of Rotational Relaxation Time T<sub>2</sub> for CH<sub>3</sub>C<sup>15</sup>N Self-and Foreign Gas Collisions. *Zeitschrift für Naturforschung A* **1979**, *34* (7), 850–857. <https://doi.org/10.1515/zna-1979-0709>.
- (8) Colmont, J.-M.; Rohart, F.; Wlodarczak, G.; Bouanich, J.-P. K-Dependence and Temperature Dependence of N<sub>2</sub>-, H<sub>2</sub>-, and He-Broadening Coefficients for the J=12–11 Transition of Acetonitrile CH<sub>3</sub>C<sup>14</sup>N Located near 220.7GHz. *Journal of Molecular Spectroscopy* **2006**, *238* (1), 98–107. <https://doi.org/10.1016/j.jms.2006.04.017>.
- (9) Colmont, J.-M.; Rohart, F.; Wlodarczak, G. N<sub>2</sub>-, H<sub>2</sub>-, and He-Induced Collisional Broadening of the J=24←23 Transition of HC<sub>3</sub>N Located near 218.3GHz at Different Temperatures. *Journal of Molecular Spectroscopy* **2007**, *241* (2), 119–123. <https://doi.org/10.1016/j.jms.2006.11.007>.

- (10) Rohart, F. Low-Temperature Dependence of the Foreign Gas Relaxation of HC3N with Microwave Coherent Transients Induced by Frequency Switching. *Journal of Molecular Spectroscopy* **1993**, *158* (2), 287–297. <https://doi.org/10.1006/jmsp.1993.1073>.
- (11) Mehrotra, S. C.; Dreizler, H.; Mäder, H. Investigations of Self-, H<sub>2</sub>- and He-Broadening for Rotational Transitions of HCCC15N, CF<sub>3</sub>D and CF<sub>3</sub>CCH by the Microwave Transient Emission Technique. *Journal of Quantitative Spectroscopy and Radiative Transfer* **1985**, *34* (3), 229–231. [https://doi.org/10.1016/0022-4073\(85\)90003-2](https://doi.org/10.1016/0022-4073(85)90003-2).
- (12) Bomsdorf, H.; Mäder, H. Investigation of T<sub>1</sub>-Relaxation by a Microwave Pulse Technique for HCCC15N Rotational Transitions. *Zeitschrift für Naturforschung A* **1984**, *39* (12), 1212–1221. <https://doi.org/10.1515/zna-1984-1212>.
- (13) Nerf, R. B. Pressure Broadening of the J = 1 ← 0 Transition of Hydrogen Cyanide. *Journal of Molecular Spectroscopy* **1975**, *58* (3), 479–480. [https://doi.org/10.1016/0022-2852\(75\)90227-1](https://doi.org/10.1016/0022-2852(75)90227-1).
- (14) Colmont, J. M. Collisional Broadening of the J = 1 ← 0 Transition of HC15N by Nitrogen, Oxygen, Helium, and Air. *Journal of Molecular Spectroscopy* **1985**, *114* (2), 298–304. [https://doi.org/10.1016/0022-2852\(85\)90227-9](https://doi.org/10.1016/0022-2852(85)90227-9).
- (15) Ronningen, T. J.; De Lucia, F. C. Helium Induced Pressure Broadening and Shifting of HCN Hyperfine Transitions between 1.3 and 20 K. *J. Chem. Phys.* **2005**, *122* (18), 184319. <https://doi.org/10.1063/1.1895905>.
- (16) McGurk, J. C.; Schmalz, T. G.; Flygare, W. H. Fast Passage in Rotational Spectroscopy: Theory and Experiment. *The Journal of Chemical Physics* **1974**, *60* (11), 4181–4188. <https://doi.org/10.1063/1.1680886>.
- (17) Hays, B. M.; Guillaume, T.; Hearne, T. S.; Cooke, I. R.; Gupta, D.; Abdelkader Khedaoui, O.; Le Picard, S. D.; Sims, I. R. Design and Performance of an E-Band Chirped Pulse Spectrometer for Kinetics Applications: OCS – He Pressure Broadening. *J. Quant. Spectrosc. Radiat. Transf.* *In press*.
- (18) Park, G. B.; Steeves, A. H.; Kuyanov-Prozument, K.; Neill, J. L.; Field, R. W. Design and Evaluation of a Pulsed-Jet Chirped-Pulse Millimeter-Wave Spectrometer for the 70–102 GHz Region. *J. Chem. Phys.* **2011**, *135* (2), 024202. <https://doi.org/10.1063/1.3597774>.

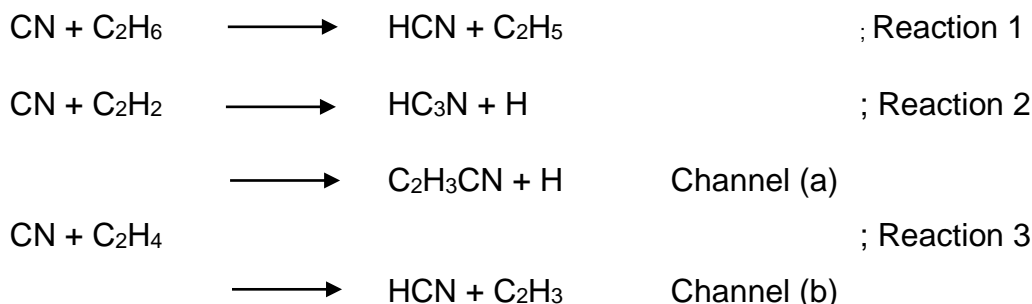
- (19) Chaussard, F.; Michaut, X.; Saint-Loup, R.; Berger, H.; Joubert, P.; Lance, B.; Bonamy, J.; Robert, D. Collisional Effects on Spectral Line Shape from the Doppler to the Collisional Regime: A Rigorous Test of a Unified Model. *The Journal of Chemical Physics* **2000**, *112* (1), 158–166. <https://doi.org/10.1063/1.480570>.
- (20) Dicke, R. H. The Effect of Collisions upon the Doppler Width of Spectral Lines. *Phys. Rev.* **1953**, *89* (2), 472–473. <https://doi.org/10.1103/PhysRev.89.472>.
- (21) Abeysekera, C.; Zack, L. N.; Park, G. B.; Joalland, B.; Oldham, J. M.; Prozument, K.; Ariyasingha, N. M.; Sims, I. R.; Field, R. W.; Suits, A. G. A Chirped-Pulse Fourier-Transform Microwave/Pulsed Uniform Flow Spectrometer. II. Performance and Applications for Reaction Dynamics. *J. Chem. Phys.* **2014**, *141* (21), 214203. <https://doi.org/10.1063/1.4903253>.
- (22) Oldham, J. M.; Abeysekera, C.; Joalland, B.; Zack, L. N.; Prozument, K.; Sims, I. R.; Park, G. B.; Field, R. W.; Suits, A. G. A Chirped-Pulse Fourier-Transform Microwave/Pulsed Uniform Flow Spectrometer. I. The Low-Temperature Flow System. *The Journal of Chemical Physics* **2014**, *141* (15), 154202. <https://doi.org/10.1063/1.4897979>.
- (23) Broderick, B. M.; Suas-David, N.; Dias, N.; Suits, A. G. Isomer-Specific Detection in the UV Photodissociation of the Propargyl Radical by Chirped-Pulse Mm-Wave Spectroscopy in a Pulsed Quasi-Uniform Flow. *Phys. Chem. Chem. Phys.* **2018**, *20* (8), 5517–5529. <https://doi.org/10.1039/C7CP06211G>.
- (24) Müller, H. S. P.; Belloche, A.; Menten, K. M.; Comito, C.; Schilke, P. Rotational Spectroscopy of Isotopic Vinyl Cyanide, H<sub>2</sub>CCHCN, in the Laboratory and in Space. *Journal of Molecular Spectroscopy* **2008**, *251* (1), 319–325. <https://doi.org/10.1016/j.jms.2008.03.016>.
- (25) Müller, H. S. P.; Thorwirth, S.; Roth, D. A.; Winnewisser, G. The Cologne Database for Molecular Spectroscopy, CDMS. *A&A* **2001**, *370* (3), L49–L52. <https://doi.org/10.1051/0004-6361:20010367>.
- (26) Mehrotra, S.; Mäder, H. Study of T<sub>1</sub>-and T<sub>2</sub>-Relaxation by Microwave Pulse Techniques: Rotational Transition J=0-1 of HCCF, J-Dependence of Rotational Transitions of SO<sub>2</sub>, and I-Type Doublet Transitions of HC<sup>15</sup>N Perturbed by Self, H<sub>2</sub>, D<sub>2</sub>, and He. *Zeitschrift für Naturforschung A* **1988**, *43*. <https://doi.org/10.1515/zna-1988-0510>.

- (27) Green, S. On the Amount of Information in Rotational Relaxation Experiments with Application to Microwave Transient  $T_1$  and  $T_2$  Rates. *The Journal of Chemical Physics* **1978**, 69 (9), 4076–4082. <https://doi.org/10.1063/1.437140>.
- (28) Patterson, D.; Doyle, J. M. Cooling Molecules in a Cell for FTMW Spectroscopy. *Molecular Physics* **2012**, 110 (15–16), 1757–1766. <https://doi.org/10.1080/00268976.2012.679632>.
- (29) Wójtewicz, S.; Gotti, R.; Gatti, D.; Lamperti, M.; Laporta, P.; Jóźwiak, H.; Thibault, F.; Wcisło, P.; Marangoni, M. Accurate Deuterium Spectroscopy and Comparison with *Ab Initio* Calculations. *Phys. Rev. A* **2020**, 101 (5), 052504. <https://doi.org/10.1103/PhysRevA.101.052504>.
- (30) Wcisło, P.; Tran, H.; Kassı, S.; Campargue, A.; Thibault, F.; Ciuryło, R. Velocity-Changing Collisions in Pure H<sub>2</sub> and H<sub>2</sub>-Ar Mixture. *J. Chem. Phys.* **2014**, 141 (7), 074301. <https://doi.org/10.1063/1.4892414>.

## V. Secondary expansion chamber: development, characterization and application to the quantitative determination of reaction product branching ratios

### Introduction

The determination of branching ratios of reactions relevant to astrochemistry requires the ability to conduct sensitive detections of multiple reaction products on the timescale of elementary reaction under study in isolation (pseudo first order) conditions (see chapter I). In the context of the CRESUCHIRP project, the three reactions of the CN radical with C<sub>2</sub> hydrocarbons were targeted:



Reactions 1 and 2 are expected to be single channel reactions that produce HCN and HC<sub>3</sub>N respectively and have been studied and presented in Theo Guillaume's thesis where both products were detected directly in cold uniform flows of argon and helium using the E band spectrometer. Reaction 3 however is a potential dual channel reaction that yields vinyl cyanide and HCN from channel (a) and (b) respectively<sup>1</sup> has also been studied directly in the cold flow, but neither product was detected under these conditions. The results confirm the pressure broadening measurements presented in the previous chapter and how its effect is strengthened with the size of the molecule

and the high pressure environment causing a quick quenching of the time domain molecular signal as a result of the rapid loss of coherence due to collisions between vinyl cyanide and the perturbing buffer (helium or argon). Although vinyl cyanide has been detected in the CRESU environment at different temperatures despite the high pressure in the chamber, this was from a direct flow source, in a reaction however vinyl cyanide is estimated to be formed at much lower concentrations. Here we remind that due to the larger flow rates of gas used in the CRESU  $\sim 50$  SLM compared to other cooling techniques, and with the limited pumping capacity, the pressures in the chamber cannot be lowered to high vacuum ( $8 \times 10^{-2}$  mbar is the lowest pressure achieved with the Ar-29.6K-0.08 nozzle).

The same argument would apply to the detection of HCN, a potential product from the second channel of reaction (3), although being less sensitive to pressure with a broadening rate around half of that of vinyl cyanide, Choi and co-workers<sup>2</sup> and Trevitt and co-workers<sup>3</sup> suggested that the HCN formation will be less than 5%, this channel efficiency may be increased with larger unsaturated hydrocarbon such as propene as reactants.<sup>1</sup> The formation of HCN at low concentration than the minimum to be detected is then possible.

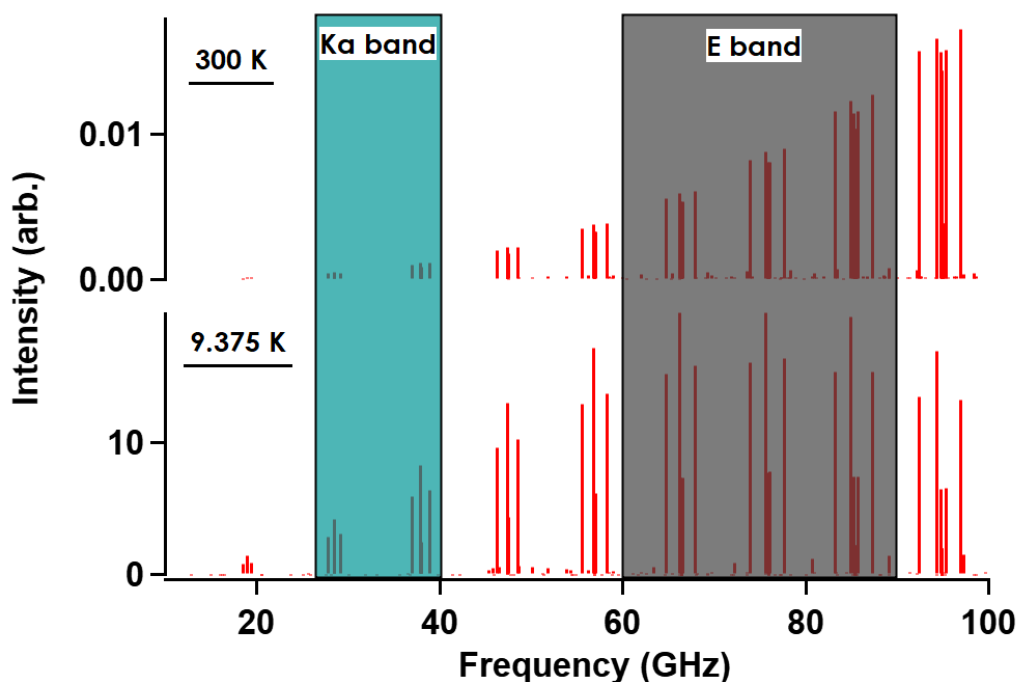


**Figure V-1. Spectrum of vinyl cyanide given by CDMS at 300 K (top) and 9.375 K (bottom), the E and Ka band ranges are displayed in grey and green respectively, at 9.375 K the vinyl cyanide strongest transition are shifted to the E band.**

In order to reduce the effect of pressure broadening, a new setup has been developed and built that relies on the concept of molecular beam sampling, where a small portion of the isentropic core of the CRESU flow at a relatively high pressure is sampled into a higher vacuum environment. The CRESU flow, already expanded via the Laval nozzle, is brought to a second expansion via a skimmer into a newly designed chamber under constant pumping. Both the temperature and the pressure of the gas are lowered which will reduce the collision rate and depopulate the higher energy levels, conditions that contribute in strengthening the molecular signal of the transitions covered by our two spectrometers (see Figure V-1 ). The reactions of interest still occur in the CRESU environment while the probing is carried out in this new chamber which gives the possibility to study reactions at higher temperatures and different pressures while still being able to detect the products since the probing is decoupled from the reaction environment, being carried out under lower temperature and pressure conditions.

The SKISURF (Skimmed uniform Supersonic Flow) setup is one of the two solutions developed in this work to increase the sensitivity of our spectrometers by upgrading the CRESU technique. The design of the secondary expansion chamber and the characterization of probing environment with both experimental measurements and modelling using DSMC and CFD calculations is presented in the first part of this chapter. Results from reactions 2 and 3 are given in the second part including the determination of the branching ratio of reaction (3). The second optimizing setup is the pulsed system which will be presented in the next chapter.

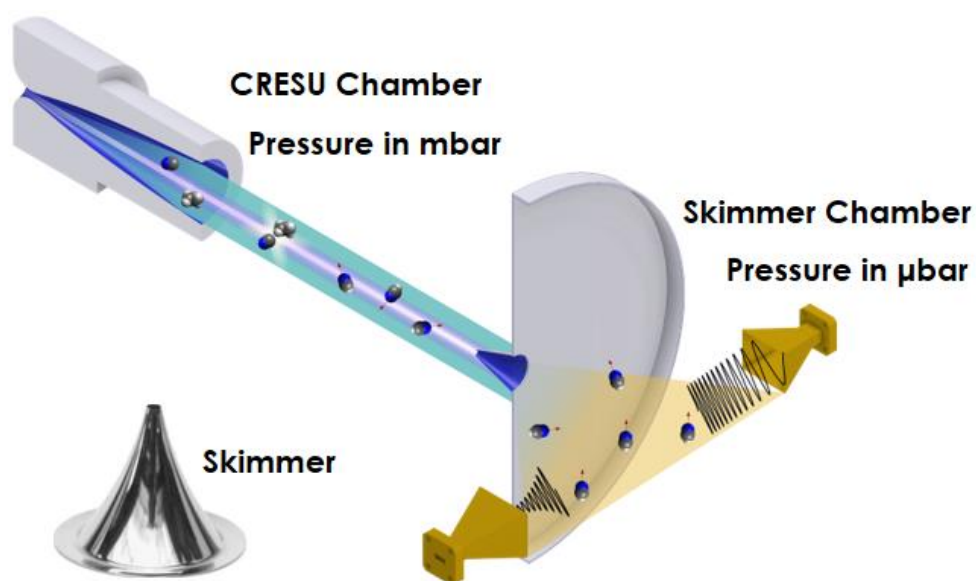


**Figure V-2. Schematic of the principle of beam sampling from CRESU flows**

## Part I: Design and characterization phase

### V.1. Secondary expansion chamber description

In order to reduce the pressure, a small portion of the isentropic core from the CRESU flow already expanded via the Laval nozzle is sampled with a skimmer into the secondary expansion chamber, a stainless steel T-shape with a diameter of 25 cm connected to two extensions, the top one is a 20 cm long tube connected to a (OSAKA-TGkine3300M) turbomolecular pump to create vacuum, the second one is connected to a 40 cm long 21.5 cm in diameter cylinder on which the skimmer and its support are mounted. Either spectrometer can be mounted on the secondary expansion chamber from the lateral part of this section where three pairs of ports are designed allowing to probe three different regions of the post-skimmer expansion flow at distances of 25.5, 62.5 and 125 mm from the skimmer exit. The third face of the T-shaped cylinder is sealed with a 25 cm flange with a Brewster window, the whole ensemble is built inside the CRESU chamber. The two chambers are connected via 40 mm flexible bellows to evacuate the thrust of the turbomolecular pump to the CRESU chamber and then to the Roots pumps. The schematic of the two chambers is given in Figure V-3.

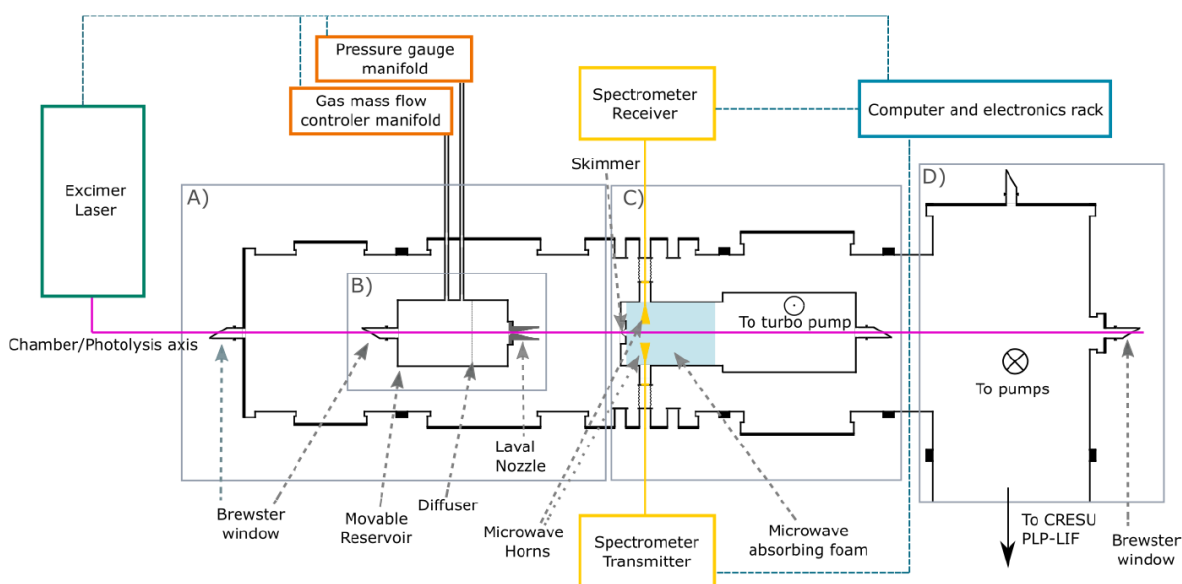


**Figure V-3. Schematic of the modified CRESU chamber containing the secondary expansion chamber, left to right: reservoir with Brewster window allowing passage of the laser beam through the Laval nozzle, followed by the skimmer chamber and its support then the turbomolecular pump. The spectrometer can be mounted via one of the three ports in the secondary expansion chamber.**

Skimmer sampling of both continuous<sup>4-7</sup> and pulsed<sup>8</sup> uniform supersonic flows has been employed in the past, mainly to enable mass spectrometric detection.

Suits and co-workers<sup>9</sup> and Leone and co-workers<sup>10</sup>, have coupled CRESU flows in pulsed mode with an airfoil allowing to sample the flow with minimum perturbation of the flow upstream (see Figure V-4). Suits and co-workers designed an airfoil adapted from Leone and coworkers that is closed at its sides with microwave-transparent polycarbonate which gives access to the early phase of the secondary expansion where the temperature of the flow is at lowest values as will be shown later.

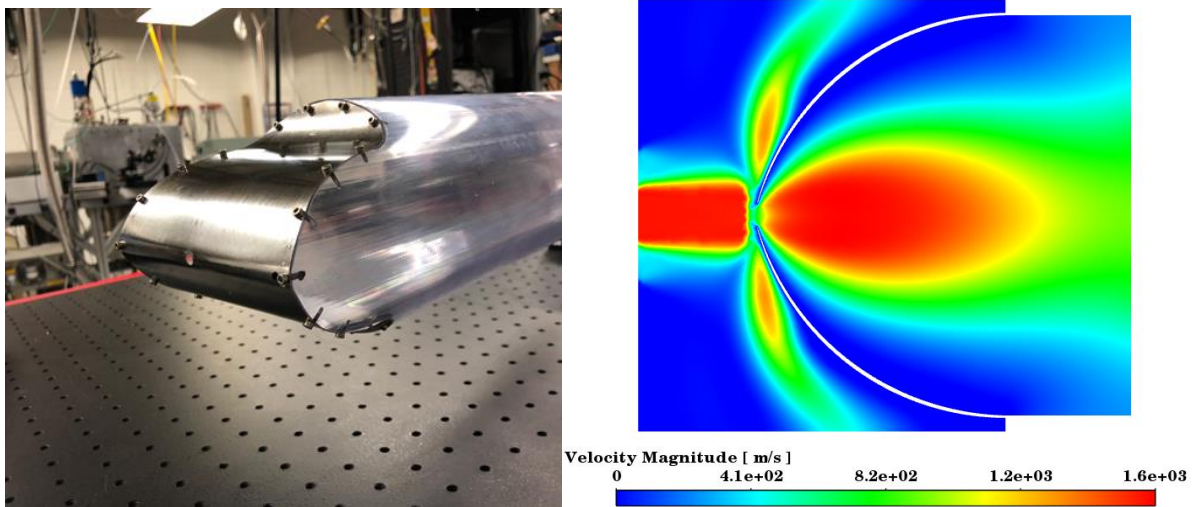


**Figure V-4. left figure shows an Airfoil system to sample CRESU flow from Das et al,<sup>11</sup> right figure represents a velocity profile from a CFD simulation of a reproduced airfoil geometry, simulating a uniform supersonic argon flow at 35 K, 0.28 mbar and Mach 4.7 expanding through the 5 mm aperture, the system poses a risk of forming a detached shockwave that destroys the supersonic flow and increases its temperature before it re-expands through the aperture.**

In this work to avoid problems prior sampling, four beam dynamics model 2 skimmers<sup>12</sup> with different orifice diameters (1,2,3 and 4 mm) have been used in our setup, the skimmers are specifically designed to avoid any flow perturbation before sampling. The incoming supersonic streamlines line with the outer profile of the skimmer and the non-sampled portion of the gas is then evacuated via a skimmer support. The geometry of this support is found to be as critical as that of the skimmer. An optimized profile of this support was developed based on CFD simulations using the Ansys-Fluent solver see A.V in appendix).

## V.2. Upstream sampling CFD simulations

Unless the non-sampled gas of the CRESU flow is evacuated quickly, it starts accumulating at the base of the skimmer, backing up until it forms a normal shockwave which manifests by a drastic and sudden drop of the flow speed to subsonic along with a surge in temperature. This will change the CRESU flow conditions and destroy its uniformity which compromises the results of the reaction studied. The position of the shockwave depends on the nature of the gas, its compressibility, the flow rate and the geometry of the obstacle.<sup>7</sup> An initial skimmer support (hereafter referred to as the non-optimized support) was fabricated and used for initial testing and simulations. Its profile is represented in the appendix (See A.V). A simulation was carried out using the non-optimized profile for the skimmer support<sup>3</sup> to investigate the possibility of the presence of a detached shockwave while sampling flow from the Ar-50K-0.3 and the Ar-50K-0.7 nozzles sharing the same temperature and flow rate but different densities.

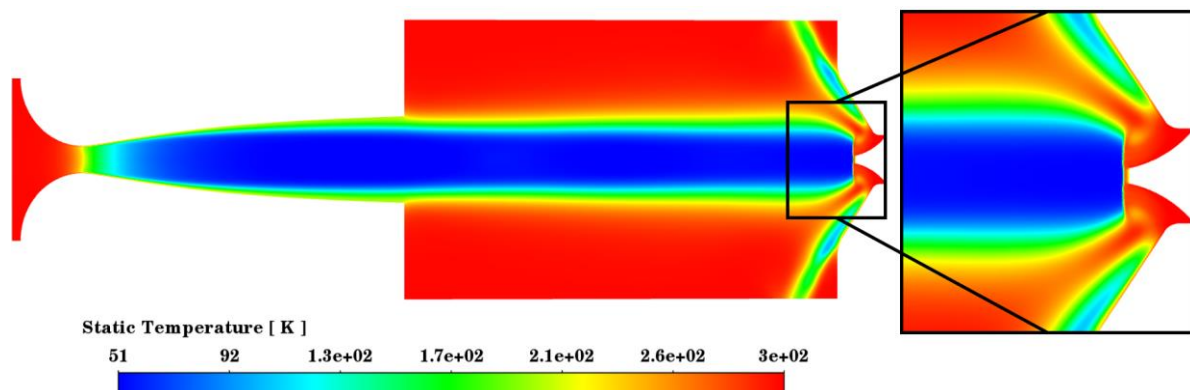


**Figure V-5. CFD simulations of the temperature as a flow property of the CRESU flow from the Ar-50K-0.3 nozzle being sampled with the 4 mm skimmer mounted on the non-optimized support, inset: zoom on the entry of the skimmer shows a detached shockwave formed before sampling.**

<sup>3</sup> The 4 mm skimmer was used for the investigation of the shockwave formation as it is the smallest in length compared to the other three skimmers and therefore the most susceptible to form detached shockwaves

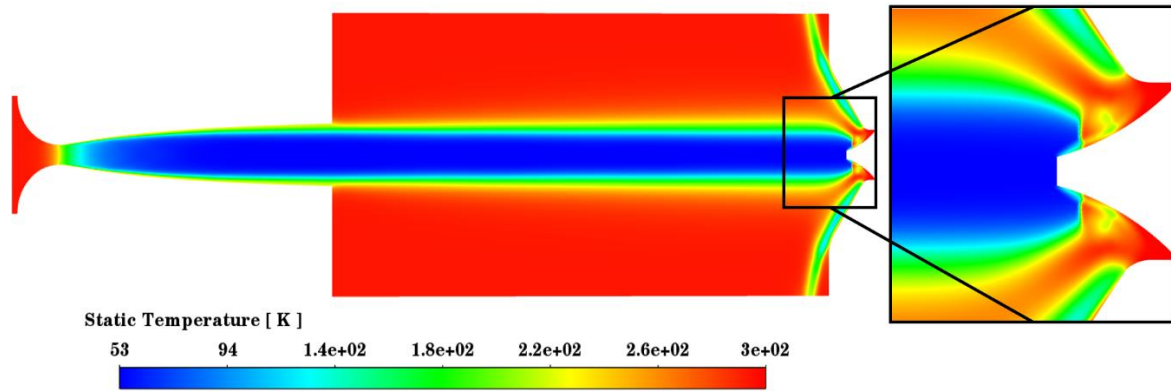


**Figure V-6.** CFD simulations of the temperature as a flow property of the CRESU flow from the Ar-50K-0.7 nozzle being sampled with the skimmer mounted on the non-optimized support, inset: zoom on the entry of the skimmer no detached shockwave has been observed before sampling.

The results shows that for the Ar-50K-0.3 nozzle a potential nozzle to be used in future work especially for pressure dependence measurements, the non-optimized skimmer setup (skimmer + support) is unable to sample the flow without perturbing the upstream CRESU flow and a normal shockwave is formed. In order for the shockwave to remain attached to the skimmer walls, the geometry of the skimmer support was therefore optimized for the different nozzle-skimmer combinations of interest which deliver the highest SNR with our CP-FTMW spectrometers using a series of CFD simulations and changing the geometry of the skimmer support until the normal shockwave is dissipated. Figure V-7 shows the successful evacuation of the non-sampled gas of the argon flow from the Ar-50K-0.3 nozzle expanding via a 4 mm skimmer mounted on the optimized skimmer support, no detached shockwave has been formed in the CRESU flow before sampling.

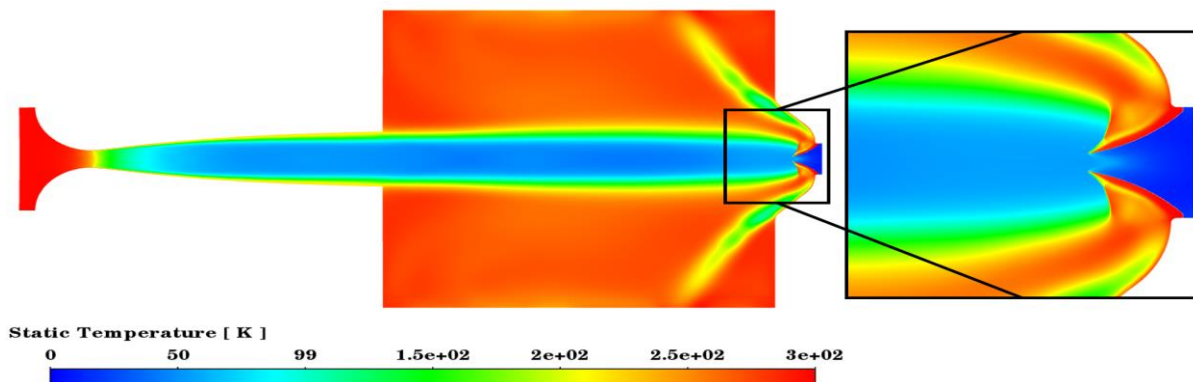


**Figure V-7.** CFD simulations of the temperature as a flow property of the argon 50 K 0.3 CRESU flow being sampled with the skimmer using an optimized skimmer support's profile, inset: zoom on the entry of the skimmer no detached shockwave has been observed before sampling.

### V.2.1. Argon flow at 35 K (Ar-35K-0.28 nozzle)

An argon nozzle has been designed specifically for the skimmer conditions able to deliver high SNR spectra, the nozzle operates at the same density as the Ar-50K-0.3 nozzle but at lower temperature; 35 K and with 20 SLM argon flow rate. The gas at a reservoir pressure of 52.7 mbar continuously expands into the chamber giving a CRESU flow at 35.1 K. The CRESU chamber is kept at 0.28 mbar. The flow was characterized by 2D impact pressure measurements using the Pitot tube as shown in Figure V-8, the experimental temperature profile is in an excellent agreement with the results given by CFD modelling.

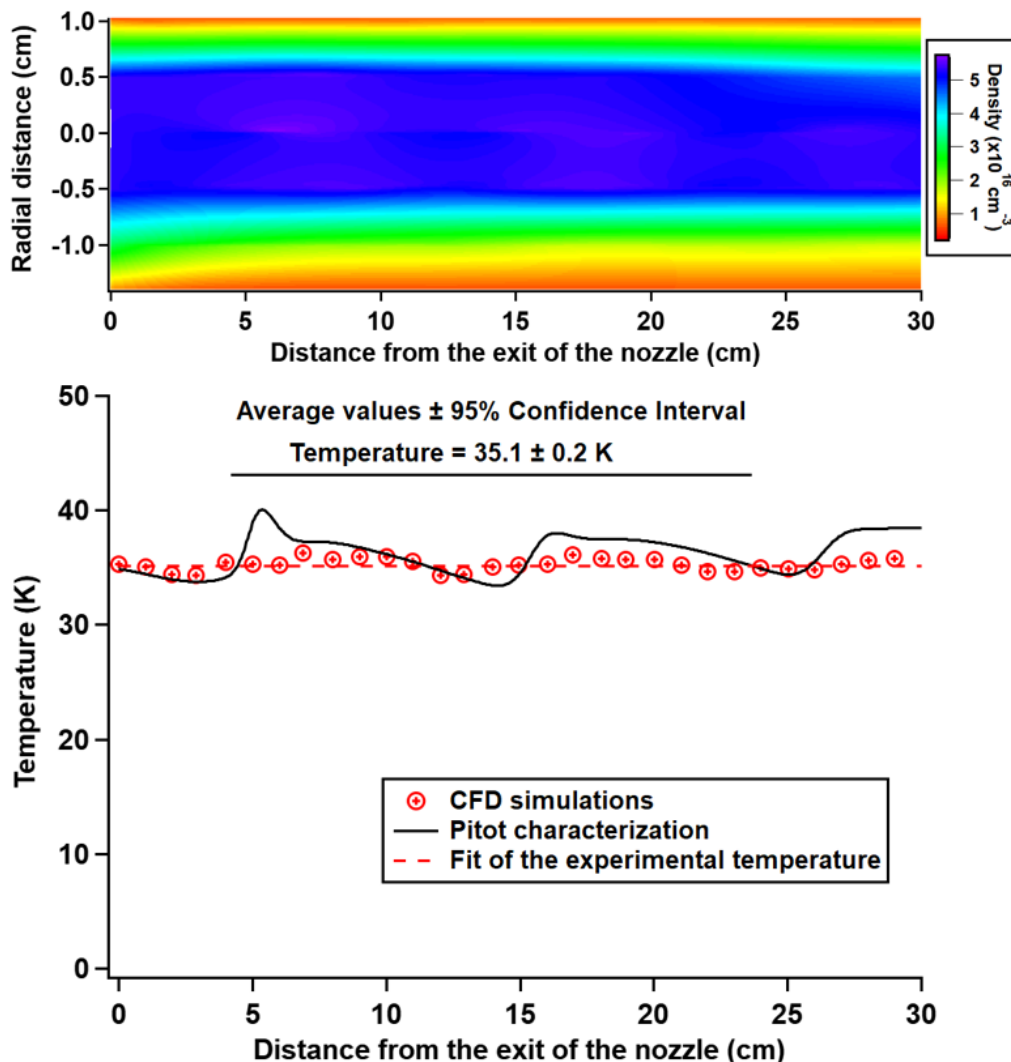
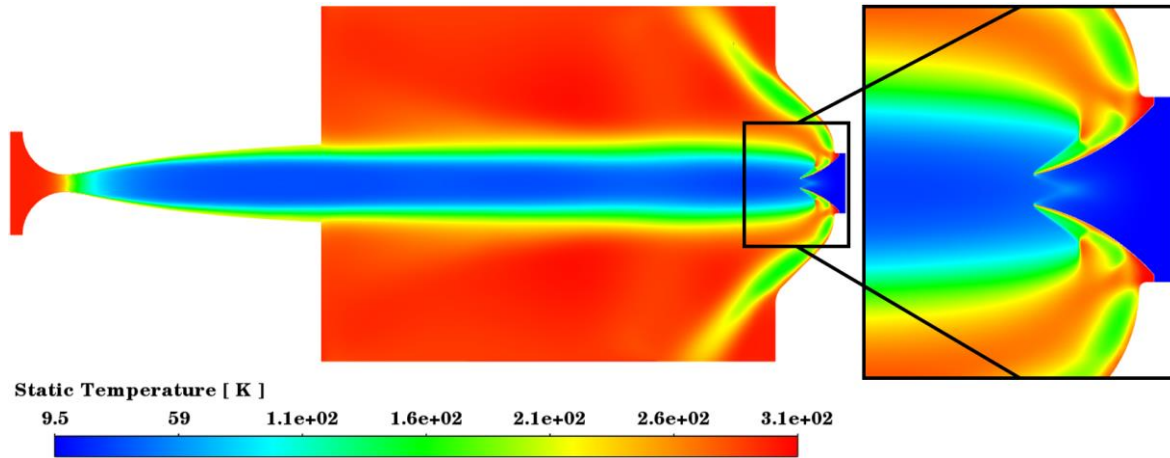


Figure V-8. Ar-35K-0.28 nozzle conditions, top panel gives the 2D density profile: the flow properties from impact pressure measurements of the CRESU flow using Pitot tube; bottom panel shows the 1D profile of temperature along the axis given by CFD simulation and Pitot tube measurements using the impact pressure. Average temperature given by CFD simulations is  $(35.1 \pm 0.2) \text{ K}$ .

The Ar-35K-0.28 nozzle was tested numerically to ensure a smooth sampling with the 4 mm skimmer and there is no sign of any perturbation in the generated CRESU flow before sampling.



**Figure V-9. CFD simulations of the temperature as a flow property of the Ar-35K-0.28 CRESU flow being sampled with the skimmer, no normal shockwave or major disturbances have been observed.**

To monitor the power of the newly designed Ar-35K-0.28 nozzle compared to the Ar-50K-0.3 nozzle, the strongest vinyl cyanide signal transition  $J_{K_a, K_c} = 7_{0,7} - 6_{0,6}$  at 66.198 GHz was targeted in the sampled CRESU flows of the Ar-35K-0.28 and the Ar-50K-0.3 nozzles via the 4 mm skimmer with the E band spectrometer in the new probing environment under the secondary expansion conditions, the results of the spectra given by Figure V-10 show an increase of more than 40 % in the SNR with Ar-35K-0.28 compared to the Ar-50K-0.3. To benefit from the higher SNR, all the results presented in this chapter are then measured with the Ar-35K-0.28 nozzle.

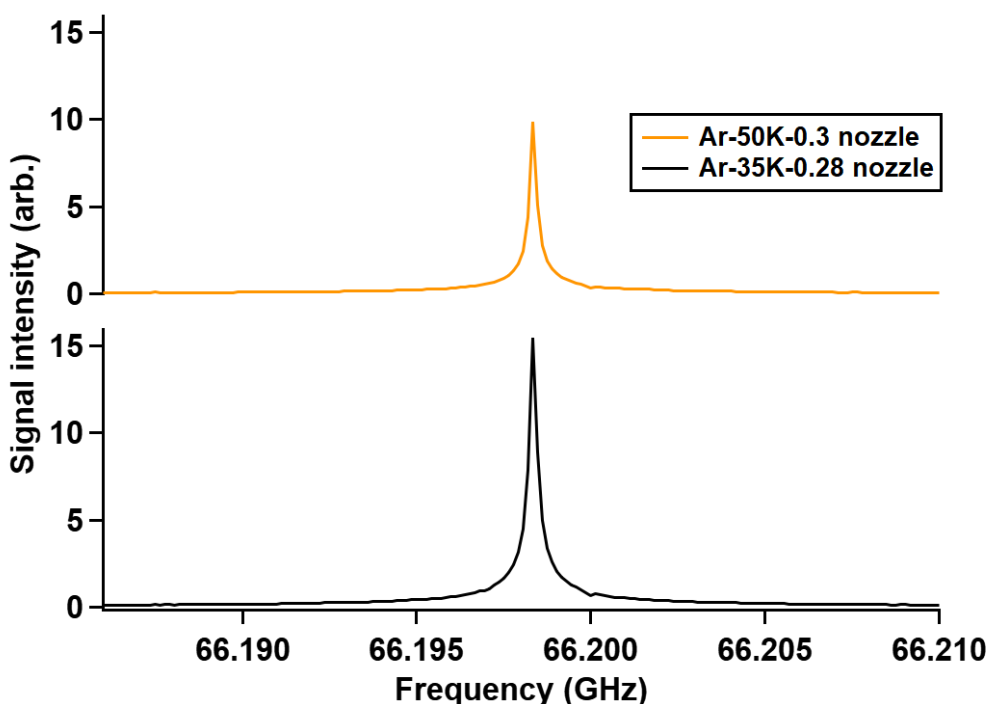


**Figure V-10.** Comparison of the signal delivered from the expansion of a CRESU flow from the Ar-50K-0.3 nozzle (in orange) and the Ar-35K-0.28 (in red) expanding via the 4 mm skimmer targeting the  $J_{K_a,K_c} = 7_{0,7} - 6_{0,6}$  rotational transition of vinyl cyanide, vinyl cyanide is at 0.0066% of the total flow. the spectra are recorded under the same condition with 10,000 averaged scans.

### V.3. Post skimmer expansion

Pressures can be lowered by orders of magnitude in the skimmer chamber compared to the CRESU chamber, the reduction factor depends on the upstream flow conditions (flow rate and the nature of the gas) as well as the skimmer orifice diameter (see Figure V-11). Although lowering the pressure to its minimum is beneficial to the molecular signal, having enough molecules to be probed in the skimmer chamber is no less important and can be even more important. This can be seen for vinyl cyanide expanding from the Ar-35K-0.28 nozzle with the 1,2,3 and 4 mm skimmers (see Figure V-12).

## Throughput

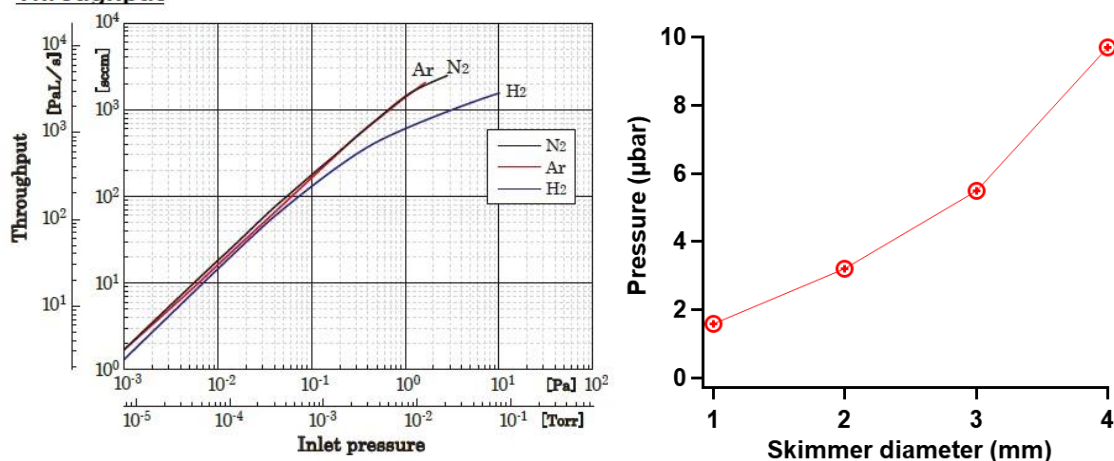


Figure V-11. (a) Turbomolecular pump characteristic curves, (b) pressure in the secondary expansion chamber with the 4 skimmers

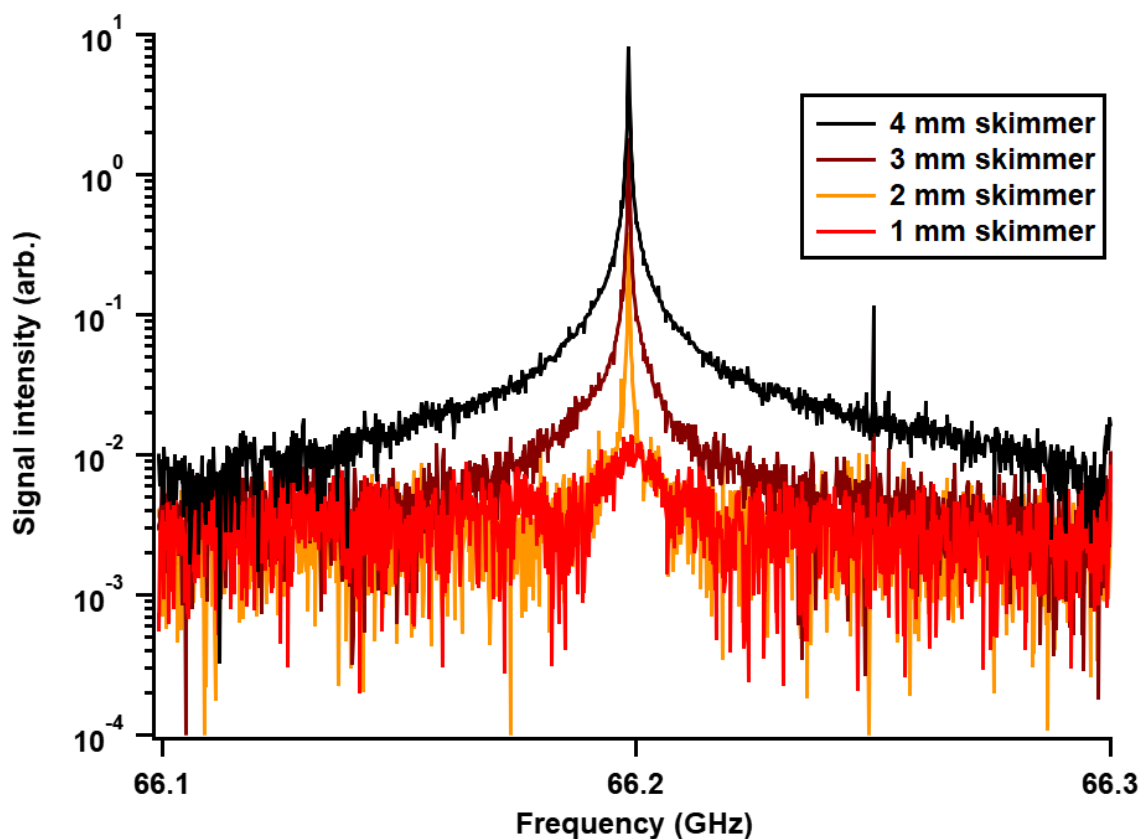


Figure V-12. Vinyl cyanide signal in an argon flow at 35 K expanding in the skimmer chamber using 1,2,3 and 4 mm skimmer diameters at 20 cm from the skimmer, all spectra are recorded with the same procedure.

The results of the signal dependence on flow conditions from Figure V-12 highlight the strong impact of density on the molecular signal intensity in microwave spectroscopy as much as the pressure does.

Since the signal is linearly proportional to the density (in a non-clustering regime), the gain on the signal intensity when using the 4 mm skimmer instead of the 1 mm skimmer is 16 times better, and given that the pressure with the 4 mm skimmer is still 30 times lower than in the CRESU, the 4 mm skimmer is used for all the measurements in this work.

The characterization of the new probing environment is conducted via simulations using DSMC and CFD modelling and experimental measurements of the rotational temperature.

### V.3.1. Post-skimmer expansion simulations

The sampled CRESU flow undergoes a second expansion in the skimmer chamber which will lower its pressure further reaching medium ( $1\text{-}10^{-3}$  mbar) and high ( $10^{-3}\text{-}10^{-6}$  mbar) vacuums when using small diameter skimmers. Under our operating pressures with the 4 mm skimmer, the vacuum reached is medium (less than  $10^{-2}$  mbar), the sampled flow can be considered to be in a slip regime. A full characterization of the post skimmer expansion is carried out via DSMC calculations using the DS2V bird program then validated by experimental measurements with the E band spectrometer at the three regions in the secondary expansion chamber. The Ar-35K-0.28 nozzle with the 4 mm skimmer are used for the characterization. Given the flow being in a nearly continuum regime, CFD simulations are also carried out with the Fluent solver of Ansys workbench using the pressure based model in the continuum regime with the slip condition which allows the velocity to vary along the inner walls of the skimmer<sup>13,14,15</sup>. This can still give predictions of the flow properties in the post skimmer expansion region. Figure V-13 shows the results from CFD and DSMC simulations respectively, both models give the same pattern of the expansion a cold region covering most of the probing positions followed by a gradual and progressive increase of temperature with no trace of shockwave, as it is the case for free jet expansions.

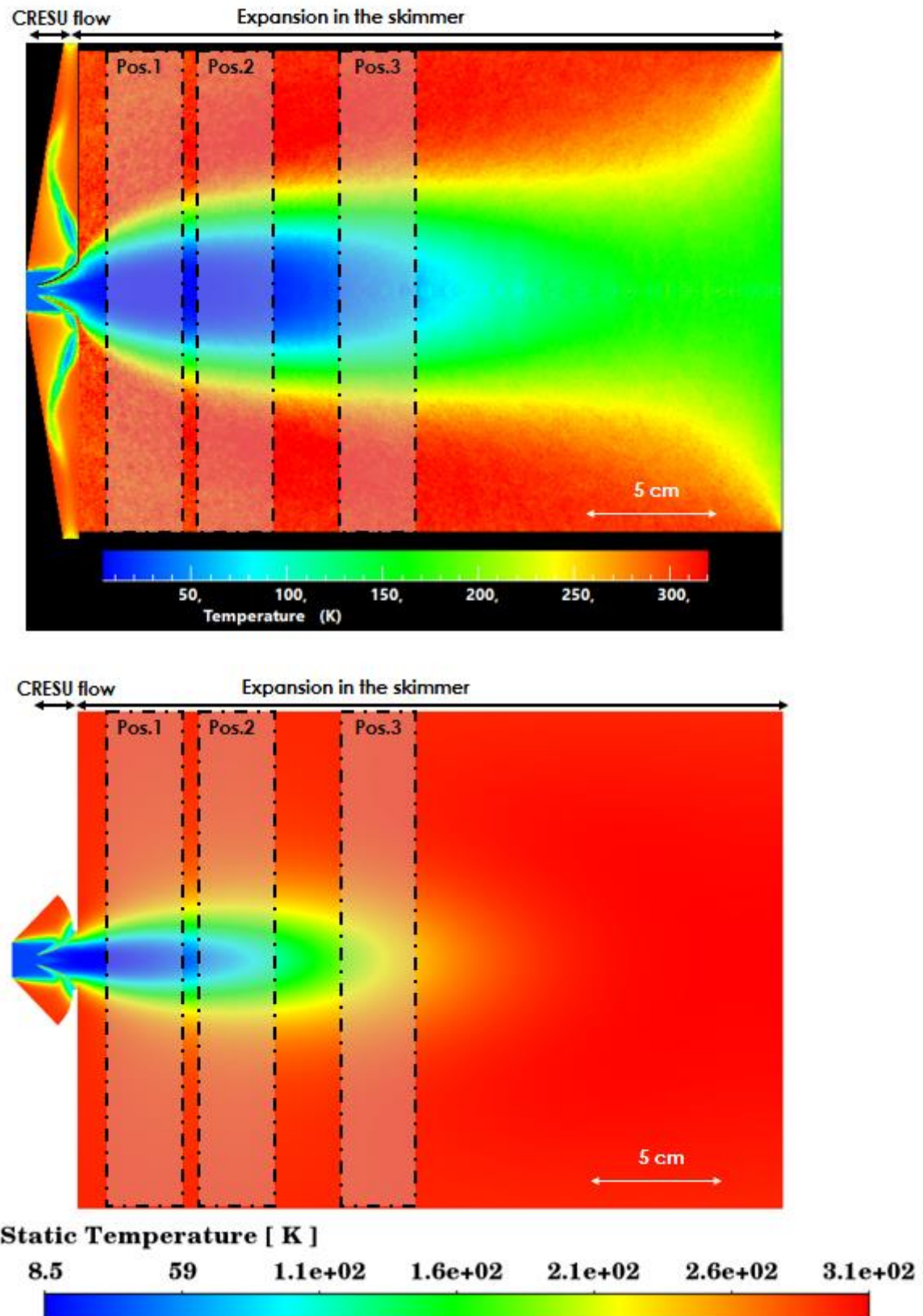
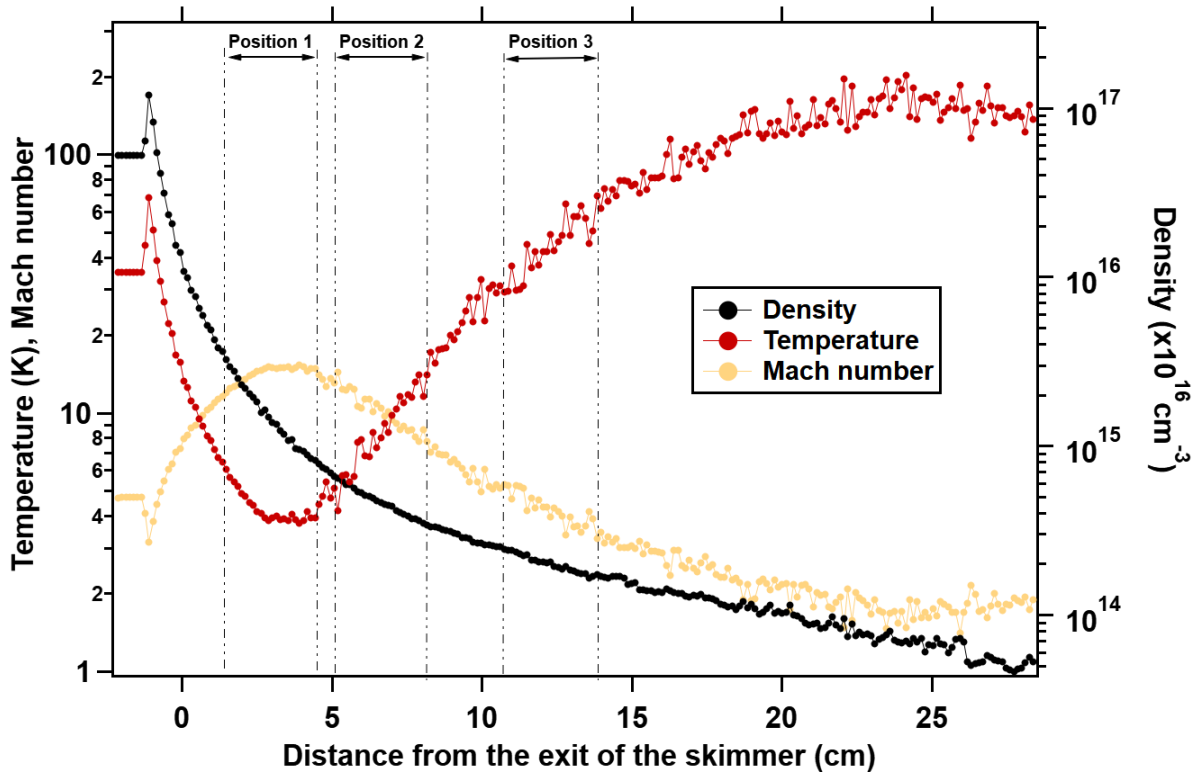


Figure V-13. Temperature map from simulations of the secondary expansion of the Ar-35K-0.28 nozzle in the 4 mm skimmer, top panel shows the DSMC results and the bottom panel gives CFD simulation results.



**Figure V-14. Temperature, density and Mach number profiles of the Ar-35K-0.28 nozzle flow expanding via the 4 mm skimmer along the axis of the secondary expansion chamber as given by DS2V program, in black is the density profile, in red is the temperature profile and in orange is the Mach number.**

Figure V-14 gives the temperature, density and Mach number profiles of the Ar-35K-0.28 nozzle flow expanding via the 4 mm skimmer along the axis of the secondary expansion chamber, it clearly shows that the first port of probing is the most suited for measurements where the temperature is at its lowest value and the density at a detectable level as will be shown later.

The CFD model does predict the same flow pattern but with discrepancies from the DSMC calculations, this is expected regarding the limitations of the Naviers-Stokes solver to predict the flow properties beyond the continuum regime, the temperature along the axis starts increasing at much faster rate than it does with the DMSC calculations (see Figure V-15 ).

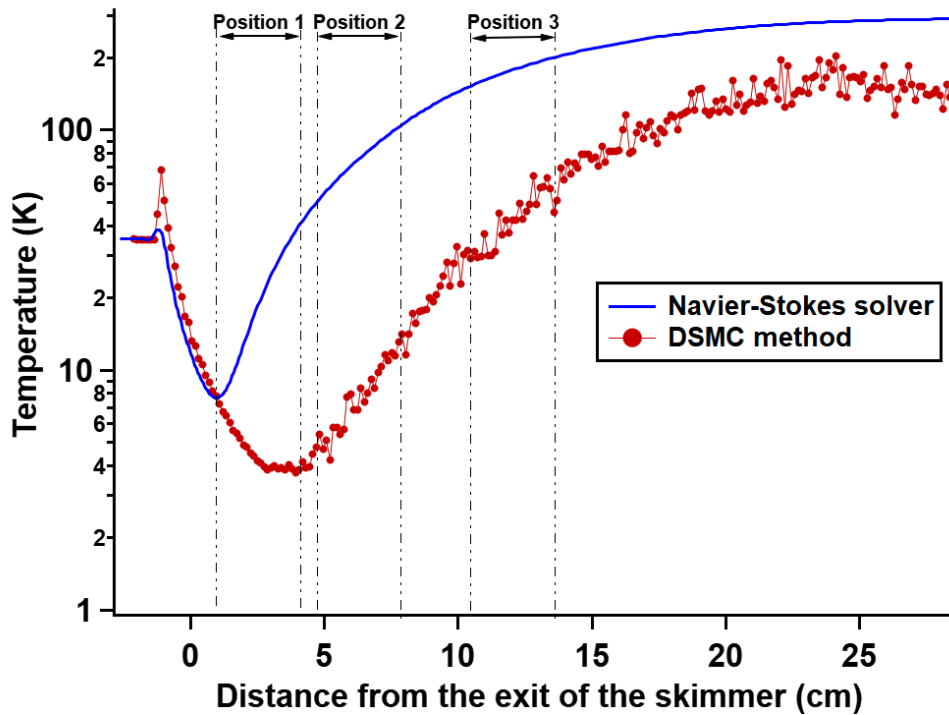


**Figure V-15.** Temperature profile along the axis of the secondary expansion chamber in blue is using the Fluent solver and in red is with the DSMC calculations.

One challenge that has been observed with simulations and experimentally demonstrated by Even and co-workers<sup>16</sup> and Narevicius and co-workers<sup>17</sup> is the clogging effect, a phenomenon caused by the skimmer geometry. The CRESU flow at a low temperature hitting at a supersonic speed the skimmer walls at room temperature creates an oblique shockwave that heats and slows the gas. Equation V-1 gives the Mach number after the shock.

$$M_2^2 \sin^2(\beta - \alpha) = \frac{(\gamma - 1)M_1^2 \sin^2(\beta)}{2\gamma M_1^2 \sin^2(\beta) - (\gamma - 1)} \quad \text{Equation V-1}$$

Where  $M_1$  and  $M_2$  are the Mach numbers before and after the shock layer,  $\beta$  is the shock angle to the horizontal and  $\alpha$  is the deflections angle of molecules to the horizontal. The oblique shockwave is not strong enough to destroy the supersonic regime of the argon flow at 35 K as shown in Figure V-16. While cooling the skimmer contributes in minimizing the clogging effect, it has not been applied in our setup given the small effect it has on the reactions studied and the associated time of the clogging which is less than 10  $\mu\text{s}$ . Furthermore, the values shown in the right panel of Figure V-16 are only for the centerline of the flow, and as such do not fully reflect the average path taken by molecules that are subsequently plotted in positions 1-3.

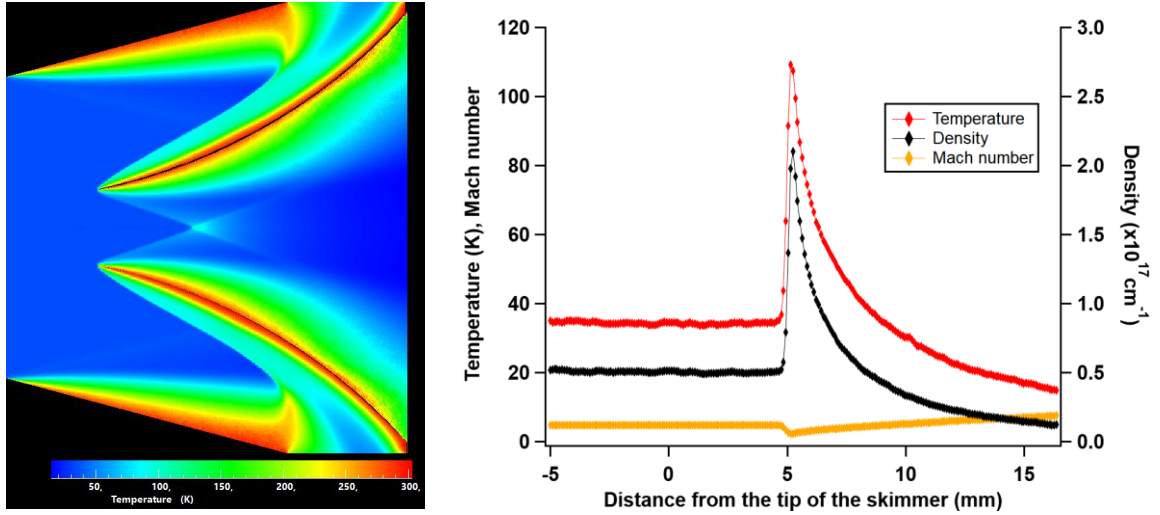


**Figure V-16. Temperature profile of the argon 35 K with 4 mm skimmer, clogging has been observed at the entry of the skimmer.**

### V.3.2. Rotation diagram (experimental characterization)

In the same way that Pitot measurements for Laval nozzles are used to validate the results given by CFD simulations, experimental measurements are needed to characterize the environment of the secondary expansion chamber into which CRESU flows are being sampled and the the probing takes place. Two vinyl cyanide spectra are recorded at each of the three different locations of the secondary expansion chamber using 5 GHz chirps targeting transitions in the range 63.85-68.85 GHz and 73-78 GHz with 250 000 averages, eight rotational transitions in the ground vibrational state have been considered in each chirp to determine the rotational temperature using the following equation:<sup>18–21</sup>

$$I = \frac{4\pi^{3/2}\omega_0^2 S \mu_i^2 g_u g_k \varepsilon}{c\sqrt{\alpha}} \frac{N_{tot}}{kTQ_{rot}} e^{-E_l/kT_{rot}} \quad \text{Equation V-2}$$

Where  $\omega_0$  is the transition frequency,  $\alpha$  the sweep rate and  $N_{tot}$ ,  $Q_{rot}$ , and  $T_{rot}$  are the column density, partition function and rotational temperature, respectively. The quantities  $S$ ,  $\mu_i$ ,  $g_u$  and  $g_k$  representing the line strength, dipole moment, nuclear spin weight and degeneracy, their values are taken from the CDMS catalogue for the multiple transitions in question,<sup>22</sup> the peak intensities of the transitions were plotted against their associated lower energy levels and fitted using a non-linear least square routine following Equation V-2 to extract the rotational temperature<sup>23</sup> as shown in Figure V-17.

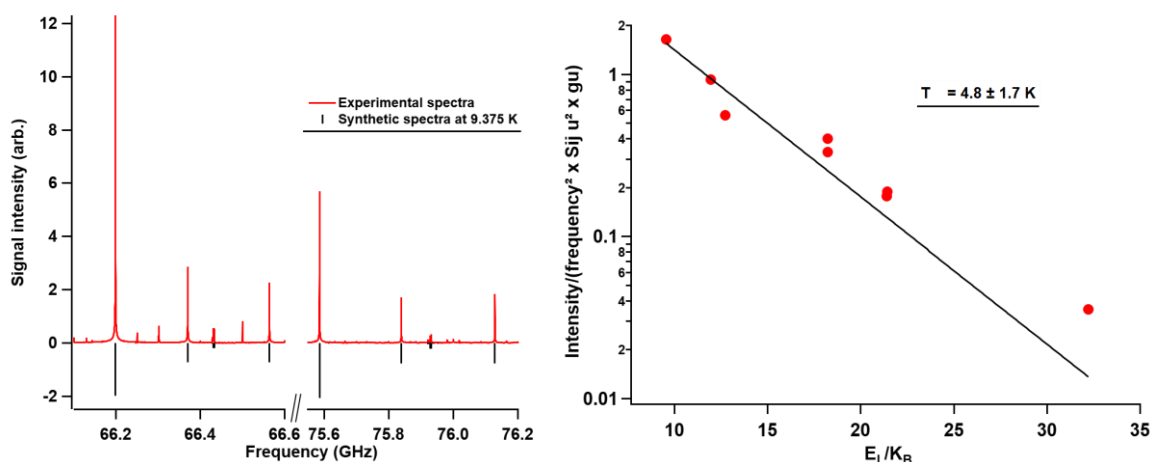


Figure V-17. Probing in the first port; left: spectrum of  $4.1 \times 10^{12}$  molecules  $\text{cm}^{-3}$  vinyl cyanide recorded from two chirps taken in argon flow at 35 K expanding via the 4 mm skimmer with 250,000 averages the black lines represent a synthetic spectrum from the CDMS at 9.375 K. On the right is the rotation diagram taken of the rotational transitions in the bands covered by the spectrum, the fitted rotational temperature is  $(4.8 \pm 1.7)$  K, with uncertainty given at the 95% confidence level.

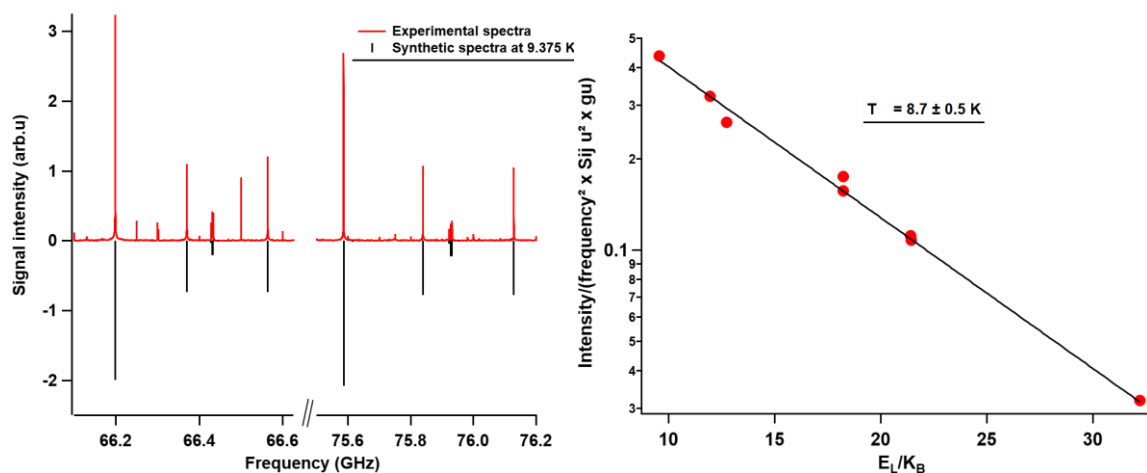


Figure V-18. Probing in the second port; ; left: spectrum of  $4.1 \times 10^{12}$  molecules  $\text{cm}^{-3}$  vinyl cyanide recorded from two chirps taken in argon flow at 35 K expanding via the 4 mm skimmer with 250,000 averages the black lines represent a synthetic spectrum from the CDMS at 9.375 K. On the right is the rotation diagram taken of the rotational transitions in the bands covered by the spectrum, the fitted rotational temperature is  $(8.7 \pm 0.5)$  K, with uncertainty given at the 95% confidence level.

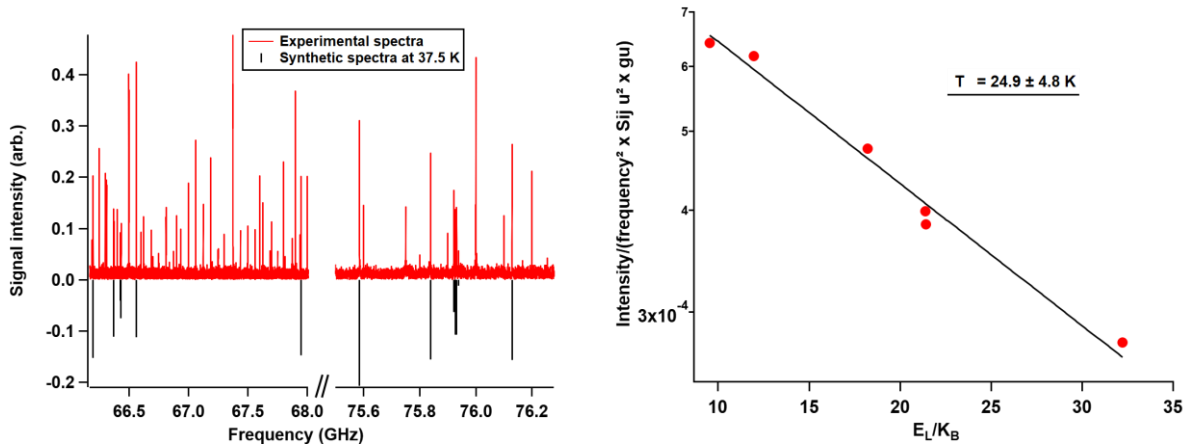


Figure V-19. Probing in the third port; left: spectrum of  $4.1 \times 10^{12}$  molecules  $\text{cm}^{-3}$  vinyl cyanide recorded from two chirps taken in argon flow at 35 K expanding via the 4 mm skimmer with 250,000 averages the black lines represent a synthetic spectrum from the CDMS at 37.5 K. On the right is the rotation diagram taken of the rotational transitions in the bands covered by the spectrum, the fitted rotational temperature is  $(24.9 \pm 4.8)$  K, with uncertainty given at the 95% confidence level.

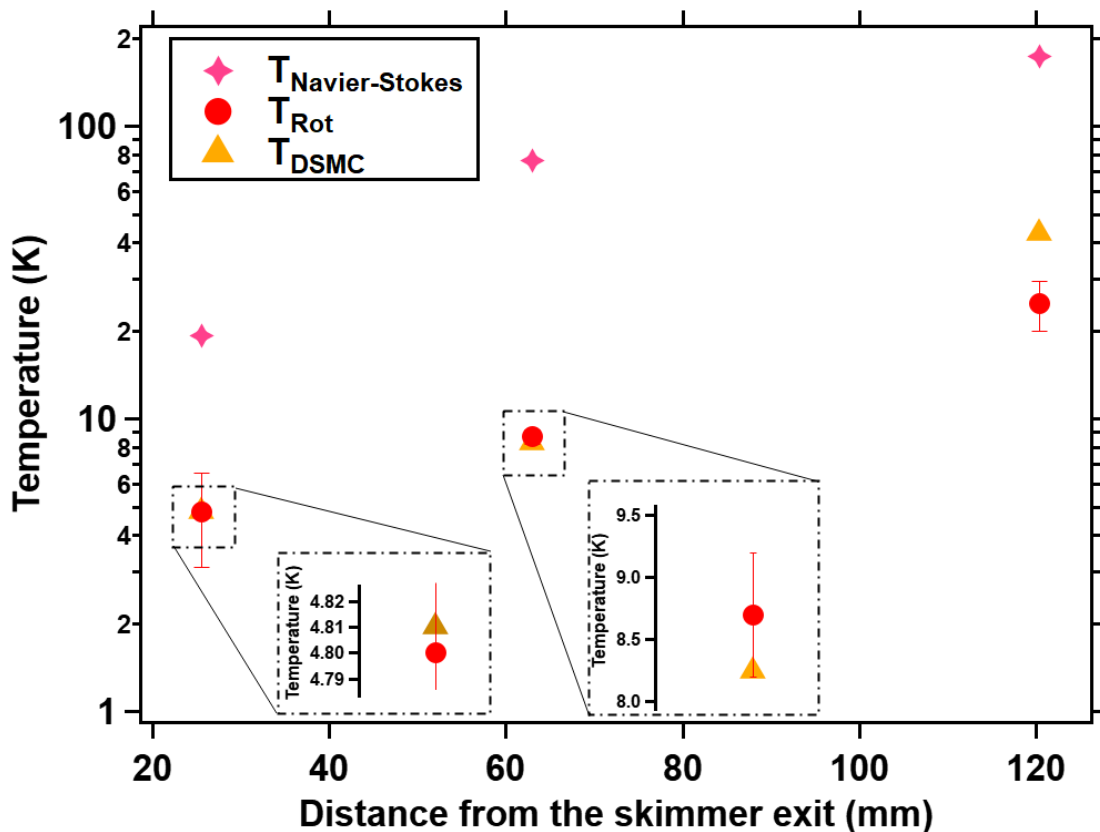
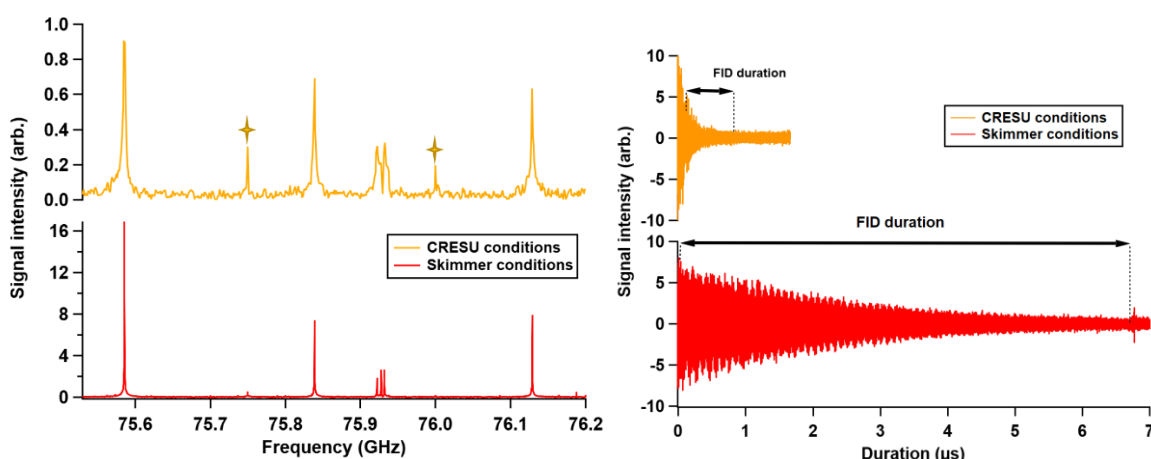


Figure V-20. Temperature plot at the three different probing locations in the skimmer chamber, the rotational temperature determined from the experiment is given in red dots, the temperature from DSMC calculations are given in orange and in purple the temperature from the Fluent solver.

The experimental results show an excellent agreement with the simulations conducted with DSMC method especially in the first two ports, in the third port there is a large discrepancy between the extracted experimental temperature and the one predicted with DSMC of about 70 %, this may stem from the low SNR of the vinyl cyanide spectrum due to the considerable density drop compared to the first port (see Figure V-14) that weakens the transition signals in addition to interferences from spurious emissions.

#### V.4. Power of the skimmer setup (comparison to classic CRESU)

To assess the improvement of the molecular signal with the secondary expansion setup, a vinyl cyanide spectrum is recorded from a 2 GHz chirp in an argon flow at 30 K (Ar-28K-0.082) under the skimmer conditions and compared to a similar spectrum under CRESU conditions. The FIDs and their associated spectra are shown in Figure V-21, the results demonstrate a big improvement in the duration of the FID which lasts for more than 5 microseconds rather than a few hundreds of nanoseconds under the CRESU conditions giving a spectrum with a considerable SNR of 1243 more than 18 times better than the one taken under the CRESU conditions, it also shows the attenuation of reflections from the excitation pulses which were one of the main challenges under the CRESU conditions as shown in the previous chapter.



**Figure V-21. Comparison of vinyl cyanide signal in an argon 30 K flow under CRESU conditions in orange and in red under the skimmer conditions using the 4 mm skimmer (a) shows the spectrum and (b) the corresponding FIDs, the stars on the spectrum under the CRESU conditions corresponds to spurs from the spectrometer electronics.**

The reduction of pressure and consequently the collision rate have increased the  $T_2$  of the molecules that measures the loss of the state of coherence created by the pulse compared to the CRESU conditions, this has its benefit on the molecular signal in terms of being able to move further away from the reflections in the FID and still acquire a decent signal. Furthermore, the reflections have been massively reduced under the new geometry of the secondary expansion chamber.

---

## Part II: Experimental results

### V.5. Photolysis and bimolecular reaction results

As shown earlier in section V.3 as the probing is taken further away from the skimmer exit, the vinyl cyanide SNR weakens, this stems from the gradual decrease of the density in the probing zone followed by the increase of the temperature. Figure V-14 that gives the flow conditions in the post skimmer expansion zone along the axis of the chamber shows that the density drops by half by moving from the first port to the second port and by an order of magnitude if the probing is taken in the third port. To benefit from the high density, low temperature conditions, all reactions are probed in the first port region.

#### V.5.1. Photolysis Results

One of the most common constraints in studying cold reactions (at 50 K and below) in supersonic beams is clustering, where radiating molecules induced by the high collision rate with the carrier gas tend to form in an aggregation process van der Waals complexes of different sizes (dimers, trimers or more). This process can lower the concentration of molecules probed or even completely destroy the uniform flow at higher densities. In either case the molecular signal is badly affected, this is why the density of the molecules of interest in the CRESU flow must be carefully controlled. Figure V-22 shows the manifestation of clustering and its effect on the molecular signal of vinyl cyanide in the Ar-35K-0.28 flow expanding via the 4 mm skimmer.

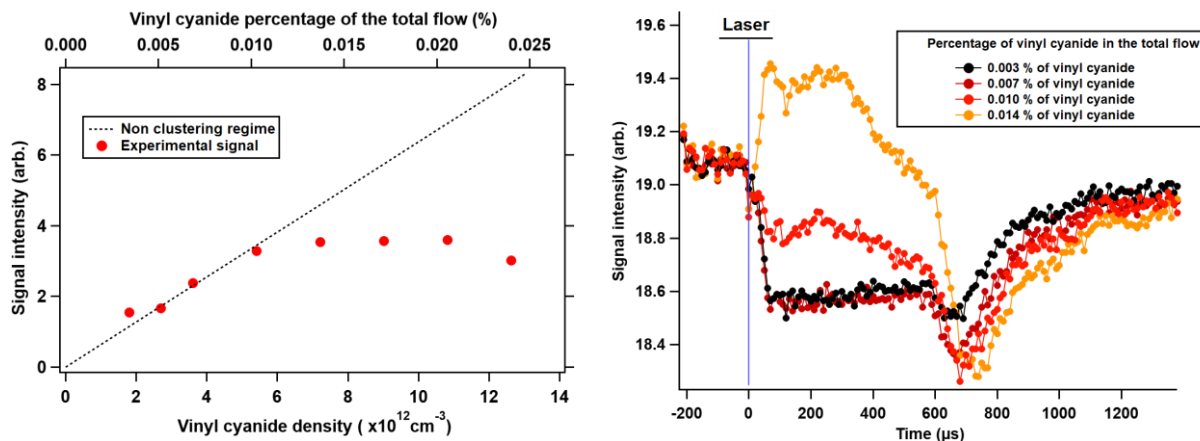


**Figure V-22.** Signal variation of vinyl cyanide at different concentration in the Ar-35K-0.28 nozzle expanding via the 4 mm skimmer, left figure shows the direct signal from the flow, right figure gives the signal variation when vinyl cyanide is photolysed by a 193 nm excimer laser. The exit of the nozzle is situated at 20 cm from the skimmer entry corresponding to 380  $\mu\text{s}$  of uniform flow conditions, for clarity the plots are offset to the same initial intensity.

At concentrations of 0.007% and lower of the total flow, the vinyl cyanide signal is linearly proportional to its concentration indicating that flow is in a non-clustering regime, the signal starts deviating from the linear regime beyond around 0.01% of the total flow. Starting from this point increasing the concentration of molecules in the flow will not contribute to increasing the signal as they will be forming clusters.

This interpretation is reinforced by results from 193 nm excimer laser photolysis along the flow. At 0.007% of vinyl cyanide from the total flow and lower, the concentration of vinyl cyanide decreases after the laser shot after 80  $\mu\text{s}$  delay which corresponds to the distance between the skimmer orifice and the probing horns. During this time, it is the vinyl cyanide flowing inside the secondary expansion chamber until the probing region that is being photolysed. As the gas is expanding rapidly after the skimmer entrance, only a small fraction of the vinyl cyanide molecules passing between the detection horns is photolysed. Once the gas that was upstream of the skimmer when the laser fires arrives between the horns, a clear depletion in the vinyl cyanide signal can be seen. The concentration of vinyl cyanide then remains constant throughout the uniform conditions of approximately 400  $\mu\text{s}$ . The dip at 700  $\mu\text{s}$  in the time dependent signal curve represents the nozzle throat region where the density is higher than the uniform flow. The vinyl cyanide curve then starts rising indicating the laser energy have been absorbed in the high density regions, nozzle throat and reservoir. The total depletion

of vinyl cyanide in the CRESU flow in the non-clustering regime is observed to be between 9 to 10 %, (plots in Figure V-22 (b) are offset).

At 0.010 % vinyl cyanide of the total flow, the depletion is less than 3% indicating that clusters are being formed in the CRESU flow, the intensity curve completely rises after the laser shot at a concentration of 0.014% of the total flow, this refers to massive formation of clusters that are getting destroyed by the laser forming monomers of vinyl cyanide, the curve then decreases over time because of the time required for the formation of the clusters.

#### **V.5.1.1. Laser through the reservoir and the skimmer**

Photolysis processes can be conducted via the skimmer to the reservoir or through reservoir towards the skimmer (see Figure V-3), the first option is beneficial to the laser fluence as the beam path is shorter with fewer optics and therefore less losses. Photolysing through the reservoir induces additional losses that stem from the long way of the laser beam to the chamber which weakens its fluence by absorption in the case of 193 nm wavelength and the use of more optics. The second option was adopted during measurements to take advantage of the photolysing laser beam size (more than 10 mm) that covers a larger section of the isentropic core. Firing through the skimmer will limit the beam size to the diameter of the skimmer (4mm and less) which makes it more sensitive to misalignment and potential diffusion to boundaries (see Figure V-23).

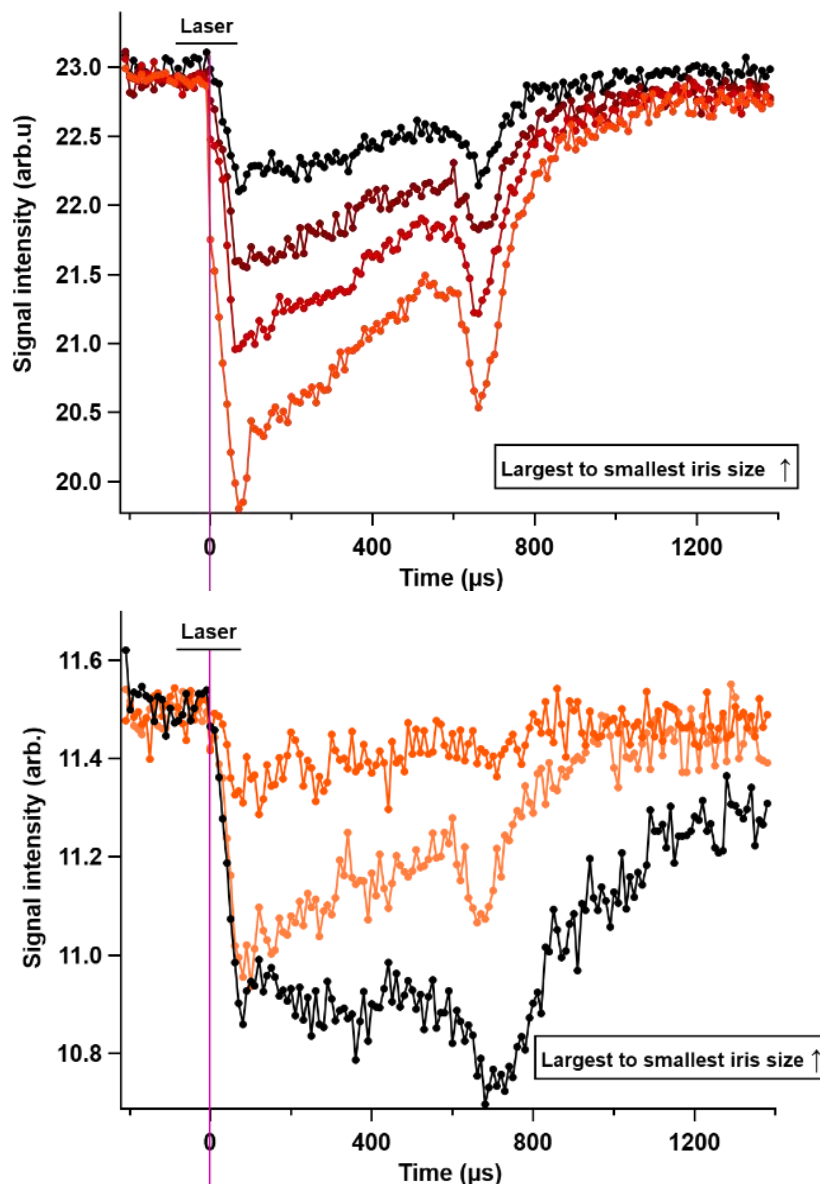
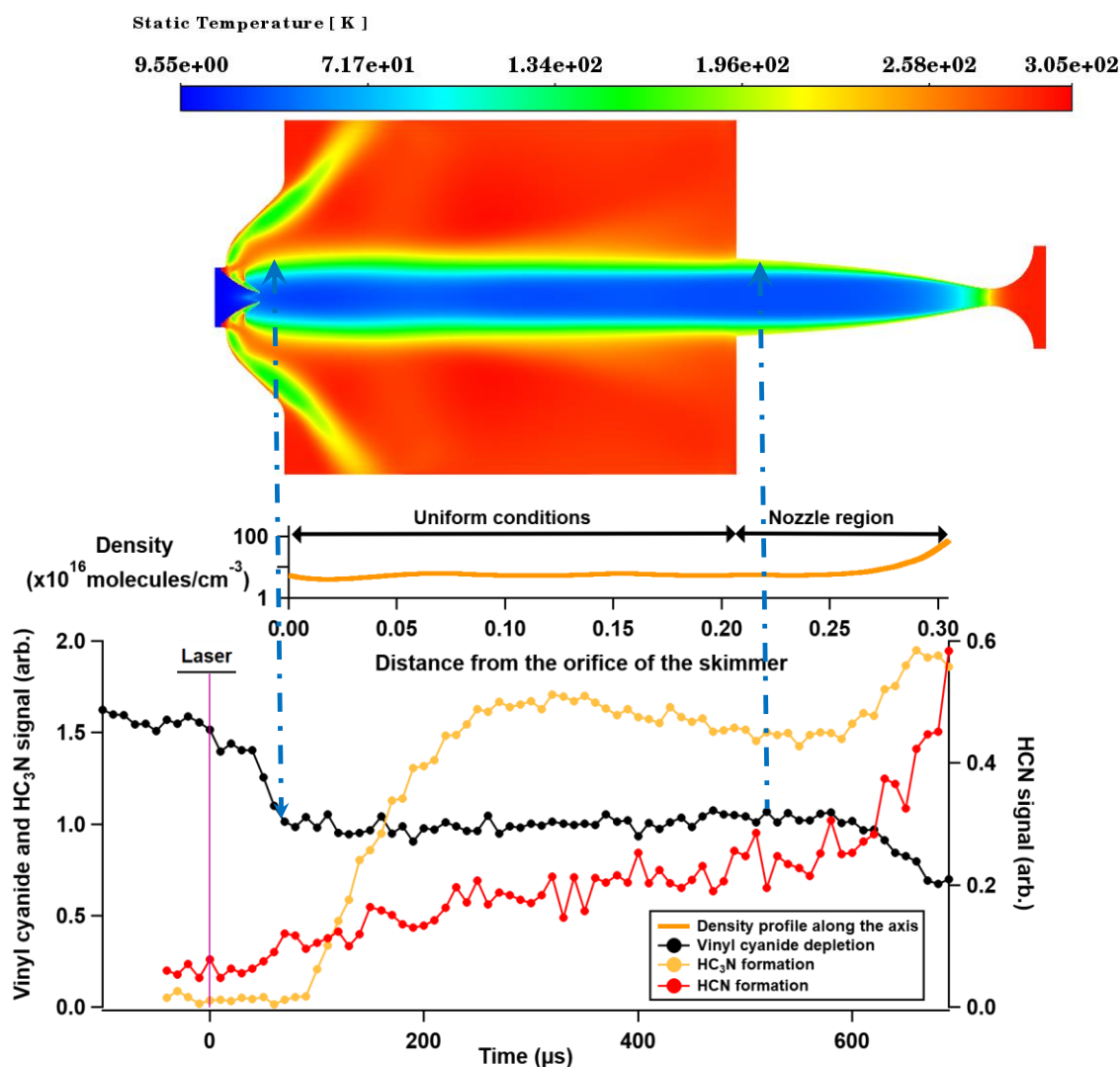


Figure V-23. Photolysis of vinyl cyanide with 193 nm excimer laser in the Ar-35K-0.28 flow expanding via the 4 mm skimmer at different laser beam sizes, top panel shows the laser firing through the skimmer, bottom panel when the laser is firing through the reservoir. For clarity, all the curves are offset to the same initial signal intensity, same concentration of vinyl cyanide and procedure of recording is used during the measurements while changing the diameter of the photolysing laser beam via the iris, the smallest iris size corresponds to 4 mm the diameter of the skimmer while the larger size corresponds to the diameter of the nozzle throat  $\sim 7.3$  mm.

Using the optimized concentration of vinyl cyanide of 0.007% of the total Ar-35K-0.28 flow, the photolysis products from vinyl cyanide at 193 nm were probed, both  $\text{HC}_3\text{N}$

and HCN have been detected and the associated time dependent signal in every region of the flow are shown in Figure V-24.



**Figure V-24.** Photolysis of vinyl cyanide with 193 nm excimer laser in the argon 35 K flow expanding via the 4 mm skimmer, on top figure a 2D temperature profile of the argon 35 K flow generated from the Ar-35K-0.28 nozzle, the middle figure shows the CFD density profile on a logarithmic scale along the axis inside the Ar-35K-0.28 nozzle and in the CRESU chamber, the bottom figure shows the vinyl cyanide depletion in black, the  $\text{HC}_3\text{N}$  and the HCN formation in orange and red probed on the  $J_{K_a, K_c} = 7_{07} - 6_{06}$ ,  $J = 7-6$  and  $J = 1-0$  respectively. Vinyl cyanide plot is offset by -5 on the signal intensity scale.

At time zero corresponding to the laser shot, the vinyl cyanide is depleted by 9% put VCN on it scale axis to get this depletion and continue with a stable concentration along the uniform flow, followed by an increase of the HCN curve indicating its formation. The HCN time dependent signal keeps gradually increasing along the uniform flow until

the throat region, this is may stem from possible relaxations from higher vibrational energy levels to the rotational transition being probed which is in the ground vibrational state. For the HC<sub>3</sub>N there is 100 microseconds of delay before detecting the first time dependent signal this may be related to the rotational relaxation time required for the molecule under those flow conditions, a similar delay is observed under the CRESU conditions.

## V.5.2. Bimolecular reactions results

Reactions (2) and (3) were carried out under the Ar-35K-0.28 nozzle conditions with the 4 mm skimmer. At first BrCN was used as precursor for its higher vapor pressure and photolysed with the 193 nm excimer laser to generate the CN radicals, though subsequent measurements were carried out with ICN at 248 nm.

### V.5.2.1. CN+ Acetylene reaction at 193 nm

Reaction (2) is a single channel reaction that yields HC<sub>3</sub>N+H as products has been studied before under the CRESU conditions at 30 K (results are given Theo Guillaume's thesis). This reaction was used to benchmark the new setup,  $2.7 \times 10^{13} \text{ cm}^{-3}$  of ICN was injected in the flow then photolysed with the 193 nm photolysis of the BrCN precursor at a laser. The CN radicals then react with  $1.18 \times 10^{14} \text{ cm}^{-3}$  of C<sub>2</sub>H<sub>2</sub>. A single frequency pulse was used targeting the J=7-6 rotational transition at 63.686052 GHz.

The time dependent spectra at different regions of the CRESU flow and the corresponding signals are shown in Figure V-25 (a) and (b) respectively. The results are obtained with averaging signal from four scans of 100,000 averages each, recorded along 800  $\mu\text{s}$  of the flow time including 100  $\mu\text{s}$  before the laser shot.

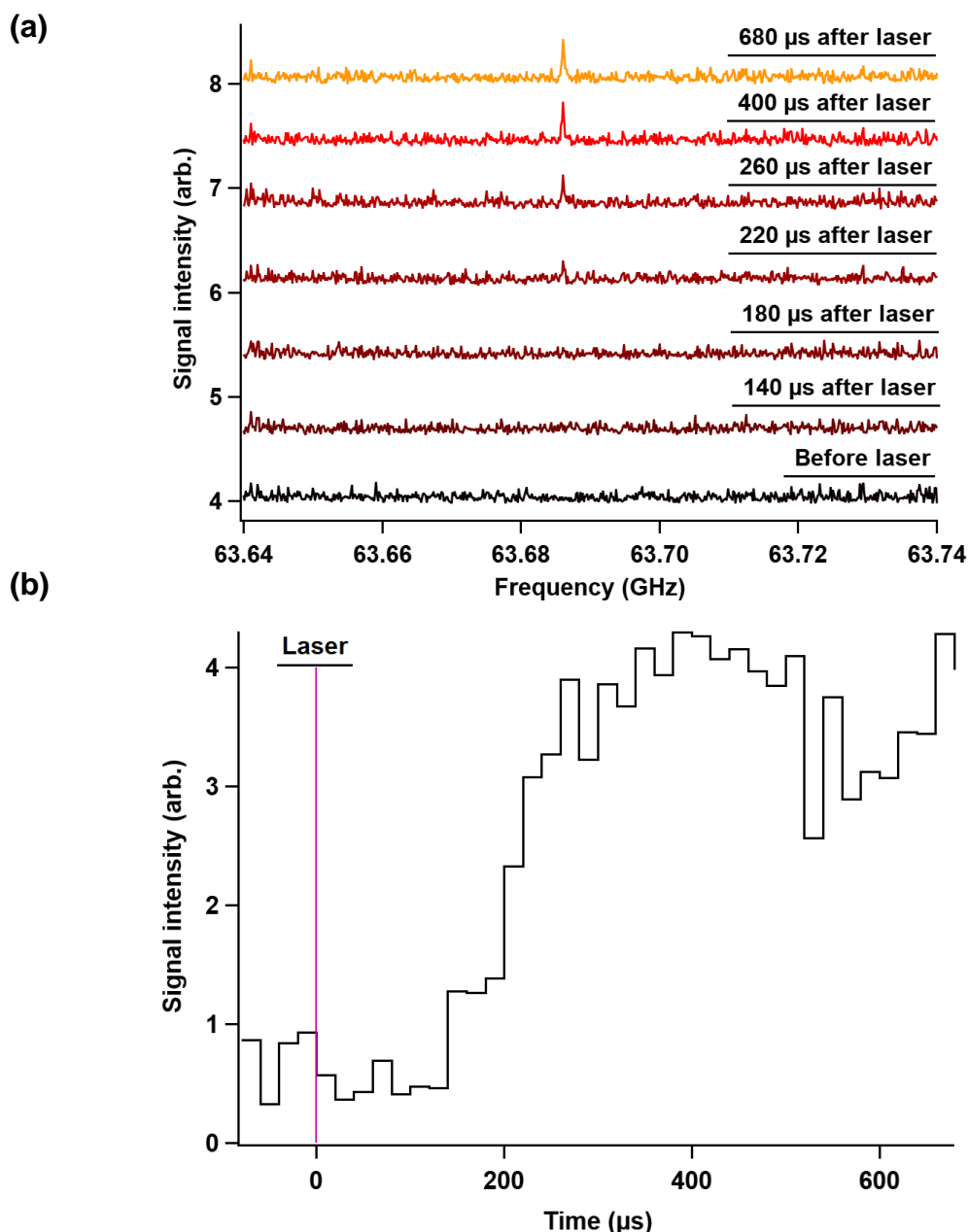


Figure V-25. HC<sub>3</sub>N from CN+C<sub>2</sub>H<sub>2</sub> reaction in the Ar-35K-0.28 flow expanding via the 4 mm skimmer; (a) is the spectrum of J=7-6 rotational transition of HC<sub>3</sub>N taken at different times of the reaction in the uniform flow, (b) is the corresponding time dependent signal, the signal is recorded by averaging 4 scans of 100,000 averages.

#### V.5.2.2. CN+ Ethylene reaction at 193 nm

The CN+C<sub>2</sub>H<sub>4</sub> reaction which is a potentially dual channel reaction was studied under the CRESU conditions as mentioned earlier, however neither vinyl cyanide nor HCN were detected in the flow, lowering the temperature and pressure in the secondary expansion created favorable condition and led to the detection of the vinyl cyanide

signal from this reaction.  $2.56 \times 10^{13} \text{ cm}^{-3}$  of BrCN with  $9.53 \times 10^{13} \text{ cm}^{-3}$  of  $\text{C}_2\text{H}_4$  were injected in the flow. Figure V-26 (a) and (b) show the time dependent spectra and the associated signals of the rotational transition  $J_{K_a, K_c} = 7_{0,7} - 6_{0,6}$  of vinyl cyanide at 66.1983390 GHz recorded from a single frequency pulse with 100 000 averages.

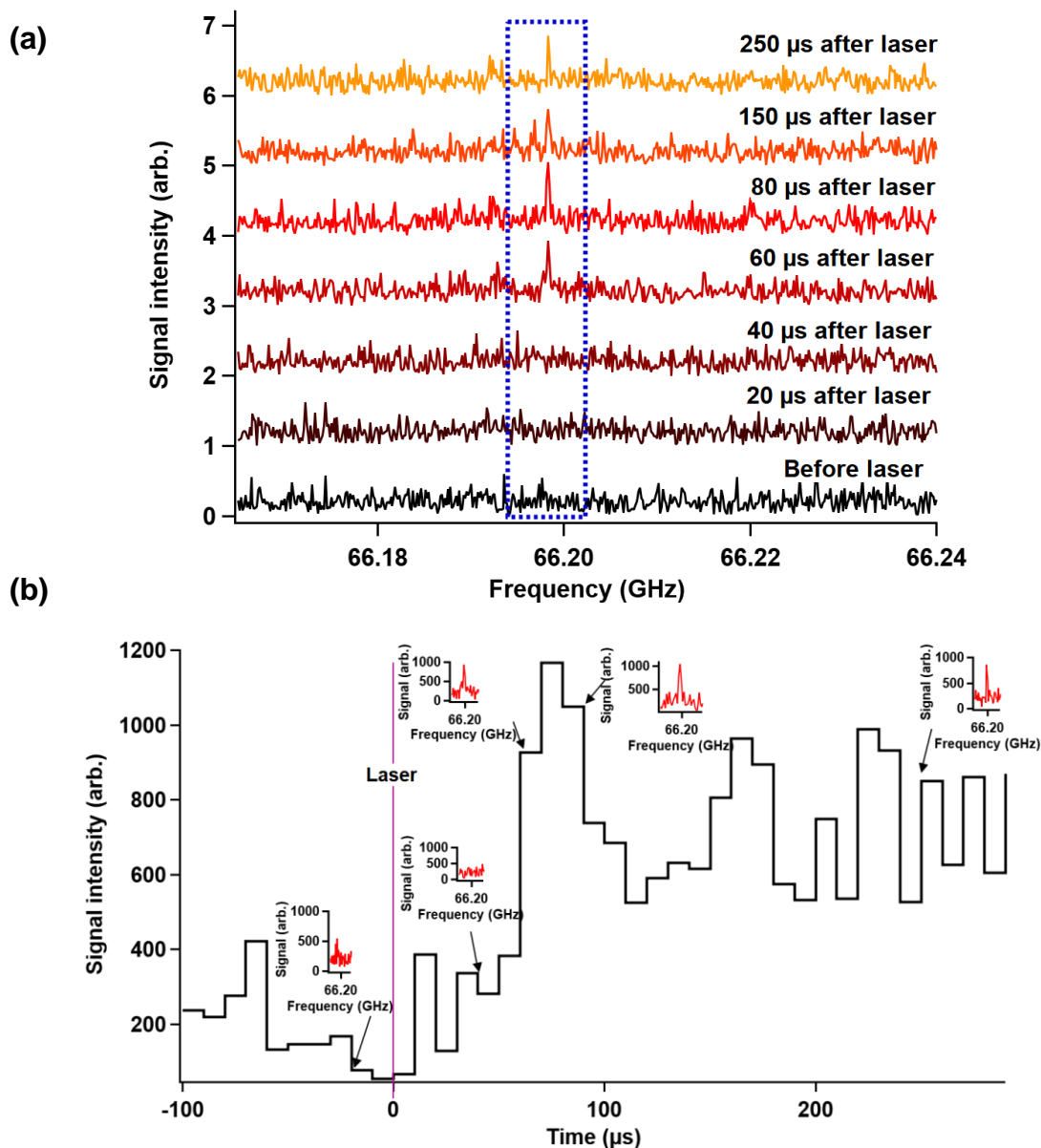


Figure V-26. Vinyl cyanide from  $\text{CN} + \text{C}_2\text{H}_4$  reaction in the Ar-35K-0.28 flow expanding via the 4 mm skimmer; (a) is the spectrum of  $J_{K_a, K_c} = 7_{07} - 6_{06}$  rotational transition of vinyl cyanide taken at different times of the reaction in the uniform flow, (b) is the corresponding time dependent signal, the signal is recorded by averaging a scan of 100,000 averages.

The vinyl cyanide SNR given by the reaction is about three which is very low, this implies that it is highly unlikely to be able to detect low concentration products such as HCN and therefore branching ratios cannot be determined. The low SNR could be due to multiple factors, first the precursor stability, as the BrCN sublimates its temperature decreases and therefore its concentration in the flow is reduced during the scan by more than 30%, secondly and most importantly, the excimer laser power drops off during the scan. At 193 nm it was needed to refill the gases used in the excimer laser every  $10^6$  shots that is 10 x 100,000 averaged scans on average in order to boost its power up. Here we note that 100,000 averaged scans take 16 minutes running at 100 Hz which is the maximum frequency of the excimer laser. Switching the excimer laser to 248 nm solves the problem of stability and increases the laser output power, thus its fluence more than it is at 193 nm. The ICN however must be used to generate the CN radicals as BrCN does not absorb sufficiently at 248 nm. A heat generator is implemented to stabilize the ICN concentrations as it sublimates (presented in chapter III), it is set at a slightly higher temperature than room temperature (generally 1-2 degrees more).

Figure V-27 shows the ICN stability over 20 minute scan with and without the heat stabilizer in the argon 35 K flow.

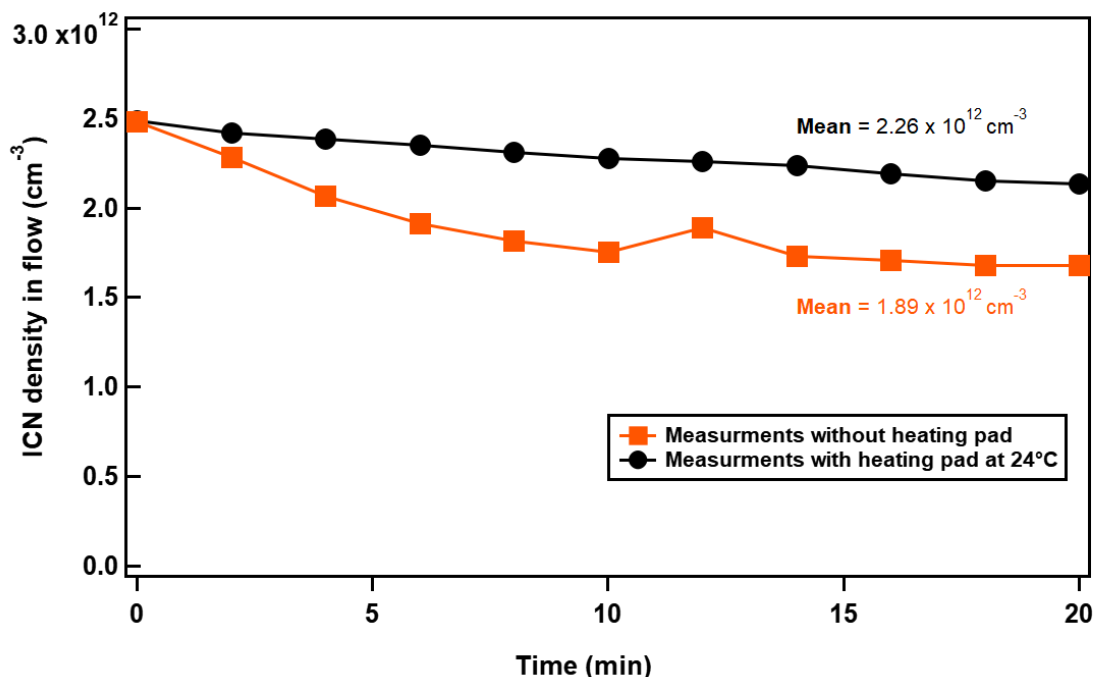
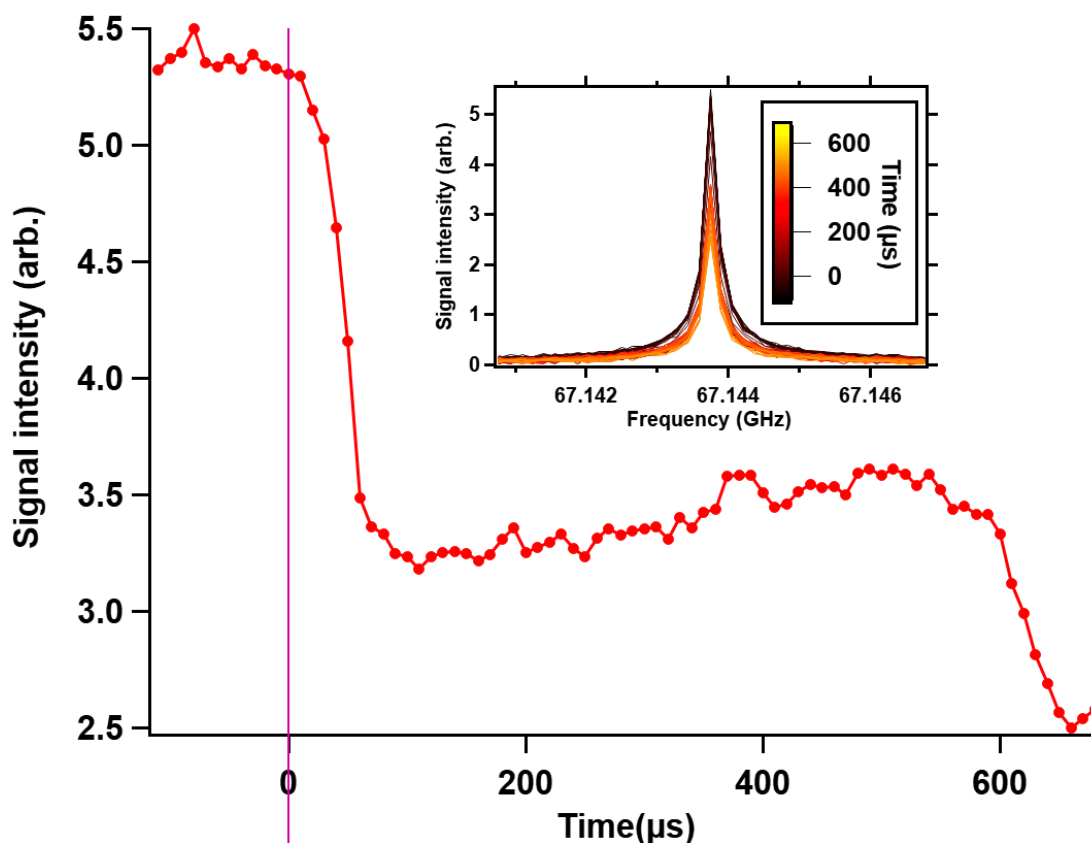


Figure V-27. ICN stability curve during a scan

As the ICN cannot be used for photolysis investigation since it has less than 1 % depletion at 248 nm, the laser alignment and its output power are investigated with the photolysis of ozone by targeting the transition at 67.1438 GHz.<sup>24</sup> The results show a depletion of more than 40% which is significant compared to vinyl cyanide and ICN making reactions involving oxygen really interesting under the new conditions.



**Figure V-28.** Photolysis of ozone with 248 nm excimer laser in the Ar-35K-0.28 flow expanding via the 4 mm skimmer, inset represents the O<sub>3</sub> time dependent spectra.

Reaction 3 is then studied by photolysing  $(2.45 \pm 0.24) \times 10^{12} \text{ cm}^{-3}$  of the ICN precursor with 248 nm at a fluence of  $2.86 \times 10^{16} \text{ pulse}^{-1} \text{ cm}^{-2}$  which generates  $(3.40 \pm 0.33) \times 10^{10} \text{ cm}^{-3}$  of the CN radicals that reacts with  $9.93 \times 10^{13} \text{ cm}^{-3}$ . 100,000 averaged scans were recorded along 800  $\mu\text{s}$  including 100  $\mu\text{s}$  before the laser shot, The results are shown in Figure V-29.

## V.5.2.3. CN+ Ethylene reaction at 248 nm

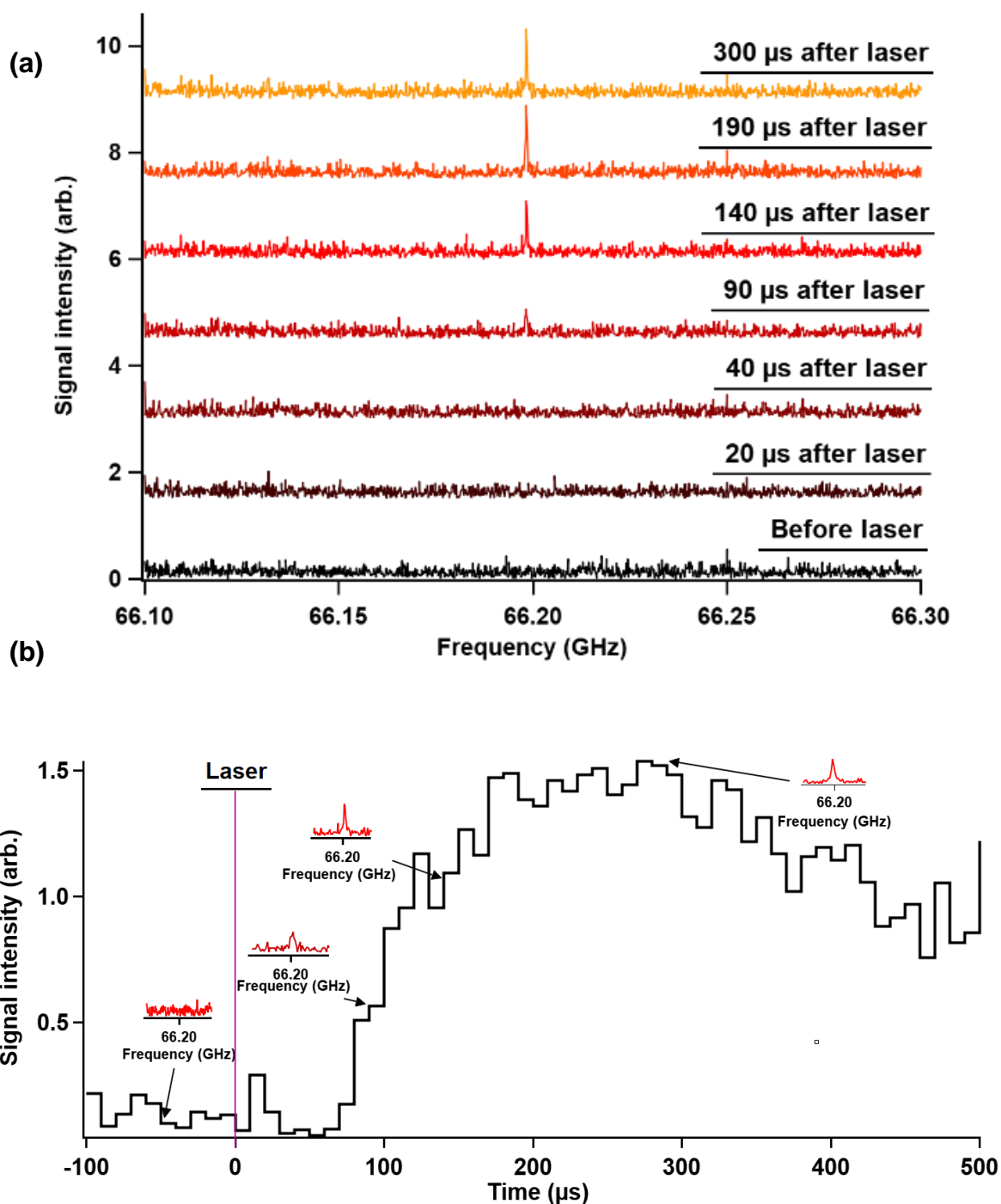
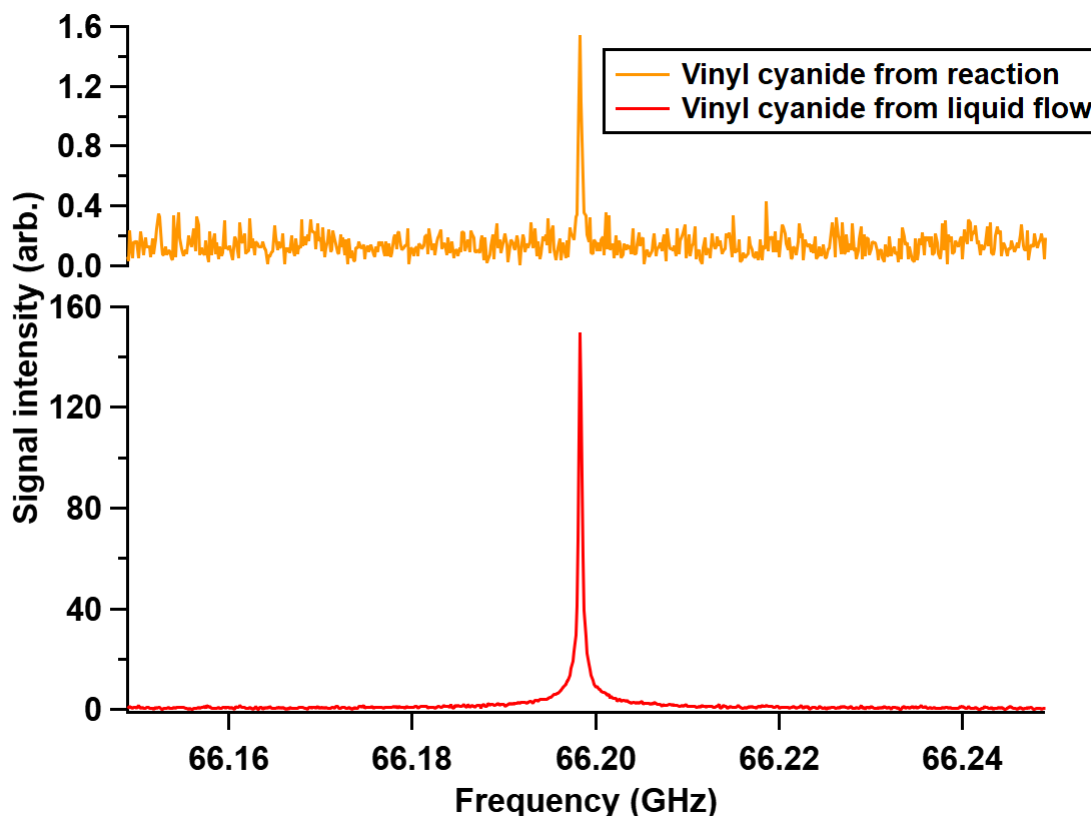


Figure V-29. Vinyl cyanide from the CN+C<sub>2</sub>H<sub>4</sub> reaction; (a) is the spectrum of  $J_{K_a,K_c} = 7_{07} - 6_{06}$  rotational transition of vinyl cyanide taken at different times of the reaction in the uniform flow, (b) is the corresponding time dependent signal.

Vinyl cyanide was detected as a product from the first channel of reaction 3 with an SNR of 24, to determine the density of the product, the signal intensity was calibrated with a signal recorded from a vinyl cyanide source of a well-known density under the same conditions and with the same analysis as shown in Figure V-30.



**Figure V-30. Calibration of vinyl cyanide from reaction; in orange  $J_{K_a, K_c} = 7_{0,7} - 6_{0,6}$  rotational transition of vinyl cyanide from reaction 3, in red same transitions of a well-known concentration of vinyl cyanide from a flow source.**

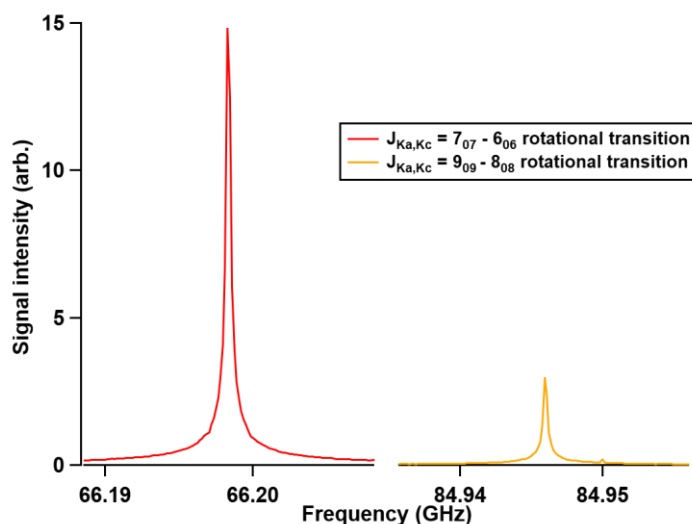
The signal from the reaction was averaged along the uniform flow after the reaction is finished between 200 and 300  $\mu\text{s}$ . The calculations are presented in Table V-1, the amount of vinyl cyanide yielded from the reaction is  $(4.84 \pm 0.35) 10^{10} \text{ cm}^{-3}$ , the result is confirmed with an estimation of the CN radicals generated from photolysing the ICN precursor assuming a quantum yield of one for photolysis and all the CN radicals produced will react with  $\text{C}_2\text{H}_4$  to yield vinyl cyanide as CN is the limiting reagent, the latter is a valid hypothesis in the linear non clustering regime. The value given by the CN concentration with the error range indicates that the vinyl cyanide is the dominant channel in reaction 3 with 92% efficiency.

Table V-1: Calibration of vinyl cyanide yielded from CN+C<sub>2</sub>H<sub>4</sub> reaction

|   | Parameters (unit)  | Values $\pm \sigma$   |
|---|--|---|
| Calibration from a vinyl cyanide source | Vinyl cyanide density (cm <sup>-3</sup> )                    | $3.54 \times 10^{12} + 0.21 \times 10^{12}$                     |
|   | Vinyl cyanide (intensity-background) (arb.)                  | $1.5 \times 10^5 \pm 89$  |
|   | Vinyl cyanide from reaction (intensity-background) (arb.)    | $1537.4 \pm 68.7$   |
|   | <b>Vinyl cyanide yielded from reaction (cm<sup>-3</sup>)</b> | <b><math>4.84 \times 10^{10} \pm 0.35 \times 10^{10}</math></b> |
| Calibration with ICN                    | ICN in the flow (cm <sup>-3</sup> )                          | $2.45 \times 10^{12} \pm 0.24 \times 10^{12}$                   |
|   | Photon flux (photons pulse <sup>-1</sup> cm <sup>-2</sup> )  | $4.42 \times 10^{16} \pm 2.21 \times 10^{17}$                   |
|   | <b>Vinyl cyanide yielded from reaction (cm<sup>-3</sup>)</b> | <b><math>5.27 \times 10^{10} \pm 0.58 \times 10^{10}</math></b> |

#### V.5.2.4. Branching ratio (vinyl cyanide and HCN from CN+C<sub>2</sub>H<sub>4</sub> reaction)

Vinyl cyanide was successfully detected via its strongest transition under the skimmer conditions, to investigate the efficiency of the second channel of reaction (3), we probed the HCN and vinyl cyanide at the same time with a two-color pulse<sup>25</sup> targeting the transitions J=1-0 and J<sub>ka,kc</sub>= 9<sub>0,9</sub> - 8<sub>0,8</sub> at 88.6316022 GHz and 84.946 GHz for HCN and vinyl cyanide respectively. The HCN transition is the only existing transition in the E band. As for the vinyl cyanide transition, although being weaker than the J<sub>ka,kc</sub>= 7<sub>0,6</sub>-6<sub>0,6</sub>, it is chosen for it is the strongest transition close to that of HCN within the digitizer bandwidth (see Figure V-31).



**Figure V-31. Comparison of the vinyl cyanide transitions in red  $J_{K_a,K_c} = 7_{0,7} - 6_{0,6}$  and in orange  $J_{K_a,K_c} = 9_{0,9} - 8_{0,8}$**

The  $\pi/2$  pulse<sup>26</sup> was determined for both transitions using the 86.1 GHz LO to compare the relative intensities and measure the branching ratio of the two channels as shown in Figure V-32 (a) and (b). 70 ns is the  $\pi/2$  duration time for HCN and 100 ns is required for vinyl cyanide.

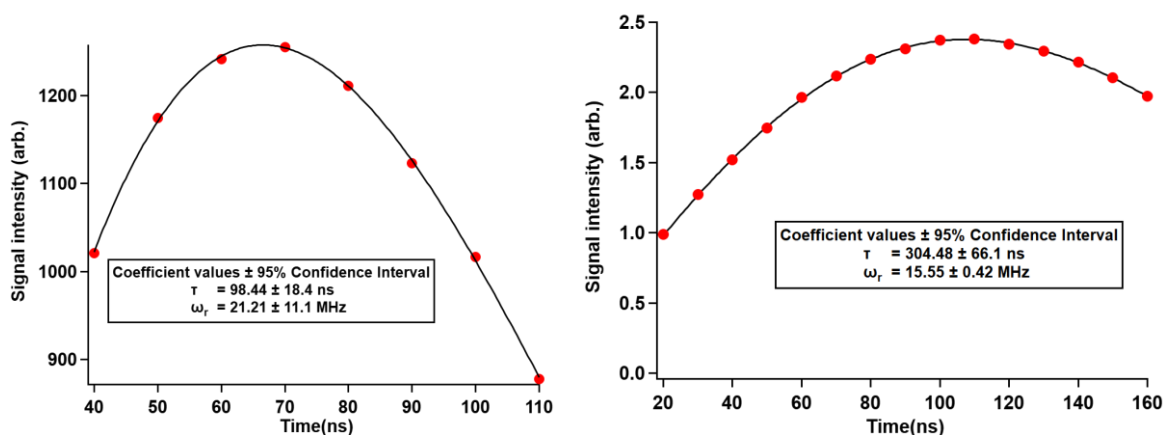


**Figure V-32.  $\pi/2$  pulse HCN and vinyl cyanide: a) the  $J = 1-0$  HCN transition, b) vinyl cyanide  $J_{K_a,K_c} = 9_{0,9} - 8_{0,8}$  transition**

Figure V-33 shows the spectrum of HCN and vinyl cyanide recorded from a two-color pulse in the Ar-35K-0.28 flow expanding through the 4 mm skimmer, 160 frames were recorded during a 100,000 averaged scans, 30 frames have been subtracted to eliminate the signal of HCN before the laser shot<sup>4</sup>, leaving 130 frames that were

<sup>4</sup> The HCN can be formed from impurities in the ICN independently of reaction 3, the signal of HCN before laser shot is subtracted from the final intensity of HCN after the reaction

horizontally averaged by 10 to get 13 time dependent signals for the determination of the reaction branching ratio(see chapter III), here we considered only the signal at 200 microseconds for HCN and VCN as the time dependent signal starts decreasing afterwards (see A.V in the appendix), the problem is discussed in the last part of the chapter).

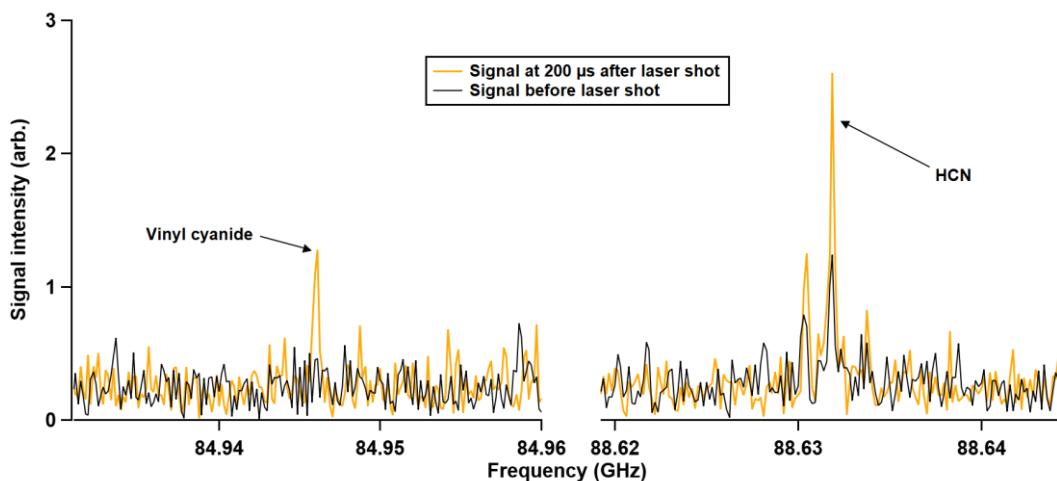


**Figure V-33.** The  $J=1-0$  and  $J_{K_a, K_c} = 9_{0,9}-8_{0,8}$  transitions of HCN and vinyl cyanide respectively recorded from a two-color pulse in the Ar-35K-0.28 flow expanding through the 4 mm skimmer, Black and orange lines represent the signal before and after the laser shot respectively.

**Table V-2: Calibration of vinyl cyanide yielded from  $CN+C_2H_4$  reaction**

| Parameters (unit) <sup>5</sup>   | Values $\pm \sigma$                 |
|--|-------------------------------------|
| Synthetic intensity of HCN (CDMS)                                      | 3.854                               |
| Synthetic intensity of vinyl cyanide (CDMS)                            | 0.063                               |
| Intensity ratio with 50% for each channel (HCN/vinyl cyanide)          | 61.17                               |
| Experimental intensity of HCN (peak-background $\pm\sigma$ )           | $136.19 \pm 13.01$                  |
| Experimental intensity of vinyl cyanide (peak-background $\pm\sigma$ ) | $81.39 \pm 13.01$                   |
| Experimental Intensity ratio (HCN/vinyl cyanide)                       | $1.67 \pm 0.31$                     |
| <b>Channel (a) efficiency</b>  | <b><math>0.973 \pm 0.155</math></b> |
| <b>Channel (b) efficiency</b>  | <b><math>0.027 \pm 0.003</math></b> |

<sup>5</sup> Synthetic intensities were taken from CDMS using the Pickett program to generated the spectra at 5 K

The branching ratio from reaction (3) are in agreement with an earlier study by Gannon et al<sup>1</sup> at higher temperature which suggests that channel one is predominant in this reaction and that HCN could be formed with C<sub>2</sub>H<sub>4</sub> but at a very low rate (less than 5 %) and could increase with larger hydrocarbons.

## Discussion

With the new setup developed, both temperature and pressure were reduced to the optimum minimum with the 4 mm skimmer, the pressure is lowered by nearly 30 times compared to the CRESU conditions, this enabled the detection of new reaction products and determination of their corresponding branching ratio.

For both reactions studied as well as photolysis, there is a delay of 80 microseconds corresponding to the distance between the entry of the skimmer and the position of the horns, during this time the reaction is not supposed to take place as it should be finished within the CRESU region before entering the skimmer. Should there be any remaining CN radicals, the density and the collisional rate are too low for the reaction to keep going under the secondary expansion conditions given that the pressure is reduced by 30 times in the skimmer environment for the Ar-35K-0.28 and the 4 mm skimmer, the reaction time is therefore significantly lowered which makes it unlikely for the reaction to proceed in the secondary expansion chamber with the assumption that the reaction occurs with the same rate constant under temperature of the sampled flow. This is clearly shown in Figure V-29 where the signal of vinyl cyanide as a reaction product remains at the noise level after the laser shot by exactly 80  $\mu$ s representing the life time of molecules in secondary expansion chamber from the entry of the skimmer to the probing horn antennas of the spectrometer.

A gradual decrease of signal after the formation of the products (see Figure V-25 and Figure V-29) is observed in the uniform flow, this pattern may stem from possible misalignments of the laser beam and/or nozzle parallelism to the axis of the chamber, the problem was also observed in photolysis measurements (see Figure V-28 and Figure V-34). The diffusion to boundary layers is also considered, although it is very unlikely to be solely responsible given that similar effects were observed with the Ar-50K-0.7 nozzle that operates at higher pressure than the Ar-35K-0.28 and the Ar-50K-0.3 nozzles. More quantitative work is needed with multiple nozzles and species to determine the sources of the problem.

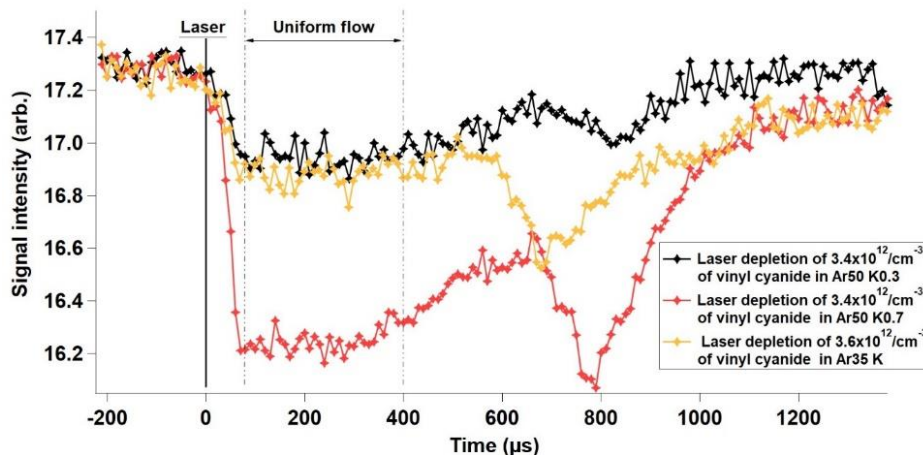


**Figure V-34. Photolysis of vinyl cyanide in the Ar-35K-0.28, Ar-50K-0.3 and Ar-50K-0.7 expanding through the 4 mm skimmer. For clarity, the plots are offset to the same initial signal intensity.**

## Conclusions and outlook

Decoupling the reaction from the probing environment gives the possibility to study reactions at high temperatures (more than 100 K) with high pressure and still be able to detect the products since the probing will take place in lower pressure and temperature environment than that of the reaction.

The detection of vinyl cyanide, a relatively heavy molecule, shows that the list of reaction products that can be studied can be extended to the Ka region for larger molecules like benzonitrile and pyridine. Another perspective that can be invoked from the photolysis results of ozone highlighting that reactions involving oxygenated molecules can be very suitable candidates especially with the limitations presented with ICN and BrCN as precursors.

The system does present some shortcomings, the pressure gain comes at the cost of density as the pressure could not be lowered to its minimum given that density would also follow which weakens the molecular signal (see Figure V-12). The fact that only regions within 4 mm diameter or less of the flow cross section is probed under the skimmer conditions is a serious limiting factor demonstrates that there are still be improvements that can be made with other techniques that can overcome those limitations and this is what will be discussed in the next chapter that introduces the pulsed system where problem of limited probing cross section, sensitive alignment and possible diffusion matter less.

## References

- (1) Gannon, K. L.; Glowacki, D. R.; Blitz, M. A.; Hughes, K. J.; Pilling, M. J.; Seakins, P. W. H Atom Yields from the Reactions of CN Radicals with C<sub>2</sub>H<sub>2</sub>, C<sub>2</sub>H<sub>4</sub>, C<sub>3</sub>H<sub>6</sub>, Trans-2-C<sub>4</sub>H<sub>8</sub>, and Iso-C<sub>4</sub>H<sub>8</sub>. *J. Phys. Chem. A* **2007**, *111* (29), 6679–6692. <https://doi.org/10.1021/jp0689520>.
- (2) Choi, N.; Blitz, M. A.; McKee, K.; Pilling, M. J.; Seakins, P. W. H Atom Branching Ratios from the Reactions of CN Radicals with C<sub>2</sub>H<sub>2</sub> and C<sub>2</sub>H<sub>4</sub>. *Chemical Physics Letters* **2004**, *384* (1–3), 68–72. <https://doi.org/10.1016/j.cplett.2003.11.100>.
- (3) Trevitt, A. J.; Goulay, F.; Meloni, G.; Osborn, D. L.; Taatjes, C. A.; Leone, S. R. Isomer-Specific Product Detection of CN Radical Reactions with Ethene and Propene by Tunable VUV Photoionization Mass Spectrometry. *International Journal of Mass Spectrometry* **2009**, *280* (1), 113–118. <https://doi.org/10.1016/j.ijms.2008.07.033>.
- (4) Biennier, L.; Sabbah, H.; Chandrasekaran, V.; Klippenstein, S. J.; Sims, I. R.; Rowe, B. R. Insights into the Role of Polycyclic Aromatic Hydrocarbon Condensation in Haze Formation in Jupiter's Atmosphere. *A&A* **2011**, *532*, A40. <https://doi.org/10.1051/0004-6361/201116653>.
- (5) Biennier, L.; Sabbah, H.; Klippenstein, S. J.; Chandrasekaran, V.; Sims, I. R.; Rowe, B. R. Insights into the Condensation of PAHs in the Envelope of IRC +10216. *EAS Publications Series* **2011**, *46*, 191–199. <https://doi.org/10.1051/eas/1146020>.
- (6) Sabbah, H.; Biennier, L.; Klippenstein, S. J.; Sims, I. R.; Rowe, B. R. Exploring the Role of PAHs in the Formation of Soot: Pyrene Dimerization. *J. Phys. Chem. Lett.* **2010**, *1* (19), 2962–2967. <https://doi.org/10.1021/jz101033t>.
- (7) Durif, O.; Capron, M.; Messinger, J. P.; Benidar, A.; Biennier, L.; Bourgalais, J.; Canosa, A.; Courbe, J.; Garcia, G. A.; Gil, J. F.; Nahon, L.; Okumura, M.; Rutkowski, L.; Sims, I. R.; Thiévin, J.; Le Picard, S. D. A New Instrument for Kinetics and Branching Ratio Studies of Gas Phase Collisional Processes at Very Low Temperatures. *Review of Scientific Instruments* **2021**, *92* (1), 014102. <https://doi.org/10.1063/5.0029991>.
- (8) Lee, S.; Hoobler, R. J.; Leone, S. R. A Pulsed Laval Nozzle Apparatus with Laser Ionization Mass Spectroscopy for Direct Measurements of Rate Coefficients at

- Low Temperatures with Condensable Gases. *Review of Scientific Instruments* **2000**, 71 (4), 1816–1823. <https://doi.org/10.1063/1.1150542>.
- (9) Gurusinghe, R. M.; Dias, N.; Krueger, R.; Suits, A. G. Uniform Supersonic Flow Sampling for Detection by Chirped-Pulse Rotational Spectroscopy. *J. Chem. Phys.* **2022**, 156 (1), 014202. <https://doi.org/10.1063/5.0073527>.
- (10) Soorkia, S.; Liu, C.-L.; Savee, J. D.; Ferrell, S. J.; Leone, S. R.; Wilson, K. R. Airfoil Sampling of a Pulsed Laval Beam with Tunable Vacuum Ultraviolet Synchrotron Ionization Quadrupole Mass Spectrometry: Application to Low-Temperature Kinetics and Product Detection. *Review of Scientific Instruments* **2011**, 82 (12), 124102. <https://doi.org/10.1063/1.3669537>.
- (11) Dias, N.; Krueger, R.; Suas-David, N.; Suits, A.; Broderick, B. M. *Product Branching and Low Temperature Reaction Kinetics by Chirped-Pulse Fourier Transform Mm-Wave Spectroscopy in a Pulsed Uniform Supersonic Flow*; 2019. <https://doi.org/10.15278/isms.2019.TF06>.
- (12) Specifications <https://www.beamdynamicsinc.com/specifications> (accessed 2022-04-14).
- (13) Sundén, B. *Heat Transfer in Aerospace Applications*; charts: Elsevier: Amsterdam, 2017.
- (14) Chen, J.; Ou, J.; Zhao, L. Simulation of Hypersonic Flows in Near-Continuum Regime Using DSMC Method and New Extended Continuum Model; Glasgow, UK, 2019; p 100007. <https://doi.org/10.1063/1.5119602>.
- (15) Chourushi, T.; Rahimi, A.; Singh, S.; Myong, R. S. Computational Simulations of Near-Continuum Gas Flow Using Navier-Stokes-Fourier Equations with Slip and Jump Conditions Based on the Modal Discontinuous Galerkin Method. *Advances in Aerodynamics* **2020**, 2 (1), 8. <https://doi.org/10.1186/s42774-020-00032-z>.
- (16) Luria, K.; Christen, W.; Even, U. Generation and Propagation of Intense Supersonic Beams. *J. Phys. Chem. A* **2011**, 115 (25), 7362–7367. <https://doi.org/10.1021/jp201342u>.
- (17) Segev, Y.; Bibelnik, N.; Akerman, N.; Shagam, Y.; Luski, A.; Karpov, M.; Narevicius, J.; Narevicius, E. Molecular Beam Brightening by Shock-Wave Suppression. *Science Advances* **2017**, 3 (3), e1602258. <https://doi.org/10.1126/sciadv.1602258>.
- (18) Abeysekera, C.; Joalland, B.; Ariyasingha, N.; Zack, L. N.; Sims, I. R.; Field, R. W.; Suits, A. G. Product Branching in the Low Temperature Reaction of CN with

- Propyne by Chirped-Pulse Microwave Spectroscopy in a Uniform Supersonic Flow. *J. Phys. Chem. Lett.* **2015**, *6* (9), 1599–1604. <https://doi.org/10.1021/acs.jpcllett.5b00519>.
- (19) Oldham, J. M.; Abeysekera, C.; Joalland, B.; Zack, L. N.; Prozument, K.; Sims, I. R.; Park, G. B.; Field, R. W.; Suits, A. G. A Chirped-Pulse Fourier-Transform Microwave/Pulsed Uniform Flow Spectrometer. I. The Low-Temperature Flow System. *J. Chem. Phys.* **2014**, *141* (15), 154202. <https://doi.org/10.1063/1.4897979>.
- (20) Abeysekera, C.; Zack, L. N.; Park, G. B.; Joalland, B.; Oldham, J. M.; Prozument, K.; Ariyasingha, N. M.; Sims, I. R.; Field, R. W.; Suits, A. G. A Chirped-Pulse Fourier-Transform Microwave/Pulsed Uniform Flow Spectrometer. II. Performance and Applications for Reaction Dynamics. *J. Chem. Phys.* **2014**, *141* (21), 214203. <https://doi.org/10.1063/1.4903253>.
- (21) Oldham, J. M.; Abeysekera, C.; Joalland, B.; Zack, L. N.; Prozument, K.; Sims, I. R.; Park, G. B.; Field, R. W.; Suits, A. G. A Chirped-Pulse Fourier-Transform Microwave/Pulsed Uniform Flow Spectrometer. I. The Low-Temperature Flow System. *The Journal of Chemical Physics* **2014**, *141* (15), 154202. <https://doi.org/10.1063/1.4897979>.
- (22) Search and Conversion Form of the CDMS <https://cdms.astro.uni-koeln.de/cgi-bin/cdmssearch> (accessed 2022 -04 -14).
- (23) Abeysekera, C. Chirped-Pulse Fourier Transform Microwave Spectroscopy In Pulsed Uniform Supersonic Flows. *Wayne State University Dissertations* **2015**.
- (24) Gora, E. K. The Rotational Spectrum of Ozone. *Journal of Molecular Spectroscopy* **1959**, *3* (1–6), 78–99. [https://doi.org/10.1016/0022-2852\(59\)90009-8](https://doi.org/10.1016/0022-2852(59)90009-8).
- (25) Broderick, B. M.; Suas-David, N.; Dias, N.; Suits, A. G. Isomer-Specific Detection in the UV Photodissociation of the Propargyl Radical by Chirped-Pulse Mm-Wave Spectroscopy in a Pulsed Quasi-Uniform Flow. *Phys. Chem. Chem. Phys.* **2018**, *20* (8), 5517–5529. <https://doi.org/10.1039/C7CP06211G>.
- (26) Park, G. B.; Steeves, A. H.; Kuyanov-Prozument, K.; Neill, J. L.; Field, R. W. Design and Evaluation of a Pulsed-Jet Chirped-Pulse Millimeter-Wave Spectrometer for the 70–102 GHz Region. *The Journal of Chemical Physics* **2011**, *135* (2), 024202. <https://doi.org/10.1063/1.3597774>.

## VI. Pulsed system: A new optimizing apparatus for CPUF applications

### Introduction

Using different cooling techniques to achieve low pressure and temperature conditions is beneficial for microwave spectroscopy in particular as it helps with the decongestion of the spectral lines and the enhancement of molecular signal as has been shown in the previous chapter, and with the limitations presented by the secondary expansion technique, it was judicious to develop a more efficient system where one can control all the flow parameters contributing in the molecular signal (pressure, temperature, density and mass flow rate). The CRESU technique uses large mass flow rates to support the uniformity of its generated flows, this requires extensive pumping capacity ( $32,000 \text{ m}^3 \text{ h}^{-1}$  for CRESUCHIRP), running continuously to maintain the lowest pressures possible that still remain higher than the ones achieved with other cooling techniques that use lower flow rates (see Chapter II). The kinetics of the reactions of interest are on the scale of hundreds of microseconds, and the excimer laser that triggers those reactions operates at a maximum repetition rate of 100 Hz leaving a delay of 10 ms between each pulse resulting in a very low duty cycle. Pulsing the CRESU flows at a corresponding frequency can therefore be of great use, first the mass flow rate of the gas will be lowered to the duration of the pulse in one duty cycle, this has an economical benefit especially for expensive reactants used and the enormous quantities of some buffers like helium. Most importantly however is that the increase in effective pumping capacity will enable lower pressure uniform supersonic flows to be established which will reduce the effect of pressure broadening and other problems like clustering which undermine the molecular signal. Finally, and as a result

of the possibility to increase the pressure ratio between the reservoir and the chamber, lower temperature flows can be established.

Unlike the secondary expansion technique, the use of pulsed flows instead of continuous flows helps reducing the pressure by increasing the pumping efficiency without the need to implement additional pumps, another technical advantage is that it does so while reducing the consumption of the main buffer gas and the reactants while in secondary expansions from continuous CRESU flows, the non-sampled gas is wasted.

Furthermore, the pulsed flow technique does present a major advantage over secondary expansions; that is both the system studied and the probing occur in the same environment which gives the opportunity to collect the signal from all the volume covered by the horn antennas (major contribution from the isentropic core), this was one of the limitations that significantly affected the molecular signal under the secondary expansion environment where only species sampled from 4 mm diameter core, constrained by the geometry of the skimmer, could be probed. In this chapter we present the development of a new instrument based on the use of pulsed CRESU flows instead of continuous flows to optimize the conditions of probing using CPUF. The design phase and the characterization of the instrument is detailed while optimization tasks and kinetic measurements are to be carried out in further work.

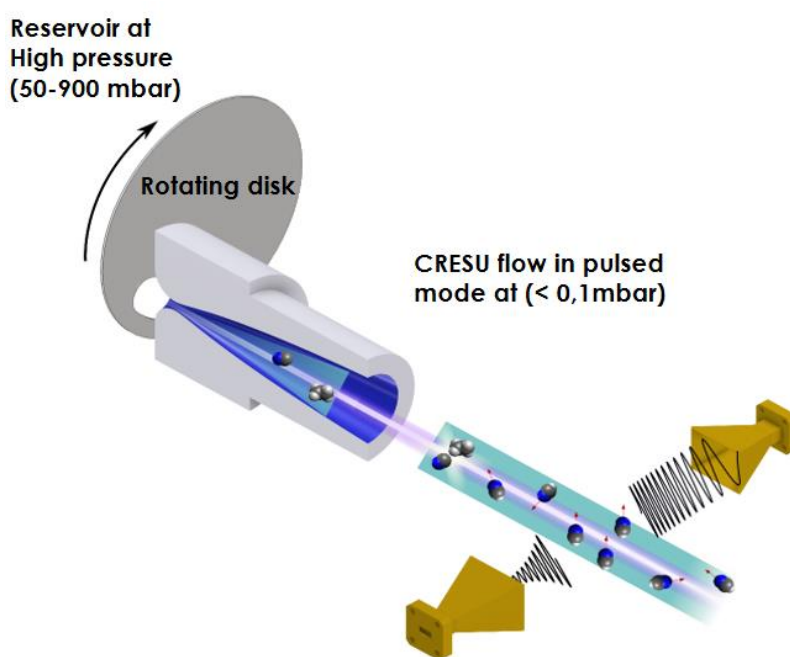


Figure VI-1. Schematic showing the principle of pulsed Laval flows

---

## Part I: Design phase

### VI.1. State of art

The first version of pulsed CRESU flows was developed in the mid-1990s by Smith and coworkers at the University of Arizona,<sup>1</sup> they developed a pulsed version in the CRESU environment using a commercial pulsed valve. Similar but improved versions were then developed by Leone and co-workers<sup>2</sup> then Heard and co-workers,<sup>3</sup> where they use pulsed solenoid valves to inject the gas into a very small volume reservoir of  $\sim 1 \text{ cm}^3$ . The technique suffers from numerous problems related to the stability of pressures, short hydrodynamic time as a result of the gas initial speed, lack of mixing of the reactants in the buffer given the small volume of the reservoir in addition to restrictions related to the functioning of the valves unable to operate at higher frequencies and fast opening times.

Suits and co-workers<sup>4,5</sup> developed a higher performance and more sophisticated version with a relatively higher volume reservoir and a fast high-throughput piezoelectric stack valve able to inject a huge mass flow and achieve lower temperatures down to 22 K, the difficulty of operating at higher frequencies however remains.

Morales and co-workers<sup>6</sup> have developed a new version of a pulsed system more suited for high flow rates involving the use of an aerodynamic chopper to pulse the flows, a perforated obstructing disk rotating at a given frequency, the disk will thereby block the gas from expanding to the CRESU chamber until the orifice on the disk is met with the nozzle allowing the gas to flow through in a similar way as pulsed valve. Rowe and co-workers<sup>7</sup> then developed an upgraded version with more mechanical features to increase performances such as maintaining stable rotation and minimizing the leaks. In both versions the aerodynamic chopper split the nozzle into two parts which required the use of a thinner disks in order not to perturb the profile of the nozzle, Morales and co-worker found that putting a disk 3 mm thick in the divergent part of the nozzle does not perturb the CRESU flow, the disk had to be close to the nozzle throat to take advantage of the small diameter to achieve maximum gain as will be explained later.

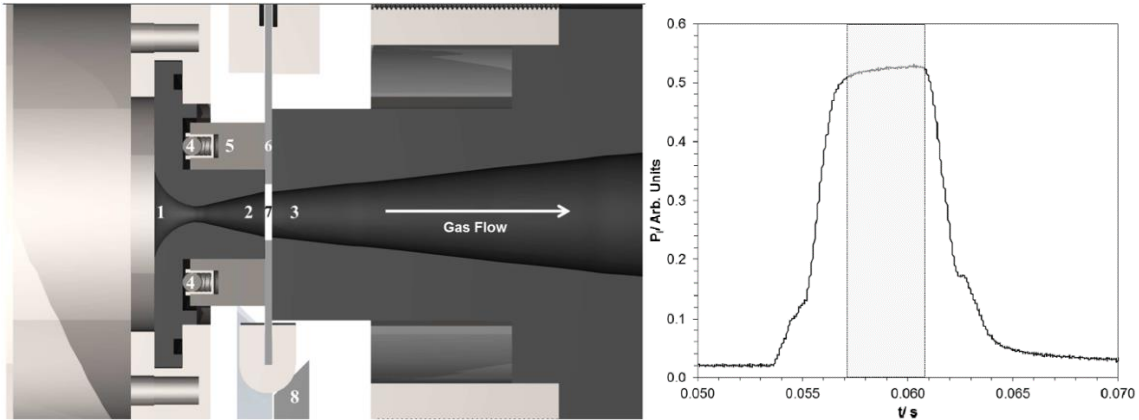


**Figure VI-2. Pulsed nozzle system developed by Rowe and co-workers<sup>7</sup> left figure gives a schematics of the Laval nozzle with; 1 Convergent part, 2 upstream contour of the divergent part, 3 downstream contour of the divergent part, 4 ball-springs, 5 stainless steel ring, 6 aerodynamic chopper, 7 aperture, and 8 45° rollers. The right figure shows the impact pressure of a gas pulse, details about the design and more results can be found in the reference.**

In this work we develop a new upgraded version of aerodynamic choppers developed by Morales and co-workers and Rowe and co-workers. The current version developed uses the same approach but with fewer mechanical complications and better performances, instead of having the disk sandwiched between the split nozzle parts which can be critical for certain nozzles especially since it is divided in the divergent part and closer to the throat which can generate disturbance in the flow in addition to significant leakage from both sides where the disk is in contact with the nozzle contours, specifically the higher pressure region upstream which requires careful alignment of the three bodies (the disk and the two parts of the nozzle) plus a refined and rigorous sealing system. In our configuration however, the aerodynamic chopper is placed in front of the nozzle which makes the assembly less complicated and facilitates the use of the system with different nozzles including the existing continuous mode ones to economize gas consumption. It also gives the opportunity to use thicker disk which limits buckling that manifests in thinner disk due to inertial forces of rotation.

Placing the disk in front of the nozzle implies that the pulsing system is to be put in the reservoir meaning that all the component including the motor used for the rotation of the disk are going to be in low vacuum (hundreds of millibars under the atmospheric pressure) which limits problems related to overheating and degassing

## VI.2. Design and construction

The most important parameter in the design phase is the disk geometry which determines the gain factor one will have on the pressure and the flow rate. The original gain was determined to be 12.5, this value is determined based on a compromise between the gain to achieve and the time required for the expansion to occur and the uniform flow to be established in case of a helium buffer at the highest rotation frequency of 100 Hz. We note that this is the maximum frequency of the excimer laser shot, the theoretical gain determined by the ratio between the disk circumference at the efficient radius at which the orifice is placed  $r_{eff}$  and the arc length of the orifice  $d$  (see Figure VI-4).

$$Gain = \frac{2\pi \cdot r_{eff}}{d} \quad \text{Equation VI-1}$$

### VI.2.1. The disk geometry

A helium nozzle operating at 6 K and 70 SLM was designed to operate in a pulsed mode, the Ansys Fluent solver is used to simulate the expansion within the nozzle and the establishment of the uniform flow, the calculations are run in the transient mode with initial conditions of the CRESU chamber.

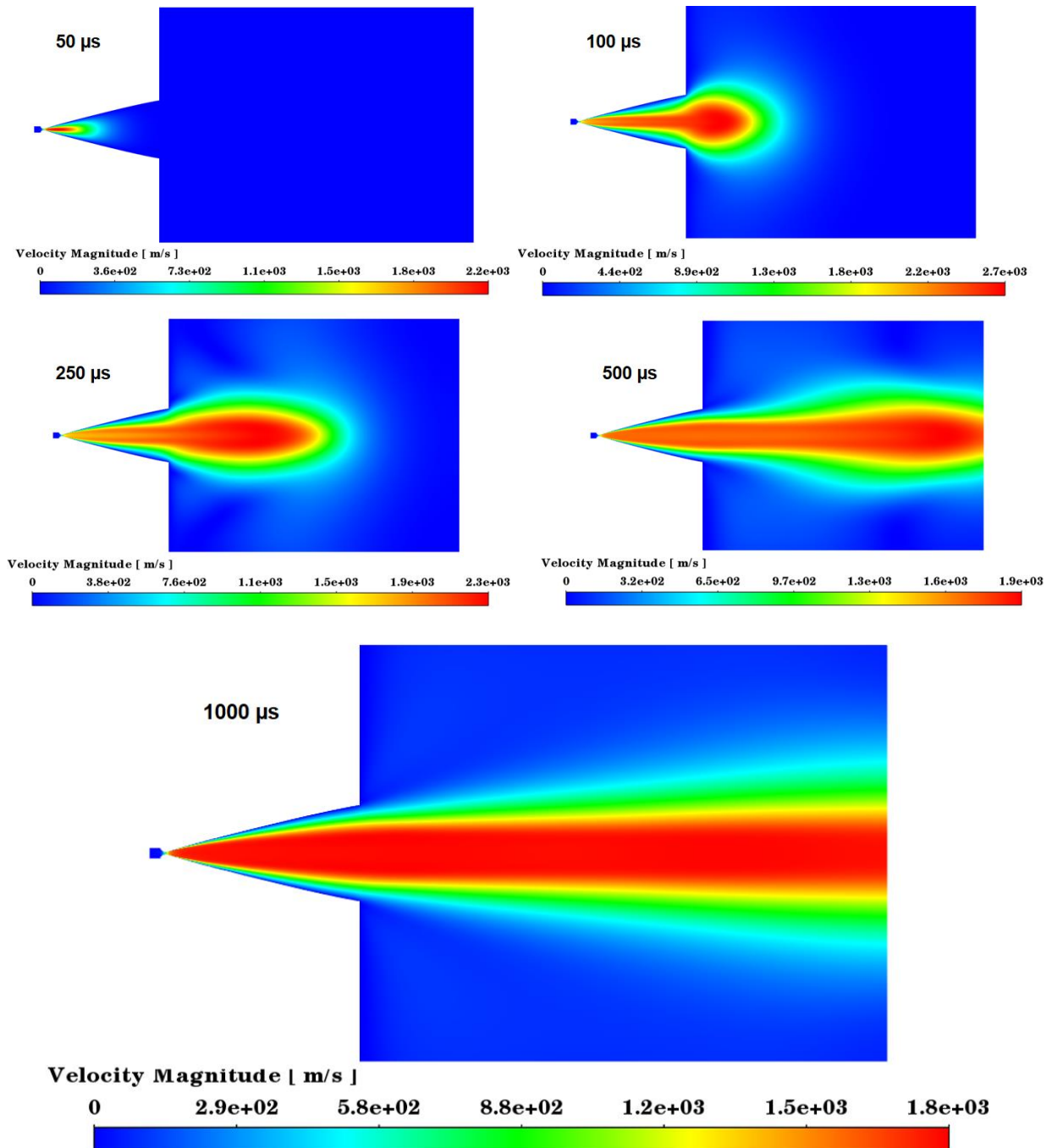


**Figure VI-3. Nozzle expansion status at different times in the helium nozzle that operates at 6 K as given by CFD simulations, the reservoir pressure is 635 mbar and chamber pressure is 0.04 mbar.**

The disk is machined from 8 mm thick 5083 aluminum alloy plate (Euralliage),<sup>8</sup> this material has been selected after considering a number of possible materials to use, it possesses a number of characteristics such as high surface flatness (proportional to the thickness) the relatively low density ( $2660 \text{ kg m}^{-3}$ ), high rigidity and resistivity to corrosion which makes it suitable for our application.

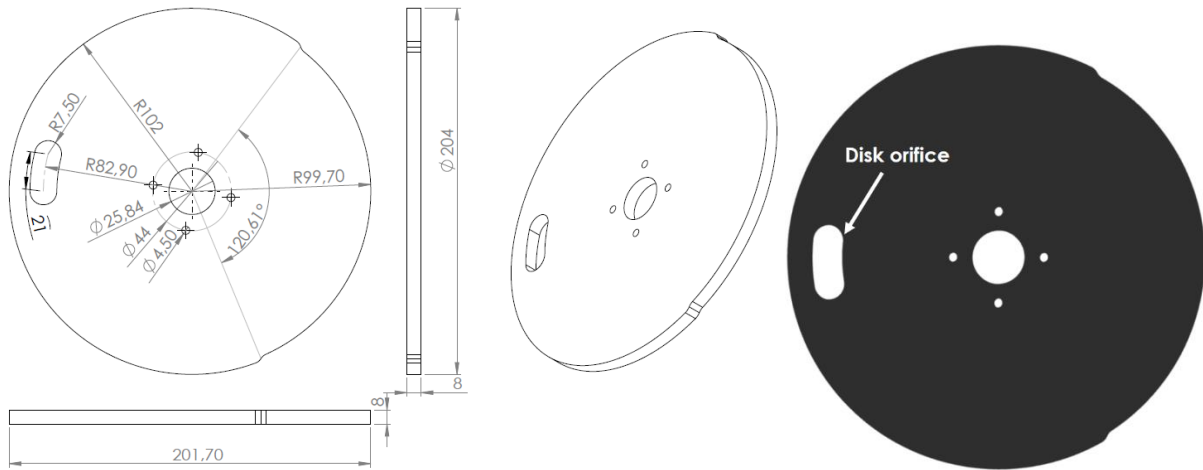


**Figure VI-4. The 8 mm disk with a theoretical gain of 14.45 used for primary tests of the pulsed system**

Placing the orifice on the side of the disk causes an uneven distribution of mass in the disk meaning that the center of mass is displaced from the center of rotation. This is a serious problem that makes the rotation unbalanced. To reestablish balance, the disk must be fitted with extra masses on the side of the orifice to compensate the mass loss, this however will add an extra torque to rotate the disk. The removal of mass from the opposite side of the orifice brings the center of mass to the center of rotation, this can be done using a computer aided design software package (see Equation VI-2).

$$U = m \cdot r \quad \text{Equation VI-2}$$

Where U is the unbalance, m is the mass and r is the eccentricity of mass.

### VI.2.2. The motor

A hydraulic motor (1SM009 Vivoil) is used to deliver the torque required for the rotation of the disk, fitted with a  $0.89 \text{ cm}^3/\text{revolution}$  pump able to generate 240 bar of pressure, the motor can deliver a torque of 3 N.m and operates in a speed interval of 600 rpm to 6000 rpm, a hydraulic plant with a 50 l oil reservoir supplies the hydraulic motor with the oil flow required for the rotation (see Figure VI-5). A Kollmorgen (AKM63N) Brushless motor is coupled with the pump in order to generate flow with the highest precision possible, an electrical cabinet with a digital screen and an Ethernet input is built to control the motor and set the speeds, the Kollmorgen Workbench 2.7 program is used to communicate with the brushless motor and select the settings as shown in the same Figure. The user can input the required speed of the hydraulic motor and the

servo drive of the brushless motor converts the input speed and initiates the rotation the brushless motor which in its turn actuates the pump to generate the proper flow rate of oil required.

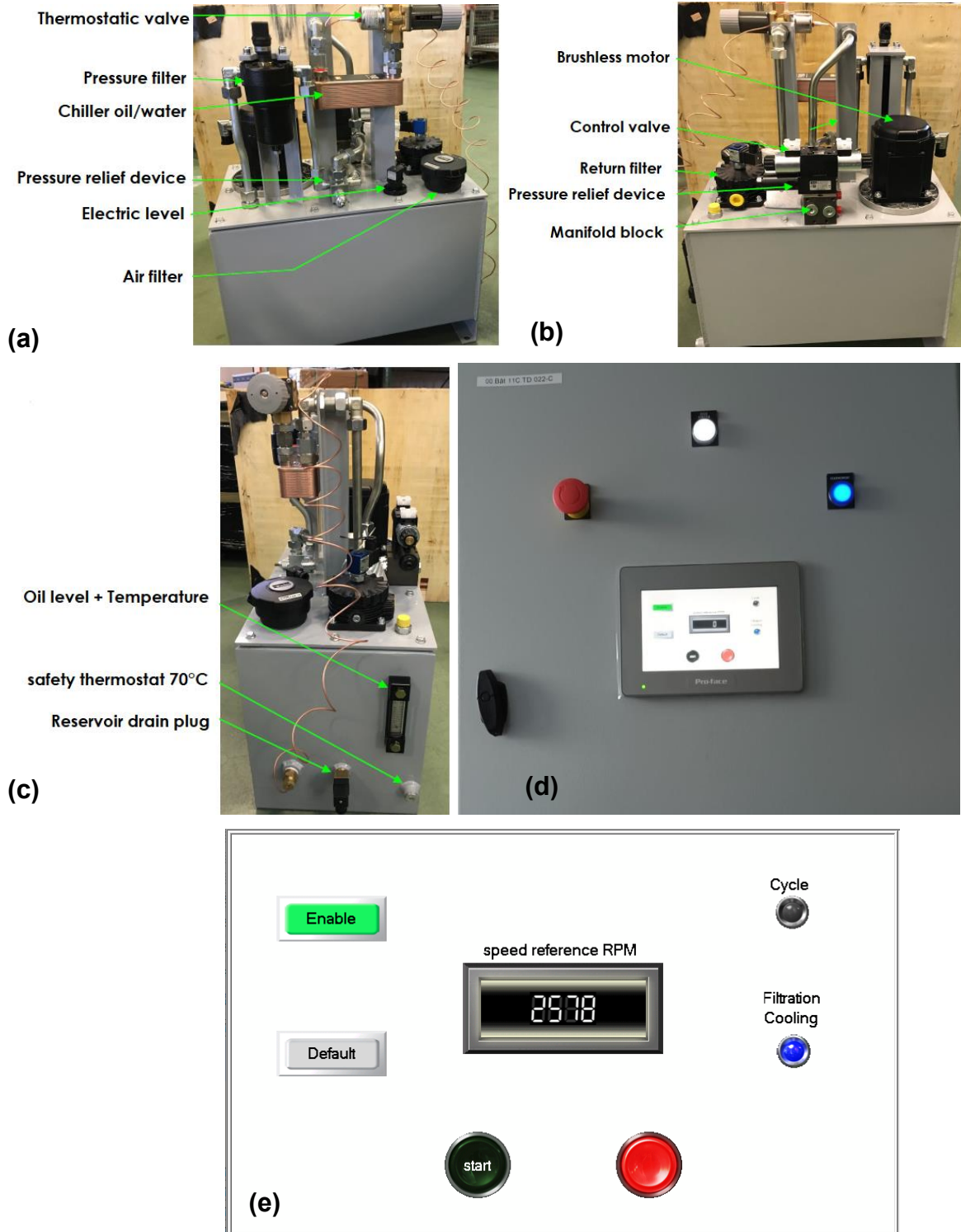
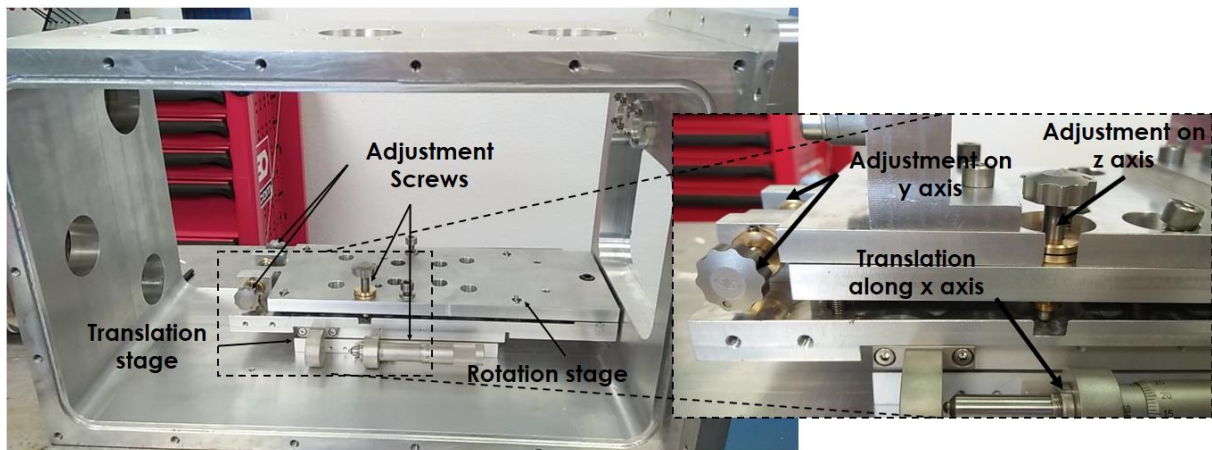


Figure VI-5. Hydraulic plant and electrical cabinet for the hydraulic motor (a, b and c) represent different views of the hydraulic plant and (d) and (e) shows the electrical cabinet and the command screen.

The use of a brushless motor directly connected to the disk to generate rotation has been considered as an option and two versions of motors have been designated, the principal limitations were the relatively larger size of the brushless motor for the required torques and second, the absence of an embedded water cooling system, the latter is highly important under vacuum conditions to evacuate the heat which can impede the motor performances (output power and torque). The implementation of water cooling system renders the size of the motor to increase which is why the hydraulic motor was considered as the best option as it can deliver notable torques with minimum size and most importantly the motor is auto cooled by the oil flow periodically cooled in the reservoir of the hydraulic plant.

### VI.2.3. The alignment

The reservoir is designed in two compartments, the first compartment harbors the motor, the rotating shaft held by a two 7004-B-XL-2RS-TVP angular contact ball bearing placed in their housings ensuring minimum axial mechanical clearance ended with an SKF locking nut, the mechanical system (motor + bearing + disk) is put on two adjustable stages, the first one built to adjust the parallelism of the disk to the front of the nozzle plane fitted with two adjustment screws on the x and y axis (see Figure VI-6). This stage sits on a (25 mm course M-436 MKS Newport) translational stage that tunes the axial position of the disk from the frontal plane of the nozzle



**Figure VI-6. Adjustment system for the parallelism of the disk, inset is a zoom on the adjusting screws, the system has a mechanical ball installed between the two pieces of the rotation stage allowing to adjust the system on the z and x axes.**

Three DN50 ports are located on the top part of the reservoir, two of them are used as feedthroughs for the oil input and output to the hydraulic motor, on the back of the reservoir, 2 DN 50 ports are situated, one for the Brewster window and the second is reserved for a flange containing three connections used as inputs for buffer gas and reactants and reservoir pressure measurements.

The two remaining ports will serve as feedthroughs, a DN40 port for the TH400R5F1B - 1x2 Multimode Fiber Optic Coupler used to detect the orifice on the disk to trigger the recording during microwave measurements, while a DN50 port will be used to control the translation stage from outside using a Miniature Stepper Motor Actuator (TRA25PPV6).

The second compartment of the reservoir contains the disk mounted on the shaft and clamped with two fixing supports. The disk is mounted perfectly parallel to a 30 mm thick 5083 flange, same material as the disk chosen for its high flatness property. The original plan was to position the disk at less than 100 microns from the flange with the disk in a free rotation, this way we avoid the addition of friction torque to the motor but due to mechanical machining imperfections and mediocre flatness profile of the disk, the leaks with this configuration are significant. A sealing system was therefore mounted on the flange to reduce the leaks; it is stainless steel housing containing a graphite gasket sitting on a spring disk with a full compression of 2.5 mm at 60 N. Other gaskets have been machined to replace the graphite including Teflon and PEEK (Polyether ether ketone) in order to increase the lifetime of the sealing system as the gasket material will deteriorate under the effect of friction with the disk while rotating. The primary tests and measurements presented below are carried out with TECAPEEK PVX BLACK. Finally, the nozzle is mounted on the other side of the flange.

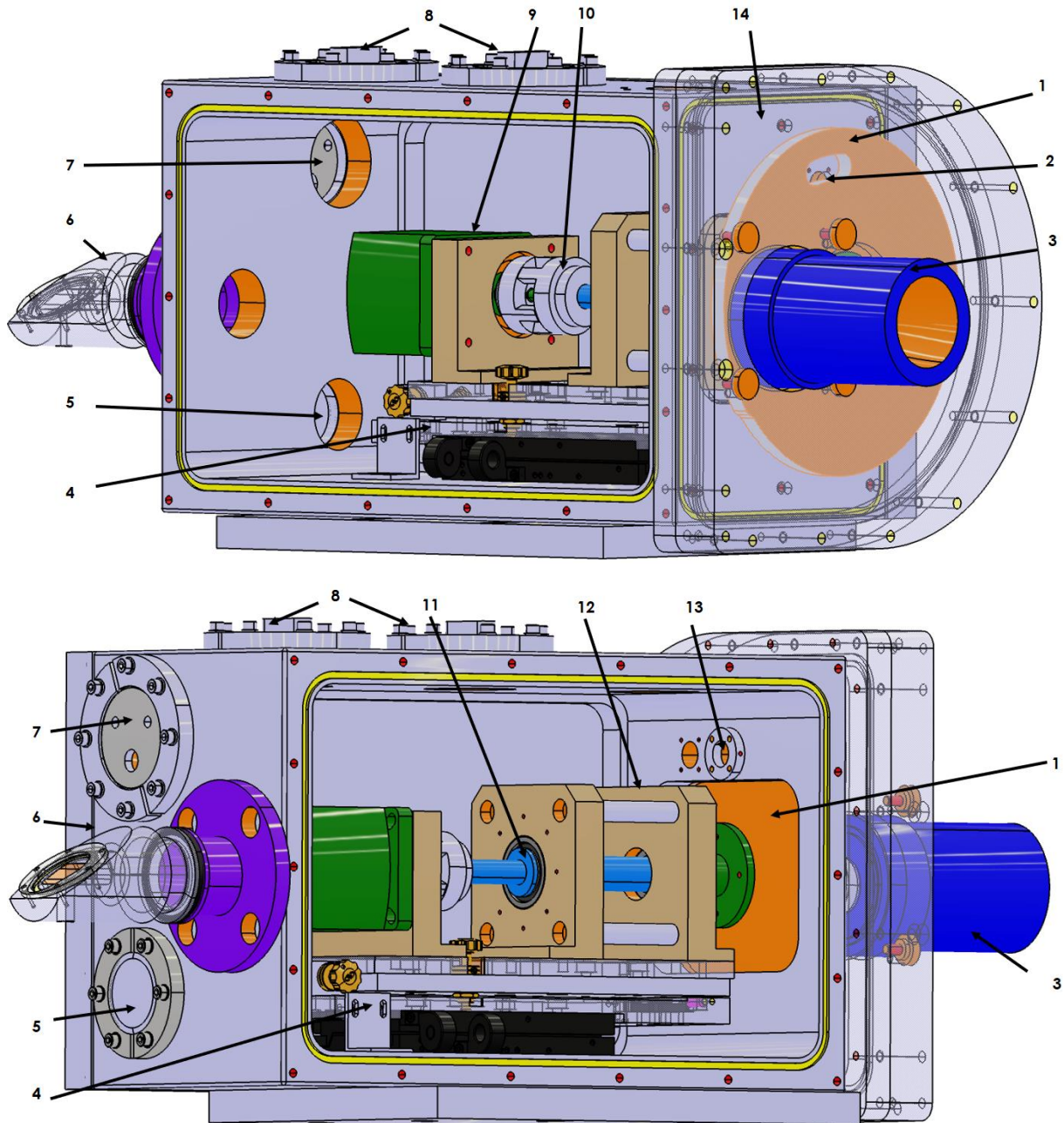


**Figure VI-7. Schematic of the pulsed system, 1. Rotating disk; 2. Disk orifice; 3. Nozzle; 4. Adjustable stages; 5. Port for stepper motor actuator; 6. Brewster window; 7. Port for gas inputs and pressure gauge connection; 8. Hydraulic connection feedthrough port; 9. Hydraulic motor; 10. Mechanical coupling; 11. Bearing; 12. Aligning bearing housing; 13. Fibre optic placement; 14. Parallel frontal flange.**

The reservoir was then assembled, aligned with diode laser and fixed in the CRESU B chamber for the first tests. The N<sub>2</sub>-30K-0.183 nozzle was put for characterization before the He-6K nozzle (see Figure VI-8). Running CRESU flows in a pulsed mode at a given frequency requires rapid pressure sensors that can respond to the quick flow

variations at scales of a few tens of microseconds at 100 Hz meaning that the classic Pitot tube attached to pressure gauge with response of few seconds cannot be used in the pulsed mode. A Kulite pressure transducer (XCQ-062) with a response of 150 kHz able to measure pressures up to 350 mbar is used to measure the impact pressure of CRESU flows in the pulsed mode, it converts the mechanical motion of the membrane to an electric signal recorded and amplified by an EFS 0582 conditioner with a gain of 10 to 3000 (see Figure VI-9). The results are then shown on the oscilloscope.

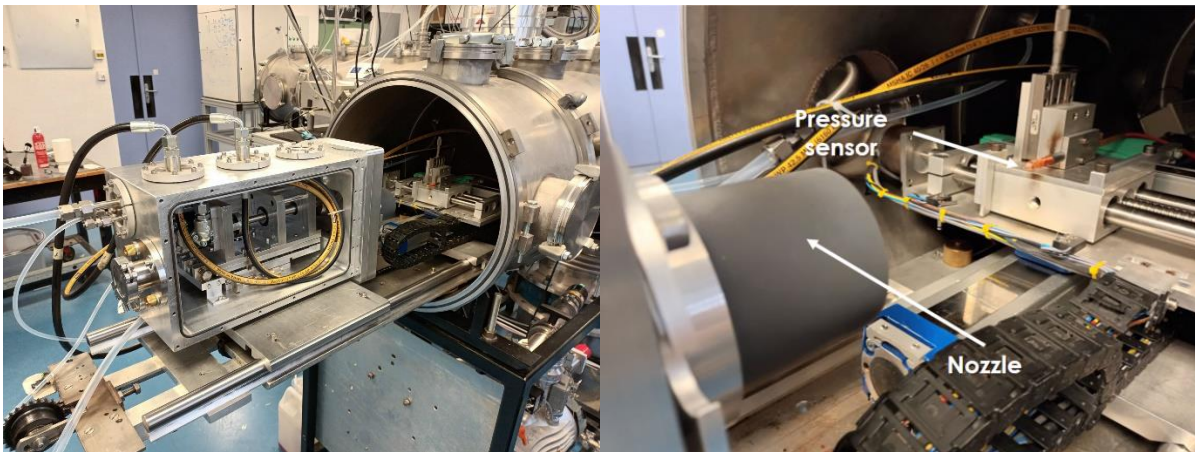


**Figure VI-8.** left figure shows the pulsed system mounted in the CRESU B chamber, right figure shows the N2-30K-0.183 nozzle and the rapid pressure sensor.



**Figure VI-9.** Left figure gives a frontal view in the direction of the flow of the rapid pressure sensor, right figure shows amplifier-filter and the Kulite conditioner (left to right), the filter has been used to filter the high frequency with a 3 KHz low pass filter.

## Part II: Characterization of the CRESU flow in the pulsed mode

### VI.3. Fast Pitot measurements

The first signal recorded with the fast Pitot is with the N<sub>2</sub>-30K-0.183 nozzle, a characterization of the nozzle was carried out in a continuous mode to serve as a proper comparison with the pulsed mode as will be shown later (see Table VI-1), Figure VI-10 shows the signal in millivolts recorded during one rotation where the rise and fall time corresponds to the time of opening and closure of the disk to the nozzle and in-between, the establishment of the “plateau”, the flat region of the signal which corresponds to the time of where the orifice is 100 % open to the CRESU chamber.

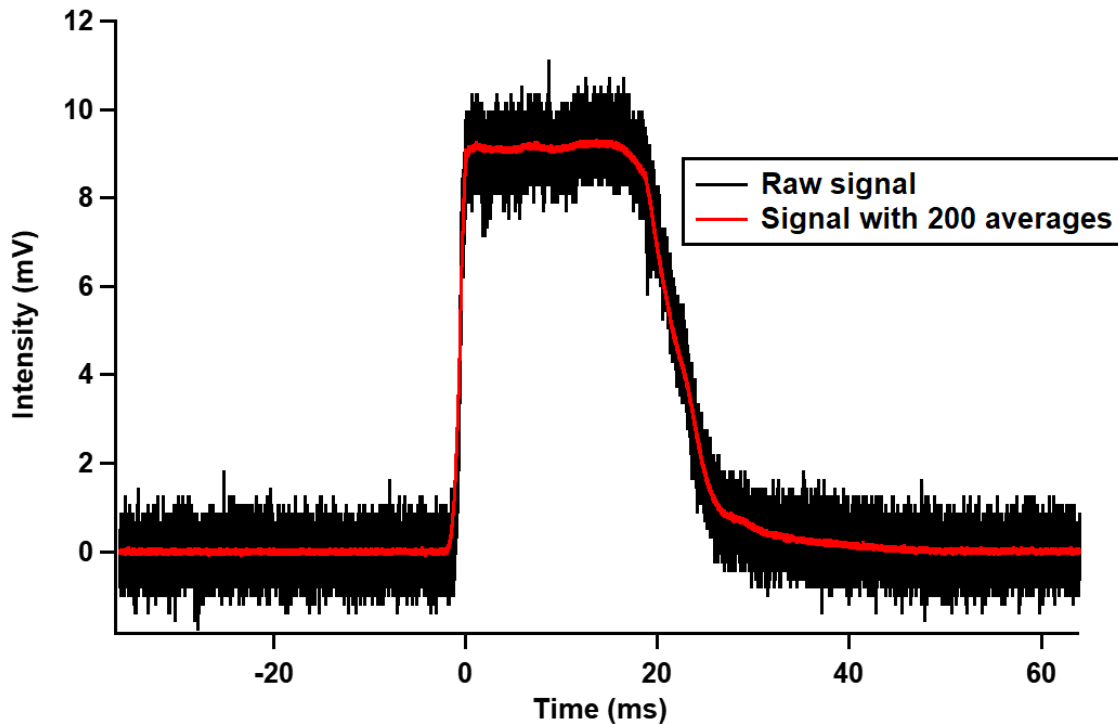


**Figure VI-10.** Signal recorded by the fast pressure sensor from the N<sub>2</sub>-30K-0.183 operating in the pulsed mode, the signal is amplified and displayed on the oscilloscope, in red, the recorded signal averaged from 200 acquisitions.

The signal measured with the fast pressure sensor is given in millivolts, a calibration signal/pressure is needed to determine the impact pressure of the CRESU flow and have access to the other flow parameters, Figure VI-11 shows the linear plot of pressures in millibar versus the associated recorded signals in millivolts. The impact pressure was then measured at different distances from the nozzle exit and given by Figure VI-12.

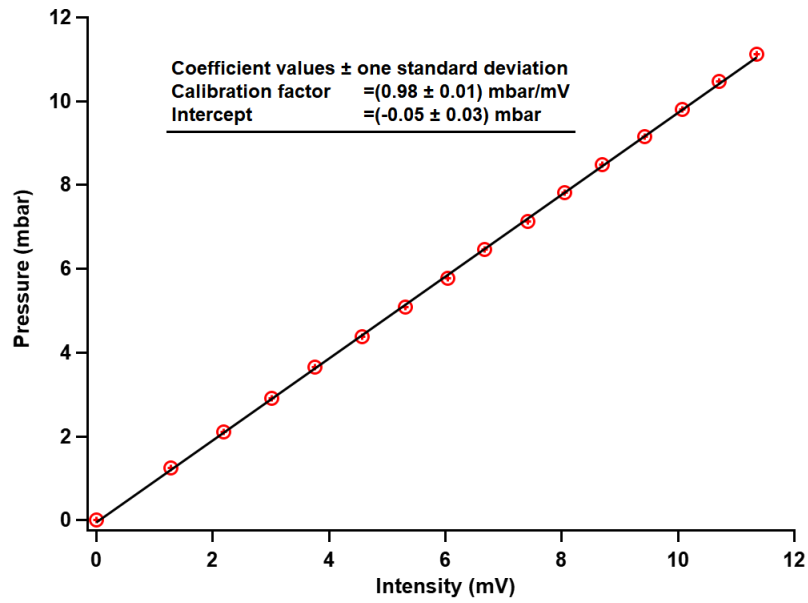


Figure VI-11. Plot of the chamber pressure with respect to recorded signal by the rapid pressure sensor

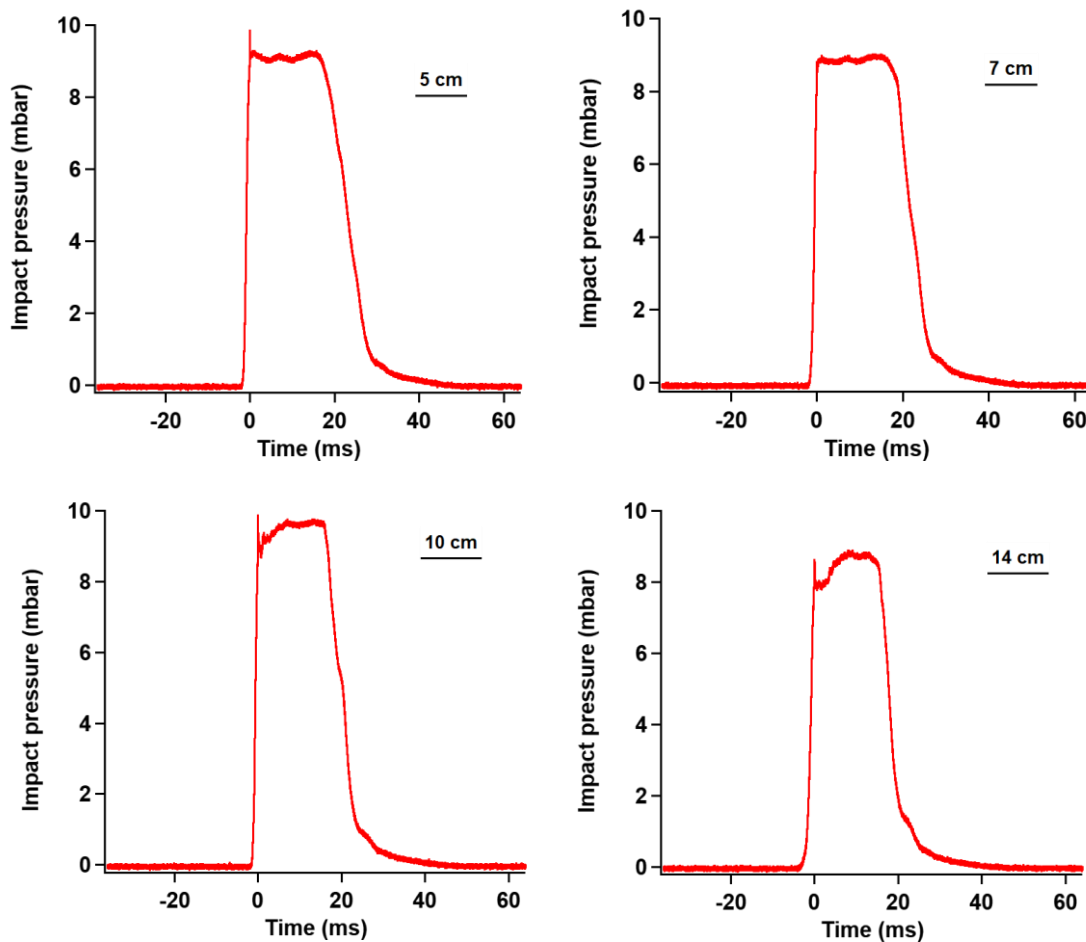


Figure VI-12. Plot of the impact pressures measured with the rapid pressure sensor at different position of the CRESU flow generated by the N<sub>2</sub>-30K-0.183 nozzle

The temperature profile along the axis of the chamber is given by Figure VI-13 in both the continuous and pulsed mode the average temperatures are similar at both modes within the error range.

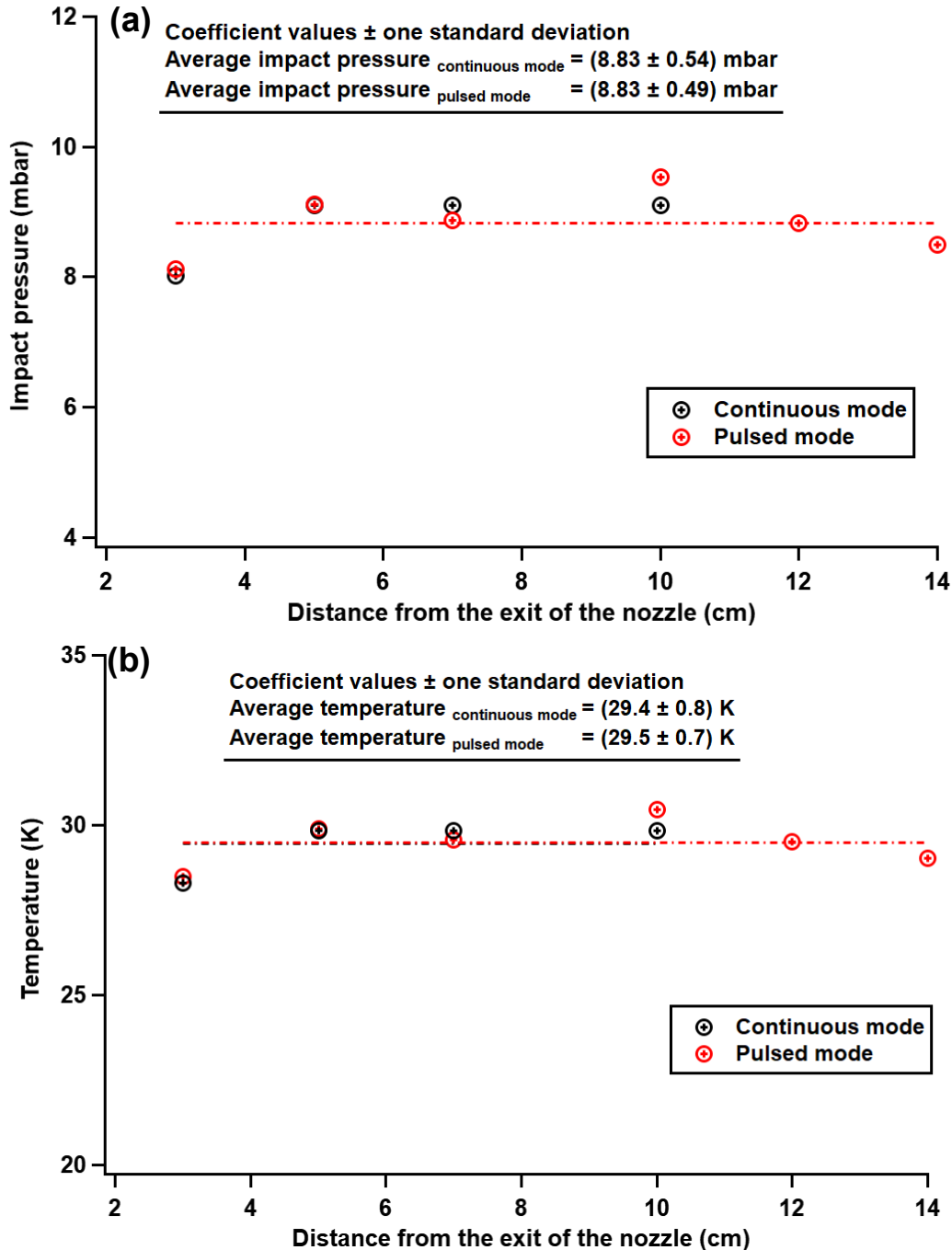


Figure VI-13. Impact pressure and temperature profiles along the axis of the chamber of the N<sub>2</sub>-30K-0.183 nozzle are given by (a) and (b) respectively, the temperatures are determined from impact pressure measurements by the rapid pressure sensor. The values for the pulsed mode are given in red and the values for the continuous mode are given in black, only three points were taken under this mode.

**Table VI-1. Comparison of the flow parameters of the N<sub>2</sub>-30K-0.183 in the continuous and the pulsed mode**

| <b>N<sub>2</sub>-30K-0.183 Nozzle</b>              | <b>Continuous mode</b> | <b>Pulsed mode</b> |
|--|------------------------|--------------------|
| <b>Reservoir pressure (mbar)</b>                   | 479.9                  | 477.9              |
| <b>Chamber pressure (mbar)</b>                     | 0.184                  | 0.183              |
| <b>Impact pressure (mbar)</b>                      | 8.83 ± 0.54            | 8.83 ± 0.49        |
| <b>Mach number</b>                                 | 6.72 ± 0.1             | 6.71 ± 0.09        |
| <b>Density (× 10<sup>16</sup> cm<sup>-3</sup>)</b> | 3.67 ± 0.23            | 3.67 ± 0.21        |
| <b>Temperature (K)</b>                             | 29.4 ± 0.8             | 29.5 ± 0.7         |
| <b>Mass flow rate (SLM)</b>                        | 22.65                  | 3.21               |

The parameters of N<sub>2</sub>-30K-0.183 in the continuous and the pulsed mode are given by Table VI-1, the experimental gain on the flow rate is determined by the ratio between the flow in the two modes and is given by Equation VI-3.

$$Gain = \frac{Q_{m,continuous\ mode}}{Q_{m,pulsed\ mode}} \approx 7.1 \quad \text{Equation VI-3}$$

The primary tests using the N<sub>2</sub>-30K-0.183 nozzle exhibits a considerable loss from the theoretical gain of 14.4, this is caused by leaks resulting from a lack of parallelism between the disk and the flange due to non-perfect planar profile and that the sealing system (gasket + compression and extension of the spring) is not compensating for the gaps created, through which the gas can escape to the CRESU chamber while the disk is blocking the nozzle inlet. Further adjustments are required including optimising the sealing system by the replacing of the gasket with more adhering material to the surface of the disk like Teflon. Another problem has been observed, there is mismatch of speed rotation of the disk between the input value given to the hydraulic motor and the frequency pulses measured on a 1 second scale (see Figure VI-14).

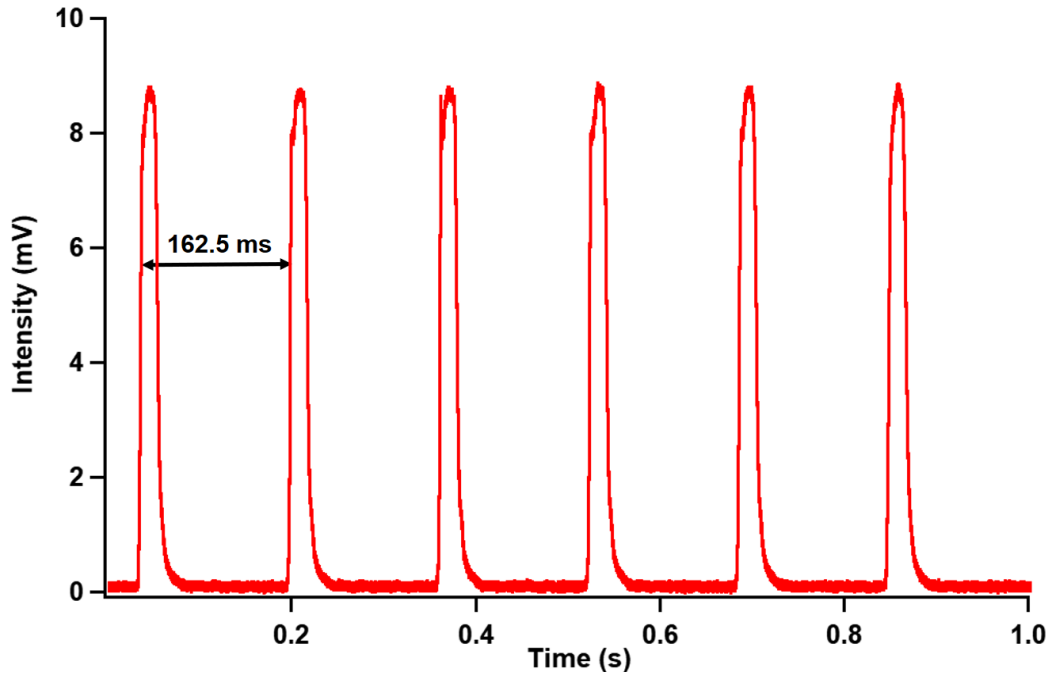


**Figure VI-14. Flow pulses in 1 second duty cycle from the N<sub>2</sub>-30K-0.183 nozzle, the frequency of pulses is 6.2 Hz corresponding to 370 rpm while the input frequency to the motor is 800 rpm.**

Perturbation in the speed of rotation of the disk were observed while doing the tests under atmospheric pressure at low rotation speeds, beyond 1500 rpm the motor rotating shaft temperature starts increasing significantly. To stabilize speed along time, it is recommended by the manufacturer to install a draining system to evacuate the residual oil that accumulates in the motor which causes perturbations of the performance and deterioration of the output parameters (extra heat, low torque...etc.)

#### **VI.4. Future work**

The primary tests show promising results with a gain of 7.1 that can certainly be increased by optimising the mounting assembly to reduce the leaks, this can be achieved via proper adjustments of the disk to account for non-planar profile, the option of rectifying the disk surface is also considered, the disk surface will have a planarity of 10 microns with a roughness, Ra between 0.2 and 0.4 microns. Teflon and TECAPET TF grey are also to be tested as sealing gasket.

The helium nozzle at 6 K is to be characterised with impact pressure measurements using the rapid pressure sensor. Like the classic Pitot tube, the current version of Pitot is mounted on the same two stages that move in x and y directions allowing to conduct fast Pitot mapping of the nozzle in the pulsed mode.

### VI.4.1. High frequency mode

For kinetic measurements, 100,000 averaged scans take 16 minutes to be recorded with the digitizer while running at 100 Hz, the maximum excimer laser frequency. In order to maintain the same timing for the same amount of averaging it is important to be able to rotate the disk at the same frequency. This high frequency mode is also beneficial for the stability of conditions in terms of reservoir and chamber pressure variations given that the gas flowing to the reservoir is continuous and constant therefore running at 100 Hz, the reservoir pressure will vary less as a result of quick opening and closing of the disk orifice to the nozzle, easily compensated by the continuous flow input to the reservoir, while running at 10 Hz for example provokes much stronger variation, the pressure decreases and increases in 10 times more than with the 100 Hz frequency mode. The same consideration applies to the chamber pressure. This gives the possibility of using a disk with two orifices in order to increase the stability of the pressure and the disk can rotate 50 Hz instead which will be more suitable for the motor as well. We can do so while maintaining the same geometrical gain by reducing the orifice length to half, the time required for the expansion will be the same as the speed of rotation is also halved however the efficient time where the orifice will be open to the chamber will be reduced as the opening time is doubled by the two orifices and the decrease of the rotation speed.

### VI.4.2. Running on microwave

For rapid Pitot measurements the gas pulse is detected with the rapid pressure sensor that measures the impact pressure. Coupling the pulsed system with our CP-FTMMW spectrometers requires the use of a detecting instrument that triggers the spectrometer when the disk orifice is open to the nozzle. As mentioned in the design phase section a fibre optic is to be used supplied with an M625F2 light source (Thorlabs), the reflected light is received by PDA36A2 gain detector (Thorlabs) fitted with a BNC connection, the latter is connected to the delay generator which that triggers the AWG, the synchronization chain is then maintained in a similar way to the one used in the previous measurements.

The gain on the microwave signal with the pulsed system is expected to be higher than the SKISURF apparatus. More details are given in the next chapter on perspectives.

## References

- (1) Atkinson, D. B.; Smith, M. A. Design and Characterization of Pulsed Uniform Supersonic Expansions for Chemical Applications. *Review of Scientific Instruments* **1995**, *66* (9), 4434–4446. <https://doi.org/10.1063/1.1145338>.
- (2) Lee, S.; Hoobler, R. J.; Leone, S. R. A Pulsed Laval Nozzle Apparatus with Laser Ionization Mass Spectroscopy for Direct Measurements of Rate Coefficients at Low Temperatures with Condensable Gases. *Review of Scientific Instruments* **2000**, *71* (4), 1816–1823. <https://doi.org/10.1063/1.1150542>.
- (3) Taylor, S. E.; Goddard, A.; Blitz, M. A.; Cleary, P. A.; Heard, D. E. Pulsed Laval Nozzle Study of the Kinetics of OH with Unsaturated Hydrocarbons at Very Low Temperatures. *Phys. Chem. Chem. Phys.* **2008**, *10* (3), 422–437. <https://doi.org/10.1039/B711411G>.
- (4) Oldham, J. M.; Abeysekera, C.; Joalland, B.; Zack, L. N.; Prozument, K.; Sims, I. R.; Park, G. B.; Field, R. W.; Suits, A. G. A Chirped-Pulse Fourier-Transform Microwave/Pulsed Uniform Flow Spectrometer. I. The Low-Temperature Flow System. *The Journal of Chemical Physics* **2014**, *141* (15), 154202. <https://doi.org/10.1063/1.4897979>.
- (5) Abeysekera, C.; Joalland, B.; Shi, Y.; Kamasah, A.; Oldham, J. M.; Suits, A. G. Note: A Short-Pulse High-Intensity Molecular Beam Valve Based on a Piezoelectric Stack Actuator. *Review of Scientific Instruments* **2014**, *85* (11), 116107. <https://doi.org/10.1063/1.4902153>.
- (6) Morales, S. Le Hacheur Aérodynamique : Un Nouvel Instrument Dédié Aux Processus Réactionnels à Ultra-Basse Température. These de doctorat, Rennes 1, 2009.
- (7) Jiménez, E.; Ballesteros, B.; Canosa, A.; Townsend, T. M.; Maigler, F. J.; Napal, V.; Rowe, B. R.; Albaladejo, J. Development of a Pulsed Uniform Supersonic Gas Expansion System Based on an Aerodynamic Chopper for Gas Phase Reaction Kinetic Studies at

Ultra-Low Temperatures. *Review of Scientific Instruments* **2015**, 86 (4), 045108. <https://doi.org/10.1063/1.4918529>.

(8) 5083 <https://www.euralliage.com/5083.htm> (accessed 2022 -04 -17).

## VII. Conclusions and perspectives

### VII.1. Conclusions and discussions

The work reported in this thesis is in the context of the CRESUCHIRP project in Rennes implementing chirped pulse mm-Wave detection of reaction products in cold uniform supersonic flows. It has covered the construction and testing of a new Ka band chirped pulse spectrometer concentrating on the effect of pressure on the molecular signal. It has been shown that in order to detect efficiently very low concentrations of polyatomic molecules in the size of vinyl cyanide and above, some modifications of the standard CRESU flow conditions is necessary to reduce the negative effect of pressure broadening on the molecular signal. Two such modifications have been designed, constructed and characterized; a skimmer leading to a secondary expansion (SKISURF); and a new pulsed Laval nozzle system.

The secondary expansion process using a skimmer has been proven efficient, the SKISURF apparatus allowed the determination of the branching ratio of the CN+ethylene reaction and enabled the sensitive measurement of its products, a relatively large molecule such as vinyl cyanide has been detected along with HCN despite yielded at low concentration, both with a decent SNR. The detection of vinyl cyanide under skimmer conditions highlights the importance of reducing the pressure broadening and its impact on the molecular signal given the unsuccessful detection in the uniform flow under CRESU conditions, as for HCN it shows the advantage of reducing the temperature in the probing medium even though being produced in a relatively higher temperature at 35 K, here we note that HCN could not be detected in an argon flow at 30 K and 0.082 mbar under the CRESU conditions.

The SKISURF apparatus gives then the possibility to study relatively high pressure and temperature systems under the CRESU conditions and still be able to detect the

molecular signal by conducting the probing in a much more favourable environment for the microwave signal.

As shown in chapter V, lowering the pressure does not come without a cost, having enough molecules for the probing is as important as the lowering the pressure. This is clearly seen by the reduction of the SNR of vinyl cyanide spectra while re-expanding the gas using low diameter skimmers (see Figure V.12), although the 2 mm skimmer can lower the pressure 3 times more than the 4 mm skimmer, the SNR of vinyl cyanide from the 2 mm skimmer is  $\sim 20$  times lower, with the 1 mm skimmer the signal could not be detected. This may also be related to the temperature. Primary results of rotational temperature from a Boltzmann plot of a vinyl cyanide spectrum recorded from E band chirps using the 4 and the 2 mm skimmers show that the temperature of the gas re-expanded through the 4 mm skimmer is 3 times lower than when re-expanded with the 2 mm skimmer despite being at lower pressure, this implies that with smaller diameter skimmers we are far from the near-continuum regime therefore the non LTE conditions might have been established and molecules are not being cooled due to infrequent collisions. This adds the factor of the temperature being higher, probably at the same temperature as the CRESU environment when using 100 micron skimmers. Small diameter skimmers have been used widely for laboratory astrophysics measurements to freeze the state of the system studied after undergoing the secondary expansion.

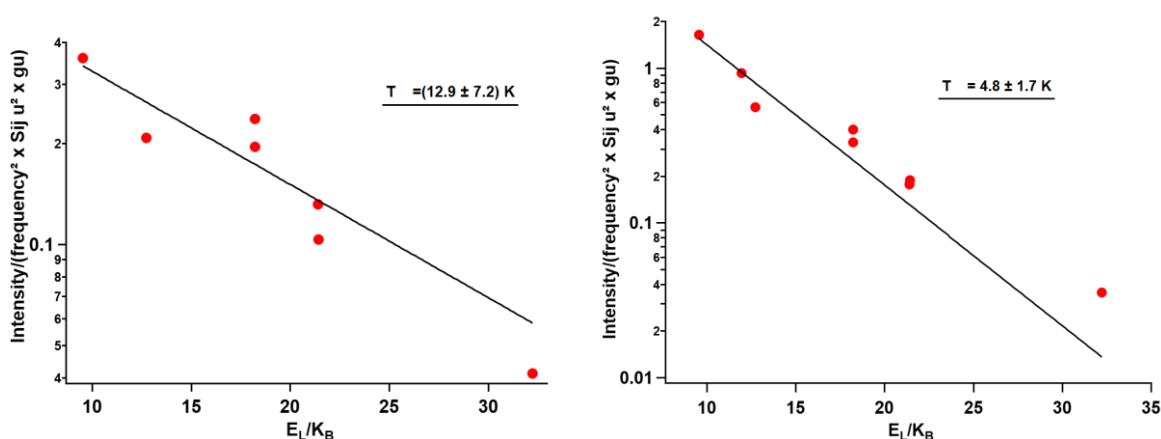


**Figure VII-1.** Rotation diagrams determined from recorded spectra of vinyl cyanide in the E band from expanding the flow generated by the AR35K0.28 nozzle via the the 2 mm skimmer (left) and the 4 mm skimmer (right), the fitted rotational temperatures are  $(4.8 \pm 1.7)$  K for the 4 mm skimmer and  $(12.9 \pm 7.2)$  K for the 2mm skimmer, with uncertainty given at the 95% confidence level.

The pulsed system is particularly efficient at this point as the pressure can be lowered as much as the geometrical gain given by the aerodynamic chopper allows, with the ability of maintaining a wide probing of the species of interest as the efficient column density.

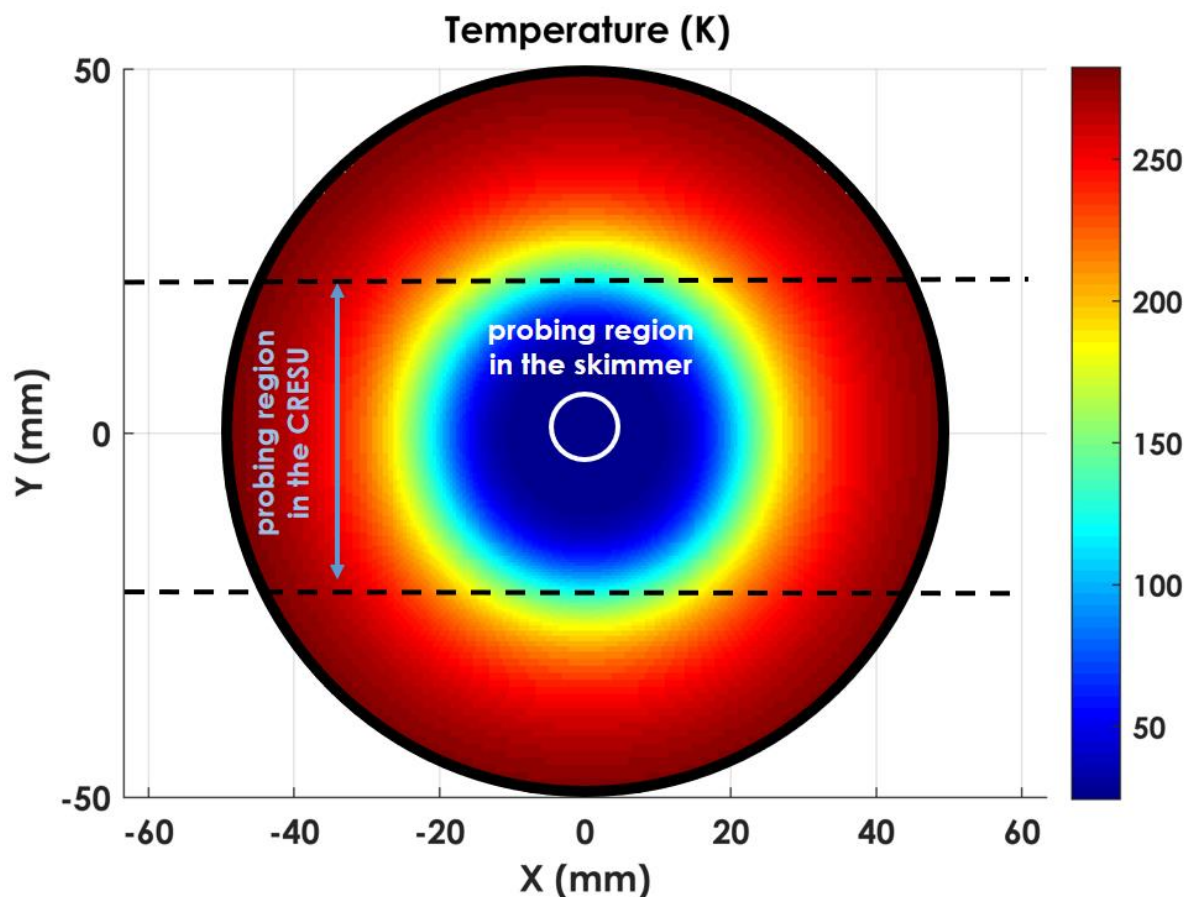


**Figure VII-2. 2D radial temperature profile of the N<sub>2</sub>-23.5K-0.21 nozzle given by CFD simulation, the figure shows the region sampled by the 4 mm skimmer in white circle and in black dashed line the region covered by the horn in the CRESU environment.**

The gain on the molecular signal from the column density of a 4 cm isentropic core is 50 times higher compared to the 4 mm skimmer currently in place for the SKISURF apparatus assuming the major contribution comes from the isentropic core (see chapter II). Although the temperature under the skimmer environment is lower which will strengthen the molecular signal, the helium operating at 6 K demonstrates that the temperature can be lowered as much as in secondary expansion with maintaining the gain on the column density.

The main advantageous point the SKISURF apparatus has over the pulsed system is, as explained earlier, the possibility to study relatively high temperature reactions without having much impact on the microwave signal as the probing is disentangled from the reaction environment. This factor is to be assessed in the case of the pulsed system and determine whether the reduced pressure solely can compensate for higher temperatures (above 100 K for instance).

Should the pulsed system be less efficient to study high temperature processes, the option of coupling the SKISURF apparatus with the pulsed system with the possibility of using higher diameter skimmers to reduce the impact of density drop may be useful, as pulsing the flow will also reduce the load on the turbomolecular pump of the secondary expansion chamber.

## VII.2. Future directions

After studying reactions involving CN first with ethane and acetylene in the CRESU environment, the development of the SKISURF apparatus opened the door for studying systems involving larger hydrocarbons, which led to the sensitive detection of vinyl cyanide and HCN from the CN + ethylene reaction. The CN + propene reaction, a system with possibly 7 channels has also been targeted and vinyl cyanide was detected under secondary expansion conditions using the Ar-35K-0.28 nozzle, the CN+ethylene reaction was used for calibration assuming yielding vinyl cyanide at ~ 100% from channel (a). The results shown that channel R4 is efficient by around 23%. Further measurements are to be carried out to determine the remaining channel efficiencies. More details can be found in the thesis of Divita Gupta.

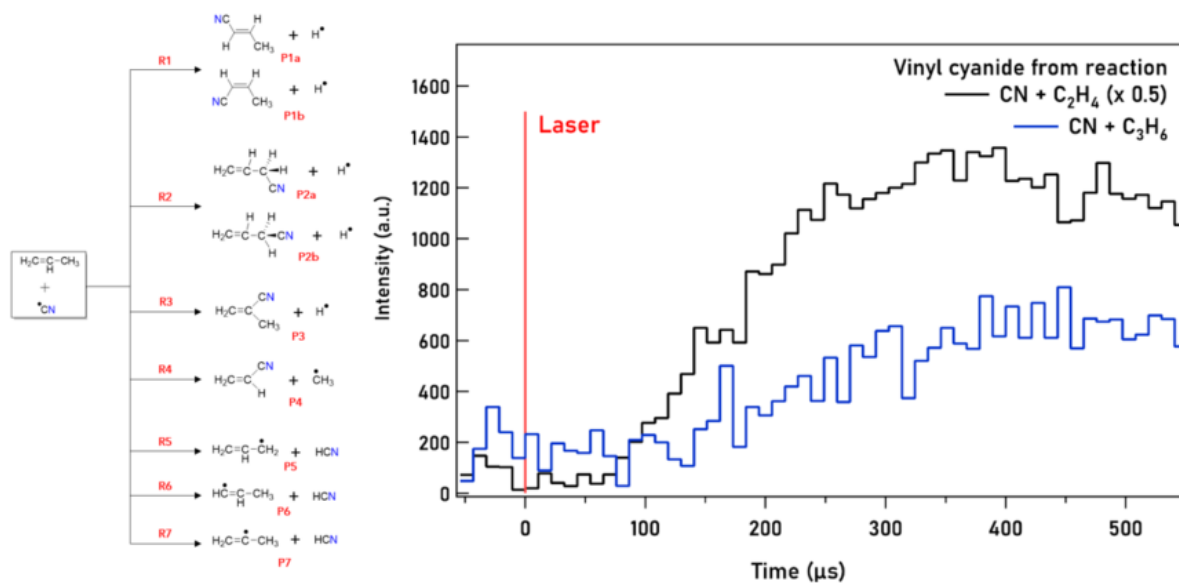


**Figure VII-3.** Left figure shows the multiple channel from the CN + propene reaction. Right figure gives the vinyl cyanide Time dependent signal intensity from the reactions of CN with ethylene and propene as a function of time. (Figure credit to Divita Gupta)

The results from the photolysis of ozone procedure carried out with the SKISURF apparatus, has opened the possibility to study reaction involving oxygen radicals rather than the cyanide radical which presented limitations related the low photo-absorption cross section in addition to technical difficulties encountered to maintain stable concentration of the precursor for different measurements due to the sublimation process. The ozone precursor however being a gas and with more than order of magnitude higher photo-absorption cross section can be a potential candidate in future work.

Optimization work is to be carried out to increase the sensitivity of the Ka band spectrometer by investigating the performances of the different electronic components in particular the low noise amplifiers as referred to in chapter IV. Increasing the sensitivity of the Ka band and couple it with the newly developed apparatuses to lower pressure broadening in the CRESU environment will enable to study larger molecules with extension to astrobiology.

On the other hand, a new project is also under development to extend the current operating frequency range of the E band spectrometer to higher frequency bands targeting smaller molecules, less sensitive to pressure broadening, the new spectrometer can be mounted on the CRESU B chamber.

## **Appendix**

### A.III. Flow conditions in CRESU environment

► He-18.7K-0.116 nozzle conditions

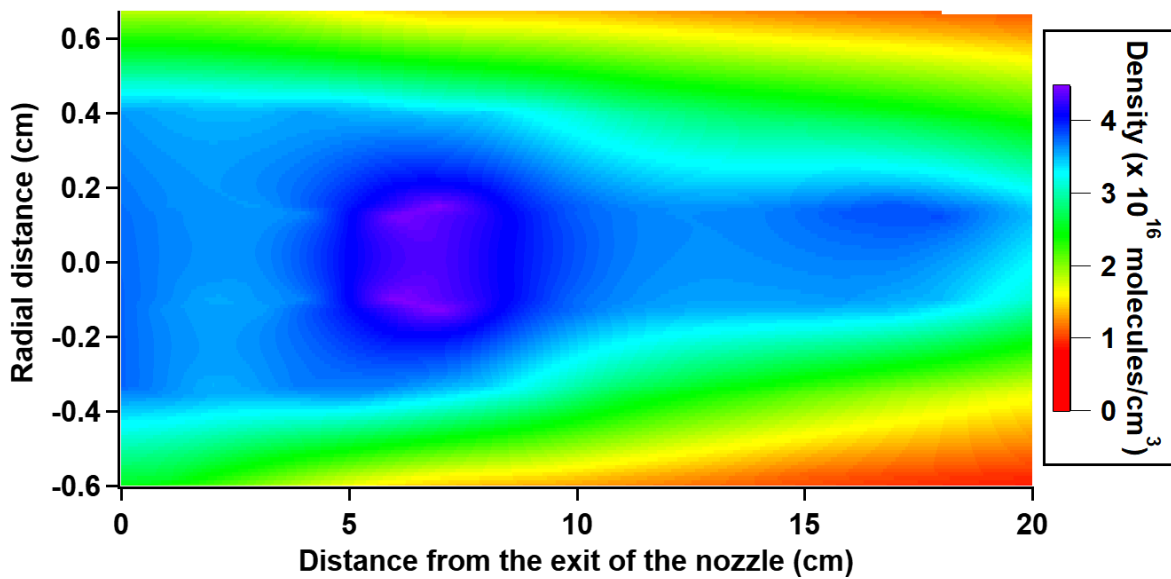
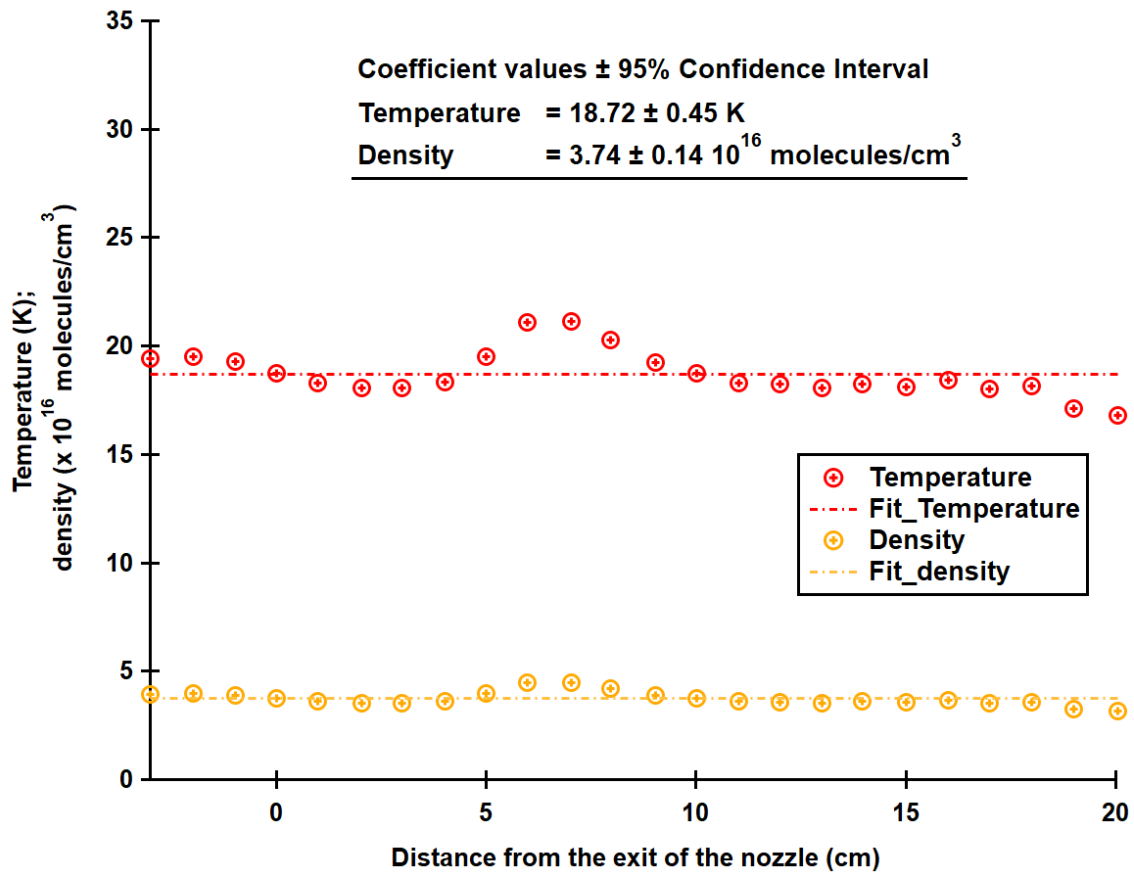


Figure A.III.1. Pitot profile of the He-20K-0.116 nozzle operating conditions

► He-17K-0.12 nozzle conditions

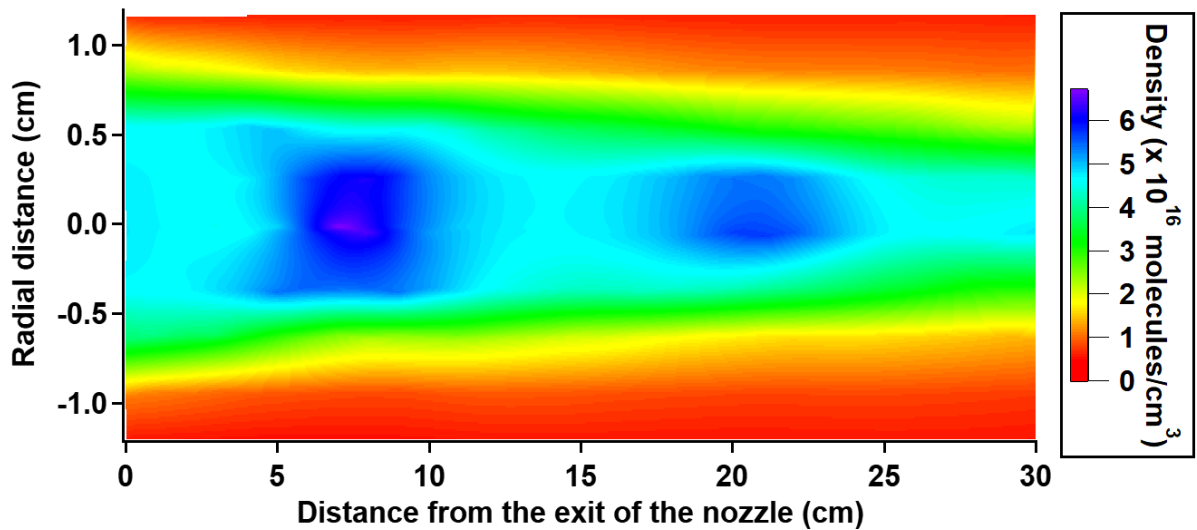
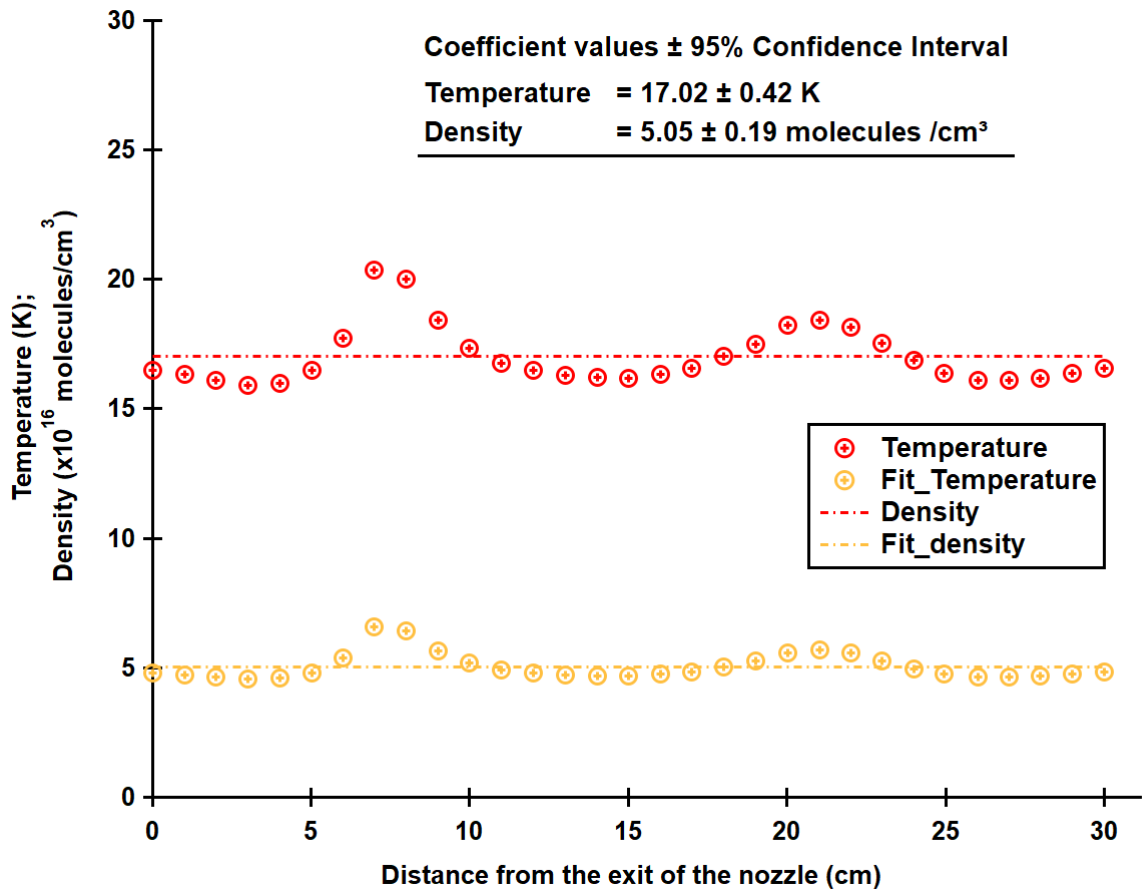
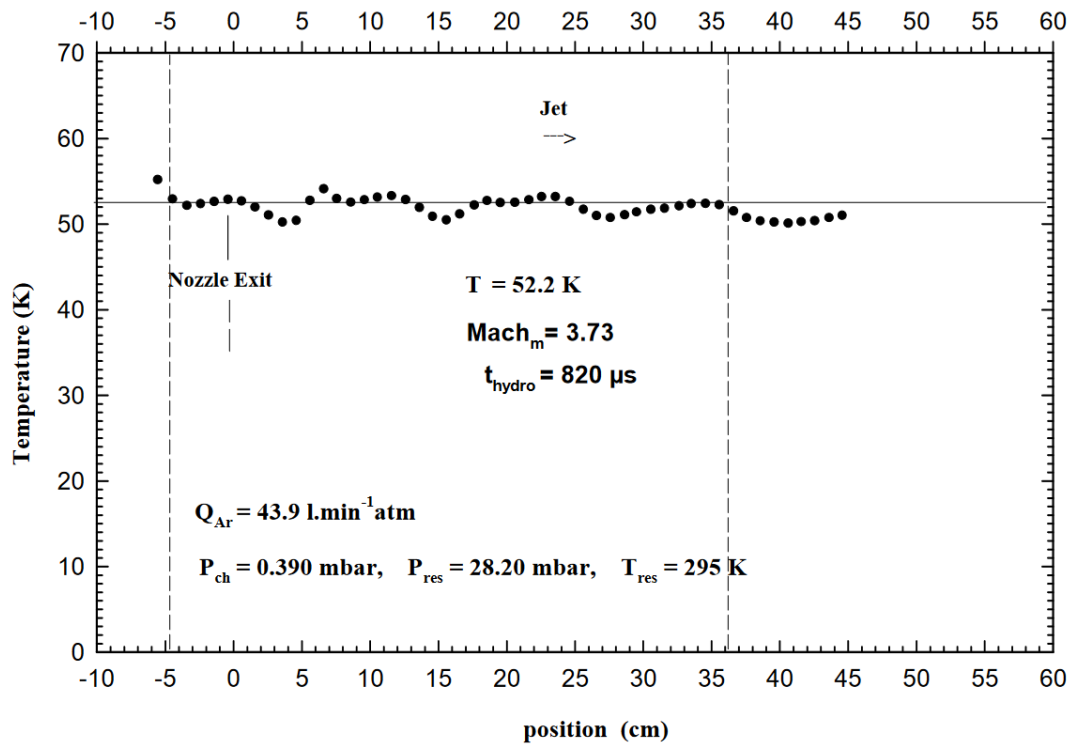


Figure A.III.2. Pitot profile of the He-17K-0,12 nozzle operating conditions

► Ar-50K-0.3 nozzle conditions



Ar\_50K\_0.3

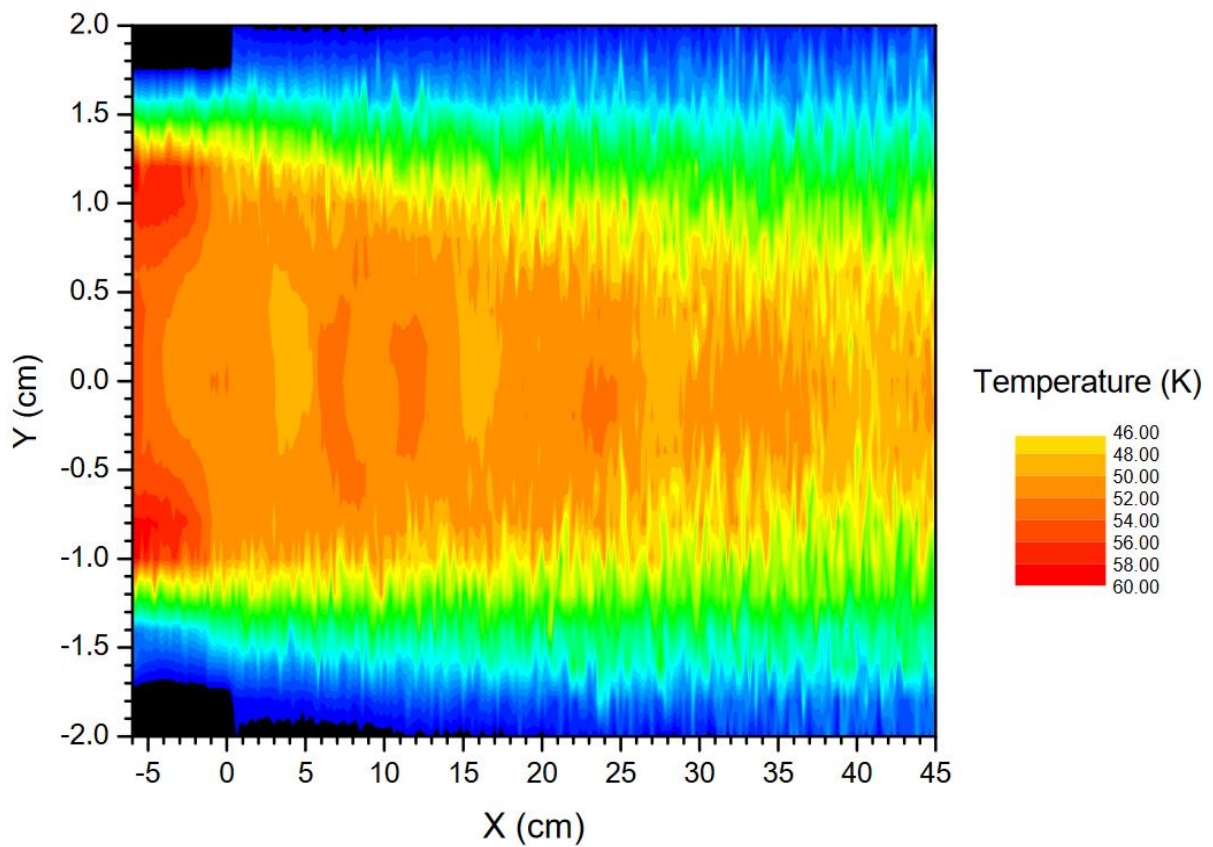


Figure A.III.3. Temperature profile of the Ar 50 K0.3 nozzle operating with argon as a carrier gas

► He-20K-0.64 conditions

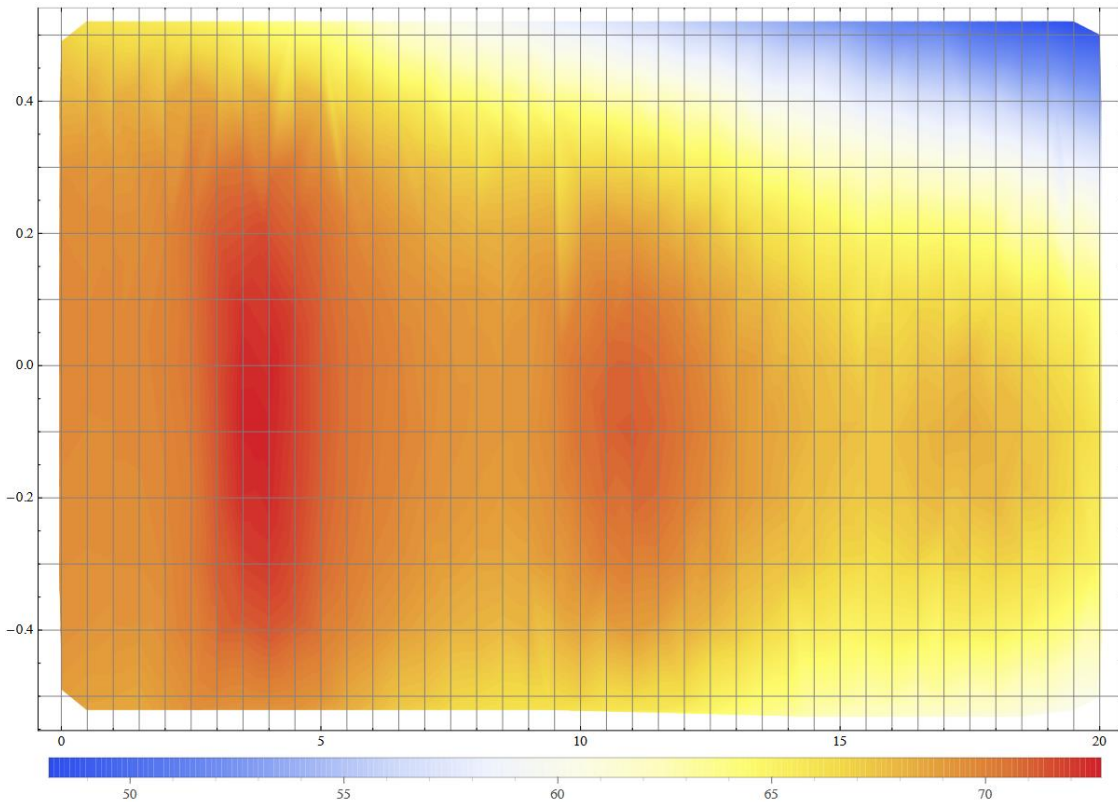
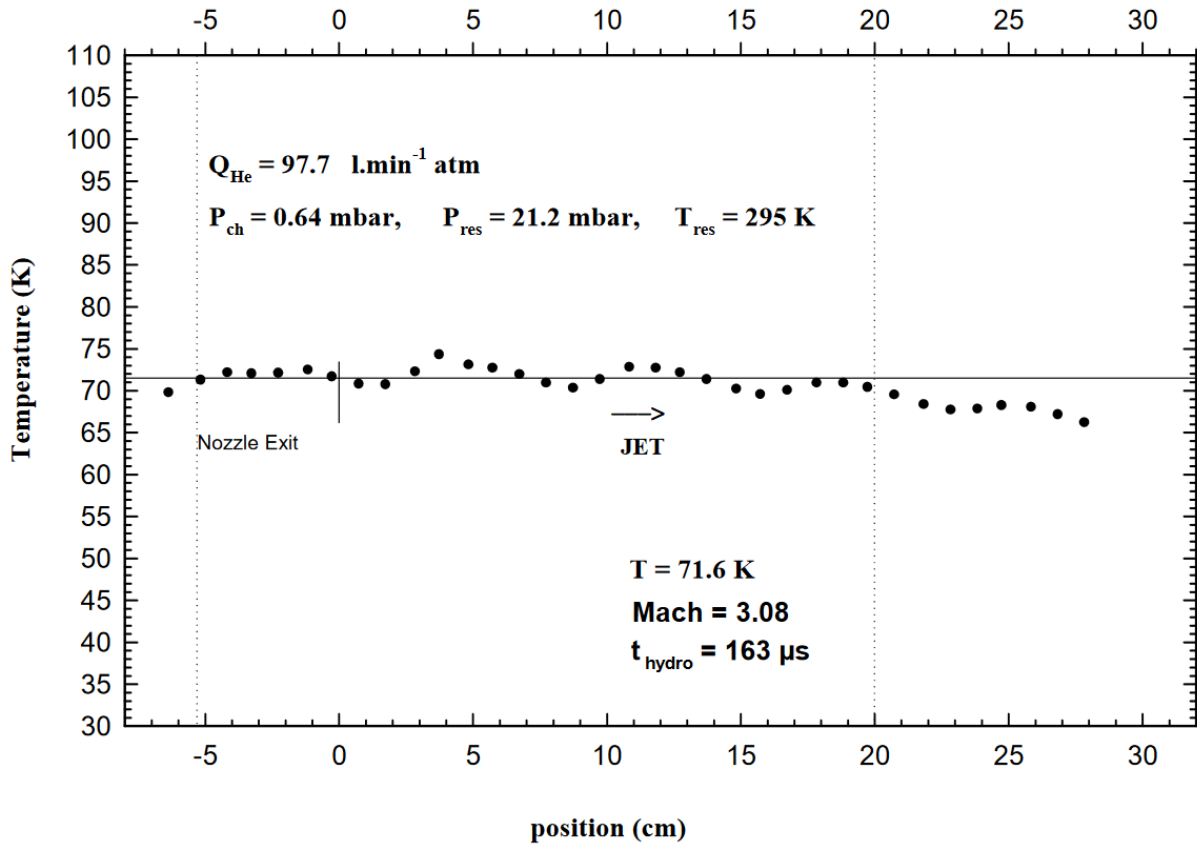


Figure A.III.4. Temperature profile of the Ar 50 K0.3 nozzle operating with helium as a carrier gas

Table A.III.1: Ar-50K0.3 operating experimental conditions with argon and helium

| Parameters | Gas    | Temperature (K) | Density | Hydrodynamic time ( $\mu\text{s}$ ) | Flow rate (slm) | Reservoir pressure (mbar) | Chamber pressure (mbar) |
|------------|--------|-----------------|---------|-------------------------------------|-----------------|---------------------------|-------------------------|
| AR 50K 0.3 | Argon  | 52.2            | 5.15    | 817                                 | 43.9            | 28.2                      | 0.39                    |
|            | Helium | 71.6            | 6.01    | 163                                 | 97.7            | 21.2                      | 0.64                    |

► Ar-29.6K-0.082 nozzle conditions

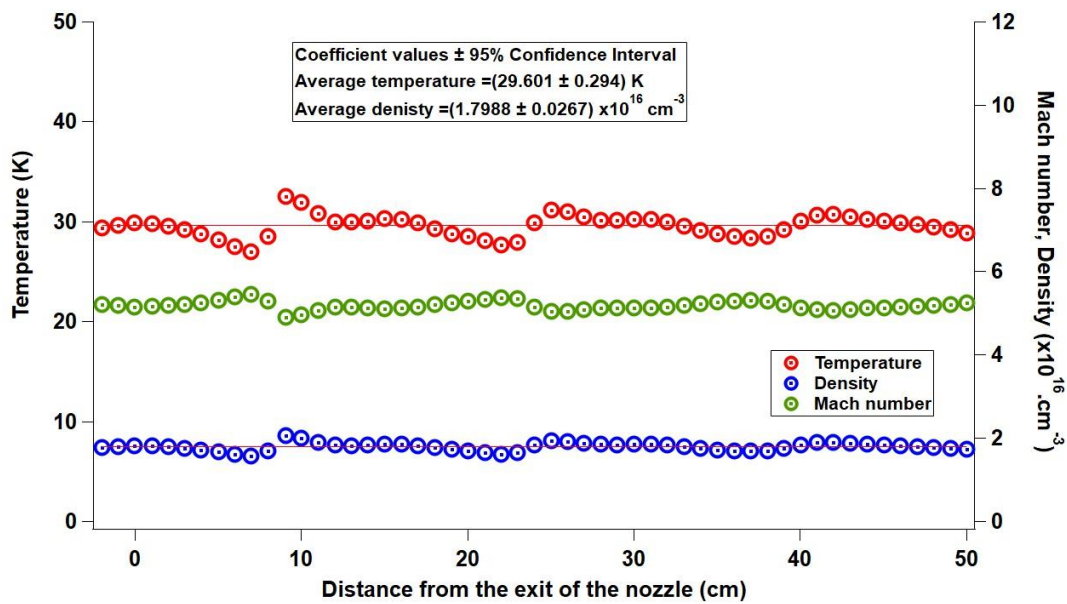
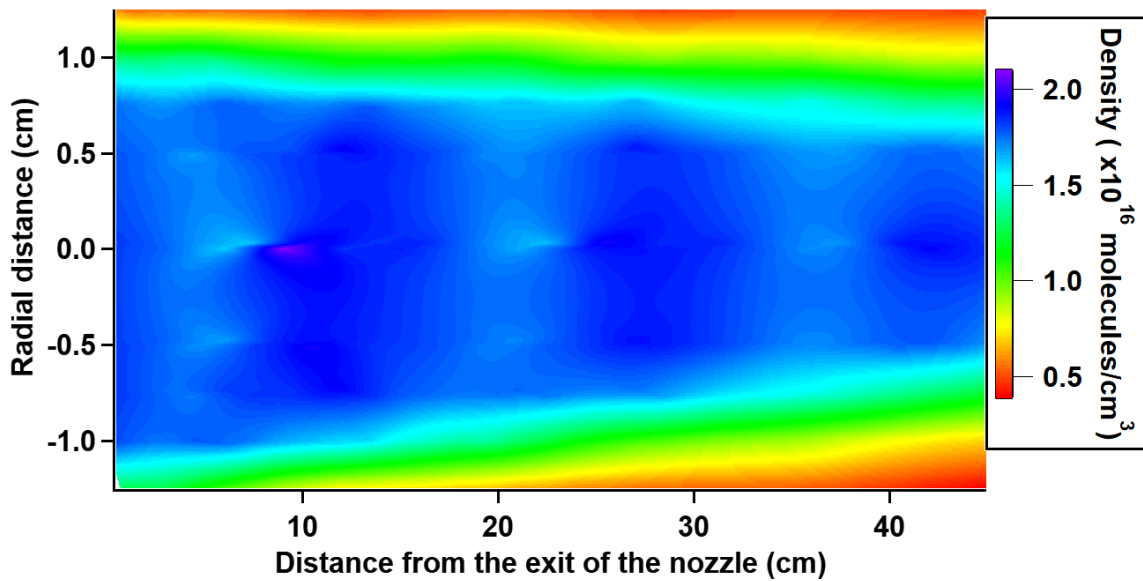


Figure A.III.5. Pitot profile of a Ar-29.6K-0.082 nozzle

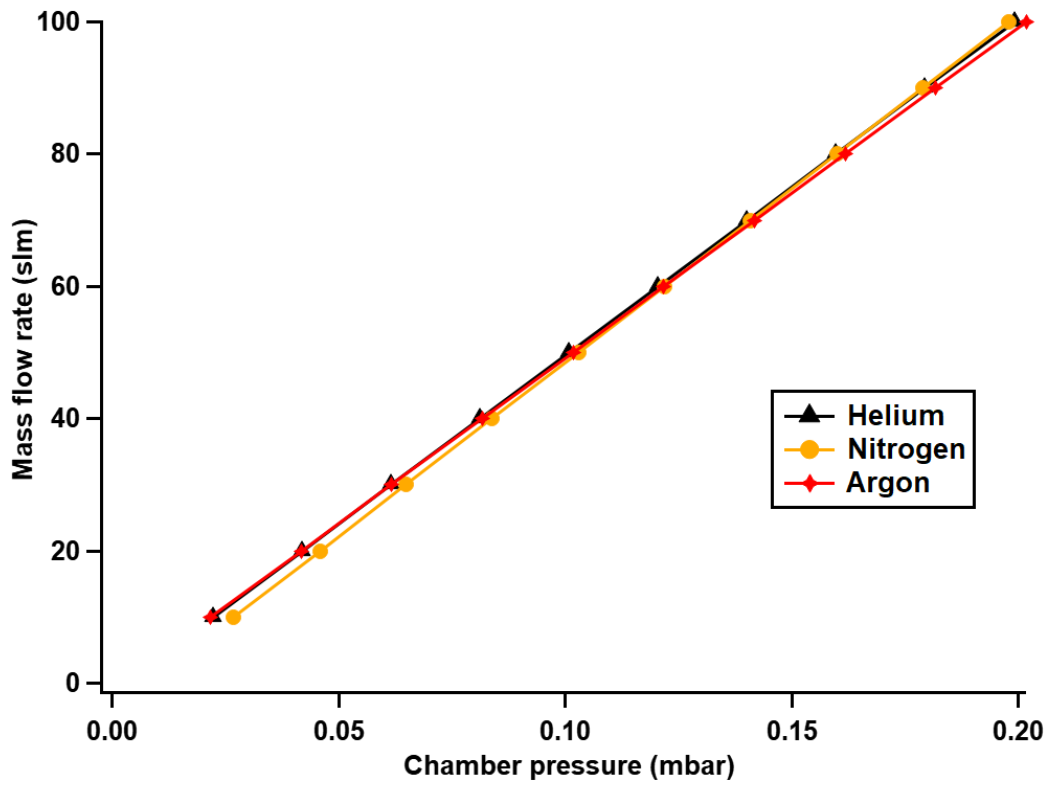


Figure A.III.5 Characteristic curves of the CRESUCHIRP pumping group

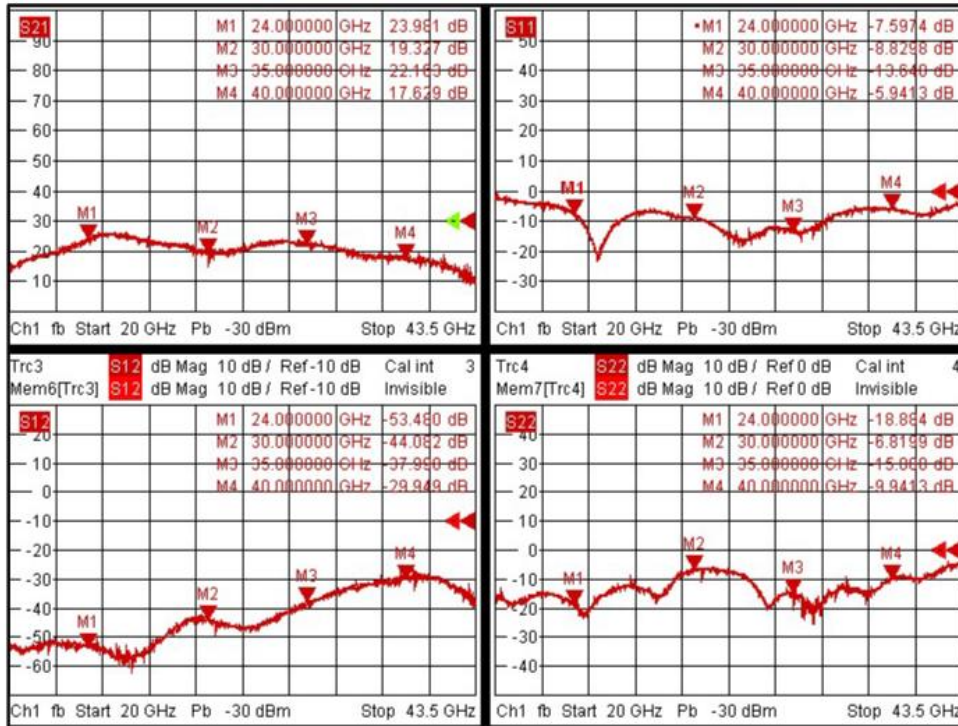
► Table of the flow conditions of the 3 D printed nozzles used in the project

**Appendix**

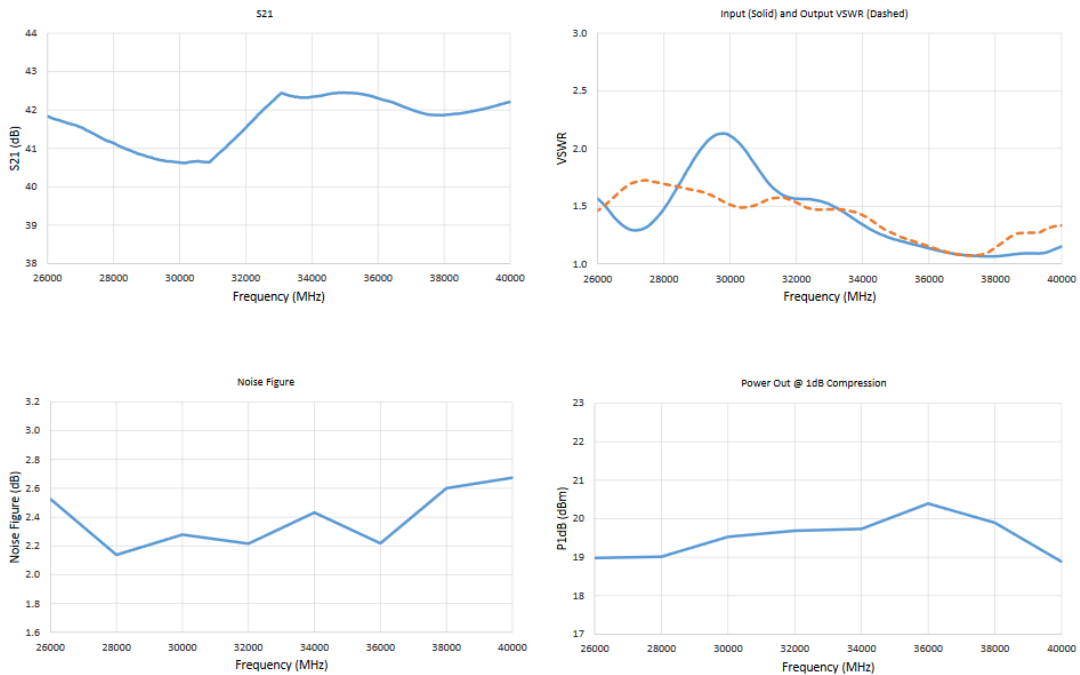
| Name           | Reference      | Gas | Flow (slm) | Reservoir temperature (K) | Reservoir pressure (mbar) | Temperature of the jet (K) | Chamber pressure (mbar) | Density ( $10^{16}$ cm <sup>-3</sup> ) | Mach number | Velocity (m/s) | Hydrodynamic time (us) | Hydrodynamic length (cm) | Type of printing resin |
|----------------|----------------|-----|------------|---------------------------|---------------------------|----------------------------|-------------------------|--|-------------|----------------|------------------------|--------------------------|------------------------|
| <b>He 35 K</b> | He-30K-0,127   | He  | 72.2       | 295                       | 37.8                      | 30.2                       | 0.146                   | 3.01                                   | 5.13        | 1659.5         | 150.6                  | 21+4                     | standard clear         |
| <b>He 20 K</b> | He-18,7K-0,116 | He  | 45.77      | 295                       | 96.3                      | 18.7                       | 0.116                   | 3.78                                   | 6.66        | 1696.2         | 135.6                  | 20+3                     | standard clear         |
|                | He-17K-0,12    | He  | 69,3       | 295                       | 149,6                     | 17                         | 0,135                   | 5,05                                   | 7           | 1701.8         | 176.3                  | 30                       | Standard clear         |
| <b>He 10 K</b> | He-10K-0.128   | He  | 51.9       | 295                       | 540.36                    | 10.04                      | 0.128                   | 8.27                                   | 9.31        | 1723.5         | 203                    | 35                       | Grey Pro               |
|                | N2-80K-0.49    | N2  | 47.76      | 295                       | 47.83                     | 80.18                      | 0.49                    | 4.27                                   | 3.68        | 6.726          | 847.45                 | 53+4                     | standard black         |
| <b>N2 83 K</b> | N2-88K-0.31    | N2  | 24.72      | 295                       | 22.72                     | 88.2                       | 0.31                    | 2.48                                   | 3.47        | 664.4          | 812.8                  | 50+4                     | standard black         |
|                | N2-97K-0.219   | N2  | 14.83      | 295                       | 11.83                     | 97.03                      | 0.219                   | 1.56                                   | 3.27        | 656.5          | 396.1                  | 22+4                     | standard black         |
| <b>N2 38 k</b> | N2-38K-0.148   | N2  | 41.83      | 295                       | 146.29                    | 41.47                      | 0.148                   | 2.47                                   | 5.56        | 730.44         | 684.5                  | 50                       | standard black         |
| <b>N2 55 K</b> | N2-55K-0.76    | N2  | 24.2       | 295                       | 270.83                    | 54.45                      | 0.76                    | 10.079                                 | 4.7         | 706.98         | 777.96                 | 55                       | Grey Pro               |
| <b>N2 55 K</b> | N2-55K-0.544   | N2  | 34         | 295                       | 204.88                    | 53.9                       | 0.544                   | 7.09                                   | 4.73        | 707.76         | 777.09                 | 55                       | Grey Pro               |
| <b>N2 38 K</b> | N2-38K-0.39    | N2  | 30.88      | 295                       | 470.04                    | 38.51                      | 0.39                    | 7.02                                   | 5.77        | 730.11         | 753.32                 | 55                       | Grey Pro               |
| <b>N2 30 K</b> | N2-30K-0.183   | N2  | 31.41      | 295                       | 477.18                    | 30.79                      | 0.183                   | 4.07                                   | 6.55        | 740.99         | 742.25                 | 55                       | Grey Pro               |
| <b>N2 24 K</b> | N2-23.5K-0.12  | N2  | 30         | 295                       | 773.5                     | 23.53                      | 0.12                    | 3.37                                   | 7.6         | 761.85         | 656.3                  | 50                       | Standard               |
|                |                |     |            |                           |                           | 35.12                      |                         |  |             |                |                        |                          | black                  |
| <b>Ar 35 K</b> | Ar-35K-0.28    | Ar  | 20.51      | 295                       | 52.7                      |                            | 0.28                    | 5.26                                   | 4.72        | 521            | 959.24                 | 55                       | Grey Pro               |

## A. IV. Ka band and pressure broadening measurements

- ▶ Ka band spectrometer low noise amplifier response
- RF-Lambda R24G40GSB



- Miteq LNA-40-26004000-35-15P



## ► First Ka band molecular detection

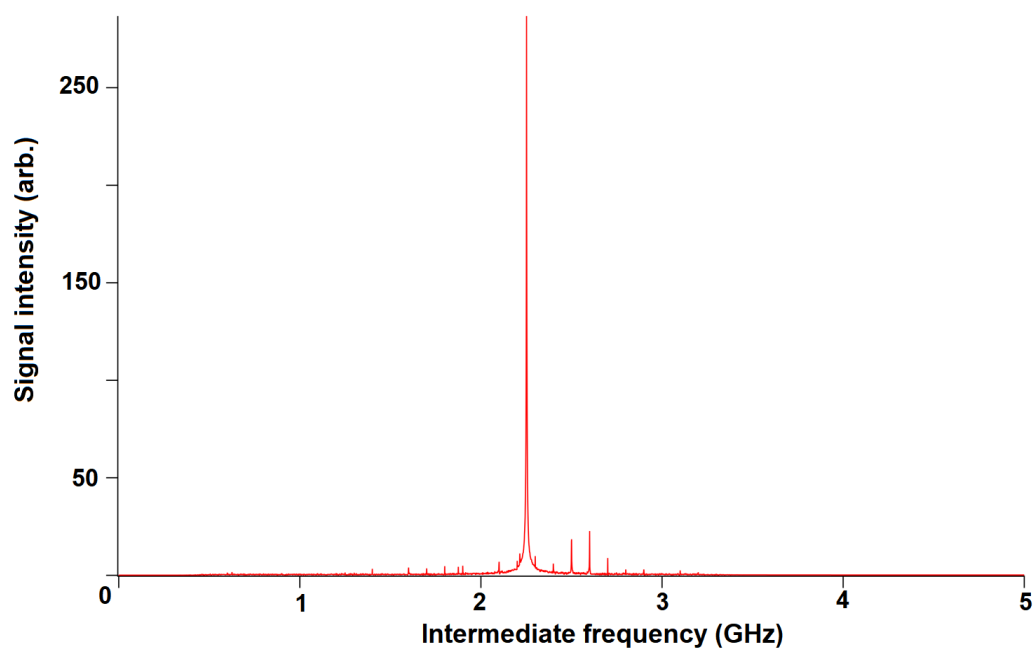


Figure A.IV.1. The first recorded Ka band spectrum for  $J_{ka}, K_c = 4_{1,3} - 3_{1,2}$  transition of vinyl cyanide at 38849.7 MHz under flow cell conditions at 295 K and 5  $\mu$ bar

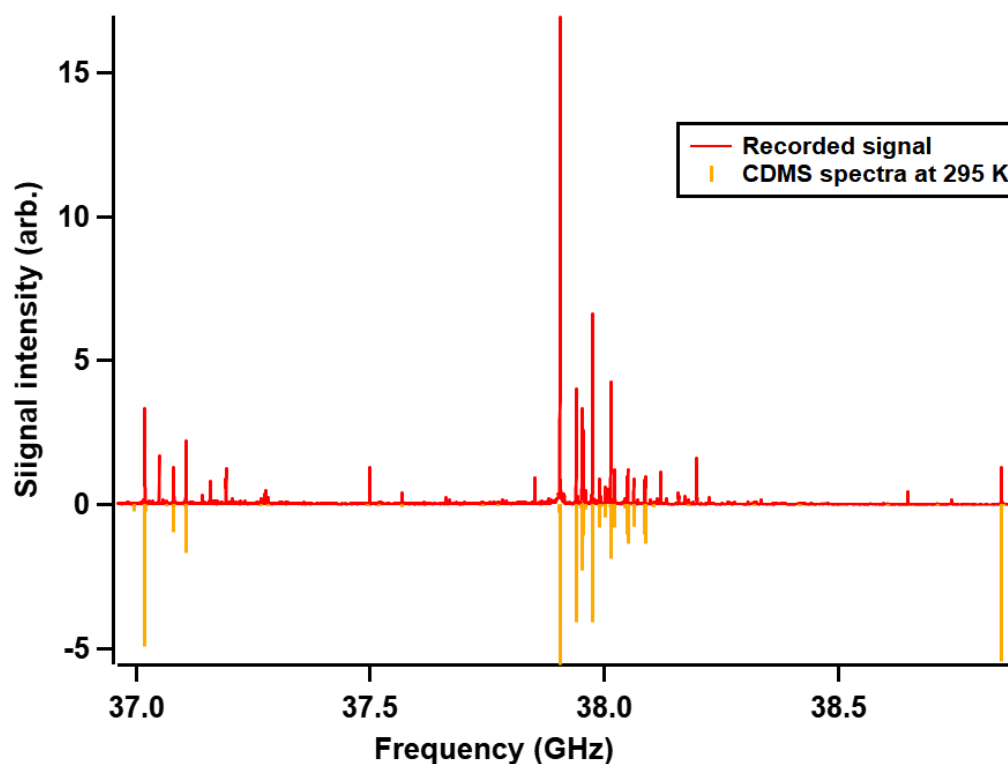


Figure A.IV.2. Vinyl cyanide spectrum from a chirp of 0.2-2 GHz mixed with a doubled LO of 19.549 GHz targeting transitions between 37.098 GHz and 40.5 GHz under the flow cell conditions filled with helium at 295 K and 4.53  $\mu$ bar

## ► Time domain frequency domain Voigt fitting

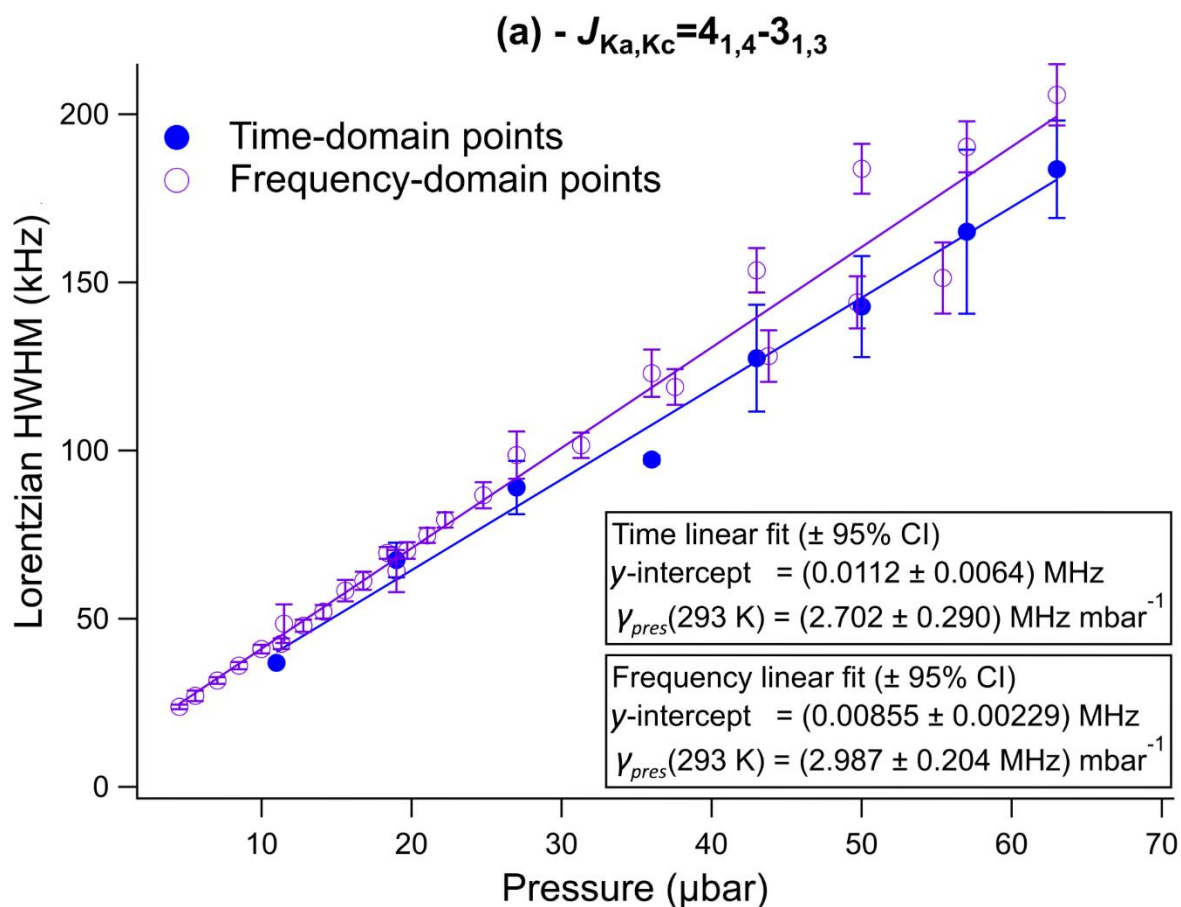


Figure A1.V.3. Plots of the HWHM of the Lorentzian component of the Voigt profile fit to FIDs using both the time fitting technique and the frequency fitting technique of the  $J_{K_a, K_c} = 3_{1,2} - 2_{1,1}$  transition of vinyl cyanide. The equations for the linear fits to each data set are also displayed.

## A.V. Secondary expansion apparatus: tools and method of characterization

### ► Optimization of the skimmer support geometry

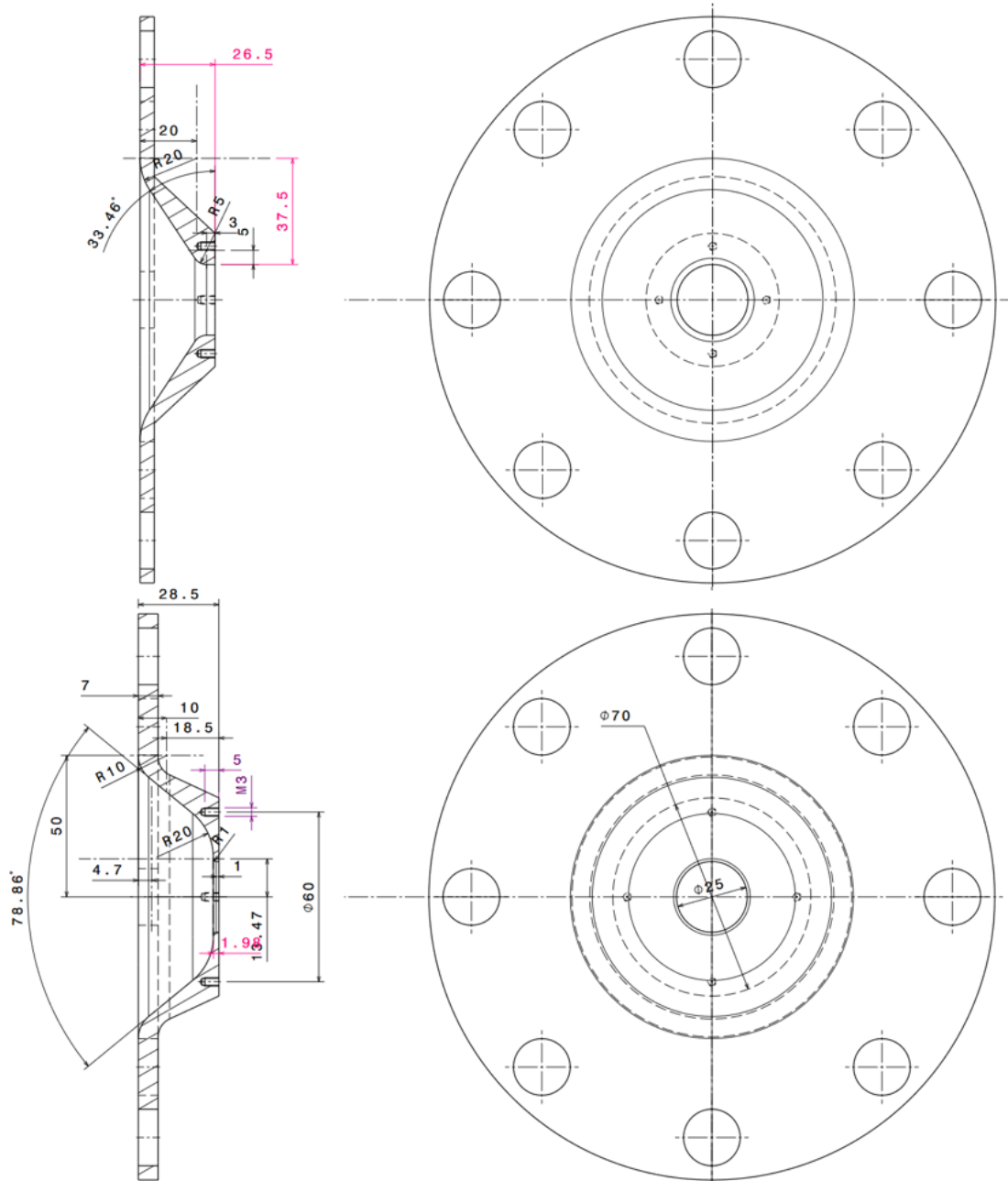


Figure A.V.1. Skimmer support profile, top panel shows the non-optimized profile with the possibility of forming shockwaves with some nozzles, bottom panel gives the optimized profile with CFD simulations

Table A.V.1. Simulation of the post skimmer expansion conditions

| Conditions and models                             | Navier-Stokes solver                 | DSMC   |
|---|--------------------------------------|--|
| Nozzle skimmer combination                        | Ar-35K-0.28 nozzle with 4 mm skimmer |  |
| Pressure far field (mbar)                         | 0.28                                 | /  |
| CRESU flow speed (m/s)                            | 521                                  |  |
| CRESU flow temperature (K)                        | 35.12                                |  |
| Flow Density ( $\times 10^{16} \text{ cm}^{-3}$ ) | 5.26                                 |  |
| Pressure CRESU chamber (mbar)                     | 0.28                                 | /  |
| Pressure skimmer ( $\mu\text{bar}$ )              | 9.8                                  |  |
| Calculation model                                 | Slip condition                       | VHS, diffuse reflection with full accommodation to the surface temperature |
| Simulated molecules                               | /                                    | 40,477,429   |

► Simulation of the Ar-50K-0.3 and the 4 mm skimmer

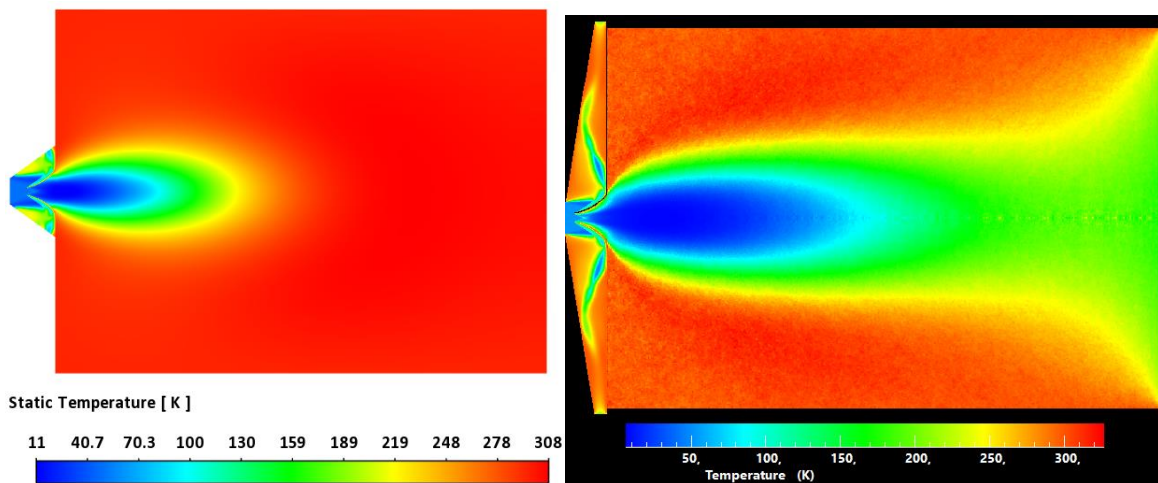


Figure A.V.2. Temperature map from simulations of the secondary expansion of the Ar-35K-0.28 nozzle in the 4 mm skimmer, left with CFD simulations and right using DSMC calculations, same procedure was followed with using the Ar50K-0.3 conditions given in Table A.III.1

## ► Vinyl cyanide signal in the secondary expansion environment

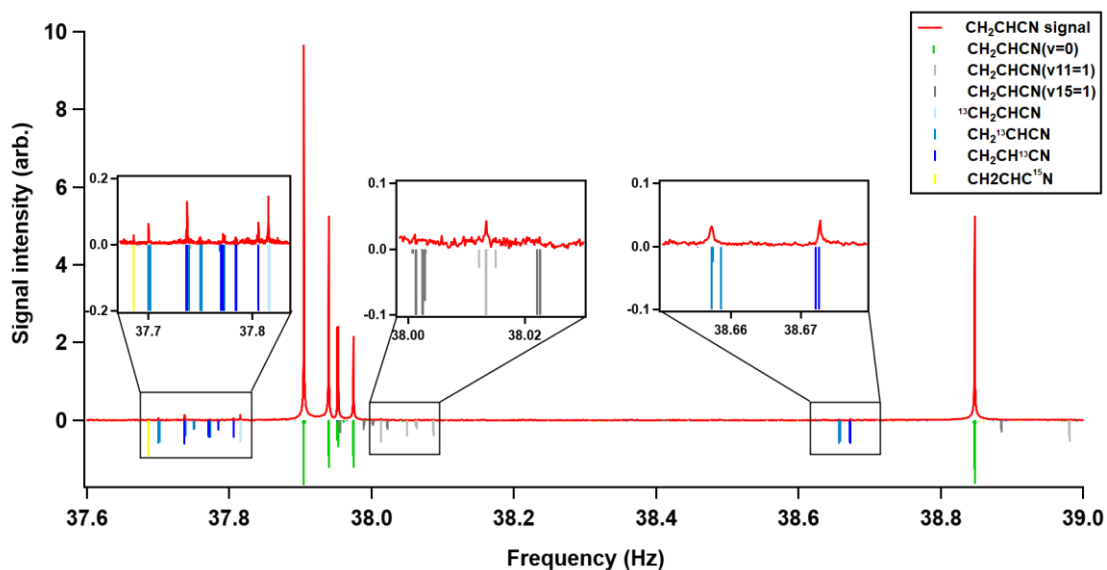


Figure A.V.3. A spectrum of vinyl cyanide in the Ka band under secondary expansion conditions from an Ar-25K-40 nozzle flow expanding in 4 mm skimmer

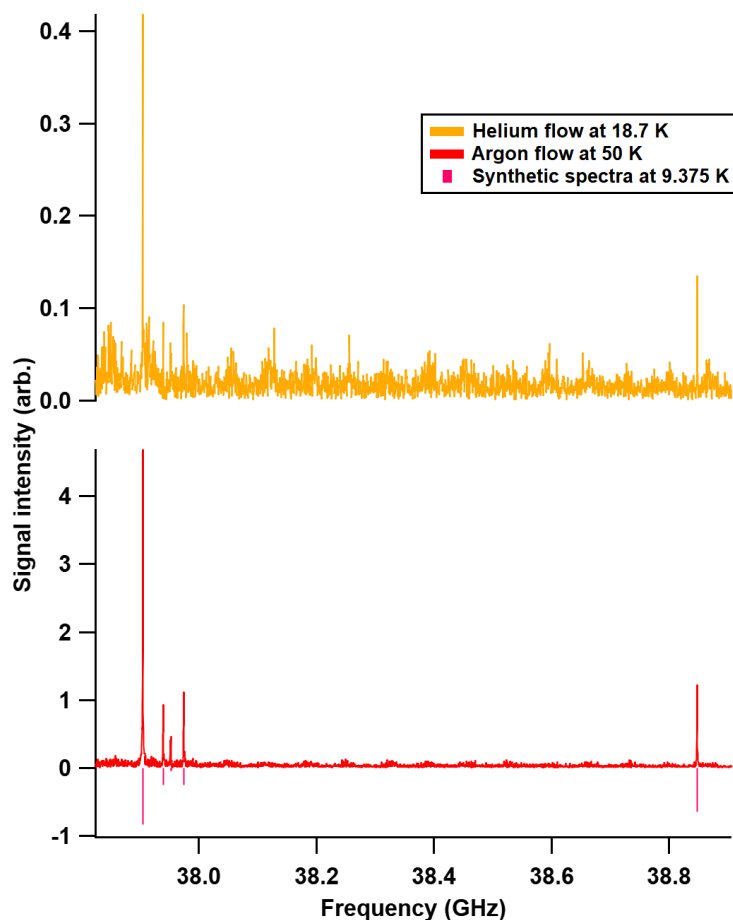
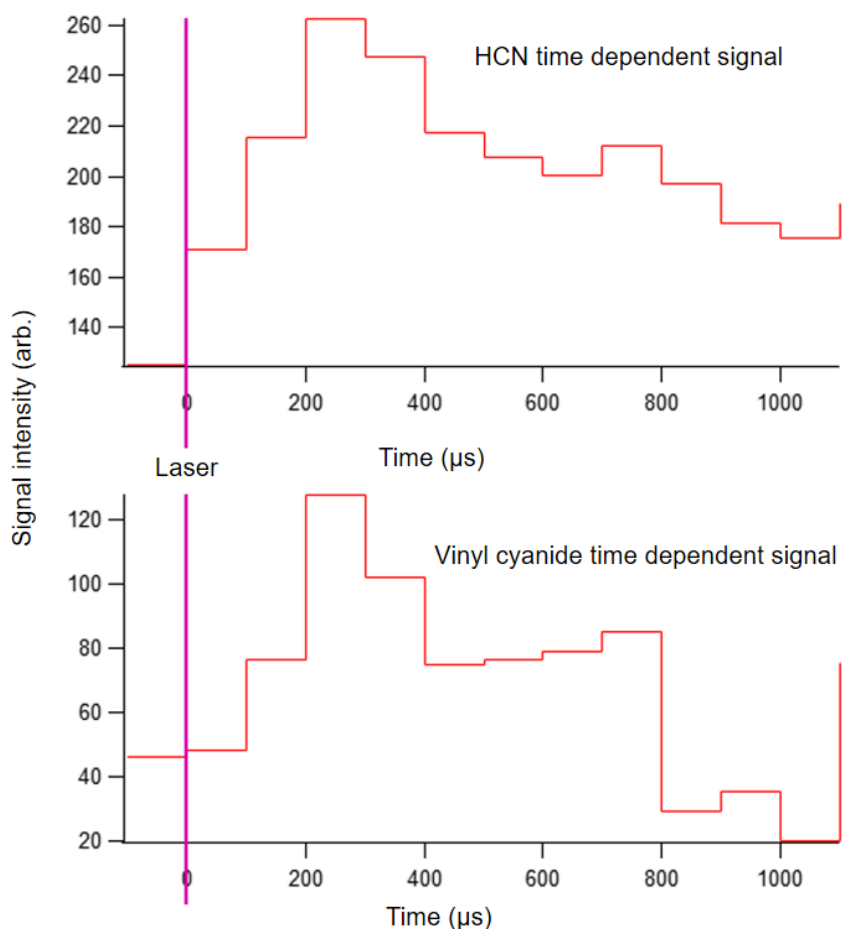


Figure A.V.4. Vinyl cyanide signal in helium flow and argon under secondary expansion conditions (Ar-50K-0.3 and the He-18.7-0.116 nozzles were used with the 4 mm skimmer)

## ► Vinyl cyanide and HCN time dependent signal from CN + ethylene reaction



**Figure A.V.5.** HCN and vinyl cyanide from reaction recorded with multicolor pulse and along 1600  $\mu\text{s}$ , 30 frames have been subtracted before the laser shot leaving 130 frames that were horizontally averaged by 10 to get 13 time dependent signals for the determination of branching ratio, here considered only the signal at 200  $\mu\text{s}$  for HCN and vinyl cyanide because of the signal gradual decrease right after this time.

► HC<sub>3</sub>N from CN + acetylene reaction at 248 nm

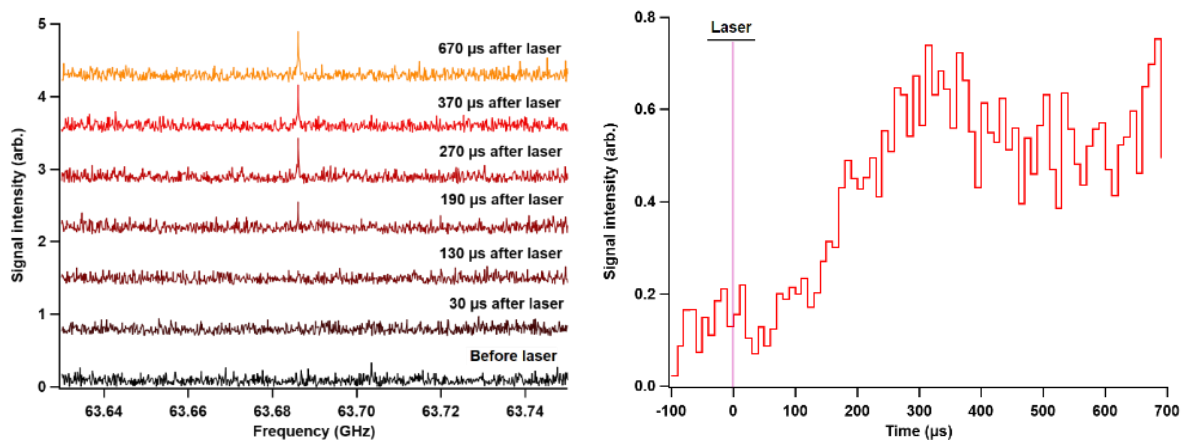


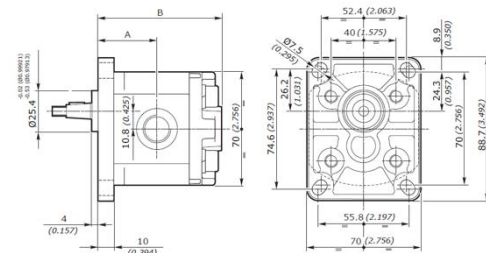
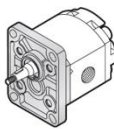
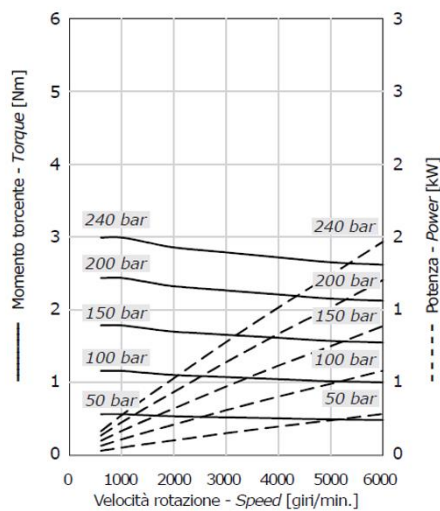
Figure A.V.6. HC<sub>3</sub>N from CN+C<sub>2</sub>H<sub>2</sub> reaction; (a) is the spectrum of  $J=7-6$  rotational transition of HC<sub>3</sub>N taken at different times of the reaction in the uniform flow, (b) is the corresponding time dependent signal. Results acquired from a single frequency pulse targeting the HCN transition with 50,000 averaged scans.

A.VI. Pulsed system: motor characteristics

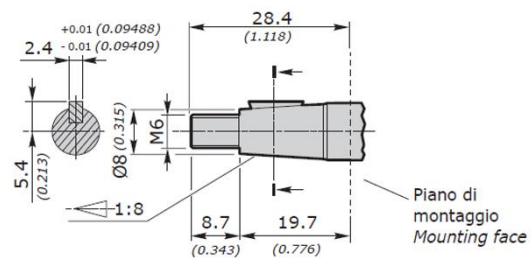
| GRUPPO GROUP<br>1SM | CILINDRATA DISPLACEMENT |                      | PRESSIONE MAX MAX PRESSURE |      |     |      | VELOCITÀ MAX MAX SPEED | PORTATA MAX MAX FLOW |         | VELOCITÀ MIN MIN SPEED | PORTATA MIN MIN FLOW |         |
|---------------------|-------------------------|----------------------|----------------------------|------|-----|------|------------------------|----------------------|---------|------------------------|----------------------|---------|
|                     | cm <sup>3</sup> /giro   | in <sup>3</sup> /rev | P1                         |      | P2  |      | giri/min - rpm         | l/min                | Gal/min | giri/min - rpm         | l/min                | Gal/min |
|                     |                         |                      | bar                        | psi  | bar | psi  |                        |                      |         |                        |                      |         |
| 1SM 009*            | 0.89                    | 0.05                 | 260                        | 3770 | 280 | 4060 | 6000                   | 5.3                  | 1.40    | 600                    | 0.49                 | 0.13    |

DIMENSIONI • DIMENSIONS

1SM 009



| GRUPPO - GROUP 1 | A     | B     | MASSA - MASS |
|------------------|-------|-------|--------------|
|                  | mm    | mm    | kg           |
| 1SM 009          | 34.80 | 73.6  | 0.91         |
|                  | 1.370 | 2.898 | 2.01         |



• Tests at 40°C with VG46 oil

Figure A.VI.1. Characteristic properties of the Hydraulic motor used for the rotation of the disk.

## **Résumé détaillé**

### **Introduction**

L'astrochimie est la discipline définie par l'intersection de la chimie et de l'astrophysique, elle s'intéresse à l'étude des différents processus de formation et de destruction des espèces chimiques et de leurs abondances dans différents environnements spatiaux et objets astronomiques tels que le milieu interstellaire et les atmosphères planétaires, des environnements présentant diverses conditions extrêmes de températures et de densités.

Le milieu interstellaire en particulier, représentant la matière existant entre les étoiles, recèle une chimie très riche, étant l'hôte de nombreuses étoiles et exposé à toutes sortes de radiations, rayons cosmiques et vent solaire. Il est constitué de trois régions principales, la première est la phase dense froide constituée de nuages moléculaires et de milieu neutre froid où les températures varient de 10 à 150 K et les densités peuvent atteindre  $10^6$  particules  $\text{cm}^{-3}$ . C'est la région la plus dense de l'ISM et elle est responsable des nombreux processus qui conduisent à la formation des étoiles. Les milieux neutres et ionisés chauds sont constitués de gaz neutres et ionisés avec des températures pouvant atteindre 6000 à 10000 K, ces régions sont principalement raréfiées avec des densités beaucoup plus faibles que le milieu neutre froid, autour de  $0,2-0,6 \text{ cm}^{-3}$ , et enfin nous avons les milieux ionisés très chauds avec des températures de l'ordre de  $10^6$  K et des densités entre  $10^{-2}$  et  $10^{-4} \text{ cm}^{-3}$ . Plus de 200 espèces comprenant des molécules, des atomes et des ions ont été découvertes au cours des 80 dernières années, l'hydrogène étant l'espèce la plus abondante, suivie de l'hélium, puis du carbone, de l'oxygène et de l'azote. Le milieu interstellaire contient également environ 1% de sa masse sous forme de poussière qui forme des grains glacés constitués principalement d'eau, de méthanol, d'ammoniac, de monoxyde et de dioxyde de carbone, responsables de la formation de nombreuses molécules organiques complexes par désorption thermique dans les régions chaudes. Ce travail est pertinent pour la phase gazeuse dans le milieu neutre froid du milieu interstellaire.

## **i. Astrophysique de laboratoire**

Suite aux progrès réalisés dans le développement d'instruments et de technologies sophistiqués qui permettent de mener des observations astronomiques des espèces multiples et complexes du milieu interstellaire en particulier, l'interprétation de ces observations et la conversion des données en résultats tangibles sont nécessaires. L'astrophysique de laboratoire contribue à élargir notre compréhension des processus physiques impliqués dans la formation des espèces observées en reproduisant les conditions du milieu étudié au laboratoire puis en réalisant des expériences pour déterminer les constantes fondamentales et les propriétés physiques. Ceci aide à créer une base de données pour les espèces d'intérêt astrochimique avec des informations sur leurs origines, leur structure moléculaire, leur durée de vie ainsi que les processus et réactions qui conduisent à leur formation et à leur dissociation. Ces bases de données fourniront aux théoriciens les données nécessaires pour effectuer des calculs de modélisation astrochimique afin d'étudier les voies de formation et de destruction des espèces. L'astrophysique de laboratoire et la modélisation astrochimique complètent les observations astronomiques et forment ensemble les axes fondamentaux de l'astrochimie.

- **Projet CRESUCHIRP et objectif de la thèse**

Motivé par les nombreuses découvertes récentes de molécules avec la radioastronomie et le manque de rapports de branchement des réactions à basse température dans les bases de données en raison de difficultés instrumentales, ce travail s'inscrit dans le cadre du projet CRESUCHIRP visant à concevoir et construire un nouveau réacteur CRESU (cinétique de réaction en écoulement supersonique uniforme) équipé de deux CP-FTmmW (chirped pulsed Fourier transform millimeter wave spectroscopy) spectromètres fonctionnant en bande Ka de 26,5 à 40 GHz et la bande E de 60 à 90 GHz dans le but de déterminer les rapports de branchement des réactions à basse température d'intérêt astrophysique.

Dans cette thèse nous focalisons sur les limitations instrumentales du couplage de la technique CRESU avec la spectroscopie CP-FTmmW définit par le terme CPUF (Chirped Pulse in Uniform Flow) et nous présentons le développement de deux

instruments pour optimiser la détection du signal moléculaire des espèces étudiées et la détermination des rapports de branchement des réactions.

Le chapitre II présente la technique CPUF (chirped pulse in uniform flow), la technique CRESU et ses différents aspects avec la spectroscopie CP-FTmmW.

Dans le chapitre III, nous présentons le développement et la construction du dispositif expérimental.

Le chapitre IV discute et évalue les limites de la technique CPUF, notamment l'impact de la pression sur le signal micro-onde, en effectuant des mesures d'élargissement collisionnel des raies du cyanure de vinyle et du benzonitrile dans la bande Ka.

Les chapitres V et VI présentent le développement de deux instruments d'optimisation pour abaisser la température et la pression des jets du CRESU afin d'améliorer le signal micro-onde.

Le chapitre V présente l'appareil SKISURF (SKImmed uniform SUpersonic Flow), un nouvel instrument développé pour optimiser les conditions d'écoulement dans la technique CRESU en générant des détentes secondaires d'une partie du jet supersonique en utilisant des skimmers. La réaction du CN avec l'éthylène est étudiée et le rapport de branchement correspondant est mesuré.

Le chapitre VI présente le développement du système CRESU pulsé, un deuxième instrument pour optimiser la technique CPUF, où la technique CRESU fonctionnera en mode pulsé à l'aide d'un hacheur aérodynamique.

## **ii. Chapitre II : la technique CPUF (chirped pulse in uniform flow)**

L'étude de la cinétique d'une réaction chimique à basse température nécessite la combinaison d'une technique de refroidissement pour créer l'environnement froids avec un instrument de détection capable de suivre l'évolution des espèces pendant la réaction. Le couplage de la technique CRESU avec la spectroscopie micro-ondes pour la détection des espèces d'intérêt astrochimique a été établi pour la première fois dans une collaboration entre les groupes d'Arthur Suits, Bob Field et Ian Sims et est apparu sous le terme CPUF (chirped pulse in uniform flow) dans une série de publications en

2014,<sup>1,2</sup> la plus pertinente pour notre étude était la détermination des rapports d'embranchement de la réaction CN et propyne en 2015<sup>3</sup> qui a prouvé la capacité de la technique dans l'étude des réactions bimoléculaires à basses températures par la détermination quantitative des rapports de branchement associés.

La technique CRESU utilise les tuyères de Laval pour générer des jets supersoniques uniformes à basses températures en détendant le gaz d'un environnement à haute pression, généralement un réservoir, dans un environnement de basse pression qu'on définit par la chambre CRESU. La différence de pression est créée par un grand groupe de pompage capable d'établir des pressions suffisamment basses avec des débits massiques élevés. La technique CRESU introduit le concept d'uniformité, c'est-à-dire les conditions de l'écoulement comme la température et la pression restent constantes dans le jet supersonique, ce qui rend la technique idéale pour étudier la cinétique des réactions dans un environnement stable à température et pression uniformes. La technique utilise de débits de gaz relativement élevés par rapport à d'autres techniques de refroidissement pour maintenir un temps d'uniformité élevé. Les jets uniformes peuvent durer des centaines de microsecondes selon la nature du gaz.

La spectroscopie (CP-FTMW) est une technique de détection distinctive à large bande, qui permet la détection de plusieurs espèces en même temps, elle est basée sur la théorie de la spectroscopie rotationnelle micro-onde étendue dans cette thèse à la bande des ondes millimétriques (CP-FTmmW), elle consiste à polariser les molécules avec des transitions dipolaires dans la gamme ciblée de l'impulsion (chirped pulse) en les exposant à un champ électromagnétique pendant une courte période de temps qui les excite à des niveaux d'énergie rotationnelle plus élevés, créant une phase de rotation cohérente. Les molécules ciblées relaxent à leur état initial en émettant un signal décroissant dans le temps connu par la FID (Free Induction Decay). Ce signal

---

<sup>1</sup> Oldham, J. M.; Abeysekera, C.; Joalland, B.; Zack, L. N.; Prozument, K.; Sims, I. R.; Park, G. B.; Field, R. W.; Suits, A. G. A Chirped-Pulse Fourier-Transform Microwave/Pulsed Uniform Flow Spectrometer. I. The Low-Temperature Flow System. *J. Chem. Phys.* **2014**, *141* (15), 154202.

<sup>2</sup> Abeysekera, C.; Zack, L. N.; Park, G. B.; Joalland, B.; Oldham, J. M.; Prozument, K.; Ariyasingha, N. M.; Sims, I. R.; Field, R. W.; Suits, A. G. A Chirped-Pulse Fourier-Transform Microwave/Pulsed Uniform Flow Spectrometer. II. Performance and Applications for Reaction Dynamics. *J. Chem. Phys.* **2014**, *141* (21), 214203.

<sup>3</sup> Abeysekera, C.; Joalland, B.; Ariyasingha, N.; Zack, L. N.; Sims, I. R.; Field, R. W.; Suits, A. G. Product Branching in the Low Temperature Reaction of CN with Propyne by Chirped-Pulse Microwave Spectroscopy in a Uniform Supersonic Flow. *The Journal of Physical Chemistry Letters* **2015**, *6* (9), 1599–1604.

dépendant du temps contient les empreintes digitales des molécules présentes dans l'échantillon irradié, la transformée de Fourier du FID donne le spectre moléculaire. La technique est considérée comme très distinctive car elle permet de différencier les molécules, définies de manière unique par les transitions rotationnelles, y compris les isotopes, les isomères et les conformères.

### iii. Chapitre III : dispositif expérimental

Le dispositif expérimental est constitué donc de l'appareil CRESUCHIRP où le réacteur CRESU est couplé à un spectromètre CP-FTmmW. Pour étudier la cinétique des réactions et pouvoir effectuer des mesures temporelles de la formation des produits et déterminer les rapports de branchement associés. Le dispositif expérimental est aussi doté d'un laser excimer pour générer les radicaux qui vont ensuite réagir et former les produits. La technique est abrégée par le terme PLP-CPUF (pulsed laser photolysis - chirped pulse in uniform flow).

### iv. Chapitre IV : Elargissement collisionnel des raies micro-onde

Dans cette partie nous présentons le développement d'un spectromètre (CP-FTmmW) fonctionnant dans la bande Ka (26.5 à 40 GHz) cet intervalle de fréquence couvre les transitions rotationnelles de plusieurs molécules d'intérêt astrochimique à basse température en particulier les molécules contenant plus de six atomes, le design et la construction du spectromètre a été détaillé dans Hearne et al 2020,<sup>4</sup> le spectromètre fonctionnant en band E a été présenté dans la thèse de Théo Guillaume et publié dans Hays et al 2020.<sup>5</sup> Le spectromètre en bande Ka est caractérisé à travers une série de mesure d'élargissement collisionnel des raies des transitions rotationnelles de cyanure de vinyle et le benzonitrile en collision avec l'hélium à différentes pressions et à température ambiante. Ces mesures contribuent à l'évaluation des effets de collisions sur le signal moléculaire. Le cyanure de vinyle et le benzonitrile sont deux molécules qui ont été détectées dans l'espace interstellaire, mais on sait relativement peu de

---

<sup>4</sup> Hearne, T. S.; Abdelkader Khedaoui, O.; Hays, B. M.; Guillaume, T.; Sims, I. R. A Novel Ka-Band Chirped-Pulse Spectrometer Used in the Determination of Pressure Broadening Coefficients of Astrochemical Molecules. *J. Chem. Phys.* **2020**, *153* (8), 084201.

<sup>5</sup> Hays, B. M.; Guillaume, T.; Hearne, T. S.; Cooke, I. R.; Gupta, D.; Abdelkader Khedaoui, O.; Le Picard, S. D.; Sims, I. R. Design and Performance of an E-Band Chirped Pulse Spectrometer for Kinetics Applications: OCS – He Pressure Broadening. *J. Quant. Spectrosc. Radiat. Transf. In press.*

choses sur leur élargissement collisionnel, surtout comme ces molécules sont des candidats pour les produits de réaction étudiés par la technique CPUF, les transitions importantes dans la bande Ka pour les espèces de cyanure de vinyle et de benzonitrile ont été identifiées et leurs FIDs caractérisées afin de déterminer leurs coefficients d'élargissement de pression dans des flux d'hélium à température ambiante. Le cyanure de vinyle a également été étudié dans un écoulement à basse température et à haute pression dans l'environnement du CRESU.

Les résultats montrent que l'élargissement de pression est une limitation sérieuse qui peut compromettre la détection de signaux micro-ondes dans des milieux à haute densité comme le CRESU, car les collisions, spécifiquement celles entre le radiateur et le gaz porteur (perturbateur), peuvent réduire le temps de relaxation de la population, et peuvent même conduire à des relaxations sans émission. Les FIDs enregistrés montrent une atténuation croissante du signal moléculaire sous l'effet de la collision induite par l'augmentation des pressions du gaz porteur dans le flux.

Des études antérieures de l'élargissement collisionnel avec l'hélium comme perturbateur avec le cyanure de méthyle ( $\text{CH}_3\text{CN}$ ), le cyanoacétylène ( $\text{HC}_3\text{N}$ ), et le cyanure d'hydrogène ( $\text{HCN}$ ) sont utilisées pour comparer avec les résultats d'élargissement de pression présentés dans ce travail. La comparaison révèle une tendance générale d'augmentation des taux d'élargissement de la pression avec l'augmentation de la taille des molécules. Les constantes pour les transitions du cyanure de vinyle sont similaires à celles du cyanoacétylène, ce qui serait attendu étant donné la similitude de taille et de composition des deux molécules. Si l'on s'intéresse aux molécules plus lourdes, qui présentent un intérêt pour le projet CRESUCHIRP utilisant le spectromètre à bande Ka, on observe une augmentation significative de l'élargissement de la pression pour le benzonitrile par rapport aux molécules plus petites comme le cyanure d'hydrogène. La préoccupation pour l'étude d'une telle molécule dans un environnement tel qu'un jet CRESU est l'augmentation de l'élargissement de la pression à des températures plus basses ce qui implique que le benzonitrile serait extrêmement difficile à détecter dans un jet CRESU à haute pression.

Bien que le cyanure de vinyle ait été détecté avec succès dans un flux froid du CRESU à 18,7 K à partir d'un flux d'une source liquide, aucun signal de cyanure de vinyle en

tant que produit de réaction de l'éthylène et du radical cyano n'a été détecté dans le jet uniforme y compris avec le spectromètre à bande E. Ceci renvoie aux jets à plus hautes pressions dans les conditions du CRESU qui raccourcissent la durée des FID à des centaines de nanosecondes au lieu de microsecondes.

Afin de pouvoir étudier les réactions potentielles en multicanal et de réaliser des mesures sensibles des produits de réaction qui peuvent être obtenus à de très faibles concentrations, des procédures d'optimisation doivent être menées sur deux axes, tout d'abord l'amélioration de la sensibilité des spectromètres, qui a été discutée dans la thèse de Théo Guillaume pour le spectromètre à bande E, quant au spectromètre à bande Ka il sera discuté dans un travail futur. Le deuxième axe, qui est abordé dans ce travail, consiste à agir sur les conditions du jet CRESU et à développer des techniques pour adapter la technique classique du CRESU et la rendre apte à être couplée avec différents instruments de détection et en particulier des spectromètres à micro-ondes et à ondes millimétriques où la détection du signal moléculaire dans le CRESU est limitée par l'élargissement du a la pression.

## **v. Chapitre V : l'appareil SKISURF**

La détermination des rapports de branchement des réactions pertinentes pour l'astrochimie nécessite de pouvoir effectuer des détections sensibles de multiples produits réactionnels à l'échelle de temps de la réaction élémentaire étudiée. Dans ce travail on étudie la réaction du CN avec l'éthylène, qui est une réaction potentiellement à deux voies qui produit du cyanure de vinyle et du HCN à partir de la première et la deuxième voie respectivement. Aucun produit n'a été détecté dans les conditions de CRESU classique, ceci confirme donc les mesures d'élargissement de la pression présentées dans le chapitre précédent et la façon dont son effet est renforcé par la taille de la molécule et l'environnement à haute pression, provoquant une extinction rapide du signal moléculaire dans le domaine temporel en raison de la perte rapide de cohérence due aux collisions entre le cyanure de vinyle et le gaz porteur (hélium ou argon).

Afin de réduire l'effet de l'élargissement collisionnel, SKISURF (Skimmed uniform Supersonic Flow), une nouvelle installation a été développée et construite qui repose sur le concept d'échantillonnage par faisceau moléculaire, où une petite partie du cœur isentropique du jet CRESU à une pression relativement élevée est échantillonnée dans

un environnement à vide plus élevé. Le jet CRESU, déjà subi une première détente par la tuyère de Laval, est amené à une seconde détente par un skimmer dans une chambre nouvellement conçue sous pompage constant. La température et la pression du gaz sont abaissées, ce qui réduit le taux de collision et dépeuple les niveaux d'énergie supérieurs, conditions qui contribuent à renforcer le signal moléculaire des transitions couvertes par nos deux spectromètres. Les réactions d'intérêt auront toujours lieu dans l'environnement du CRESU tandis que le sondage est effectué dans cette nouvelle chambre. Ceci permet d'étudier des réactions à des températures plus élevées et à des pressions différentes tout en étant capable de détecter les produits puisque le sondage est découplé de l'environnement de la réaction, étant effectué dans des conditions de température et de pression plus basses.

SKISURF est l'une des deux solutions développées dans ce travail pour augmenter la sensibilité de nos spectromètres en améliorant la technique CRESU. Avec la nouvelle installation développée, la température et la pression ont été réduites au minimum optimal avec le skimmer de 4 mm, la pression est abaissée de près de 30 fois par rapport aux conditions du CRESU, ce qui a permis la détection de nouveaux produits de réaction et la détermination de leur rapport de branchement correspondant, la température dans le nouvel environnement de sondage est 4.8 K.

Le cyanure de vinyle a été détecté en tant que produit du premier canal de la réaction avec un rapport signal/bruit de 24. Un rapport assez élevé qui nous a permis de déterminer la densité du produit en calibrant avec un signal enregistré à partir d'une source de cyanure de vinyle de densité bien connue, dans les mêmes conditions et avec la même analyse. Pour déterminer l'efficacité de la seconde voie de la réaction, nous avons sondé le HCN et le cyanure de vinyle en même temps. A noter que la transition du HCN est la seule transition existante dans la bande E. Les mesures montrent que la première voie de la réaction qui produit le cyanure de vinyle est efficace de 97.3% quand à HCN, il est produit à 2.7%, résultat en accord avec les travaux de Trevitt et al<sup>6</sup> et Gannon et al<sup>7</sup> qui ont suggéré que la formation de HCN sera

---

<sup>6</sup> Gannon, K. L.; Glowacki, D. R.; Blitz, M. A.; Hughes, K. J.; Pilling, M. J.; Seakins, P. W. H Atom Yields from the Reactions of CN Radicals with C<sub>2</sub>H<sub>2</sub>, C<sub>2</sub>H<sub>4</sub>, C<sub>3</sub>H<sub>6</sub>, Trans-2-C<sub>4</sub>H<sub>8</sub>, and Iso-C<sub>4</sub>H<sub>8</sub>. *J. Phys. Chem. A* **2007**, *111* (29), 6679–6692. .

<sup>7</sup> Trevitt, A. J.; Goulay, F.; Meloni, G.; Osborn, D. L.; Taatjes, C. A.; Leone, S. R. Isomer-Specific Product Detection of CN Radical Reactions with Ethene and Propene by Tunable VUV Photoionization Mass Spectrometry. *International Journal of Mass Spectrometry* **2009**, *280* (1), 113–118

inférieure à 5%, et qu'elle peut être augmentée avec de plus grands hydrocarbures insaturés tels que le propène comme réactifs.

La détection du cyanure de vinyle, une molécule relativement lourde, montre que la liste des produits de réaction pouvant être étudiés peut-être étendue à la bande Ka pour des molécules plus grandes comme le benzonitrile et la pyridine.

Le système SKISURF présente quelques limitations : le gain de pression se fait au détriment de la densité, car la pression ne peut pas être abaissée à son minimum étant donné que la densité suivrait également, ce qui affaiblit le signal moléculaire. Le fait que seules les régions de 4 mm de diamètre ou moins de la section transversale de l'écoulement soient sondées dans les conditions du skimmer est un facteur limitant majeur qui démontre qu'il y a encore des améliorations possibles avec d'autres techniques qui peuvent surmonter ces limitations.

## **vi. Chapitre VI : System de tuyère de Laval pulsée**

Avec les limitations présentées par le SKISURF, il était judicieux de développer un système plus efficace où l'on peut contrôler tous les paramètres d'écoulement contribuant au signal moléculaire (pression, température, densité et débit massique). La technique du CRESU utilise de grands débits massiques pour soutenir l'uniformité des flux générés, ce qui nécessite une capacité de pompage importante ( $32\ 000\ \text{m}^3\ \text{h}^{-1}$  pour le CRESUCHIRP), fonctionnant en continu pour maintenir les pressions les plus basses possibles qui restent néanmoins supérieures à celles atteintes avec d'autres techniques de refroidissement utilisant des débits plus faibles. La cinétique des réactions d'intérêt est de l'ordre de centaines de microsecondes, et le laser excimer qui déclenche ces réactions fonctionne à une fréquence de répétition maximale de 100 Hz en laissant un délai de 10 ms entre chaque impulsion, ce qui donne un rapport cyclique très faible. Le fait de pulser les flux du CRESU à une fréquence correspondante peut donc être d'une grande utilité, tout d'abord le débit massique du gaz sera abaissé à la durée de l'impulsion en un cycle de service, ce qui présente un avantage économique notamment pour les réactifs coûteux utilisés et les énormes quantités de certains tampons comme l'hélium. Mais le plus important est que l'augmentation de la capacité de pompage effective permettra d'établir des jets supersoniques uniformes à basse pression, ce qui réduira l'effet d'élargissement du a la pression qui affaiblit le signal moléculaire. Enfin, et grâce à la possibilité d'augmenter

le rapport de pression entre le réservoir et la chambre, des jets à plus basse température peuvent être établis.

Contrairement à la technique de la détente secondaire, l'utilisation d'écoulements pulsés au lieu d'écoulements continus permet de réduire la pression en augmentant l'efficacité du pompage sans qu'il soit nécessaire de mettre en œuvre des pompes supplémentaires. Un autre avantage technique est qu'elle le fait en réduisant la consommation du gaz tampon principal et des réactifs alors que dans les détentes secondaires à partir d'écoulements CRESU continus, le gaz non échantillonné est évacué et donc perdu. En outre, avec la technique du jet pulsé, la réaction étudiée et le sondage des produits se déroulent dans le même environnement, ce qui permet de capter le signal de tout le volume couvert par les antennes du spectromètre. Ceci était l'une des limitations qui affectait de manière significative le signal moléculaire dans l'environnement de la détente secondaire, où seules les espèces échantillonnées à partir d'un noyau de 4 mm de diamètre, limité par la géométrie du skimmer, pouvaient être sondées.

Le système développé consiste à placer un hacheur aérodynamique devant la tuyère de Laval pour pulser les flux de gaz, un disque d'obstruction perforé tournant à une fréquence donnée, le disque bloquera ainsi la détente du gaz vers la chambre du CRESU jusqu'à ce que l'orifice du disque rencontre la tuyère permettant au gaz de s'écouler de manière similaire à une valve pulsée.

Le premier signal enregistré avec le Pitot rapide est celui de la tuyère N2-30K-0.183, une caractérisation de la tuyère a été effectuée en mode continu pour servir de comparaison adéquate avec le mode pulsé. La pression d'impact a été mesurée à différentes distances de la sortie de la tuyère en utilisant un tube de Pitot rapide. Le profil de température le long de l'axe de la chambre est ensuite déterminé en mode continu et en mode pulsé ; les températures moyennes sont similaires dans les deux modes dans la plage d'erreur. Les tests primaires montrent des résultats prometteurs avec un gain de 7,1 comme montré par Table VI-1, ce gain peut être augmenté en optimisant l'assemblage de montage pour réduire les fuites, ceci peut être réalisé par des ajustements appropriés du disque pour tenir compte de son profil non plan, l'option de rectification de la surface du disque est considérée.

La tuyère d'hélium à 6 K qui est désignée pour fonctionner seulement en mode pulsé sera caractérisée par des mesures de pression d'impact à l'aide du capteur de pression rapide.

▪ **Fonctionnement avec le spectromètre (CP-FTmmW)**

Pour les mesures rapides de Pitot, l'impulsion de gaz est détectée avec le capteur de pression rapide qui mesure la pression d'impact. Le couplage du système pulsé avec nos spectromètres CP-FTmmW nécessite l'utilisation d'un instrument de détection qui déclenche le spectromètre lorsque l'orifice du disque est ouvert sur la tuyère de Laval. Une fibre optique sera donc utilisée alimentée par une source lumineuse, la lumière réfléchie est reçue par un détecteur de gain PDA36A2 de Thorlabs équipé d'une connexion BNC, ce dernier est connecté à un générateur de délai qui déclenche le spectromètre, la chaîne de synchronisation est alors maintenue de manière similaire à celle utilisée dans les mesures précédentes.

• **Conclusion**

Les travaux rapportés dans cette thèse s'inscrivent dans le cadre du projet CRESUCHIRP à Rennes mettant en œuvre la détection par la spectroscopie CP-FTmmW des produits de réaction dans des écoulements supersoniques uniformes à basses températures. Il a porté sur la construction et la caractérisation d'un nouveau CP-FTmmW spectromètre en bande Ka se concentrant sur l'effet de la pression sur le signal moléculaire. Il a été démontré que pour détecter efficacement de très faibles concentrations de molécules polyatomiques de la taille du cyanure de vinyle et plus, il est nécessaire de modifier les conditions d'écoulement classique du CRESU afin de réduire l'effet négatif de l'élargissement des raies dû à la pression sur le signal moléculaire. Deux instruments de ce type ont été conçus, construits et caractérisés: une chambre de détente secondaire (SKISURF) et un système de tuyère de Laval pulsée.

Le processus de la détente secondaire utilisant un skimmer s'est avéré efficace, l'appareil SKISURF a permis de déterminer le rapport de branchement de la réaction CN + éthylène et a permis la mesure sensible de ses produits, une molécule relativement grande comme le cyanure de vinyle a été détectée ainsi que le HCN qui est produit à faible concentration, tous deux avec un rapport signal/bruit élevé. La

détection du cyanure de vinyle dans ces conditions souligne l'importance de réduire l'élargissement du à la pression et son impact sur le signal moléculaire étant donné l'incapacité de pouvoir le détecter dans le jet uniforme dans les conditions du CRESU classique. Quant au HCN, il montre l'avantage de réduire la température dans le milieu de sondage même s'il est produit à une température relativement plus élevée de 35 K. Nous notons que le HCN n'a pas pu être détecté dans un flux d'argon à 30 K et 0,082 mbar dans les conditions du CRESU classique.

L'appareil SKISURF offre donc la possibilité d'étudier des systèmes à pression et température relativement élevées dans les conditions du CRESU, tout en étant capable de détecter le signal moléculaire en effectuant le sondage dans un environnement beaucoup plus favorable au signal micro-onde. L'abaissement de la pression par contre est limité par la densité, en effet il est aussi important de disposer d'un nombre suffisant de molécules pour le sondage que d'abaisser la pression. Ceci est clairement illustré par la réduction du rapport signal/bruit des spectres de cyanure de vinyle lors de la détente secondaire du gaz à l'aide des skimmers de faible diamètres.

Le système pulsé est particulièrement efficace à ce stade car la pression peut être abaissée autant que le permet le gain géométrique donné par le hacheur aérodynamique, avec la possibilité de maintenir une densité de colonne efficace à sonder et donc un rapport signal/bruit élevé.

- **Perspectives**

Le développement de l'appareil SKISURF a ouvert la porte à l'étude de systèmes impliquant des hydrocarbures plus importants, ce qui a conduit à la détection sensible du cyanure de vinyle et du HCN provenant de la réaction  $\text{CN} + \text{éthylène}$ . La réaction  $\text{CN} + \text{propène}$ , un système comportant 7 voies à travers lesquelles peut procéder, a également été ciblée et le cyanure de vinyle a été détecté dans des conditions de détente secondaire à l'aide de la tuyère Ar-35K-0.28. La réaction  $\text{CN} + \text{éthylène}$  a été utilisée pour l'étalonnage en supposant que le cyanure de vinyle était produit à  $\sim 100\%$  par la première voie de la réaction. Les résultats montrent que la voie de formation du cyanure de vinyle de la réaction  $\text{CN} + \text{propène}$  est efficace d'environ 23%. D'autres mesures doivent être effectuées pour déterminer les efficacités des autres voies. Plus de détails peuvent être trouvés dans la thèse de Divita Gupta.

Des résultats provenant de la procédure de photolyse de l'ozone effectuée avec l'appareil SKISURF, ont ouvert la possibilité d'étudier les réactions impliquant des radicaux d'oxygène plutôt que le radical cyanure qui présentait des limitations liées à la faible section de photo-absorption en plus des difficultés techniques rencontrées pour maintenir une concentration stable au cours des mesures. Cependant, le précurseur d'ozone, étant un gaz et ayant une section de photo-absorption supérieure de plus d'un ordre de grandeur, peut être un candidat potentiel pour des travaux futurs.

D'autre part, un nouveau projet est également en cours de développement pour étendre la gamme de fréquences de fonctionnement actuelle du spectromètre de la bande E à des bandes de fréquences plus élevées ciblant des molécules plus petites, et donc moins sensibles à l'élargissement du  $\alpha$  la pression.